The University Of Sheffield.

Adaptive Modelling and Image-Based Monitoring for Artificially Ventilated Patients in the Intensive Care Unit (ICU)

A thesis submitted to the University of Sheffield for the degree of Doctor of Philosophy

By

SITI HAZURAH INDERA PUTERA

Department of Automatic Control and Systems Engineering
The University of Sheffield

OCTOBER 2018

Abstract

The Intensive Care Unit (ICU) is where the critically-ill are treated. The first 24-hours ('the golden hours') of treatment is crucial to determine patient's recovery and survival, and mechanical ventilation plays a major role as the main life support system in the ICU. The efficiency of mechanical ventilation and its management strategy are assessed by observing the arterial blood gases (ABG), which are sampled every few hours using a catheter inserted into the patient's artery. This procedure is invasive thus can only be performed a handful of times each day. The ICU also has an abundance of underutilized data which until recently can only be translated by expert clinicians, who unfortunately always have clinical responsibilities to undertake concomitantly.

This thesis proposes a series of new fuzzy logic-based models with a new type of fuzzy sets (type-2), which have not been investigated before in this clinical setting, for the relative dead-space (Kd), the carbon-dioxide production (VCO_2), and the shunt sub-components for the SOPAVent (Sheffield Simulation of Patients under Artificial Ventilation) system, which performs predictions of arterial blood gases non-invasively and automatically. The Kd model, the VCO_2 model and the resulting overall SOPAVent model are validated with retrospective real ICU patient data obtained from the Sheffield Royal Hallamshire Hospital (UK). The SOPAVent model is also validated with newly obtained data from patients diagnosed with Faecal Peritonitis (FP), from the Sheffield Royal Hallamshire Hospital (UK). Results showed an improved prediction accuracy for the Kd and the VCO_2 sub-components when compared to existing systems. The prediction capability of SOPAVent is also improved from previous models for arterial blood gases before and after ventilator settings changes are made.

A second new simplified model for predicting ABG using ventilator settings is also proposed with excellent prediction outcomes. Additionally, this thesis also looks into Electrical Impedance Tomography (EIT) as a potential bedside monitoring tool for pulmonary functions. EIT has the ability to provide a non-invasive, portable, and a relatively low cost alternative to other medical imaging systems. This thesis details the

development of the hardware for a compact 16-electrode EIT measurement system, with the objective for future pulmonary applications. A method to generate three-dimensional (3D) images of the lungs from two-dimensional (2D) medical images of the thorax is also proposed with the estimation of lung volumes being presented.

Acknowledgements

In the name of Allah, the most Gracious, the most Merciful. Praise be to Him for His blessings that have granted me knowledge and strength to complete this journey.

My greatest appreciation goes to my supervisor, Professor Mahdi Mahfouf, for his precious guidance, knowledge and patience throughout this research.

I would also like to give a special appreciation to Professor Gary Mills, the consultant anaesthetist, for his clinical knowledge and support and to Paul Eastwood for his technical help during the development of the EIT system.

I am also grateful to Majlis Amanah Rakyat (MARA), Malaysia for sponsoring my study.

Last but not least, my heartfelt appreciation goes to my loving and understanding family. My husband, Armi for his patience and support, my beloved parents Indera and Azizah for their wisdom and prayers. May Allah reward them with great happiness in this life and the next.

List of Figures

List of Tables

Abbreviations

FP	Faecal Peritonitis
GDF	Gas Dissociation Function
GPSR	Gradient Projection for Sparse Reconstruction
Hb	Haemoglobin Concentration
HCO_3	Bicarbonate
HiFlo	High-flow Face Mask Oxygen
HR	Heart Rate
I:E	Ratio of Inspiratory Time to Expiratory Time
ICU	Intensive Care Unit
INVENT	The Intelligent Ventilator
IT2FLS	Interval Type-2 Fuzzy Logic System
Kd	Relative Dead-space
LMF	Lower Membership Function
LoFlo	Low-flow Face Mask Oxygen
MAE	Mean Absolute Errror
MF	Membership Function
MRI	Magnetic Resonance Imaging
MSE	Mean Squared Error
MV	Minute Volume
NHS	National Health Service
NIV	Non-invasive Ventilation
nPSO	New Structure Particle Swarm Optimization
O_2	Oxygen
PAC	Pulmonary Artery Catheter
$PaCO_2$	Arterial Partial Pressure of Carbon-dioxide
PAO_2	Alveolar Partial Pressure of Oxygen

PaO_2	Arterial Partial Pressure of Oxygen
P_b	Atmospheric Pressure
PCB	Printed Circuit Board
PCG	Preconditioned Conjugate Gradient
PCO_2	Partial Pressure of Carbon Dioxide
PCV	Packed Cell Volume
PDE	Partial Differential Equation
PDMS	Patient Data Management System
PEEP	Positive End-expiratory Pressure
pH	Acid-base Measurement
Pinsp	Inspiratory Pressure
PIP	Peak Inspiratory Pressure
Pmean	Mean Airway Pressure
PO_2	Partial Pressure Of Oxygen
$PpCO_2$	Pulmonary Partial Pressure of Carbon-dioxide
PSO	Particle Swarm Optimization
R^2	Correlation Coefficient
Raw	Airway Resistance
RI	Respiratory Index
RQ	Respiratory Quotient
RR	Respiratory Rate
SD	Standard Deviation
SIVA	Sheffield Intelligent Ventilator Advisor
SOPAVent	Simulation of Patient under Artificial Ventilation
SpO_2	Oxygen Saturation of the Blood
T_I	Inspiratory Time
TOP	Threshold Opening Pressure
T2FLS	Type-2 Fuzzy Logic System
UMF	Upper Membership Function

V/Q	Ventilation-perfusion Ratio
VCC	Voltage to Current Converter
VCO	Voltage-controlled Oscillator
VCO_2	Carbon-dioxide Production
V_D	Physiological Dead-space
VO_2	Oxygen Consumption
VT	Tidal Volume
αb	Oxygen Carrying Capacity Of The Blood
βh	Haemoglobin Oxygen Binding Capacity

Table of Contents

Chapter 4
Fuzzy C-Means Clustering Models for Relative Dead-Space and Carbon-dioxide Production and Validation of the SOPAVent Blood Gas Model

Chapter 5
Validation of Blood Gas Models for Patients with Faecal Peritonitis

Chapter 1

Introduction

1.1 Research motivation

1.1.1 Blood Gas Sampling for Artificially Ventilated Patients in the Intensive Care Unit

The intensive care unit (ICU) is where severely-ill patients requiring constant monitoring are treated. Patients are usually admitted to the ICU to recover following major surgery, or when one or more of their organs fail from injuries or serious infections. Between 2015 and 2016 the UK National Health Service (NHS) estimated that 270,000 adults were admitted into ICUs in England, with 75% of them being above 50 years old. Each year an estimated 20% of patients admitted to the ICU did not survive to leave the ICU (ICNARC report, 2013/14). The first 24 hours (the so-called 'golden hours') of care is the most critical, and will eventually determine the outcome of the patient. However, due to severe constraints on health services, patients in the ICU are monitored by only a few nurses, who have many tasks to perform concomitantly and are of varying levels of seniority and experience. The intensive care medical staff are spread thinly, with responsibility for seeing critically-ill patients inside and outside the ICU.

Artificial ventilation plays a key role as the main life support system for patients in the ICU. The NHS estimated that 45% of patients admitted to the ICU require respiratory support from artificial ventilators. Artificial ventilation aids spontaneous breathing, and can also take over the normal breathing functions for patients who are unable to do this for themselves. Patients are usually artificially ventilated when they suffer from respiratory failure, circulatory failure or neurological failure. Clinicians optimize ventilator settings to ensure appropriate oxygenation,

which would allow tissues to metabolize effectively, and at the same time would try to reduce the risk of ventilator induced injuries to the lungs, trachea or vocal cords.

To evaluate the efficiency of artificial ventilation, blood samples are taken from the patient's arteries, usually every two to three hours. Blood samples are also taken from the veins, although much less frequently. Blood gas analysis is performed on the blood samples to determine the partial arterial pressure of oxygen (PaO_2), the partial arterial pressure of carbon-dioxide ($PaCO_2$) and the acid-base levels (pH). When necessary, adjustments in ventilator settings are made following the blood gas results to ensure proper oxygenation is achieved.

Changes in ventilator settings can induce a response in blood gas parameters in as early as 30 minutes. However, verification of this can only be carried-out when the next blood sampling is due in two or three hours. The procedure to take arterial blood samples is invasive: a catheter must be inserted to the artery at the wrist, or other parts of the body if the artery at the wrist cannot be accessed. Careful consideration is usually given before this procedure is performed. These considerations can include the quality of blood supply, i.e. poor blood supply or blood clots and damaged arteries, and sometimes this may be challenging in the awake patient, especially if they are very young or confused. These factors can potentially reduce the number of blood gas samples for a 24-hour period which lead to a lack of knowledge of the blood gases qualities. A ballpark estimation of blood gases however, may lead to the wrong clinical decisions being made.

The ICU generates data from multiple sources, some of which can only be interpreted and cross-correlated by expert clinicians. Unfortunately, clinicians, often become very busy, with other clinical and non-clinical duties. These data include measurements of physiological parameters, medication dosage and frequency, ventilator settings, sensor readings, and results from tissue, urine and blood analyses. An objective and evidence-based approach towards interpreting this rich data can help towards the strategy for patient recovery and survival. An automatic and non-invasive blood gas prediction tool is highly desired to bridge the time gap and information between actual blood gas analyses. Furthermore, computerization can relieve tedium for clinicians and nurses, so they can focus on other more critical decisions.

1.1.2 Electrical Impedance Tomography for a Non-invasive Bedside Monitoring of the Lungs

The management of ventilated patients is achieved through the optimal setting of ventilator parameters, such as the tidal volume (VT), the positive-end expiratory pressure (PEEP) and the inspiration time (Tinsp). The patient's physiological information, the result of blood gas samplings, and the measurements of pressures and volumes obtained by the artificial ventilator provide the gold standard for assessing the global functions of the lungs, and ultimately guide the decisions taken by clinicians in ventilator management strategy.

However, blood gas sampling and ventilator measurements alone do not provide clinicians with enough information regarding regional lung behaviour. Thus, imaging techniques such as x-ray, computed tomography (CT), and magnetic resonance imaging (MRI) are used to provide a comprehensive representation of the regional lung condition. Unfortunately, some of these imaging techniques expose the patients to harmful radiations and involve transporting critically-ill patients outside of the ICU. These imaging techniques are also costly and labour intensive. Thus, the case for an alternative for a portable, safe and a non-invasive bedside monitoring approach for the imaging of the lungs can easily be made.

Electrical Impedance Tomography (EIT) aims to reconstruct the spatial image of the lungs by mapping the internal distribution of conductivities within the thorax. This is done by placing a set of electrodes at equal distances around the circumference of the thorax. A small alternating current is injected via one pair of adjacent electrodes and measurements are taken from all other adjacent electrode pairs. EIT is non-invasive and radiation free, and allows for the estimation of the lung's absolute resistance, which is then used to derive the lung volume and lung density. Relative EIT however, allows for comparison of impedances at two different times and can be translated into images. These images can be used in tracking the process of respiration during artificial ventilation. The merging of EIT imaging and the estimation of lung volume and lung density from EIT, with blood gas predictions and interval blood gas samplings, and ventilator measurements can provide clinicians

with an increased knowledge on the lungs' regional and global behaviour. This may lead to the improved quality for the management of artificially ventilated patients in the ICU.

1.2 Aims and Objective of the Research

The main objective of this thesis is to improve existing blood gas models for ventilated patients and validation of these models with real ICU patient data. In this thesis an EIT measurement system for pulmonary application is also proposed. Several sub-objectives are outlined as follows:

1. To further improve the prediction accuracy of the relative dead-space (Kd) model, the carbon-dioxide production (VCO_2) model, and the shunt model of SOPAVent, and to validate the Kd, VCO_2, and shunt models with real ICU patient data.

2. To integrate the VCO_2, Kd and shunt models into the SOPAVent system for the prediction of partial arterial pressure of oxygen (PaO_2), the partial arterial pressure of carbon-dioxide ($PaCO_2$), and the acid-base measurement (pH) of arterial blood gases, and to systematically validate the SOPAVent blood gas models with retrospective ICU patient data and some newly obtained ICU patients' data.

3. To model the relationship of ventilator settings to arterial blood gas parameters for the newly obtained ICU patients' data using the synergy between expert knowledge and a data driven approach.

4. To investigate the Electrical Impedance Tomography (EIT) as a potential bedside monitoring tool for pulmonary applications and to develop the hardware of an EIT system.

5. To estimate the lung volume from 2D conventional magnetic resonance (MRI) and computed tomography (CT) medical images of

the human thorax and to perform 3D rendering of the lungs from 2D MRI and CT medical images of the human thorax.

1.3 Outline of thesis

This thesis is distributed over seven chapters.

Chapter 2. Literature Review

This chapter is divided into two major sections. The first section discusses pioneering work and current trends in blood gas modelling for ventilated patients in the ICU. The second section describes previous and recent works involving the application of electrical impedance tomography (EIT) for pulmonary monitoring.

Chapter 3. Evolutionary Fuzzy Type-2 Blood gas Models for Ventilated Patients in ICU

This chapter provides in detail the modelling of the relative dead-space (Kd), the carbon-dioxide production (VCO_2) and the shunt using interval type-2 fuzzy logic system (IT2FLS). The Kd, the VCO_2 and the shunt models are further improved using the 'new structure' particle swarm optimization (nPSO) and is validated using real ICU patient data. A performance comparison with previously developed models is also provided.

Chapter 4. Fuzzy C-means Clustering (FCM) for Kd and VCO_2 Models and Validation of SOPAVent with ICU Data

In this chapter, the fuzzy c-means clustering (FCM) algorithm is employed to model the Kd and the VCO_2 subcomponents. The Kd, the VCO_2 and the shunt models are integrated into the SOPAVent (Simulation of Patients under Artificial Ventilation) model for the prediction of partial arterial

pressure of oxygen (PaO_2), the partial arterial pressure of carbon-dioxide ($PaCO_2$) and the acid-base measurement (pH) of arterial blood gases. The SOPAVent blood gas model is validated using real ICU patient data and the performance comparison of different Kd, VCO_2 and shunt models in SOPAVent is also presented.

Chapter 5. Validation of Blood Gas Models for Patients with Faecal Peritonitis

This chapter provides the results of the SOPAVent blood gas models for the prediction of PaO_2, $PaCO_2$ and pH blood gas parameters on newly obtained ICU patient data, where patients were diagnosed with faecal peritonitis. This chapter also details a simplified modelling approach of blood gas components of PaO_2, $PaCO_2$ and pH of faecal peritonitis patients' data via an adaptive neural-fuzzy inference system (ANFIS), using ventilator settings as model inputs.

Chapter 6. Electrical Impedance Tomography (EIT) for Monitoring of the Lungs

Chapter 6 details the fundamentals of electrical impedance tomography (EIT) in pulmonary applications, and the development of a microcontroller-based, portable hardware, of a 16-electrode, EIT system. This chapter also describes the process for rendering 3D images of the lungs by utilising 2D medical images such as magnetic resonance imaging (MRI) and computed tomography (CT) images of the human thorax. The estimation of lung volumes using MRI and CT images is also presented in this chapter.

Chapter 7. Conclusion

The final chapter provides an overall summary of works done in the thesis and highlights the achievements of the project. A set of recommendations for future works is also presented.

1.4 Related Publications

Published articles from this research are listed as follows:

Indera-Putera S H, Mahfouf, M, and Mills, G H, (2016). Blood-gas modelling for artificially ventilated patients using interval type-2 fuzzy logic system. XIV Mediterranean Conference on Medical and Biological Engineering and Computing (MEDICON), Cyprus (Published)

Indera-Putera S H and Mahfouf M, (2017). Evolutionary type-2 fuzzy blood gas models for artificially ventilated patients in ICU, 14th international Conference on Informatics in Control. Automation and Robotics, ICINCO, Spain. (Published and received the '**Best Student Paper Award'**)

Indera-Putera S H, Mahfouf M and Mills G H, (2018). Blood gas predictions for patients under artificial ventilation using fuzzy logic models. Lecture Notes in Electrical Engineering, Springer. (In Press)

Chapter 2

Literature Review

2.1 Blood Gas Models and Decision Support for Ventilator Management in the Intensive Care Unit

Mechanical ventilation plays a critical role in the Intensive Care Unit (ICU). The integration of sensor measurements, ventilator settings and other routine clinical data should provide clinicians with information that enables them to implement immediate and appropriate treatments that may save lives. Ventilation management is a complex process involving not only ventilator settings and ventilator measurements, but also the patient's physiological parameters. Large and interdependent dataset generated by the ICU can lead to challenges as the information contained in the dataset can only be interpreted by a small number of expert clinicians. Researches have been focusing on developing Decision Support Systems (DSS), in order to provide clinicians with solutions to integrating and processing the large amount of information in the ICU. Sim *et al.,* (2001) defined DSS as 'a software-based application that matches the patient-specific characteristic to computerised knowledge in order to provide recommendations for clinical decisions'.

DSS for ventilator management can either be an open-loop system or a closed-loop system, with an open-loop system providing advice for clinicians without performing therapeutic actions, while a closed loop system directly executes decisions for ventilator control. The DSS can be either knowledge-based, model-based or a combination of both. A knowledge-based DSS is a computer-based decision support using the expert opinion of clinicians. However, decisions can also vary from one clinician to another based on the clinician's experience, knowledge and standard of practice. Meanwhile, an accurate, and purely model-based system for such a complex process is very hard to achieve. Most parameters required in the mathematical models

are non-linear, while some parameters are not routinely available in the ICU setting. Therefore, a combination of expert knowledge and patient model is seen as rational approach for an accurate and practical system that compensate for the weaknesses of knowledge-based and model-based systems.

The Intelligent Ventilator (INVENT) is a model-based DSS for ventilator settings that was developed by Rees *et al*., (2006), which included a mathematical model for blood gas estimations called ARTY, and a mathematical model for pulmonary gas exchange called ALPE. Figure 2.1 shows the structure of INVENT. ALPE was developed to replace the conventional definition of oxygenation from PaO_2/FiO_2 ratio. ARTY and ALPE simulated the effects of mechanical ventilation strategy on patient's physiological state. INVENT is an open loop DSS that provided ventilator settings advice for the fractions of inspired oxygen (FiO2), the tidal volume (VT), and the respiratory rate (RR), with the inclusion of penalty functions for barotrauma, hypoxia, acidosis/alkalosis and oxygen toxicity.

Allerød *et al*., 2008 performed a validation of INVENT for VT, RR, and FiO_2 ventilator settings using retrospective ICU data. From the simulations performed, the DSS was able to provide reasonable advice when compared to a clinician's decisions, apart for variables concerning oxygenation such as the arterial partial pressure of oxygen (PaO_2) and the oxygen saturation (SpO_2). All parameters were assumed to be constant and the DSS did not account for large changes in ventilation. The system also required the tuning of parameters for individual patients thus limiting the system's generalization properties. Furthermore, all patients used in this study had pulmonary-artery catheters (PAC) inserted.

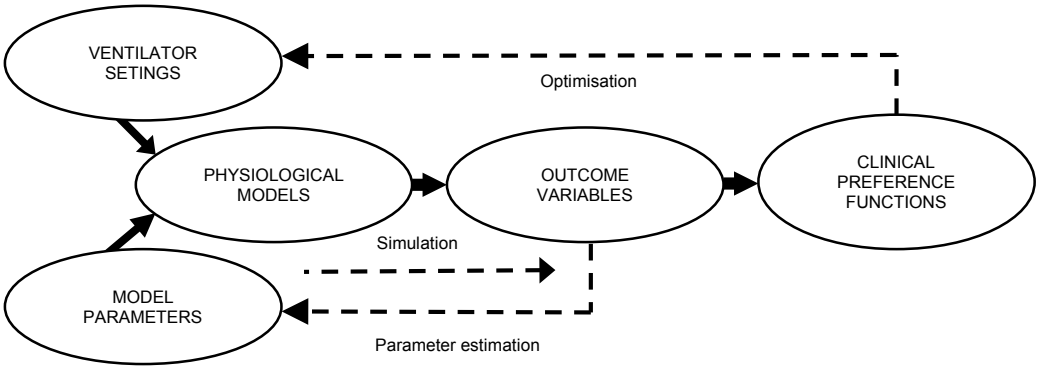

Figure 2.1 The INVENT structure (Rees *et al*., 2011)

An advisory system named FLEX, was developed by Tehrani and Roum, (2008), to provide ventilator settings suggestions and also to provide advice on when patients should be weaned-off ventilators in volume control mode or pressure control mode. FLEX computes the optimal ventilation from the levels of the arterial partial pressure of carbon-dioxide ($PaCO_2$), SpO_2 and body weight, and also provided advice on weaning by checking the patient's parameters. The DSS has been validated with decision made by clinicians. From the simulations performed, FLEX was able to predict the failure of weaning for two patients it suggested not to wean. However, FLEX was not designed to simulate the oxygen and carbon-dioxide transport models but instead derives the parameters of gas exchange from hypotheses. Figure 2.2 shows the structure of the FLEX system.

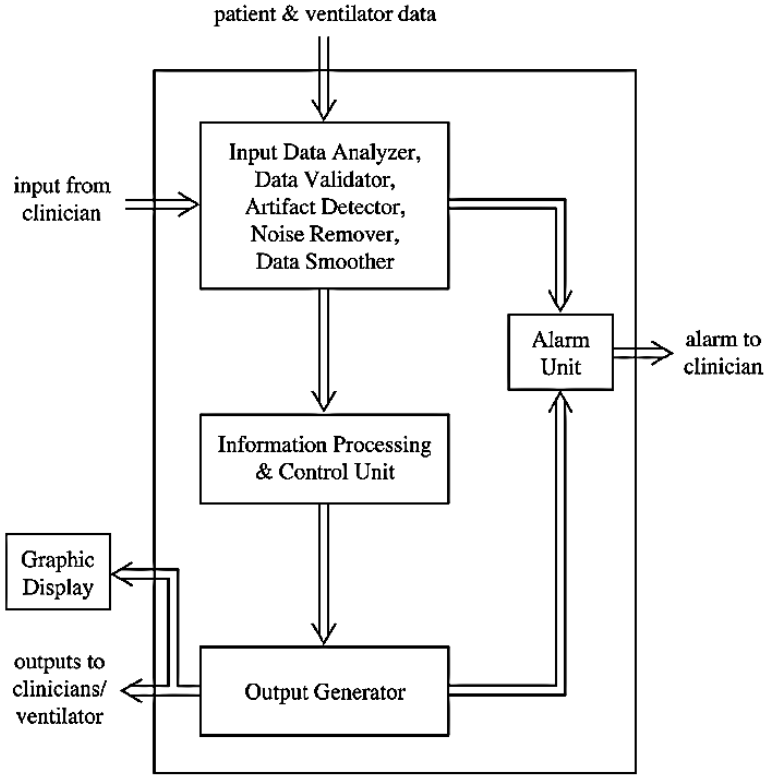

Figure 2.2. The structure of the FLEX system (Tehrani and Roum, 2008).

Kretschmer *et al*., (2014) proposed four models to represent the gas exchange process in ventilated patients. The gas exchange models are shown in Figure 2.3. The first model consisted of the shunt compartment and the alveolar compartment receiving 100% ventilation, and used to simulate the value of PaO_2 only, and was calibrated by deriving shunt from patient data. The second model represented the dead-

space compartment and was used to simulate the value of $PaCO_2$. The third model was a combination of the first and the second model, but it was unable to reproduce the effect of ventilation/perfusion (V/Q) mismatch. The fourth model had fixed perfusion distribution of compartments, and an additional alveolar compartment was included, which resulted in a variable of perfusion distribution amongst the compartments. The respiratory mechanics were developed using a first order R-C model to represent the resistive effect of the lungs and compliant effect of the lung. The system computed the suggestions for RR, FiO_2, inspiration pressure (Pinsp), minute volume (MV), inspiration to expiration (I:E) ratio and inspiration time (Tin). From the simulations performed, the authors showed the system's ability to provide plausible clinical predictions. However, the ventilator settings advice for MV was higher in models two and three for the same target $PaCO_2$. The system also provided multiple recommendations, hence a decision had to be made on which recommendation to use. The system also needed validation with clinical data.

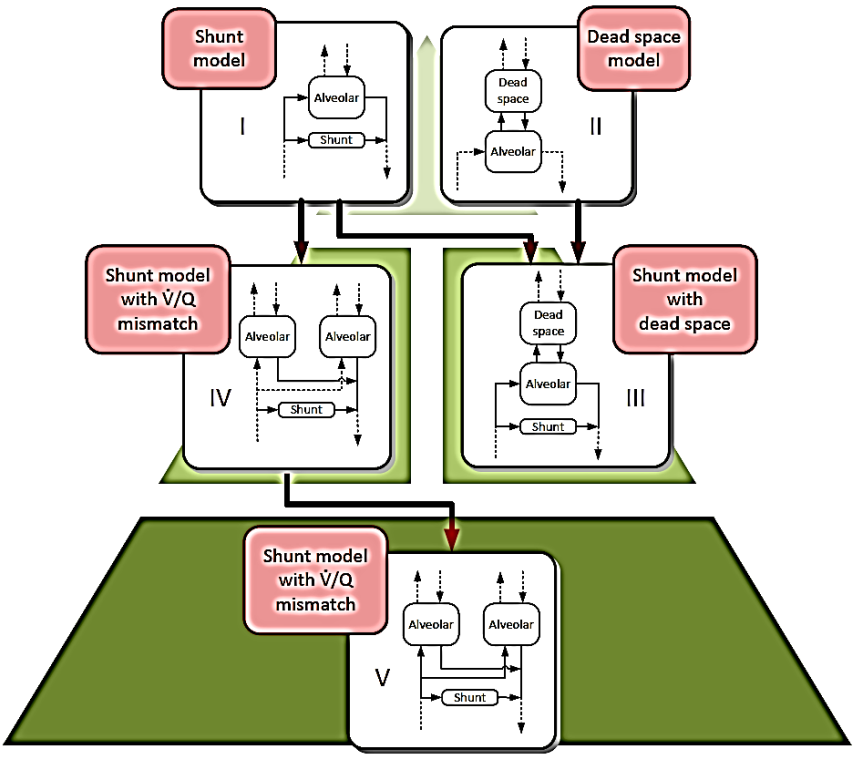

Figure 2.3. The gas exchange models in the decision support for ventilator settings (Kretschmer *et al*., 2014)

The Sheffield's Simulation of Patient under Artificial Ventilation (SOPAVent), is a mathematical model for pulmonary gas transports which was also able to predict the arterial blood gases (ABG) in ventilated patients. It was first developed by Goode, (2000). The blood gases produced by the SOPAVent system were the PaO_2, the $PaCO_2$ and the acid-base measurement, pH. The SOPAVent model was used in a fuzzy logic-based DSS for artificially ventilated patients called FAVEM, which provided suggestions for ventilator settings (see Figure 2.4). The fuzzy rules of FAVEM were hand-crafted through consultations with an expert clinician, and later refined after closed-loop simulations were performed. The DSS produced suggestions for FiO_2, VT, RR and Pinsp ventilator settings. ICU patient data was used to validate FAVEM. The author reported that 23% of the generated advice gave poor results when compared to an expert clinician's decision and suggested further improvements to be made. Some parameters used in SOPAVent such as the cardiac output (CO), the carbon-dioxide production (VCO_2), and the relative dead-space (Kd) also required the use of a metabolic tester, or included invasive procedures, which resulted in a very small number of usable data.

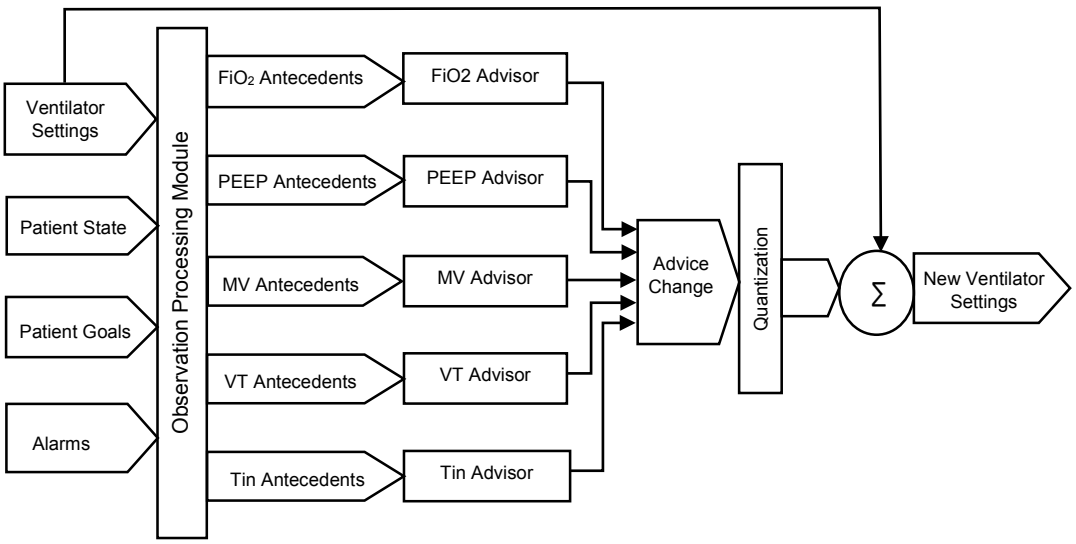

Figure 2.4 Overview of the FAVEM structure (Goode, 2000)

Modifications to the SOPAVent blood gas models were proposed and implemented by Kwok *et al.,* (2001), by replacing the CO and the VCO_2 subcomponents, which initially were obtained from metabolic tester, to estimations from population means. The shunt component was replaced with an adaptive neural-

fuzzy inference system (ANFIS), and the relative dead-space (Kd) component was replaced with a fuzzy model. The advisory system was developed using fuzzy principles and was called the Sheffield Intelligent Ventilator Advisor (SIVA) (Kwok et al., 2004a and 2004b) (see Figure 2.5). The input variables of SIVA were decided upon following discussions with a clinical expert and the fuzzy rules were obtained from observations during simulation studies. SIVA provided advice for the direction of change and the amount of change to be made to the ventilator settings. Real ICU data was used for validation of SIVA. Simulation results showed that SIVA was able to improve the accuracy of FAVEM when the generated advice were validated with the clinician's decisions. However, the use of population means from a limited number of patients significantly reduced the system's ability to predict blood gases when some parameters lie outside of the existing limits.

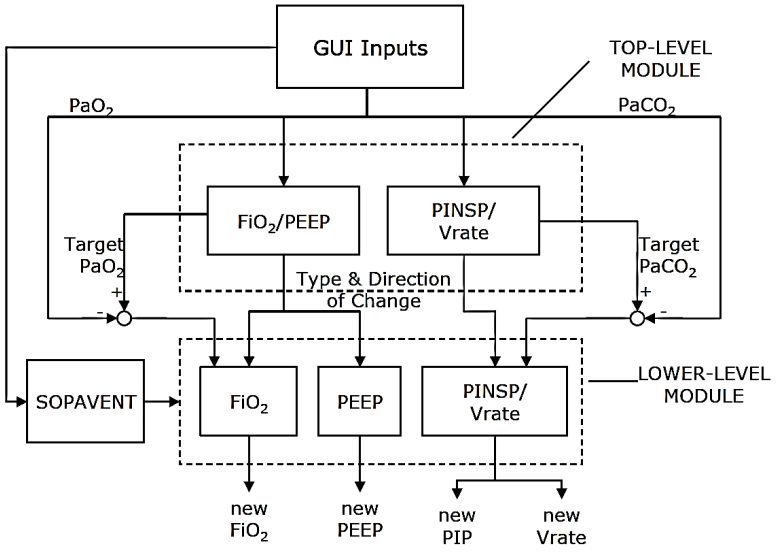

Figure 2.5. The overall system structure of SIVA (Kwok *et al*., 2004a)

Wang *et al.*, (2010a) proposed new models for the Kd and the VCO_2 subcomponents of SOPAVent using ANFIS to improve the accuracy of the blood gas predictions that enabled the elicitation of a non-invasive patient model. This was done using data from a new ventilator that was able to record the measurements of Kd and VCO_2. The blood gas models were then integrated into a DSS for optimizing the ventilator management strategy (Wang 2010b). The objective of the system is to achieve target PaO_2 and $PaCO_2$, while at the same time avoiding excessive airway pressures. Figure 2.6 shows the structure of the proposed DSS. The author also

proposed a patient specific model of SOPAVent that automatically updated the patient's parameters every 30 minutes. Retrospective real ICU data was used to evaluate the DSS. From the closed-looped simulation of the DSS, the author was satisfied of the system's performance. However, the DSS was designed with fixed ventilator targets which were unpractical in real clinical settings. The data-driven approach of the ANFIS models also reduced the system's capability to predict parameters outside of the modelling range.

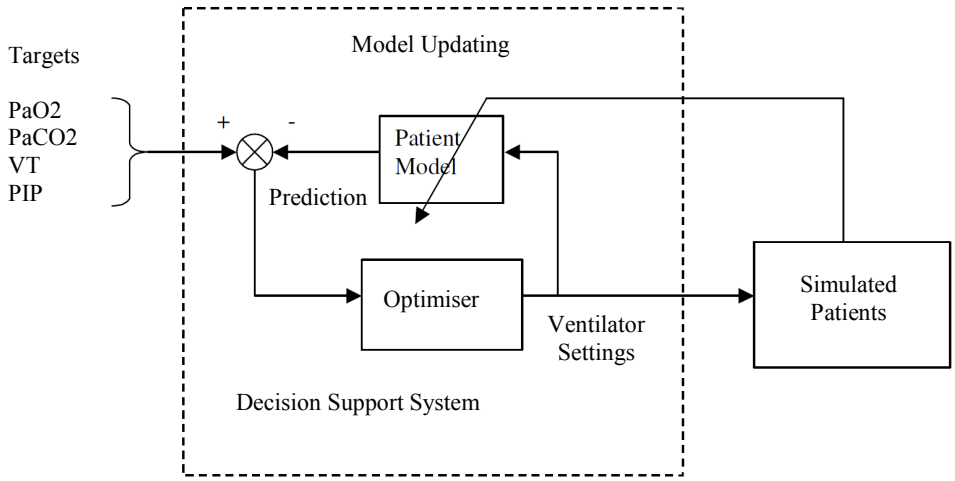

Figure 2.6. Ventilator management decision support system (Wang *et al*., 2010)

Al Otaibi and Hardman (2011), proposed a new mathematical model for predicting the absolute change of magnitude for the arterial blood gas component of PaO_2, at 20 minutes after the change of the FiO_2 ventilator setting, with the assumption that the ratio of PaO_2/FiO_2 and the ratio of PaO_2/PAO_2 remained constant. The prediction results were compared with the absolute change of magnitude for PaO_2 from ABG sampling, and from the estimations using a standard isoshunt diagram. Simulation results showed that the bias and the 95% limit of agreement between the measured change of PaO_2 and the predicted change of PaO_2 for the new model were lower when compared to the bias and the 95% limit of agreement between the measured change of PaO_2 and the estimated change of PaO_2 from the isoshunt diagram. The new model was proposed as an alternative to PaO_2 estimation, however the authors only recommend the use of the model for stable ventilated patients. The model also did not indicate the direction of change of the PaO_2 magnitude.

In summary, blood gas modelling and DSS for mechanical ventilators are promising tools that can provide comprehensive information to clinicians in order to effectively plan the best course of treatment. This is made obvious due to the fact that most ventilators still maintain an open-loop control approach, and clinicians are made responsible to manually select the ventilator settings. Thus, for a DSS to be practical it should validate well against real data, detect and correct artefacts, is applicable to various ventilator modes and should be able to elicit all the ventilator parameters. Most importantly it should be flexible enough to be implemented for a wide range of patients' state, accounting for both intra-patient variability and inter-patient variability.

2.2 Electrical Impedance Tomography for Lung Monitoring

Electrical Impedance Tomography (EIT) is an emerging technology that enables a real-time, non-invasive, and low-cost approach to map the internal conductivity distribution of an object. It is defined by the potential distribution within a conducive volume when current is applied (Brown, 2003). Obtaining the conductivity distributions enables the mapping of unknown structures within the object. Normally, a pair of electrodes are used to inject a low amplitude current into the surface of a conducive object. The generated boundary potentials are then measured by a second pair of electrodes. This is called the four-electrode configuration (Brown *et. al,* 2000). An even number of electrodes are used in the drive-and-measure process.

Electrodes are commonly arranged as an equally-spaced ring around the circumference of an object. Measurements are taken in sequence for every adjacent pair of electrodes (see Figure 2.7 and Table 2.1), while excluding measurements taken from electrodes involved in driving the input current. A total of n^2-$3n$ independent measurements are produced in one complete cycle called a '*frame*', with '*n*' representing the number of electrodes. The number of electrodes can vary from as little as four electrodes to more than a thousand electrodes depending on the type of application, the geometry and size of the object, and if a two-dimensional (2D) plane, or three-dimensional (3D) representation is required. Rods, probes or flexible strips are also used in non-uniformed areas.

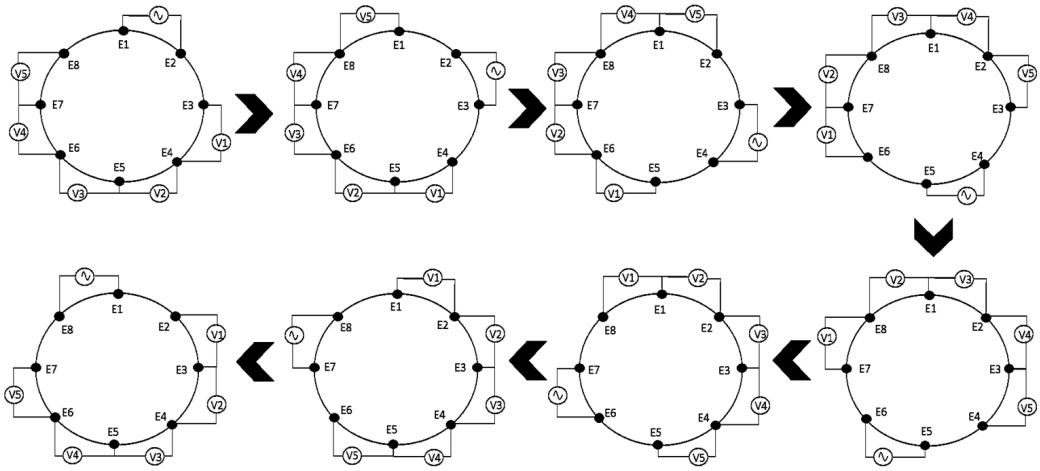

Figure 2.7. An example of an 8-electrode, E_i, (i = 1 to 8) EIT, drive-and-measure sequence producing 40 measurements for each frame

Table 2.1. Voltage measurements, V_k, (k = 1 to 40), for one frame of an 8-electrode EIT system

Measured pair	Drive pair							
	E1 E2	E2 E3	E3 E4	E4 E5	E5 E6	E6 E7	E7 E8	E8 E1
E1 E2	-	-	V_{11}	V_{16}	V_{21}	V_{26}	V_{31}	-
E2 E3	-	-	-	V_{17}	V_{22}	V_{27}	V_{32}	V_{36}
E3 E4	V_1	-	-	-	V_{23}	V_{28}	V_{33}	V_{37}
E4 E5	V_2	V_6	-	-	-	V_{29}	V_{34}	V_{38}
E5 E6	V_3	V_7	V_{12}	-	-	-	V_{35}	V_{39}
E6 E7	V_4	V_8	V_{13}	V_{18}	-	-	-	V_{40}
E7 E8	V_5	V_9	V_{14}	V_{19}	V_{24}	-	-	-
E8 E1	-	V_{10}	V_{15}	V_{20}	V_{25}	V_{30}	-	-

The impedance of a conducive object can be calculated using Ohm's law. If the potentials on the surface are known, the distribution of conductivity within the volume can be obtained. The measured potential and conductivity parameters can be processed to produce an image of the surface boundary and internal profile of the object using methods similar to x-ray or computed tomography (CT). The filtered back projection algorithm (Brown *et al*., 1985) is largely employed to reconstruct a two-dimensional image of a cross-sectional plane. Static reconstruction refers to the generation of absolute conductivities from a single set of measurement, and often referred to as 'absolute EIT'. Dynamic reconstruction is the change of resistivity based on two measurements at different times, or at different frequencies, and is often referred to as 'relative EIT' (Brown *et al*., 2002).

Table 2.2 shows the resistivity of human tissues when injected with a small current at 10 kHz. Blood, muscle, bones and soft tissues are good conductors of electricity. The lung, however is porous, filled with air and is very poor in conducting electricity. During respiration, the conductivity of the lung changes. At high frequencies, the tissues of the lung are made up of only two components; condensed matter and air. Condensed matter has homogenous resistivity, while air has an almost infinite resistivity. It is then possible to calculate the air volume and the lung density, if the lung resistivity is known, and the knowledge of lung volume and lung density can be used to monitor the respiratory process effectively (Brown *et. al*., 2007).

Table 2.2. Resistivity of human tissues at 10 kHz (Brown, 2003)

Type of tissue	Resistivity (Ωm)
Muscle	2 - 4
Fat	20
Lungs	7 – 20 (range due to respiration activity)
Liver	3.5
Blood	1.6
Bone	> 40

Electrical Impedance Tomography is now considered to be an emerging technology in monitoring of pulmonary functions. Its non-invasiveness, portability, minimal and simple construction suggest a promising bedside monitoring support. A portable and non-invasive bedside monitoring systems can reduce the danger of moving critically ill patients and can, as a result, limit their exposure to harmful radiations. Currently, two-dimensional (2D) EIT has proven to be effective in determining lung volume and density using relative and absolute resistivity. It is also able to produce low resolution images of the lung during respiratory activity. In EIT for lung monitoring, electrocardiogram (ECG) electrodes are arranged in equal distances circling the thorax, at approximately 5 cm above the xyphoid process (see Figure 2.8). A small current is injected via one pair of electrodes, and electrical potential measurements are taken from all other adjacent pairs of electrodes. The frequency of the drive current in EIT systems for pulmonary application is typically a single frequency between 1 kHz and 50 kHz (Holder, 2004). EIT systems can also

employ multiple frequencies between 1 kHz and 1 MHz, if any impedances at different frequencies are required.

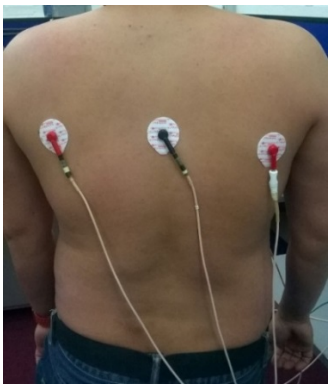

Figure 2.8 ECG electrode placement on the thorax

Riedel *et.al*, (2005) examined the effects of body position on conductivity distribution for subjects on mechanical ventilation using EIT measurements. Supine, prone, left lateral and right lateral body positions were examined. Sulphur hexafluoride washout were used to monitor respiratory activities. Lissajous loop analysis was used to calculate the phase angles between the independent lung and the dependent lung to the total lung distribution and the lung clearance index. The study concluded that the body position did not influence the ventilation of the dependent lung, while the independent lung showed good ventilation in the supine position. It was also reported that both lateral positions showed less tidal volume for the independent lung.

Pulletz *et.al*, (2012) evaluated the effects of peak end expiratory pressure (PEEP) and regional respiratory time constant using EIT on patients under mechanical ventilation. Patients with healthy lung but undergoing surgical procedures were compared to patients with Acute Respiratory Disorder Syndrome (ARDS). A modified Sheffield back projection method was used to reconstruct the EIT images. The research showed that patients with ARDS had a lower time constant compared to patients with healthy lungs. The time constant was larger in the dorsal region of the lungs compared to the ventral region of the lungs. Is was also reported that PEEP caused significant changes to the time constants. The setback of the system is that the set up was for the regional lung instead of the global lung and the differences in pressure caused higher flow rates.

Denaï *et.al*, (2008) also developed a simulation model based on the EIT system to demonstrate ventilated patients with ARDS. Electrodes were placed on the surface of the thorax to monitor lung activity. Relationships between lung volume and lung conductivities were established, and predictions of the lung volume based on EIT measurements were elicited. The lung's image was estimated using a finite element model (FEM) for the cross section of the thorax. The lungs assumed two possible states; recruited lungs or de-recruited lungs, governed by a Threshold Opening Pressure (TOP). Effects of PEEP changes on lungs with moderate ARDS and severe ARDS were examined. Simulation results showed that EIT was able to detect ventilation distribution and has the potential to become indicators for adjusting ventilator PEEP values. Images of the lungs with ARDS were also produced.

A continuation study provided consistent images of ventilation distribution in collapsed or injured lung using absolute EIT (Denaï *et.al*, 2010). The model combined respiratory mechanics with a 2-D finite element mesh of the thorax and absolute resistivity representing the content of air. Specific tissues of the thorax (blood, muscle, bones and organs) were assigned with fixed resistivity values between 3 Ω and 80 Ω. The fixed values were compared with actual measured resistivity varying from 3 Ω to 80 Ω. The model was successful in producing images of the ventilation distribution for injured and collapsed lungs. A DSS for ventilator management combining blood gas predictions from SOPAVent and absolute EIT was also proposed.

Mohammad Samuri *et.al*, (2011) proposed a subject-specific adaptive neural-fuzzy inference system (ANFIS) to determine lung volume from absolute EIT measurements (see Figure 2.9). The resulting lung volumes were validated with data collected from volunteers using a spirometer and a body plethysmograph. The study showed that the model was able to successfully predict the lung volume, but with a 20% mean error when comparing the lung volume from absolute EIT measurements with measurements taken from the spirometer and the body plethysmograph, due to inaccuracies inherited from the EIT measurements. The authors suggested performing an extension to the model that allows for auto-calibration in order to rectify the inaccuracies of the EIT system, and also to take account of inter-subject variability.

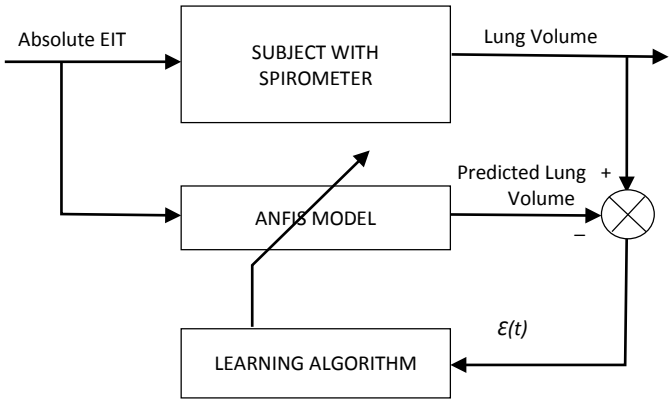

Figure 2.9. ANFIS model for predicting lung volume from absolute EIT

2.2.1 Three-Dimensional Electrical Impedance Tomography

The flow of electrical current is characteristically 3D in nature, and when flowing through a conducive body, cannot be confined to flow at the electrodes planes only. However, most work on pulmonary EIT uses 2D approach to represent a 3D domain. A 2D representation is the common assumption made to reduce the complexity of computations and associated hardware equipment (Stephenson *et. al*, 2009). This often causes distortions of the results due to off-plane conductivities and requires constant calibration. Researchers are now showing a strong interest in 3D EIT for monitoring pulmonary functions. The 3D EIT of the lung during ventilation can provide significant information of the lung function. In combinations with an optimal ventilator management system and an accurate blood gas prediction system, 3D pulmonary EIT has the ability to provide a non-invasive and effective real-time monitoring support for ventilated patients in the ICU.

In 3D EIT, the same drive and measure configuration of 2D EIT can be applied for multiple planes. The electrodes can be placed in several configurations such as planar, zigzag, offset, spiral or square as describe by Graham and Adler (2007). The number of independent measurements is the same regardless of the electrode configuration or the number of planes. A 16-electrode EIT, with 8 electrodes arranged in two layers around the circumference of the thorax in equal spacing, will produce a frame of 208 data.

Studies into three-dimensional (3D) EIT in pulmonary and ventilation management have expanded due to the advancement of computational systems. 3D EIT imaging is gaining popularity as a potential tool for bedside monitoring. Fan *et.al*, (2009) studied the modeling of the human thorax using 3D EIT integrated with CT scan. Three finite element mesh models were selected to represent the human thorax; the cylindrical mesh, the elliptical mesh and the thorax mesh. 32 electrodes were arrange in three configuration; a two-layer 16-electrode planar configuration, a two-layer 16-electrode spiral configuration and a three-layer 8-electrode spiral configuration. The forward problem was solved using COMSOL Multiphysics® optimization module, and the inverse problem was solved using SChur Conjugate Gradient (CG) algorithm. It was reported that the thorax mesh and the three-layer 8-electrode spiral configuration provided a close approximation to the human thorax. It also produced the highest correlation and minimal relative error.

Yang *et.al*, (2013) designed an anatomically realistic forward solver for the thorax. The work involved predicting the surface impedance as well as the electrical field in the interior of the thorax. A consensus framework for thoracic impedance from gated MRI imaging was also developed. To solve the forward problem, manual segmentation of the lung tissue was done from MRI images into 36 categories addressing conductivity. 3D volumetric masks created for each category and the 3D volumetric masks were discretized into hexahedral elements. The inverse problem was solved using the Sheffield filtered back projection method (Brown *et al*., 1985).

Despite the positive attributes of EIT such as being non-invasive, safe and relatively inexpensive in comparison to other medical imaging approaches, EIT is still not widely used in standard clinical settings for producing diagnostic and monitoring images, due to its low image resolution. However, more attention has recently been given to EIT for representing ventilation distribution, determining regional and global lung volumes and lung densities, and further understanding of lung functions. Studies in absolute EIT enables the measurement of absolute resistivity which is used to generate absolute lung volumes. Absolute lung volumes can be compared with normal clinical range and can then be used in DSS for setting of ventilator parameters.

Chapter 3

Evolutionary Fuzzy Type-2 Blood Gas Models for Ventilated Patients in Intensive Care Unit

3.1 Introduction

The human respiratory system under artificial ventilation is complex to model. There is a higher degree of uncertainty in ICU patients when compared to the general population. This is attributed to the variation in the diagnosed illness of patients, the treatment they are undertaking and possible changes in treatment, medications prescribed, pre-existing conditions they might have, and the physiological variations from body size, age and gender. The goal for modelling the human respiratory system under artificial ventilation is for it to be exploited for optimal ventilator settings, to avoid morbidity and reduce mortality.

The human respiratory and circulatory systems can be divided into five compartments (see Figure 3.1). These compartments are the alveolar, pulmonary, arterial, tissue, and venous compartment. The lungs are composed of three types of alveolar; the normal alveolar, when there is ideal ratio between ventilation and perfusion (V/Q = 1), the dead-space alveolar where there is ventilation but no perfusion (V/Q = ∞), and the shunted alveolar where there is perfusion but no ventilation (V/Q = 0). Blood from the venous compartment which is lower in oxygen passes through the pulmonary compartment where carbon-dioxide is transferred into the alveolar compartment and oxygen is transferred from the alveolar compartment into the pulmonary compartment to oxygenate the blood.

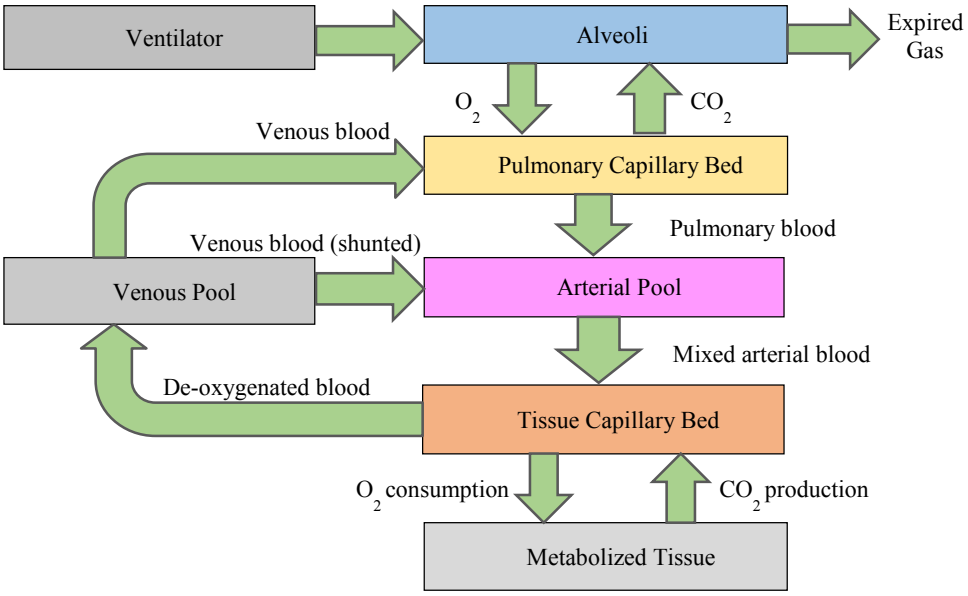

Figure 3.1. Human respiratory and circulatory systems under artificial ventilation (adapted from Goode, 2000).

Blood that leaves the pulmonary compartment mixes with a portion of shunted blood from the venous compartment which did not participate in the gas transfer process. Blood then passes into the arterial compartment which is then transferred into the tissue compartment. The tissue compartment diffuses oxygen into various types of tissues to allow normal metabolic process to take place. Tissues then diffuse carbon-dioxide back into the bloodstream in return. The de-oxygenated blood is then carried to the venous compartment, and back to the pulmonary compartment where gas transfers can continue to occur (Goode, 2000).

3.2 The Sheffield SOPAVent Model

The SOPAVent model (Sheffield Simulation of Patients under Artificial Ventilation) is a mathematical model that simulates the human respiratory system when it is under artificial ventilation, and was first developed at The University of Sheffield (Goode, 2000). SOPAVent derived itself from fundamentals of gas exchange in lung mechanics. The gas exchange equations that governs SOPAVent are divided into oxygen transport equations, carbon-dioxide transport equations, oxygen dissociation function and carbon-dioxide dissociation function.

Oxygen (O_2) Transport Equations in SOPAVent:

$$\frac{dCaO_2}{dt}V_a = \dot{Q}_t\left[XC_vO_2 + (1-X)C_pO_2 - CaO_2\right] \quad (3.1)$$

$$\frac{dCtO_2}{dt}V_t = \dot{Q}_t[CaO_2 - CtO_2] - \dot{V}_{O_2} \quad (3.2)$$

$$\frac{dCvO_2}{dt}V_v = \dot{Q}_t[CtO_2 - CvO_2] \quad (3.3)$$

$$\frac{dCpO_2}{dt}V_p = \dot{Q}_t(1-X)[(CvO_2 - CpO_2) + O_2Diff] \quad (3.4)$$

$$\frac{dCAO_2}{dt}V_A = RR(V_T - V_D)\left(FiO_2 - \frac{CAO_2}{1000}\right) - \dot{Q}_t(1-X)O_2Diff \quad (3.5)$$

$$O_2Diff = B_{O_2}\left[P_{mean}\left(\frac{C_AO_2}{1000}\right) - P_pO_2\right] \quad (3.6)$$

$$P_PO_2 = f_{inv}(CpO_2) \quad (3.7)$$

Where,

V_x Volume (l), where *x* is *A* (alveolar), *a* (arterial), *t* (tissue), *v* (venous) and *p* (pulmonary)

$\dot{Q}_t$ Cardiac output (ml/min)

X Fraction of blood shunted passed the lungs

$\dot{V_{O_2}}$ O_2 consumption by tissues (ml/min)

V_D Alveolar dead-space volume (ml)

V_T Tidal volume (ml)

RR Respiratory rate (breath/min)

CxO_2 O_2 concentration (ml/l).

B_{O_2} O_2 diffusion constant (ml/kPa/l)

P_{mean} Mean airway pressure (kPa)

FiO_2 Inspired fraction of O_2

PpO_2 Pulmonary partial pressure of O_2 (kPa)

f_{inv} Inverse of the O_2 dissociation function

Carbon-dioxide (CO_2) Transport Equations in SOPAVent:

$$\frac{dCaCO_2}{dt}V_a = \dot{Q}_t\left[XC_vCO_2 + (1-X)C_pCO_2 - CaCO_2\right] \quad (3.8)$$

$$\frac{dCtCO_2}{dt}V_t = \dot{Q}_t[CaCO_2 - CtCO_2] + \dot{V}_{CO_2} \quad (3.9)$$

$$\frac{dCvCO_2}{dt}V_v = \dot{Q}_t[CtCO_2 - CvCO_2] \quad (3.10)$$

$$\frac{dCpCO_2}{dt}V_p = \dot{Q}_t(1-X)[(CvCO_2 - CpCO_2) - CO_2Diff] \quad (3.11)$$

$$\frac{dC_ACO_2}{dt}V_A = RR(V_T - V_D)\left(FiCO_2 - \frac{C_ACO_2}{1000}\right) + \dot{Q}_t(1-X)CO_2Diff \quad (3.12)$$

$$CO_2Diff = B_{CO_2}\left[Pmean\left(\frac{C_ACO_2}{1000}\right) - P_pCO_2\right] \quad (3.13)$$

$$P_PCO_2 = f_{inv}(CpCO_2) \quad (3.14)$$

Where,

$\dot{V_{CO_2}}$ CO_2 production (ml/min)

$CxCO_2$ CO_2 concentration (ml/l)

B_{CO_2} CO_2 diffusion constant (ml/kPa/l)

$FiCO_2$ Inspired fraction of CO_2

$PpCO_2$ Pulmonary partial pressure of CO_2 (kPa)

f_{inv} Inverse of the CO_2 dissociation function

O_2 Dissociation Function

$$C(O_2) = \beta_h.Hb.SO_2 + \alpha_b\,.PO_2 \quad (3.15)$$

Where,

Hb Haemoglobin concentration

SO_2 O_2 saturation

β_h Haemoglobin O_2 combining capacity

α_b O_2 plasma carrying capacity

CO_2 Dissociation Function

$$[CO_2]Blood = 22.2\,[CO_2]plasma\,\{d.PCV + (1 - PCV)\} \quad (3.16)$$

Where,

PCV Packed cell volume (haematocrit)

The mean airway pressure Pmean is derived from the following equation:

$$Pmean = \left[(PIP - PEEP).\frac{t_I}{t_I + t_E}\right] + PEEP + P_B \quad (3.17)$$

$$\text{And, } \frac{t_I}{t_I + t_E} = \frac{I{:}E}{I{:}E + 1}$$

Where *PEEP* is the positive end expiratory pressure (kPa), *PIP* is the peak inspiratory pressure (kPa), t_I is the inspiration time (s), t_E is the expiration time (s), P_B is the barometric pressure (kPa), and $I{:}E$ is the ratio of inspiration time to expiration time

The main objective of SOPAVent is to provide accurate predictions of the partial arterial pressure of oxygen (PaO_2), the partial arterial pressure of carbon-dioxide ($PaCO_2$) and the acid-base measurement (pH) of arterial blood gases, which prior to this, were only made available from blood sampling and blood gas analysis (see Figure 3.2). SOPAVent can also be integrated into advisory models to provide decision support for parameters of ventilators in the ICU, such as the settings for fraction of inspired oxygen (FiO_2), PEEP, respiratory rate (RR), tidal volume (VT) and inspiration time (T_I) as described by Goode (2000), Kwok *et al.,* (2004a, 2004b) and Wang *et al.,* (2010b).

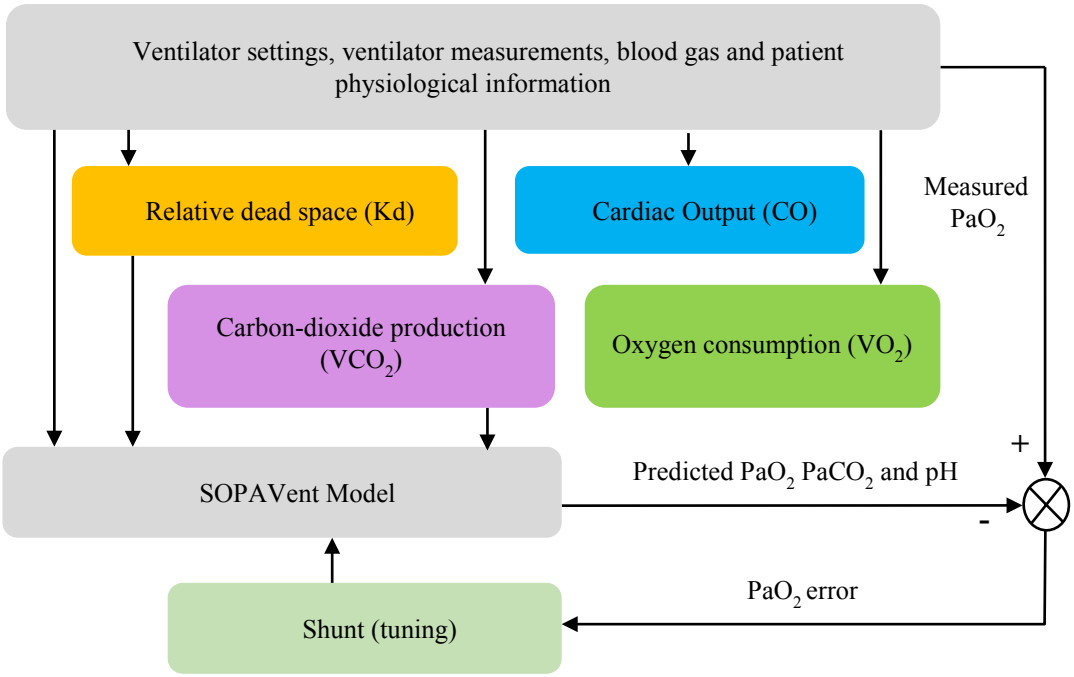

Figure 3.2. The SOPAVent model structure (adapted from Wang *et.al* 2010b).

SOPAVent was also integrated with electrical impedance tomography (EIT) for monitoring of the lungs during artificial ventilation as described by Denaï *et al*., (2010) and Mohammad-Samuri *et al.*, (2011). SOPAVent utilized routine ICU data as inputs to the model. SOPAVent also required parameters which were not routinely available in the ICU. These parameters were either derived from existing parameters, represented by constants, measured using special equipment and estimated or modelled using artificial intelligence approach.

i. Ventilator settings and monitoring parameters: positive end expiratory pressure (PEEP), respiratory rate (RR), inspiratory pressure (Pinsp), minute volume (MV), ratio of inspiratory time to expiratory time (I:E), fraction of inspired oxygen (FiO_2) and tidal volume (VT)

ii. Blood gas parameters: partial arterial pressure of oxygen (PaO_2), partial arterial pressure of carbon-dioxide ($PaCO_2$), acid-base measurement (pH), oxygen saturation (SpO_2), haemoglobin concentration (Hb) and bicarbonate level (HCO_3).

iii. Physiological information: body surface area, mean arterial pressure, body temperature, and end-tidal carbon-dioxide production ($EtCO_2$)

iv. Secondary parameters derived from routine ICU data: Mean airway pressure (Pmean) is derived from PEEP, I:E ratio, and Pb. Volume for each compartment is derived from weight, functional residual capacity (FRC) is derived from height, airway compliance is derived from weight, and packed cell volume (PCV) is derived from Hb

v. Parameters in SOPAVent represented by constants: the O_2 and CO_2 diffusion coefficients, haemoglobin binding capacity (βh), and plasma absorption coefficients (αb).

vi. Parameters that required the use of special equipment, estimated or modelled: carbon-dioxide production (VCO_2), oxygen consumption (VO_2), cardiac output (CO), dead-space (Kd) and shunt.

In the earliest version of the SOPAVent, the VCO_2 was measured using a metabolic tester (Goode, 2000). The need for a special equipment limited the measurements to a very small dataset, and this dataset was unable to represent the varying levels of VCO_2 parameters in ICU patients. VCO_2 was then estimated using a mean population value, using earlier measurements obtained from the metabolic tester (Kwok *et al.*, 2004b). This approach, however, may result in significant error when patient's parameter deviated from the original test group. When newer ventilators were able to perform measurements of VCO_2, and more data became available, the VCO_2 parameter was modelled using an adaptive neural-fuzzy inference system (ANFIS) (Wang *et al*., 2010a). Although newer ventilators are now able to measure VCO_2, it is not routine practice for ICUs to track or use this measurement to evaluate the ventilator's performance. Moreover, not all hospitals are equipped with the latest ventilator technology. Thus, it is still deemed necessary to model the VCO_2 component. However, ANFIS modelling can sometimes lead to overfitting that may fail to generalize to future observations in a reliable way.

The dead-space (Vd) is a share of tidal volume (VT) which did not contribute to gas exchange. The ratio of Vd over VT is known as the relative dead-space (Kd). The understanding of Kd will deliver crucial information on the patient's physiological condition. In the first version of SOPAVent, the relative dead-space (Kd) was tuned to match the measured $PaCO_2$ (Goode, 2000). The tuning process in the early version was time-consuming and often lead to no solution being found. Kwok *et al.*, (2004b), attempted to model Kd with a fuzzy inference system (FIS) using the relationship of hypoxemia index ($PaO2/FiO_2$) and Kd. However, when validated with real patient data, results were poor. When more data became available from newer ventilators, the relative dead space was modelled using ANFIS (Wang *et al*., 2010a). Similarly to the ANFIS model for VCO_2, the model was unable to produce satisfactory predictions when the tested data falls outside of the range of the training data used in ANFIS.

The cardiac output (CO) was first measured with the use of a pulmonary-artery catheter (PAC) (Goode, 2000). This procedure is invasive and also limits the number of usable data. CO was then estimated using the population mean of patients with PAC (Kwok *et al.*, 2004b). This approach may result in significant deviation of expected results due to inter and intra patient variability, common in ICU patients. Wang *et al*. (2010a) then proposed a method for estimating CO from Body Surface Area (BSA). Although this approach provided a patient specific estimation of CO when compared to using the population mean, patients with similar BSA may produce different CO values due to factors such as age, and the severity of illnesses. Shunt was first tuned to match the $PaCO_2$ (Goode, 2000). Kwok *et al.,* (2004b) attempted to model shunt with ANFIS using the relationship of respiratory index (RI) and shunt. VO_2 was derived from the relationship of respiratory quotient (RQ) with VCO_2 using the following equation from Wang *et al*., (2010a):

$$VO_2 = (VCO_2/RQ), \text{ with } RQ = 0.8 \tag{3.18}$$

The following sections in this chapter will discuss the modelling of Kd, VCO_2 and shunt parameters using interval type-2 fuzzy logic system (IT2FLS) and the optimization of the fuzzy parameters using a 'new structure' particle swarm optimization (nPSO), to improve prediction accuracy.

3.3 Type-2 Fuzzy Logic System for Modelling of Relative Dead-space, Carbon-dioxide Production, and Shunt

The type-2 fuzzy logic system (T2FLS) is a relatively new formalism that is gaining popularity in designing complex, non-linear systems (see Figure 3.3). Unlike type-1 fuzzy logic systems, the membership function (MF) of type-2 fuzzy systems is in itself fuzzy. This enables for robust and adaptable models, which would be suitable for designing and controlling of systems with higher degrees of uncertainty (Wu, 2012). The MF of T2FLS is conceptually three-dimensional, represented by a footprint of uncertainty (FOU) that leads to an extra degree of freedom (Mendel *et al*., 2001). An example of an FOU for a type-2 trapezoidal MF is shown as the shaded area of Figure 3.4. The shaded area is constrained by the upper membership function (UMF) and the lower membership function (UMF).

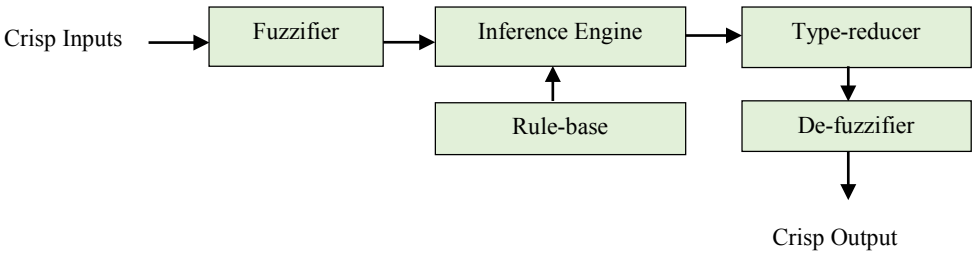

Figure 3.3. Type-2 fuzzy system.

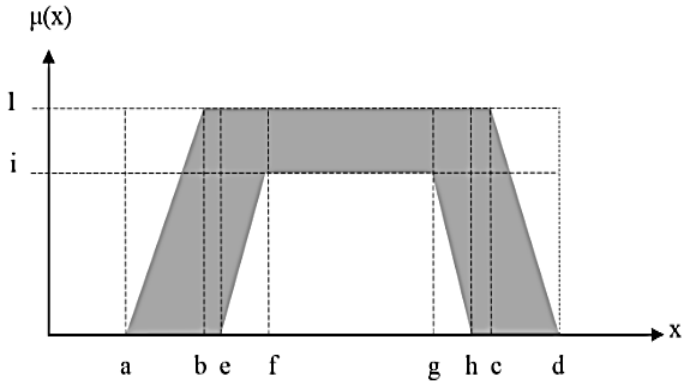

Figure 3.4**.** Footprint of uncertainty (FOU) in a type-2 membership function (MF) (Indera-Putera *et.al*, 2016)

In this section, the interval type-2 fuzzy logic system (IT2FLS) was used instead of the general type-2 fuzzy logic system. This is to reduce the computational burden and to reduce the overall system complexity. A 9-point trapezoidal MFs were selected for the input fuzzy sets of the Kd and the VCO_2 models. Each input parameter was provided with three MFs, named '*low*', '*moderate*' and '*high*'. The number of fuzzy rules were N^M, with M being the number of inputs and N the number of MFs for each input.

To generate the fuzzy rules, the output data, with its corresponding inputs were arranged in ascending sequence. The average measured output values were calculated for each available unique combination of input MFs. The outputs were crisp intervals with the lower value for each output being set to the minimum output value and the upper value being set to the maximum output value for the specific input combination. An example of the fuzzy rule for the Kd sub-component is shown in Table 3.4.

The input MFs were set as equally-spaced fuzzy sets with the distance between UMFs and LMFs of the fuzzy sets assigned as 10% of the input range. These parameters were then manually tuned to achieve a satisfactory prediction. Figure 3.5 shows the manual membership function selection process for IT2FLS. The Kd model, with five inputs and three MFs for each input generated 243 fuzzy rules. The VCO_2 model, with three inputs and three MFs for each input generated 27 rules. The shunt model with one input and three MFs for each input generated three rules.

A revised Kd model was also proposed to reduce the number of rules from 243 to 44 by eliminating the input combinations which did not produce any output from the input-output sequence mapping. A sample of the fuzzy rule (Rule 22) for the Kd model with 44 rules reads as follows:

IF PaCO2 is Moderate AND RR is Low AND VT is Moderate AND Pinsp is Low AND PEEP is High THEN Kd is [16-46]

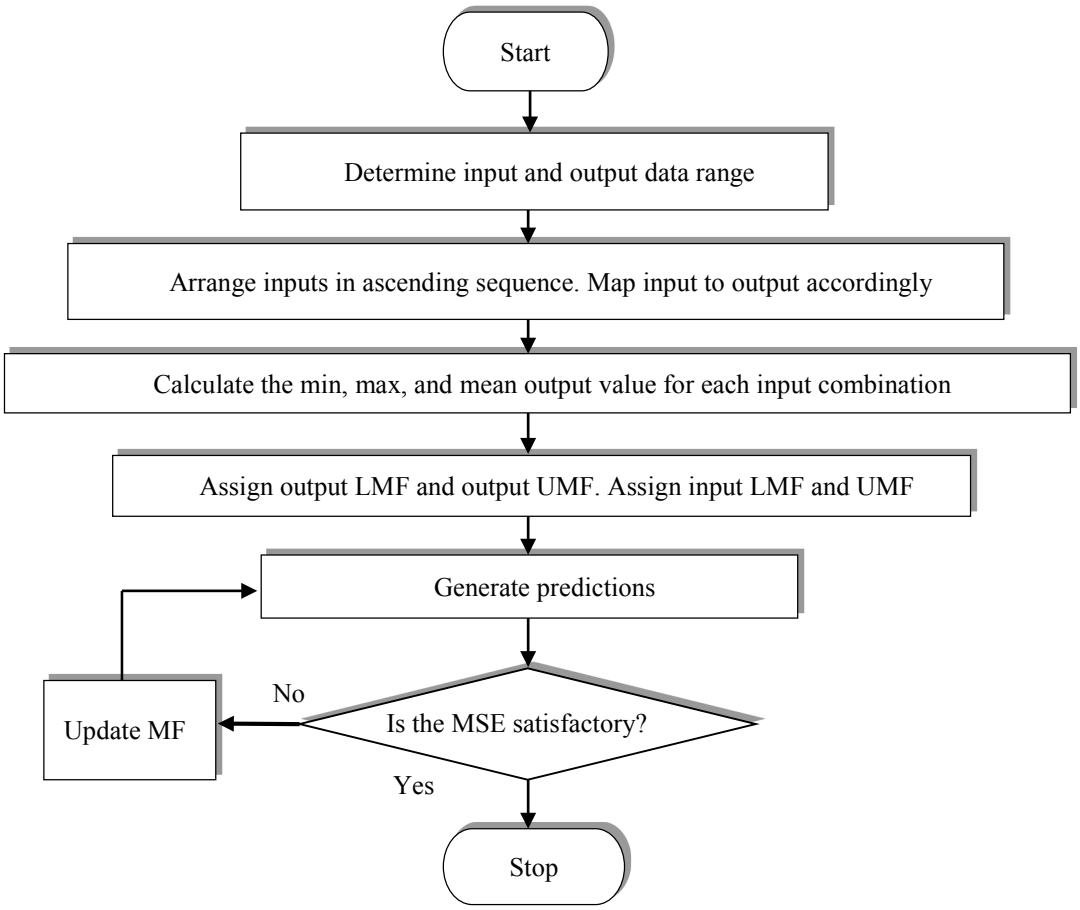

(MF: membership function, LMF: lower membership function, UMF: upper membership function, MSE: Mean Squared Error)

Figure 3.5. Manual membership function (MF) selection process for IT2FLS.

3.4 Modelling of the Relative Dead-space Parameter

The inputs to the relative dead-space (Kd) model was selected based on a sensitivity analysis found in Goode, (2000), that studied how well the parameters of inspiratory pressure (Pisnp), positive end expiratory pressure (PEEP), peak inspiratory pressure (PIP), respiratory rate (RR), partial arterial pressure of carbon-dioxide ($PaCO_2$), tidal volume (VT), and minute volume (MV) correlated with Kd. The Kd was found to be most sensitive to $PaCO_2$ and moderately sensitive to Pinsp, RR and VT. There was also a small correlation between Kd and PEEP (see Table 3.1). Thus, these five parameters: $PaCO_2$, Pinsp, RR, VT and PEEP were selected as inputs to the Kd model as shown in Figure 3.6. Kd was found to be least sensitive to changes in MV and PIP, hence these two parameters were excluded from the modelling of Kd.

Table 3.1. Sensitivity analysis for the selection of Kd model inputs

Parameter	Pisnp	PIP	RR	PEEP	$PaCO_2$	VT	MV
Correlation	-0.39	-0.08	0.49	0.22	0.66	-0.41	0.11

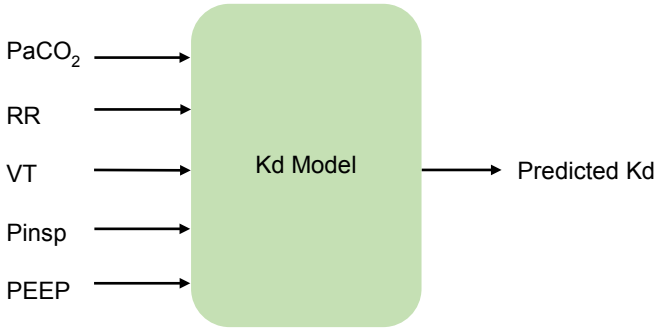

Figure 3.6. The Kd model

3.4.1 Modelling Data and Validation Data for the Relative Dead-space Model

Data from patients was obtained from the Sheffield Royal Hallamshire Hospital patient data management system (PDMS) and have been previously approved by the ethics committee. A total of 447 data from 25 patients was used for modelling of Kd, and a further 67 data was used for validation. The 67 data used for validation was collected from 13 patients. Patient demography is shown in Table 3.2. The summary for the data used in the Kd modelling and validation is shown in Table 3.3. All parameters, apart from PEEP, showed a normal curve based on the standard deviation (SD) that is smaller than one third of its mean value. PEEP however, has a slightly larger S.D., this can be due to the ventilator adjustments made throughout the patient's course of treatment. Figure 3.7 shows the distribution of the validation data for the Kd model.

Table 3.2. Patient demography for the Kd model

Indicator	Gender		Age	Weight (kg)	Height (cm)
mean±S.D.	Male	Female	59±14.61	70.7±23.8	167.9±10.45
	13	12			

Table 3.3. Kd modelling and validation data

Data	Parameter	Mean ± σ	Min	Max
Modelling	$PaCO_2$ (kPa)	5.69 ± 1.05	3.67	10.1
	RR (breath/min)	16.96 ± 3.27	12	28
	VT (l)	0.52 ± 0.12	0.26	0.89
	Pinsp (cmH_2O)	13.93 ± 3.64	6	30
	PEEP (cmH_2O)	10.62 ± 3.88	5	20
	Kd	27.95 ± 6.72	13	52
Validation	$PaCO_2$ (kPa)	5.39 ± 0.84	3.74	7.62
	RR (breath/min)	16.21 ± 4.19	12	28
	VT (l)	0.47 ± 0.11	0.17	0.75
	Pinsp (cmH_2O)	13.30 ± 3.23	8	20
	PEEP (cmH_2O)	9.01 ± 2.87	5	15
	Kd	29.10 ± 7.37	14	50

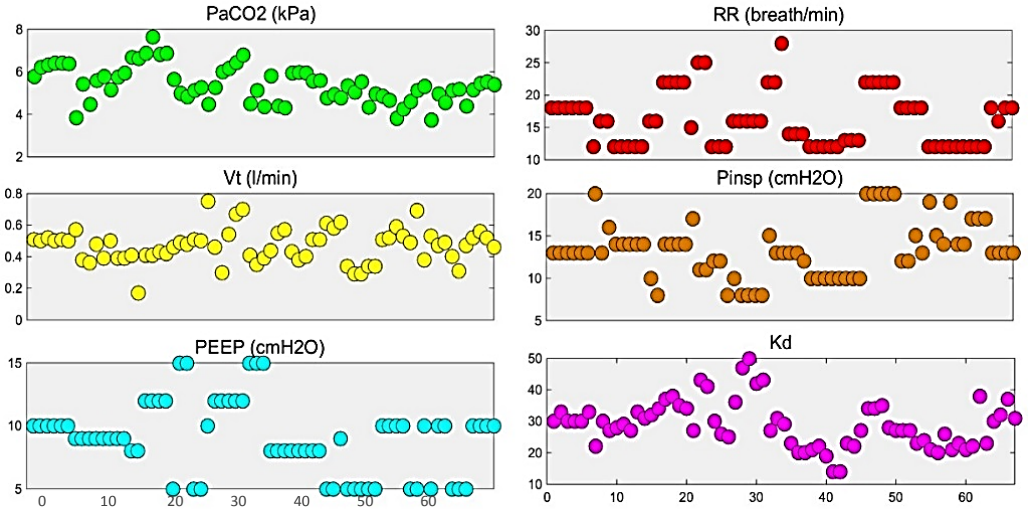

Figure 3.7. Input-output data distribution for Kd validation

3.4.2 Interval Type-2 Fuzzy Logic System Modelling Parameters for Relative Dead-space

The Kd component was modelled using the interval type-2 fuzzy logic system (IT2FLS). Each of its five inputs were allocated three trapezoidal membership functions (MF) known as *'low'*, *'moderate'* and *'high'* that were equally spaced. Each membership function has a footprint of uncertainty (FOU), which is the shaded area between the upper membership function (UMF) and lower membership function (LMF). The FOU for the Kd model was only applied on to the horizontal axis. The FOUs were approximately 10% of the width of data. For an example, in Table 3.3, RR has a minimum value of 12 and a maximum of 28, thus the width is 16. The width of

the FOU for RR will be approximately 1.6. This will only be used to determine the baseline for the horizontal FOU, which will be adjusted later as required.

Each trapezoidal MF was associated with nine reference points (‘*a’* to *‘i’* in Figure 3.4). These points showed the exact location for each MF in its fuzzy set. The trapezoidal MF was selected for this purpose to accommodate the algorithm developed for IT2FLS by Wu and Mendel (2009 and 2014). The 9-point value for the trapezoidal input MF is shown in Table 3.4. The fuzzy set for the input parameters of Kd is shown in Figure 3.8. The output parameter Kd was mapped to all possible input combinations. Since there were five inputs with three MF each, a total of $3^5 = 243$ input combinations was mapped to their corresponding Kd outputs. The crisp values of LMF and UMF of the output fuzzy MFs were determined by the minimum and maximum value of Kd for the set of inputs mapped to Kd. The rule base for Y1 to Y243 is available in Appendix A. The Kd fuzzy rules were then reduced to 44 by selecting the combination of inputs/output that provided the most significant mapping between the inputs $PaCO_2$, RR, VT, Pinsp and PEEP with the output, Kd. The crisp intervals for LMF and UMF of the output MFs were determined by the minimum and the maximum value of Kd for the set of inputs mapped to Kd. These 44 output intervals were used to represents the fuzzy rules for the IT2FLS system (Y1 to Y44) as shown in Table 3.5.

Table 3.4. The 9-point trapezoidal MF for Kd input parameters

Input	MF	a	b	c	d	e	f	g	h	i
$PaCO_2$	Low	1	2.5	5	6.5	2	3.5	4	5.5	1
	Moderate	3.5	5	7.5	9	5	6	6.5	8	1
	High	6	7.5	10	11.5	7	8.5	9	10.5	1
RR	Low	6	9	15	18	8	11	13	16	1
	Moderate	13	16	22	25	15	18	20	23	1
	High	20	23	29	32	22	25	27	30	1
VT	Low	-0.15	0.05	0.3	0.5	-0.05	0.15	0.2	0.4	1
	Moderate	0.2	0.4	0.65	0.85	0.30	0.5	0.55	0.75	1
	High	0.55	0.75	1.05	1.2	0.65	0.85	0.95	1.1	1
Pinsp	Low	-3	3	11	17	-1	5	9	15	1
	Moderate	9	15	21	27	11	17	19	25	1
	High	19	25	33	39	21	27	31	37	1
PEEP	Low	-1	2	8	11	1	4	6	9	1
	Moderate	6	9	16	19	8	11	14	17	1
	High	14	17	23	26	16	19	21	24	1

Table 3.5. Input MF to output MF mapping for Kd model

Input					Output Kd		
$PaCO_2$	RR	VT	Pinsp	PEEP	Y	LMF	UMF
Low	Low	Moderate	Low	Low	Y1	6	36
Low	Low	Moderate	Low	Moderate	Y2	11	41
Low	Low	Moderate	Moderate	Low	Y3	6	36
Low	Low	Moderate	Moderate	Moderate	Y4	5	35
Low	Low	High	Low	Moderate	Y5	7	37
Low	Low	High	Moderate	Low	Y6	4	34
Low	Low	High	Moderate	Moderate	Y7	2	32
Low	Moderate	Low	Moderate	Low	Y8	13	43
Low	Moderate	Moderate	Low	Low	Y9	7	37
Low	Moderate	Moderate	Low	Moderate	Y10	15	45
Low	Moderate	Moderate	Moderate	Low	Y11	13	43
Low	Moderate	Moderate	Moderate	Moderate	Y12	9	39
Low	Moderate	High	Moderate	Low	Y13	8	38
Low	Moderate	High	Moderate	Moderate	Y14	8	38
Low	High	Moderate	Low	Moderate	Y15	27	57
Low	High	Moderate	Moderate	Moderate	Y16	14	44
Moderate	Low	Low	Low	Low	Y17	20	50
Moderate	Low	Low	Moderate	Low	Y18	19	49
Moderate	Low	Low	Moderate	Moderate	Y19	16	46
Moderate	Low	Moderate	Low	Low	Y20	14	44
Moderate	Low	Moderate	Low	Moderate	Y21	20	50
Moderate	Low	Moderate	Low	High	Y22	16	46
Moderate	Low	Moderate	Moderate	Low	Y23	15	45
Moderate	Moderate	Low	Low	Low	Y24	15	45
Moderate	Moderate	Low	Moderate	Low	Y25	19	49
Moderate	Moderate	Low	Moderate	Moderate	Y26	16	46
Moderate	Moderate	Moderate	Low	Low	Y27	16	46
Moderate	Moderate	Moderate	Low	Moderate	Y28	19	49
Moderate	Moderate	Moderate	Low	High	Y29	16	46
Moderate	Moderate	Moderate	Moderate	Low	Y30	17	47
Moderate	Moderate	Moderate	Moderate	Moderate	Y31	13	43
Moderate	Moderate	Moderate	Moderate	High	Y32	15	45
Moderate	Moderate	High	Low	Low	Y33	16	46
Moderate	Moderate	High	Moderate	Moderate	Y34	9	39
Moderate	High	Low	Moderate	Moderate	Y35	20	50
Moderate	High	Moderate	Moderate	Moderate	Y36	26	56
High	Low	Low	Low	Low	Y37	11	41
High	Low	Moderate	Low	High	Y38	17	47
High	Moderate	Low	Low	Moderate	Y39	29	59
High	Moderate	Moderate	Low	Low	Y40	27	57
High	Moderate	Moderate	Low	Moderate	Y41	26	56
High	Moderate	Moderate	Moderate	Moderate	Y42	19	49
High	Moderate	Moderate	Moderate	High	Y43	25	55
High	High	Moderate	Low	Moderate	Y44	33	63

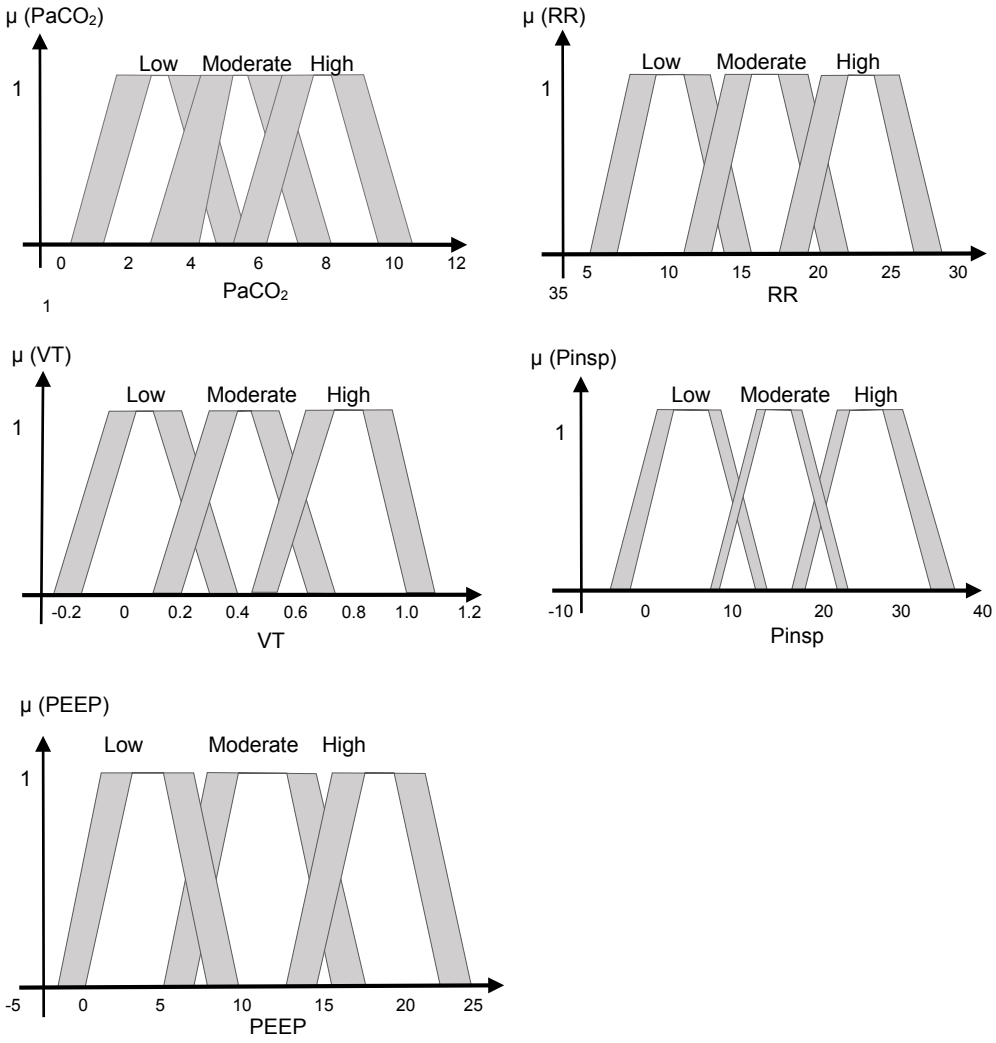

Figure 3.8. Input fuzzy sets for the Kd model: PaCO2, RR, VT, Pinsp and PEEP

3.4.3 Validation of the Relative Dead-space Model with Real Patient Data

The IT2FLS model was used to predict the Kd values of 68 input data sets from 13 patients. The Mean Absolute Error (MAE), the Mean Squared Error (MSE) and the coefficient of determination (R^2) were used to evaluate the prediction performance against real Kd values. The prediction results were also compared with the ANFIS model previously developed by Wang *et al*., (2010a). The prediction plots for the modelling and the validation datasets for the Kd model are shown in Figure 3.9.

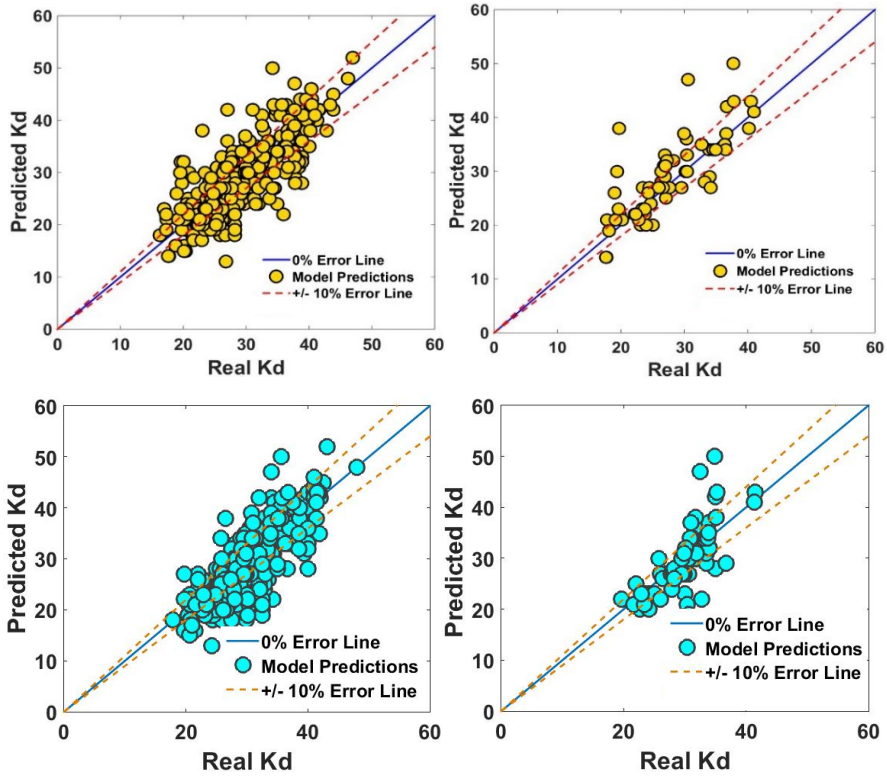

Figure 3.9. Kd prediction results. Top: Kd with 243 rules result for modelling data and validation data. Bottom: Kd with 44 rules for modelling data and validation data

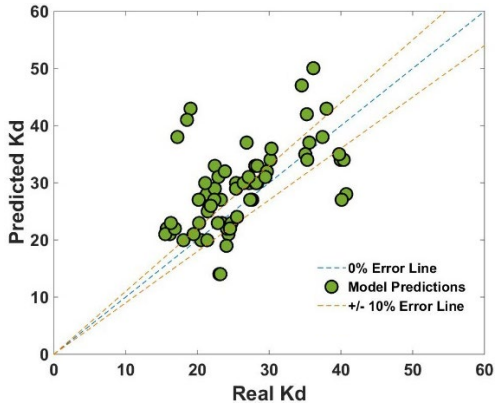

Figure 3.10. ANFIS Kd model prediction results for validation data

For the IT2FLS Kd model with 243 fuzzy rules, most of the predictions were centred within the ±10% confidence band. Although a small number of predictions were outside of the ±10% confidence band, there were significant improvements for the validation data predictions from the previous ANFIS model shown in Figure 3.10. The new model has reduced the MSE of the validation data from 53.88 to 32.76 and reduced the MAE from 18.52 to 14.96. It has also improved the R^2 from 0.54 to 0.62.

It can also be seen for the IT2FLS Kd model with 44 fuzzy rules, most of the predictions were centred within the ±10% confidence band. Although a small number of predictions were outside of the ±10% confidence band, there were significant improvements for the validation data prediction from the previous ANFIS model. The new model has reduced the MSE of the validation data from 53.88 to 28.91 and reduced the MAE from 18.52 to 14.62. It has also improved the R^2 from 0.54 to 0.69. Table 3.6 summarize the performances of the IT2FLS models against the ANFIS model performances for Kd prediction.

Table 3.6. Kd performance comparison for IT2FLS model with ANFIS model

Approach	Modelling Data			Validation Data		
	MSE	MAE	R^2	MSE	MAE	R^2
ANFIS	10	8.71	0.88	53	18.52	0.54
IT2FLS (243 rules)	21.76	14.48	0.74	32.76	14.96	0.62
IT2FLS (44 rules)	19.6	13.45	0.79	28.91	14.62	0.69

3.5 Modelling of the Carbon-dioxide Production Component

The inputs for the carbon-dioxide production (VCO_2) model were selected based on the sensitivity analysis described in Goode (2000). Table 3.7 shows the correlation between the carbon-dioxide production (VCO_2) with the end-tidal carbon-dioxide production ($EtCO_2$), the minute volume (MV), the peak inspiratory pressure (PIP), the fraction of inspired oxygen (FiO_2), VT, PEEP and RR. It appeared that the VCO_2 was most sensitive to MV and $EtCO_2$. VCO_2 was also moderately sensitive to VT. Thus, these three parameters, MV, VT and $EtCO_2$ were selected to be the inputs to the VCO_2 model as shown in Figure 3.11. VCO_2 appears to be less sensitive to the changes of PIP, PEEP and FiO_2 parameters. Hence, these three parameters were excluded from the modelling of VCO_2. It can also be seen that VCO_2 was moderately sensitive to RR. Here, RR was used to generate MV using the following equation:

$$MV = (VT)(RR) \tag{3.19}$$

Table 3.7. Sensitivity analysis for the selection of VCO_2 model inputs

Parameter	$EtCO_2$	VT	MV	PEEP	RR	PIP	FiO_2
Correlation	0.69	0.39	0.64	0.15	0.24	0.01	0.10

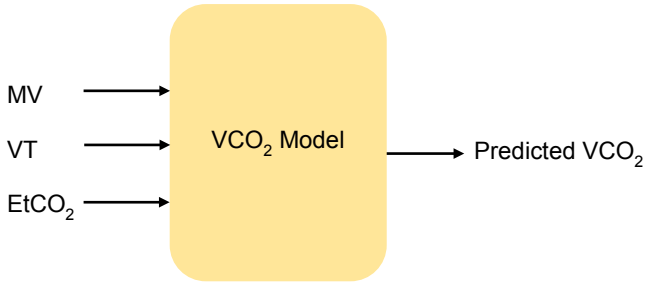

Figure 3.11. VCO_2 model

3.5.1 Modelling Data and Validation Data for the Carbon-dioxide Production Model

A total of 764 data from 21 patients was used for the modelling of VCO_2, and a further 82 data from 5 patients was used for validation. Patient demography is shown in Table 3.8. The summary for the data used in VCO_2 modelling and validation is shown in Table 3.9. All parameters showed a normal bell-shaped curved based on the standard deviation (SD) that is smaller than one third of its mean value. Figure 3.12 shows the distribution of the data for validation of VCO_2.

Table 3.8. Patient demography for the VCO_2 model

Indicator	Gender		Age	Weight (kg)	Height (cm)
mean±S.D.	Male	Female	56±17.83	74±21.22	170.4±8.95
	5	11			

Table 3.9. VCO_2 modelling and validation data

Data	Parameter	Mean ± σ	Min	Max
Modelling	MV (l/min)	7.89 ± 1.79	4.09	15.55
	VT (l)	0.54 ± 0.09	0.29	0.90
	$EtCO_2$ (kPa)	4.89 ± 0.96	3.18	8.51
	VCO_2 (ml/min)	217.27 ± 56.77	144	405.9
Validation	MV (l/min)	8.90 ± 1.79	5.66	15.55
	VT (l)	0.54 ± 0.07	0.39	0.65
	$EtCO_2$ (kPa)	4.68 ± 0.69	3.38	6.39
	VCO_2 (ml/min)	217.75 ± 33.42	144.5	292

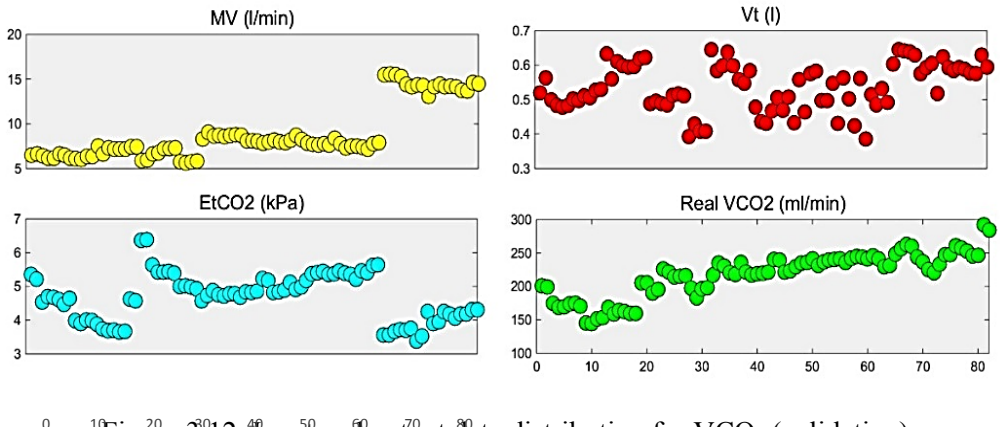

Figure 3.12. Input and output data distribution for VCO_2 (validation)

3.5.2 Interval Type-2 Fuzzy Logic System Modelling Parameters for Carbon-dioxide Production

The VCO_2 component was modelled using the interval type-2 fuzzy logic system (IT2FLS). Each of its three inputs was allocated three trapezoidal membership functions (MF) known as *'low'*, *'moderate'* and *'high'* that were equally spaced. Each MF has an FOU, which was approximately 10% of the entire data range. Each trapezoidal MF was associated with the same nine reference points ('*a*' to '*i*') shown in Figure 3.4. The output parameter, VCO_2 was mapped to all possible input combinations. Since there were three inputs with three MF each, a total of 27 input combinations were mapped to VCO_2. The average VCO_2 value was then calculated for each combination of inputs, resulting in 27 VCO_2 values. An approximated $\pm$10% margin was introduced to the averaged VCO_2 values to provide crisp intervals for UMF and LMF for each VCO_2 MFs. The UMF and LMF were then manually adjusted to increase prediction accuracy. The 27 VCO_2 MFs were used to represents the fuzzy rules for the IT2FLS system (Y1 to Y27) as shown in Table 3.10. The 9-point values for the trapezoidal input MF is shown in Table 3.11. The fuzzy set for the VCO_2 model is shown in Figure 3.13. A sample fuzzy rule (Rule 23) reads as follows:

IF MV is Moderate AND VT is Low AND $ETCO_2$ is HIGH, THEN VCO_2 is Y12

[360 370]

Table 3.10. Input MF to output MF mapping for VCO_2 model

Input			VCO_2		
MV	VT	$EtCO_2$	Y	LMF	UMF
low	low	low	Y1	0	160
low	low	moderate	Y2	195	205
low	low	high	Y3	260	270
low	moderate	low	Y4	175	185
low	moderate	moderate	Y5	215	220
low	moderate	high	Y6	280	290
low	high	low	Y7	195	205
low	high	moderate	Y8	185	195
low	high	high	Y9	280	290
moderate	low	low	Y10	195	205
moderate	low	moderate	Y11	250	260
moderate	low	high	Y12	360	370
moderate	moderate	low	Y13	215	225
moderate	moderate	moderate	Y14	385	395
moderate	moderate	high	Y15	345	355
moderate	high	low	Y16	225	235
moderate	high	moderate	Y17	295	305
moderate	high	high	Y18	350	360
high	low	low	Y19	215	225
high	low	moderate	Y20	275	285
high	low	high	Y21	325	335
high	moderate	low	Y22	240	250
high	moderate	moderate	Y23	365	375
high	moderate	high	Y24	380	390
high	high	low	Y25	305	315
high	high	moderate	Y26	350	360
high	high	high	Y27	385	395

Table 3.11. The 9-point trapezoidal MF for VCO_2 input parameters

Input	MF	a	b	c	d	e	f	g	h	i
MV	Low	-0.5	2	6	10	0.5	2	6	9	1
	Moderate	6	10.5	13.5	16	7	10.5	13.5	15	1
	High	13	16	18	18	14	16	18	18	1
VT	Low	-0.05	0.2	0.4	0.65	0.05	0.2	0.4	0.55	1
	Moderate	0.35	0.55	0.65	0.85	0.45	0.55	0.65	0.75	1
	High	0.65	0.85	0.9	1.1	0.75	0.85	0.9	1	1
$ETCO_2$	Low	-1	1	3.5	6	1	1	3.5	5	1
	Moderate	3	5	7	9	4	5	7	8	1
	High	5.5	8	9.5	12	7.5	8	9.5	10	1

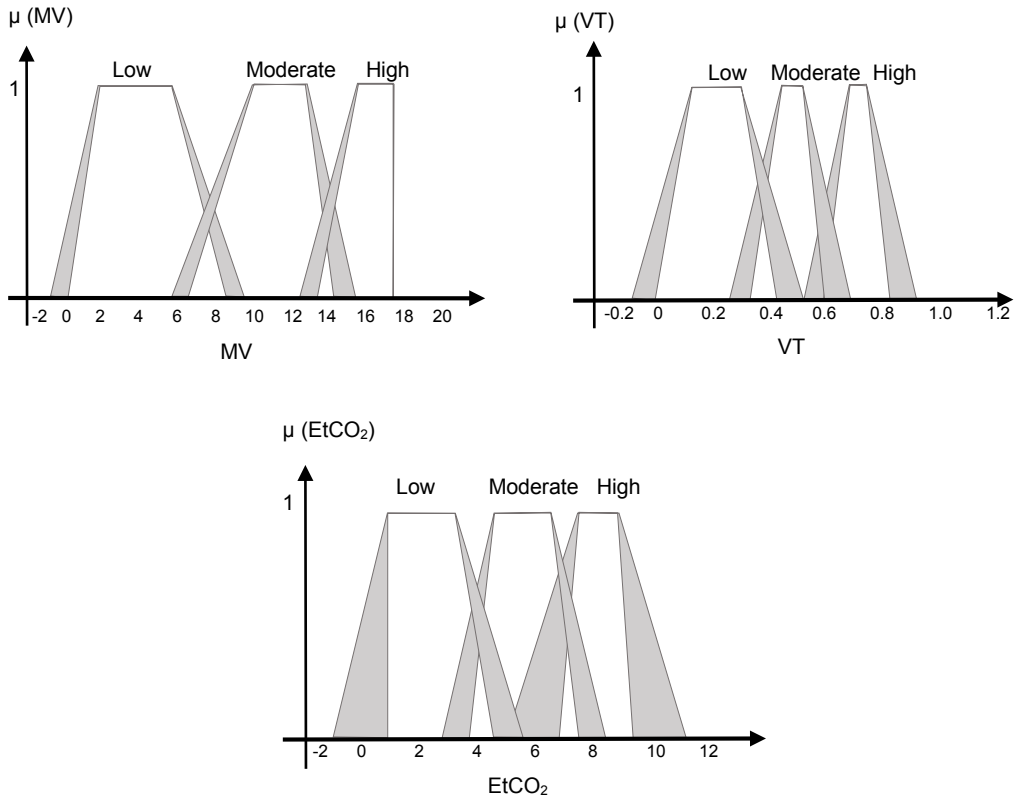

Figure 3.13. Input fuzzy sets for the VCO_2 model: MV, VT, and EtCO

3.5.3 Validation of the Carbon-dioxide Production Model with Real Patient Data

The IT2FLS model was used to predict the VCO_2 values of 82 input data sets from five patients. MSE, MAE and R^2 were used to evaluate the prediction performance against real VCO_2 values. The results were also compared with the ANFIS model previously developed by Wang *et al.,* (2010a). The prediction plots for modelling and validation data for VCO_2 model are shown in Figure 3.14. Most of the prediction were within the $\pm$10% confidence band with some improvements observed when compared to the ANFIS model (see Figure 3.15). From the results of the predictions of the validation data, the new model reduced the MSE from 451.89 to 395.72, and reduced the MAE from 7.86 to 6.98. The R^2 was slightly improved from 0.84 to 0.86 (see Table 3.12).

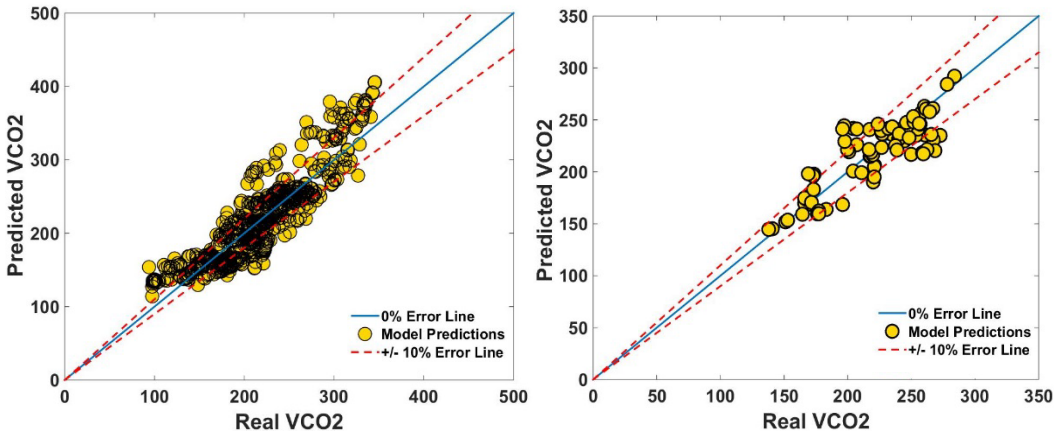

Figure 3.14. IT2FLS VCO_2 model prediction results for modelling data, and validation data

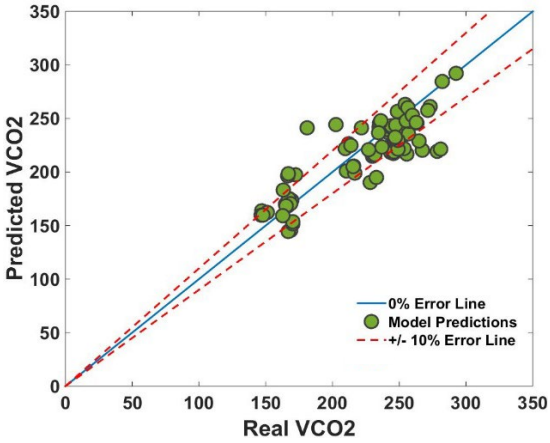

Figure 3.15. ANFIS VCO_2 model prediction results for the validation data

Table 3.12. VCO_2 performance comparison for IT2FLS model with ANFIS model

Approach	Modelling Data			Validation Data		
	MSE	MAE	R^2	MSE	MAE	R^2
ANFIS	189.33	4.59	0.97	451.89	6.98	0.84
IT2FLS	629.97	9.65	0.88	395.72	7.86	0.86

3.6 Modelling of the Shunt Component

The shunt model described by Kwok *et al., (2004b)* was investigated again. In this model, the input to the model was selected based on the relationship of the effective shunt and the Respiratory Index (RI) (see Figure 3.16). In the above study, the R^2 between the Respiratory Index and the effective shunt was reported to be 0.7214. Respiratory index (RI) is the difference between partial alveolar pressures of oxygen (PAO_2) and partial arterial pressure of oxygen (PaO_2) divided by PaO_2. The PAO_2 is calculated using the following alveolar equation:

$$PAO_2 = FiO_2\,(P_B - P_{H2O}) - PaCO_2*(FiO_2 + (1 - FiO_2)*RQ) \quad (3.20)$$

$$RI = (PAO_2 - PaO_2)/PaO_2 \quad (3.21)$$

Here, FiO_2 is the fraction of inspired oxygen, P_B is the barometric pressure, P_{H2O} is the water vapour pressure, $PaCO_2$ is the partial arterial pressure of carbon-dioxide and RQ is the respiratory quotient that was set to 0.8. The effective shunt is the estimated shunt produced by the SOPAVent system using the secant method (Goode, 2000). Thus, RI was selected as the sole input to the IT2FLS shunt model as shown in Figure 3.17.

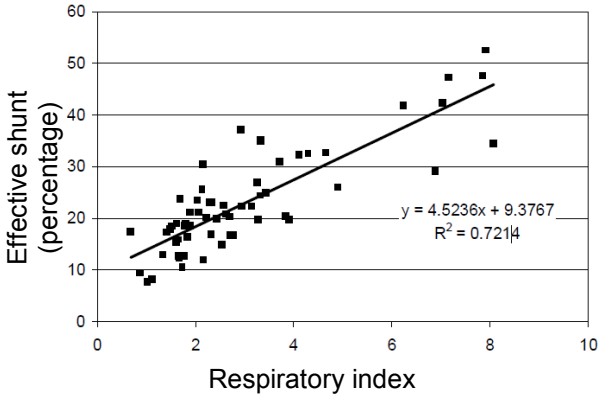

Figure 3.16. Relationship between RI and effective shunt (Kwok *et al.*, 2004)

Figure 3.17. Shunt model

3.6.1 Modelling Data and Validation Data for the Shunt Model

A total of 156 data from 12 patients was used for modelling of shunt and a total of 96 data from 12 patients was used for validation. The summary for the data used for the shunt modelling and validation is shown in Table 3.13. Figure 3.18 shows the distribution of the data for the validation of the shunt model.

Table 3.13. Shunt modelling and validation data

Data	Parameter	Mean $\pm$ σ	Min	Max
Modelling	RI	2.85 $\pm$ 1.69	0.62	8.11
	Effective shunt	23.15 $\pm$ 9.50	5.57	54.11
Validation	RI	2.75 $\pm$ 1.59	0.62	8.11
	Effective shunt	23.23 $\pm$ 9.34	5.57	54.11

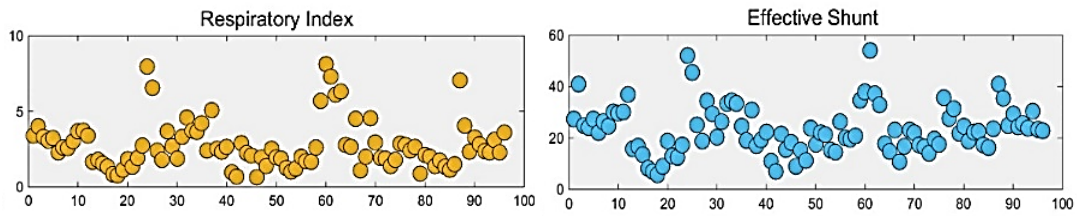

Figure 3.18. Data distribution for shunt model validation

3.6.2 Interval Type-2 Fuzzy Logic System Modelling Parameter for Shunt

The input to the shunt model, the Respiratory Index (RI), was assigned with 5 fuzzy membership functions (MFs): '*Very Low', 'Low', 'Moderate', 'High'* and '*Very High'*. These MFs were 9-point trapezoidal MFs which were equally spaced with an FOU of approximately 10% of the input range. Each input corresponded to one output with a crisp interval. A total of five output MFs map the RI value to the effective shunt (Y1 to Y5) as shown in Table 3.14. The 9-point values for the trapezoidal input MF are shown in Table 3.15. The fuzzy set for the shunt model is shown in Figure 3.19. An example of the fuzzy rule (Rule 2) used is given as follows:

IF RI is Low THEN Shunt is [13.5 29.5]

Table 3.14. Input MF to output MF mapping for Shunt model

Input	Output		
RI	Y	LMF	UMF
Very Low	Y1	-10	17.5
Low	Y2	13.5	29.5
Moderate	Y3	24	37.5
High	Y4	30	44
Very High	Y5	30	55

Table 3.15. 9-point trapezoidal MF for Shunt input parameters

Input	MF	a	b	c	d	e	f	g	h	i
RI	Very Low	-2.5	0	0	2.5	-1.5	0	0	1.5	1
	Low	-0.5	2	2	4.5	0.5	2	2	3.5	1
	Moderate	1.5	4	4	6.5	2.5	4	4	5.5	1
	High	3.5	6	6	8.5	4.5	6	6	7.5	1
	Very High	5.5	8	8	10.5	6.5	8	8	9.5	1

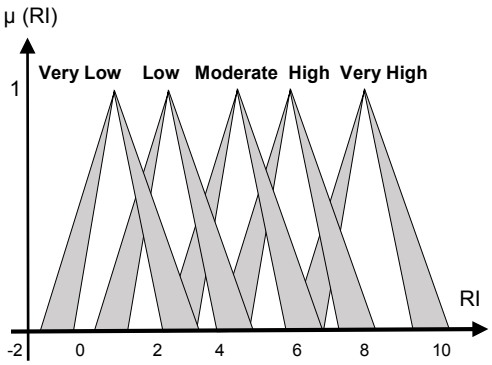

Figure 3.19. RI fuzzy set for shunt input

3.6.3 Validation of Shunt Model

The IT2FLS model was used to predict the shunt values of 96 datasets from 12 patients. The MAE, MSE and R^2 indices were used to evaluate the prediction performance against effective shunt values. The prediction results were also compared with the ANFIS model previously developed by Kwok *et al.,* (2004b). The prediction plots for the validation data of the shunt model are shown in Figure 3.20. From Table 3.16, it can be seen that the new IT2FLS shunt model has reduced the MSE from 25.48 to 22.91. The MAE was marginally reduced from 19.07 to 18.90 and the R^2 was also marginally improved from 0.85 to 0.86.

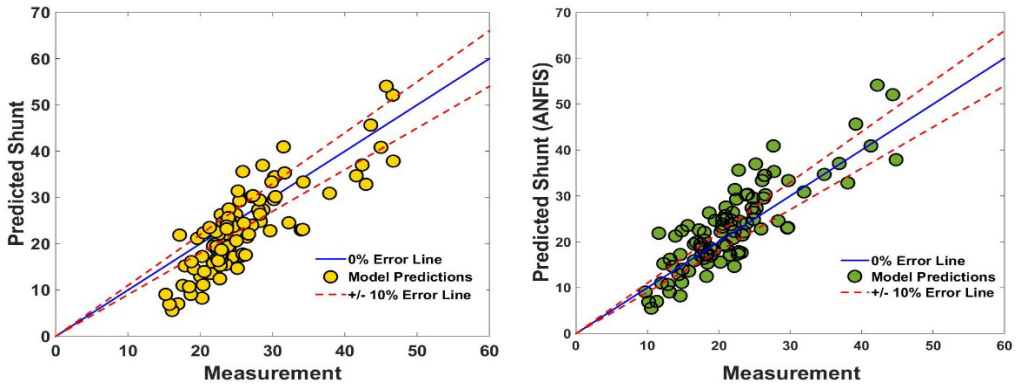

Figure 3.20. IT2FLS shunt model prediction results for IT2FLS and ANFIS (validation data)

Table 3.16. Shunt performance comparison for IT2FLS model with ANFIS model

Approach	Validation Data		
	MSE	MAE	R^2
ANFIS	25.48	19.07	0.85
IT2FLS	22.91	18.90	0.86

3.7 New Particle Swarm Optimization for the Optimal Selection of Fuzzy Membership Functions

Particle swarm optimization (PSO) follows the behaviour of a flock of birds or a school of fish in search of the best location for resources. Each individual in the swarm is called a '*particle*'. Each particle has information on the best location for resources from its own experience, and shares this information with the other members in the swarm. Upon receiving this information, all the other particles adjust their speeds and directions towards the optimal location, also known as the '*global best*'. PSO is a powerful yet simple algorithm to implement on non-linear systems, and has the ability to generally converge to a good solution quickly (Zhang and Mahfouf, 2006). In this work, an updated version of the PSO, called the 'new structure' PSO (nPSO), was used to increase the accuracy of the VCO_2, Kd and the shunt prediction models by tuning the output membership functions (MFs) (see Figure 3.21). In nPSO, the term '*momentum*' was used to replace the term '*inertia*' of the original PSO algorithm. This should enable the particles to circumvent any local optimum and prevent premature convergence (Zhang and Mahfouf, 2006).

$$v_{id}(t+1) = [w_{id}(t+1)*r_1*(t+1)v_{maxi}] + [c_1*r_2(t+1)*[p_{id}(t) - x_{id}(t)] + c_2*r_3(t+1)*[p_{gd}(t) - x_{id}(t)] \quad (3.22)$$

$$x_{id}(t+1) = x_{id}(t) + v_{id}(t+1) \quad (3.23)$$

$$w_{id}(t+1) = \begin{cases} 1, & if\ V_i(t) \leq \varepsilon * V_{max}\ and\ pos_{id}\ (t+1)=1; \\ w_{id}(t)*m_1, & If(not V_i(t)) \leq *V_{max}\ and\ f(X_i(t) \geq f(P_i(t-1)); \\ w_{id}(t)*m_2, & if(not V_i(t) \leq \varepsilon * V_{max}) and\ f(X_i(t) < f(P_i(t-1)) \end{cases} \quad (3.24)$$

$$m_1 < 1 \text{ and } m_2 > 1 \quad (3.25)$$

Here, i is the particle number, d is the dimension number, v_{id} is the velocity or change in particle position within its search area, w is the momentum weight, $r1$, $r2$ and $r3$ are random variables between 0 and 1, V_{max} is the maximum velocity, x_{id} is the particle position, $c1$ and $c2$ are acceleration constants, $m1$ and $m2$ are scaling parameters, $\mathcal{E}$ is a positive coefficient, and pos_{id} is a discrete variable (0 or 1). The dimension of nPSO is equal to the number of output MFs multiplied by two, since each MF is represented by an upper MF (UMF) and lower MF (LMF). The nPSO was used to tune the Kd model with 44 fuzzy rules, the VCO_2 model with 27 fuzzy rules and the shunt model with 5 fuzzy rules. The nPSO algorithm selects the fuzzy sets that produced the least mean squared error (MSE).

The relative dead-space (Kd) with 44 output MFs has a particle dimension of 88. The carbon-dioxide production (VCO_2) with 27 output MFs has a particle dimension of 54, and the shunt model with 5 output MFs has a particle dimension of 10. The input MFs for the shunt model were also tuned using nPSO, since the model is less complex than Kd or VCO_2. The fuzzy sets were tested on the models until the maximum epoch is reached. The nPSO algorithm then returned the fuzzy set with the least MSE. The initialising parameters for nPSO are shown in Table 3.17. The result for shunt input MF tuning are shown in Figure 3.22 and Table 3.18. The nPSO optimization result for the output MFs for the Kd model, the VCO_2 model and the shunt model is shown in Table 3.19.

Table 3.17. Parameters for nPSO Initialization

Parameter	c1, c2	m1, m2	d	V_{xar}	V_{max}	epoch	r1,r2,r3
Value	1.8, 1.8	0.5, 2	88, 54, 10	data range	$0.5V_{xar}$	30	[0, 1]

Table 3.18. 9-point trapezoidal MF for shunt input after tuning

Input	MF	a	b	c	d	e	f	g	h	i
RI	Very Low	-2.999	-2.476	5.407	7.165	-1.307	1	1.983	2.255	1
	Low	-1.277	0.352	3.587	3.806	1	2.186	3.321	3.372	1
	Moderate	-0.287	1	6.269	6.540	1.861	5.370	5.606	5.861	1
	High	0.485	1	5.169	9.905	2.879	3.490	4.044	4.447	1
	Very High	1	2.050	10.113	10.348	3.734	5.415	6.518	8.254	1

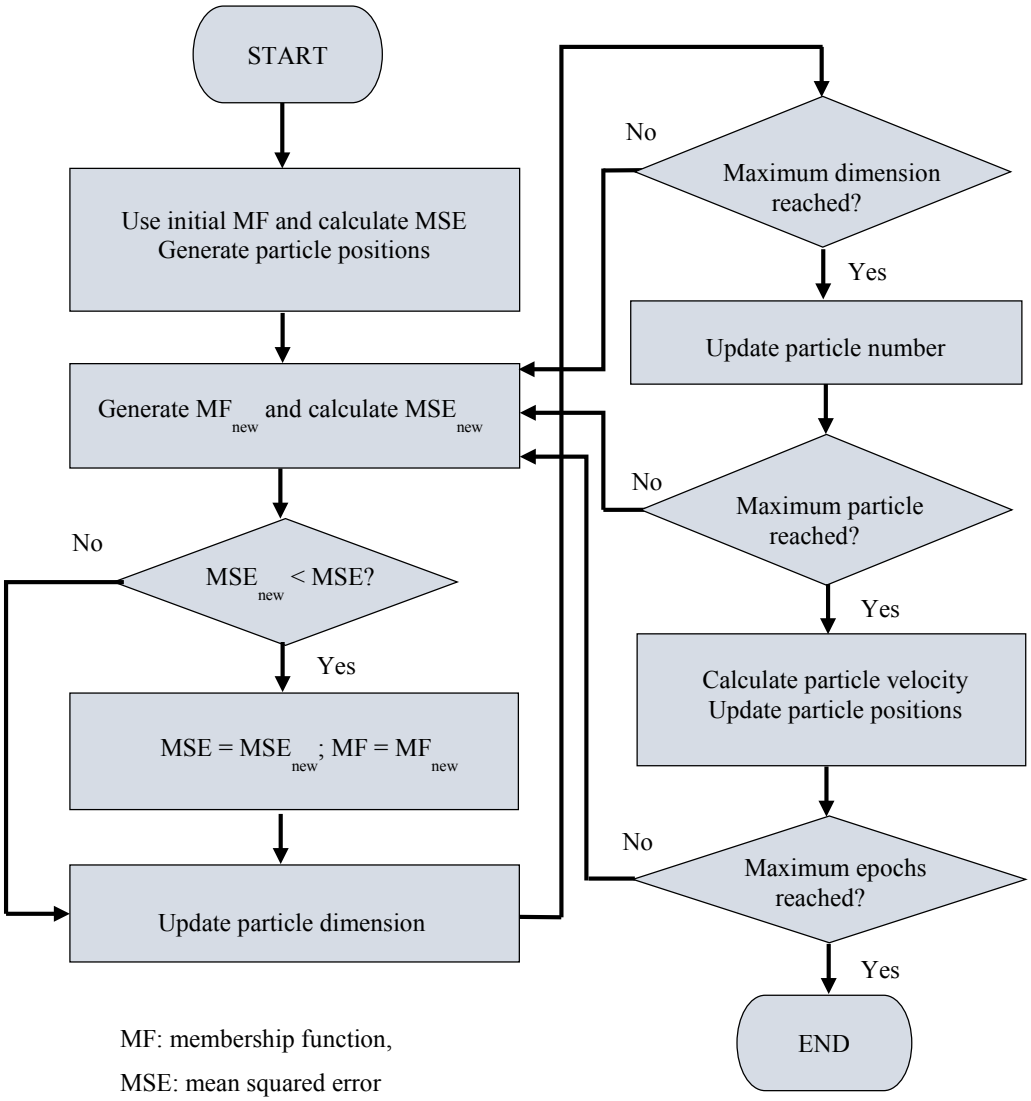

Figure 3.21. Membership function selection using nPSO

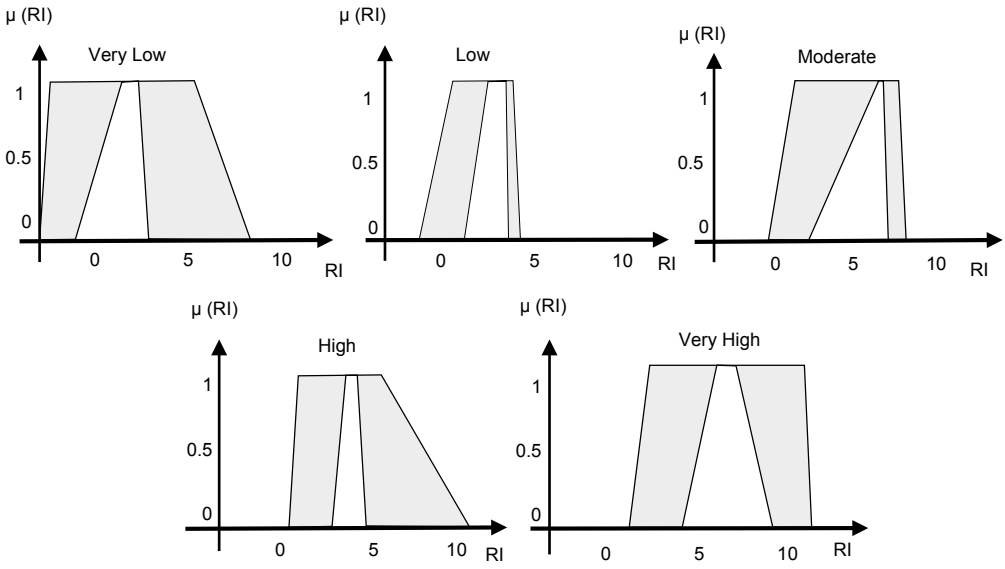

Figure 3.22. Tuned input membership function for the shunt model

Table 3.19. The tuning result for the Kd model, the VCO_2 model and the shunt model

Kd Model					
Output	LMF	UMF	Output	LMF	UMF
Y1	11.95153	26.76352	Y23	16.54308	34.90325
Y2	1.943871	56.02744	Y24	31.71382	36.85449
Y3	6.304774	31.59038	Y25	5.272399	60.15405
Y4	5.425955	30.37743	Y26	7.554265	43.93199
Y5	10.69186	41.88724	Y27	18.45848	21.67796
Y6	1.216366	20.79793	Y28	22.83077	52.56087
Y7	4.495041	34.15593	Y29	14.5068	56.95415
Y8	27.24409	47.87682	Y30	22.11961	42.20132
Y9	8.394214	34.18694	Y31	3.707069	44.68312
Y10	6.767473	41.18542	Y32	15.3378	41.18921
Y11	25.00115	36.49195	Y33	10.43651	51.1443
Y12	10.72191	35.61868	Y34	33.12716	28.20647
Y13	3.764249	39.6861	Y35	9.10398	48.95976
Y14	7.693577	38.45613	Y36	14.28307	62.15822
Y15	32.81382	62.29011	Y37	20.07898	24.57227
Y16	20.45761	57.78256	Y38	14.96541	40.86009
Y17	18.34761	54.16636	Y39	36.52609	58.41877
Y18	8.254939	41.41683	Y40	4.991641	41.8549
Y19	17.69926	53.48385	Y41	34.64175	47.68374
Y20	2.782323	27.29492	Y42	27.9155	47.64417
Y21	12.17879	36.73364	Y43	23.86115	49.22595
Y22	2.292789	23.1341	Y44	28.57476	62.56782
VCO_2 Model					
Y1	25.59264	134.0487	Y15	368.8466	341.2231
Y2	152.3353	235.2353	Y16	327.3282	200.9932
Y3	167.9844	259.7977	Y17	353.6114	273.1941
Y4	138.059	165.9586	Y18	339.9651	228.385
Y5	188.5205	253.9587	Y19	64.85753	210.9764
Y6	430	217.4145	Y20	312.2349	254.5367
Y7	230.7809	279.2906	Y21	318.9626	289.1905
Y8	178.7078	268.8228	Y22	301.7819	193.5026
Y9	86.2252	301.1571	Y23	393.8858	429.1923
Y10	156.7144	15.36991	Y24	327.2807	280.544
Y11	230.1731	397.9124	Y25	293.2346	249.3352
Y12	426.6639	430	Y26	430	358.9201
Y13	190.7528	152.7474	Y27	398.4007	275.6278
Y14	370.4015	319.7526			
Shunt Model					
Y1	-12.0433	21.63106	Y4	35.41843	43.66498
Y2	13.85383	30.1571	Y5	35.4893	55.27925
Y3	17.54528	39.32554			

3.7.1 Validation of the New Structure Particle Swarm Optimization-tuned Relative Dead-space Model, Carbon-dioxide Production Model and Shunt Model using Real Patient Data

The surface plots for the Kd model before and after tuning were performed are shown in Figure 3.23, with the tuned Kd prediction curve shown in Figure 3.24. Prediction results for Kd are shown in Table 3.20. The optimized Kd model has reduced the number of predictions outside of the $\pm$10% confidence band. However, some predictions were slightly higher than the actual measurements. The new model has reduced the overshooting error that exists when $PaCO_2$ is between 8.0 kPa and 8.18 kPa, and when PEEP is between 16cmH2O and 20cmH2O. There still exist 'plateaus' in the lower regions of PaCO2 which are related to the middle and upper regions of PEEP. This was probably due to the existing fuzzy rules which were unable to represent the entire range of inputs.

When compared to the manually tuned IT2FLS model, the optimized model has reduced the MSE of the modelling data set from 19.61 to 14.47, and improved the MAE from 13.45 to 10.92. It has also increased the coefficient of R^2 from 0.79 to 0.83. For the validation data set, the optimized model has reduced the MSE of the manually tuned IT2FLS Kd model from 28.91 to 22.39 and improved the MAE from 14.62 to 10.98. It has also increased the R^2 from 0.69 to 0.80.

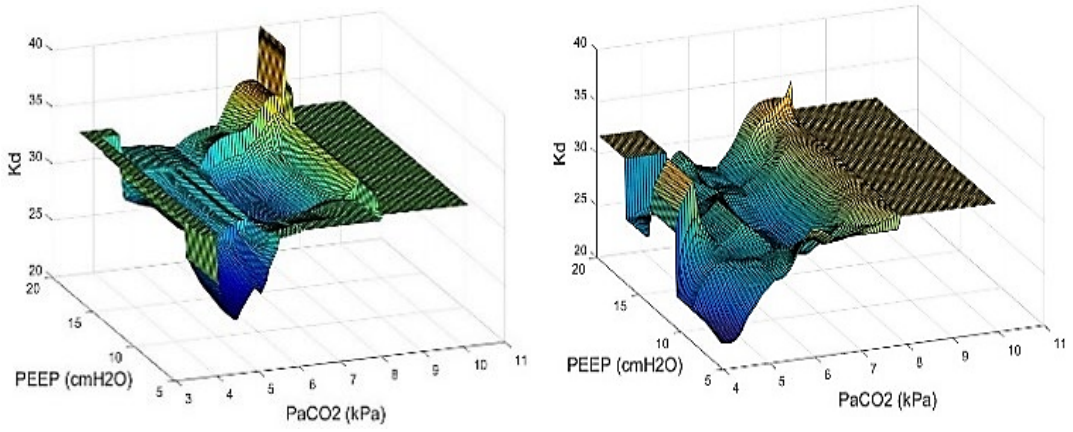

Figure 3.23 Surface plot for the IT2FLS Kd model. Left: manual tuning. Right: nPSO-tuned

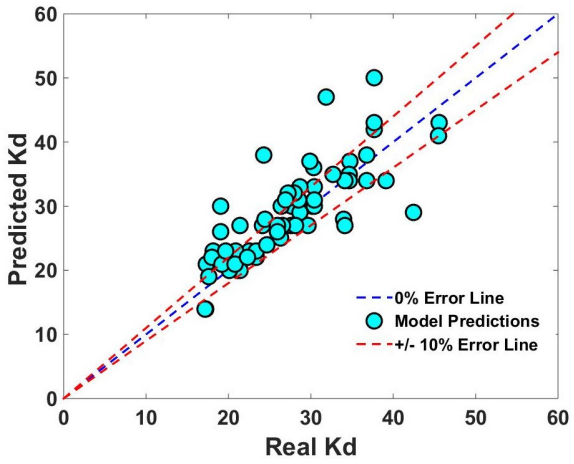

Figure 3.24 Prediction result for the nPSO-tuned IT2FLS Kd model (validation data)

Table 3.20 Prediction results for IT2FLS Kd model

Tuning Method	Modelling Data			Validation Data		
	MSE	MAE	R^2	MSE	MAE	R^2
Manual	19.61	13.45	0.79	28.91	14.62	0.69
nPSO	14.47	10.92	0.83	22.39	10.98	0.80

The surface plots for the VCO_2 model before and after tuning were performed are shown in Figure 3.25, with the tuned VCO_2 prediction curve shown in Figure 3.26. The prediction results for VCO_2 are shown in Table 3.21. The optimized VCO_2 model has removed most of predictions outside of the $\pm$10% margin of error. The model has smoothed the indentation observed for MV values between 12 l/min and 14 l/min. A plateauing effect can be seen on the upper region of the input, this is due to the limitation of the lungs to produce carbon-dioxide (CO_2) more than its maximum capacity. When compared to the manually tuned IT2FLS model, the optimized model has reduced the MSE of the modelling data sets from 629.97 to 476.85, and improved the MAE from 9.65 to 7.96. It has also increased the R^2 significantly from 0.79 to 0.92. For the validation data set, the optimized model has reduced the MSE from 395.72 to 315.46, and improved the MAE marginally from 6.98 to 6.33. It has also increased the R^2 from 0.84 to 0.91.

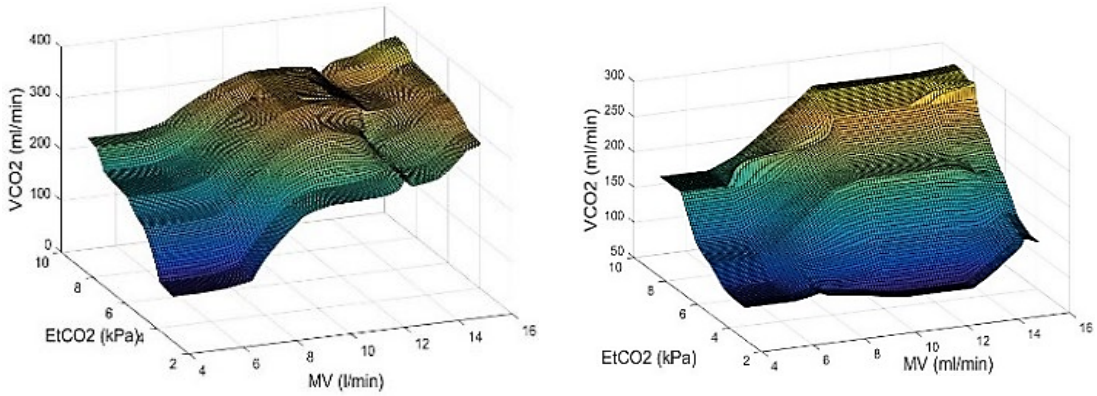

Figure 3.25 Surface plot for the IT2FLS VCO_2 model. Left: manually tuned. Right: nPSO-tuned.

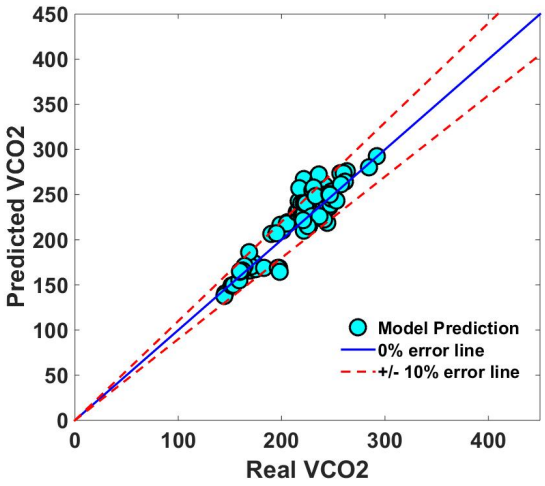

Figure 3.26 Prediction result for the nPSO-tuned IT2FLS VCO_2 model (validation data)

Table 3.21 Prediction results for IT2FLS VCO_2 model

Tuning Method	Modelling Data			Validation Data		
	MSE	MAE	R^2	MSE	MAE	R^2
Manual	629.97	9.65	0.88	395.72	6.98	0.84
nPSO	476.85	7.96	0.92	315.46	6.33	0.91

The prediction curve for the nPSO tuned shunt model is shown in Figure 3.27. The prediction results for shunt are shown in Table 3.22. When compared to the manually tuned IT2FLS model, the optimized model has reduced the MSE of the validation data set from 22.91 to 20.55, and reduced the MAE marginally from 18.90 to 18.31. It has also increased the R^2 slightly from 0.86 to 0.88.

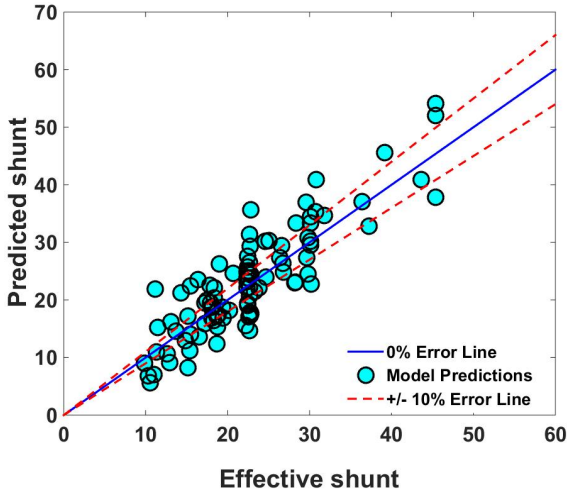

Figure 3.27 Prediction result for the nPSO-tuned IT2FLS shunt model (validation data)

Table 3.22 Prediction results for IT2FLS shunt model

Tuning Method	Validation Data		
	MSE	MAE	R^2
Manual	22.91	18.90	0.86
nPSO	20.55	18.31	0.88

3.8 Summary

Interval type-2 fuzzy logic system (IT2FLS) was used to model the blood gas parameters of relative dead-space (Kd), carbon-dioxide production (VCO_2) and shunt. The new IT2FLS models also showed a better generalization capability as compared to the ANFIS models, as a result allowing them to be more robust and adaptive to uncertainties and inter/intra ICU patient parameter variability respectively.

A 'new structure' particle swarm optimization (nPSO) algorithm was then used to tune the IT2FLS models of Kd, VCO_2 and shunt in the SOPAVent model. The manually tuned IT2FLS model showed a better prediction accuracy for the validation data when compared to the ANFIS models. The nPSO tuned models showed a better prediction accuracy when compared to the manually tuned ones. The new 'momentum' term in nPSO enables the algorithm to avoid premature convergence and creates an adaptive search process for the particles. The new modelling framework has smoothed the output curve for the manually tuned VCO_2 model, and partly reduced the anomalies which related to the 'plateaus' and 'peaks' in certain input ranges as

seen in the manually tuned Kd model. A more complex Kd model with 243 fuzzy rules was also considered. However, the fuzzy rules for the Kd model with 243 rules were not optimized.

In the next chapter, further explorations of the blood gas parameters using fuzzy c-means clustering for type-1 fuzzy inference system (FIS) and type-2 fuzzy logic systems will be discussed. These are then followed with the integration of the Kd, VCO_2 and the shunt models into the original model structure, SOPAVent as well as validation of SOPAVent for the prediction of PaO_2, $PaCO_2$ and pH.

Chapter 4

Fuzzy C-Means Clustering Models for Relative Dead-Space and Carbon-dioxide Production and Validation of the SOPAVent Blood Gas Model

4.1 Introduction

Fuzzy C-Means Clustering (FCM) is a prototype-based clustering algorithm that partitions or 'clusters' data according to their similarities (in the Euclidian sense) (Hwang *et al.*, 2007). Each data point has a certain membership grade associated to every cluster and each cluster has a centre. The cluster centres and membership grades are iteratively updated until the cluster centres are moved to their optimal location. This is achieved by reducing the distance between data points and their cluster centres. By creating natural groupings from a large dataset, one can extract a meaningful knowledge about the system (Chiu, 1994). FCM minimizes the following cost function:

$$J = \sum_{k=1}^{n} \sum_{i=1}^{c} \mu_{ik}^{m} \left| |x_k - v_i| \right|^2 \tag{4.1}$$

$$\text{Where, } \mu_{ik} = \frac{1}{\sum_{j=1}^{c} \left(\frac{||x_k - v_i||}{||x_k - v_j||} \right)^{2/(m-1)}} \tag{4.2}$$

Here, n is data size, c is cluster number, x_k is the k^{th} data, v_i is the i^{th} cluster centre, μ_{ik} is the degree of membership of the k^{th} data in the i^{th} cluster, and m is a constant typically set at 2. The effectiveness of FCM is dependent on the number of clusters and the initial cluster centres (Chiu, 1994).

In this chapter a new approach for modelling the Kd and the VCO_2 sub-components using FCM is proposed. The resulting models will then be validated with real patient data and later will be integrated with the SOPAVent blood gas model for prediction of PaO_2, $PaCO_2$ and pH. The results of the SOPAVent model where Kd and VCO_2 were designed using FCM will be compared with the results of the SOPAVent versions where Kd and VCO_2 models were developed using interval type-2 fuzzy logic system (IT2FLS) (refer to Chapter 3), and will also be compared with the results of the SOPAVent model where Kd and VCO_2 were designed using adaptive network-based fuzzy inference system (ANFIS) as described by Wang *et al*., 2010a.

4.2 Fuzzy C-Means Clustering for the Selection of Fuzzy Sets for the Kd and the VCO_2 Models

In this work, FCM was employed to design type-1 fuzzy sets for the VCO_2 and the Kd models. The dataset used in the FCM is the modelling data defined in Chapter 3. Figures 4.1 and 4.2 show the data distribution for the Kd model, while figures 4.3 and 4.4 show the data distribution for the VCO_2 model. The selection of the cluster number, c was carried-out on a trial and error basis, starting from $c = 4$ up to a maximum of $c = 30$. The cluster centre and standard deviation for each cluster were used to generate the Gaussian membership functions (MFs) for the fuzzy system using a Mamdani rule-base.

The Mean Squared Error (MSE), Mean Absolute Error (MAE), and coefficient of determination (R^2) were used as the selection criteria for the optimal cluster number. The results for the FCM simulations are shown in Table 4.1. From these simulations performed, the cluster number $c = 28$ has shown to be the optimal setting to represent the behaviour of the Kd model, and the cluster number $c = 17$ was the best as far as the VCO_2 model was concerned. Figure 4.5 shows the MSE against the cluster number for the Kd and the VCO_2 model.

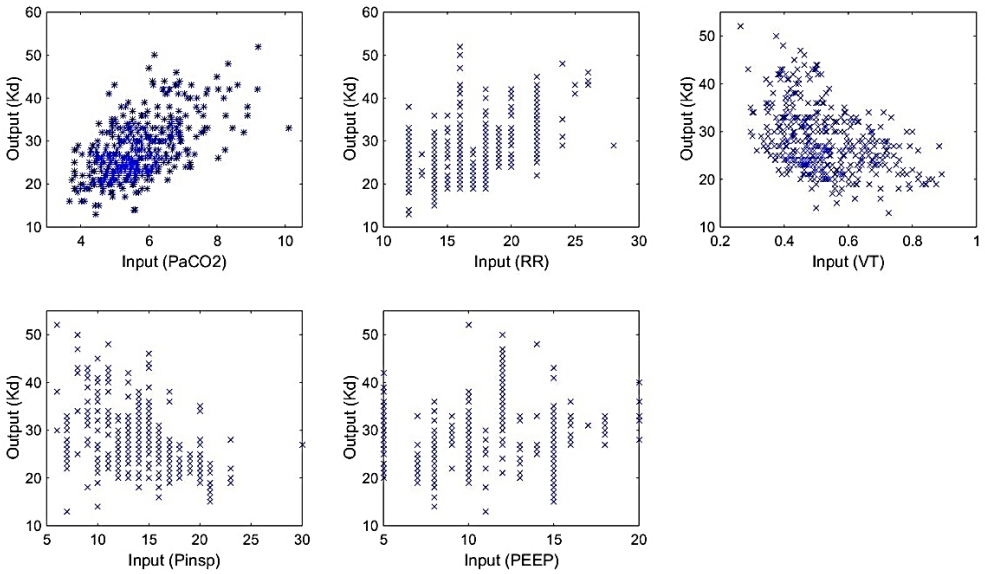

Figure 4.1. Kd model output against model inputs ($PaCO_2$, RR, VT, Pinsp and PEEP)

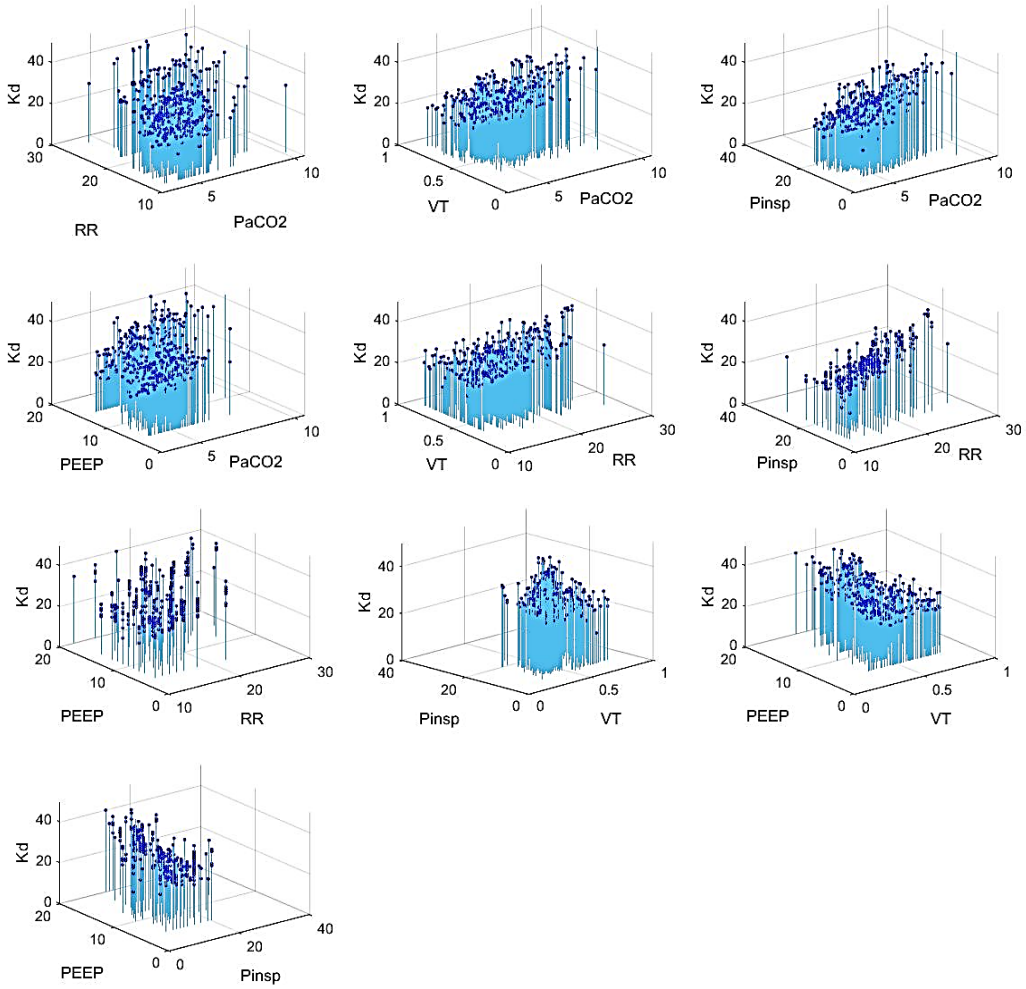

Figure 4.2 Three-dimensional distribution for the Kd model showing relationship of inputs ($PaCO_2$, RR, VT, Pinsp and PEEP) to the output, Kd

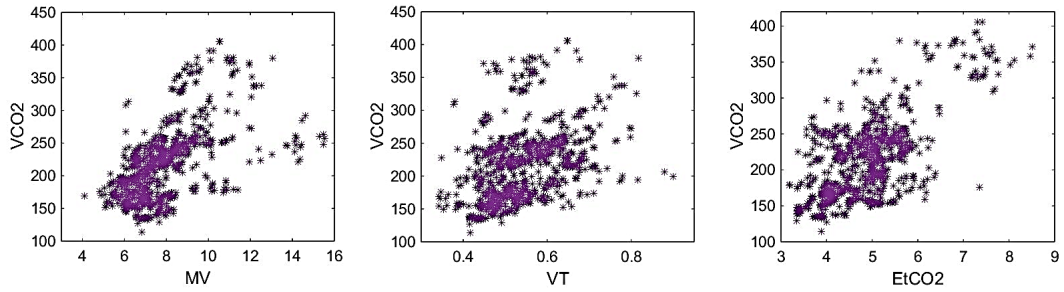

Figure 4.3. VCO_2 model output against model inputs (MV, VT and $ETCO_2$)

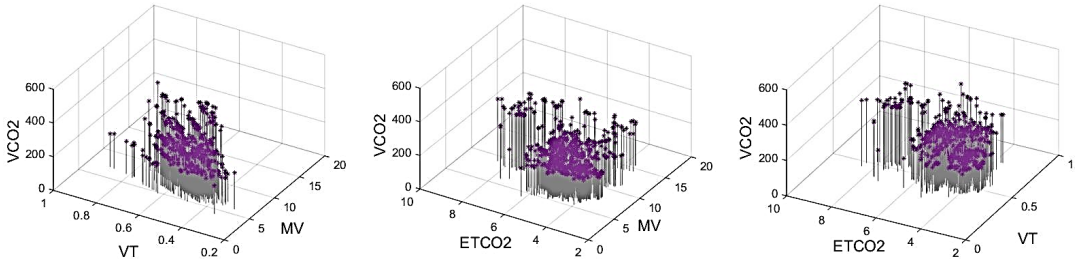

Figure 4.4 Three-dimensional distribution for the VCO_2 model showing relationship of inputs (MV, VT and $ETCO_2$) to the output, VCO_2

Table 4.1. FCM clustering results for the Kd and the VCO_2 sub-components based on predictions of modelling data

Sub-component	Cluster Number	MSE	MAE	R^2
Kd	28	13.05	10.89	0.85
VCO_2	17	1146.01	15.00	0.91

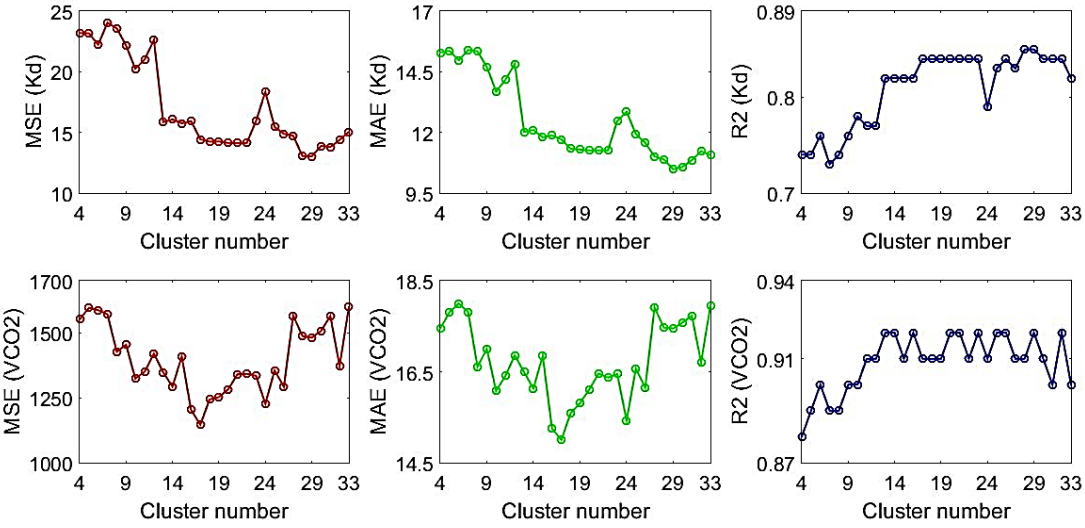

Figure 4.5 MSE against cluster number for the Kd model (top) and the VCO_2 model (bottom).

The following figures show the results obtained from the FCM process for the Kd sub-component. The clusters generated for the Kd model are shown in Figure 4.6 and the prediction results for the modelling and the validation datasets of the Kd model using FCM are shown in Figure 4.7 and Table 4.2. The model was tested with the same data sets as in Chapter 3. The model produced an MSE of 13.05, an MAE of 10.89 and R^2 of 0.85 for the modelling dataset. For the validation dataset, the model produced an MSE of 23.53, an MAE of 12.94 and R^2 of 0.75. A majority of the predictions were within the $\pm$10% confidence band, however, further improvements are required to reduce prediction errors.

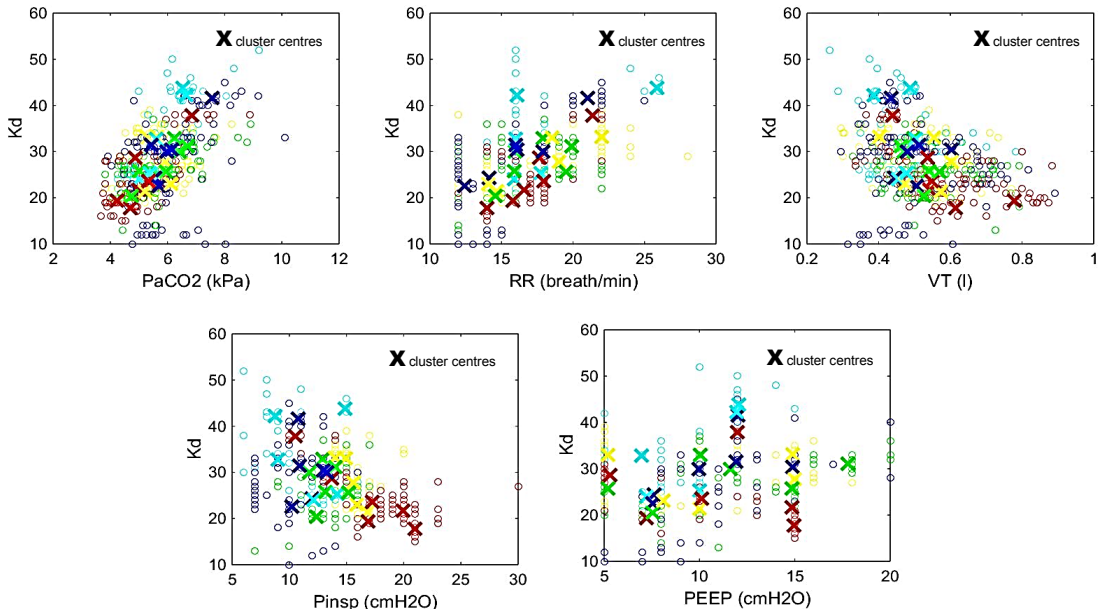

Figure 4.6. FCM result for the clustering of the Kd model inputs ($PaCO_2$, RR, VT, Pinsp and PEEP)

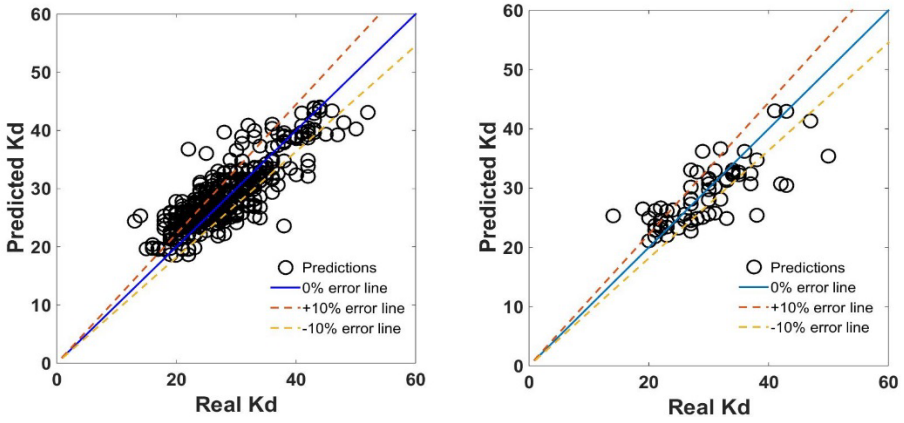

Figure 4.7. Prediction results for the FCM generated fuzzy sets for the Kd sub-component. Left: modelling data, and right: validation data

Table 4.2. Prediction results of the modelling and the validation datasets for the FCM Kd sub-component

Modelling Data			Validation Data		
MSE	MAE	R^2	MSE	MAE	R^2
13.05	10.89	0.85	23.53	12.94	0.75

The following figures show the results obtained from the FCM process for the VCO_2 sub-component. The clusters generated for the VCO_2 sub-component are shown in Figure 4.8, and the prediction results for the modelling and the validation datasets of the VCO_2 sub-component are shown in Figure 4.9 and Table 4.3. The model was tested with the same datasets as in Chapter 3. For the modelling dataset, the FCM model produced an MSE of 1146.01, an MAE of 15.00 and R^2 of 0.91. For the validation dataset, the model produced an MSE of 704.63, an MAE of 11.23 and R^2 of 0.86.

Although the R^2 values can be deemed to be good at 0.91 and 0.86 respectively, it can be seen that for the lower-end values of VCO_2, where VCO_2 is between 125ml/min to 200ml/min, the predictions were significantly higher than the expected ones. This resulted in a large number of predictions sitting outside of the $\pm$10% confidence band. Thus, further improvements were necessary to reduce the number of predictions which lie outside of the $\pm$10% confidence band.

The fuzzy sets and the fuzzy surface plots generated by the FCM process for the Kd and the VCO_2 components are available in Appendix B1.

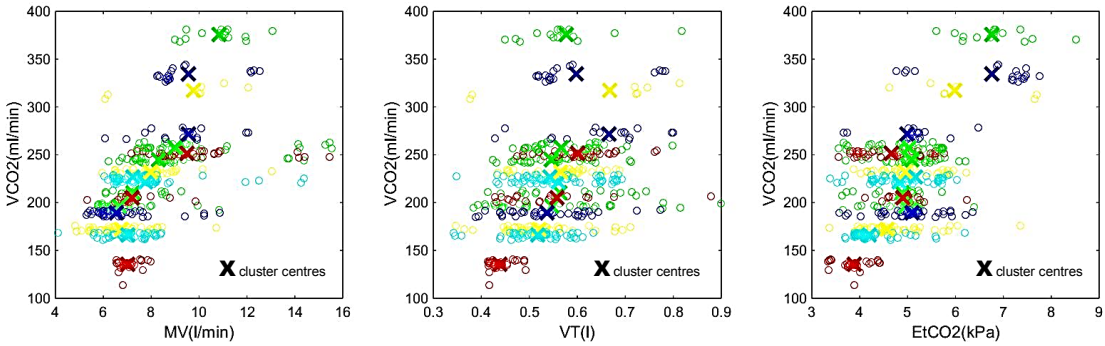

Figure 4.8. FCM result for the clustering of VCO_2 model's inputs (MV, VT and $EtCO_2$)

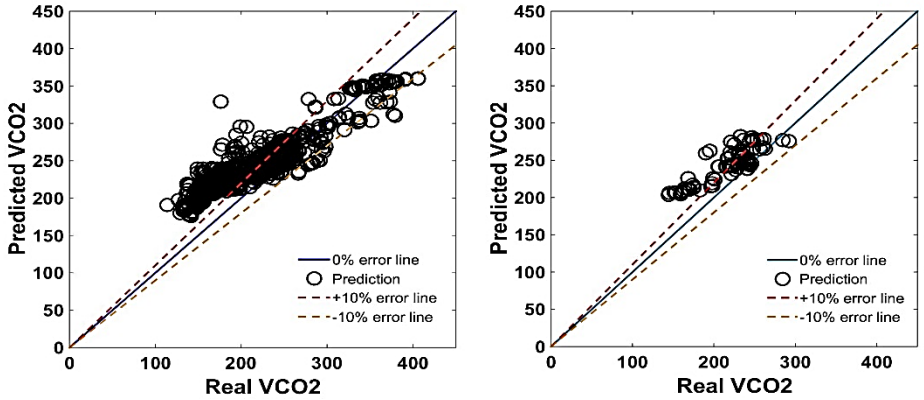

Figure 4.9. Prediction results for the FCM generated fuzzy sets for the VCO_2 model. Left: modelling dataset, and right: validation dataset

Table 4.3. Prediction results of modelling and validation datasets for the FCM VCO_2 model

Modelling Data			Validation Data		
MSE	MAE	R^2	MSE	MAE	R^2
1146.01	15.00	0.91	704.63	11.23	0.86

4.3 New Structure Particle Swarm Optimization for the Selection of the Membership Functions for Fuzzy C-Means Clustering Relative Dead-space and Carbon-dioxide Production Models

To increase the prediction accuracy of the Kd and the VCO_2 sub-components, the fuzzy sets generated from the FCM process were further tuned using the nPSO algorithm described in Chapter 3. The nPSO algorithm was first applied for the selection of the output MFs, and then followed by the selection of the input MFs. The smallest Mean Squared Error (MSE) was selected as the first objective of the optimization algorithm, and the largest coefficient of determination (R^2) was selected as the second objective of the optimization algorithm.

4.3.1 Validation Results

Table 4.4 shows the results for the modelling and the validation dataset for the FCM nPSO optimized Kd and VCO_2 models. The prediction plots for the FCM

nPSO optimized Kd and the FCM nPSO optimized VCO_2 models are shown in Figures 4.10 and 4.11 respectively. The surface plots and the fuzzy sets generated from the FCM nPSO optimization of Kd and VCO_2 models are available in Appendix B2.

The FCM Kd model with nPSO optimization based on the least MSE has generated an MSE of 9.95, an MAE of 9.12 and R^2 of 0.89 for the modelling dataset. For the validation dataset, the model has produced an MSE of 19.52, an MAE of 11.14 and an R^2 of 0.82. The FCM Kd model with nPSO optimization based on the largest R^2 has produced an MSE of 6.46, an MAE of 7.18 and R^2 of 0.93 for the modelling dataset. For the validation dataset, the model has generated an MSE of 16.93, an MAE of 9.73 and R^2 of 0.86. Several predictions of the Kd parameter were outside of the $\pm$10% confidence band, however, significant improvements were observed for the MSE, MAE and R^2 when compared with the previous FCM models for both data sets.

The FCM VCO_2 model with nPSO optimization based on the least MSE has generated an MSE of 379.10, an MAE of 7.01 and R^2 of 0.94 for the modelling dataset. For the validation dataset, the model has generated an MSE of 245.85, an MAE of 5.80 and R^2 of 0.91. The FCM VCO_2 model with nPSO optimization based on the largest R^2 has produced an MSE of 246.38, an MAE of 5.61 and the R^2 of 0.96 for the modelling dataset. For the validation dataset, the model has generated an MSE of 268.74, an MAE of 5.79 and the R^2 of 0.91. The nPSO optimization has significantly reduced the number of predictions which were outside of the $\pm$10% confidence band, and has improved the prediction accuracy of VCO_2 within the range of 125 ml/min and 200 ml/min of the previous FCM model.

Table 4.4. Prediction results of modelling and validation datasets for the FCM nPSO Kd and the FCM nPSO VCO_2 models, based on the least MSE and largest R^2

Indices	Kd Model				VCO_2 Model			
	Modelling Data		Validation Data		Modelling Data		Validation Data	
	Least MSE	Largest R^2	Least MSE	Largest R^2	Least MSE	Largest R^2	Least MSE	Largest R^2
MSE	9.95	6.46	19.52	16.93	379.10	246.38	245.85	268.74
MAE	9.12	7.18	11.14	9.73	7.01	5.61	5.80	5.79
R^2	0.89	0.93	0.82	0.86	0.94	0.96	0.91	0.91

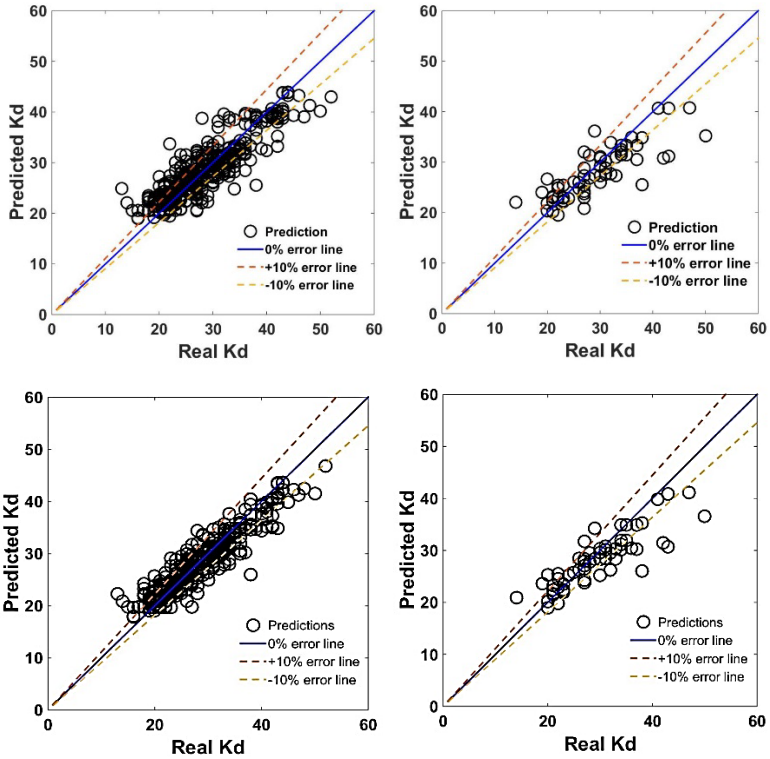

Figure 4.10. Prediction results for the FCM nPSO generated fuzzy sets for the Kd model. Top: Optimized based on the least MSE for the modelling and the validation datasets. Bottom: Optimized based on the largest R^2 for modelling and validation datasets

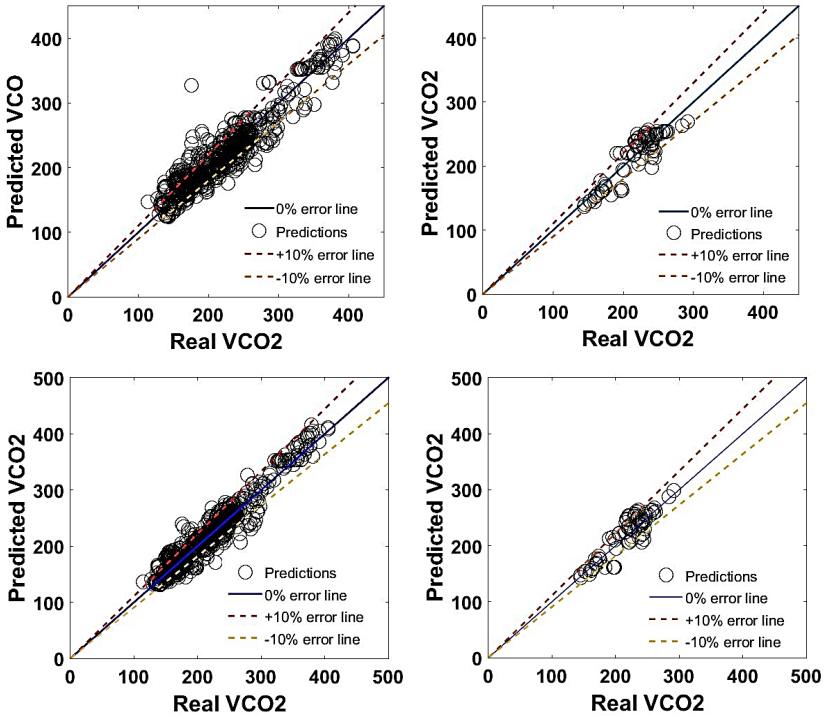

Figure 4.11. Prediction results for the FCM nPSO generated fuzzy sets for the VCO_2 model. Top: Optimized based on the least MSE for the modelling and the validation datasets. Bottom: Optimized based on the largest R^2 for the modelling and the validation datasets

4.4 Validation of the Sheffield SOPAVent Blood Gas Model using Real Patient Data from the Intensive Care Unit

To allow for SOPAVent to predict the arterial blood gas parameters (ABG) (PaO_2, $PaCO_2$ and pH), the Kd, the VCO_2 and the shunt models were integrated into SOPAVent together with other inputs. The prediction of SOPAVent was then compared with actual blood gas measurements for performance evaluation. SOPAVent generated two sets of outputs. The first set are the initial ABG predictions, which are predictions before changes in ventilator settings were applied. The second set of outputs are the ABG predictions after the ventilator settings were adjusted. As ABG parameters can change as early as 30 minutes after ventilator settings changes were made, an immediate prediction will be beneficial for the following treatment strategy.

4.4.1 Data Selection for the SOPAVent Model

The data used for this work is retrospective from the Sheffield Royal Hallamshire Hospital, United Kingdom. The data for SOPAVent validation met the following conditions as previously been defined in Wang *et al*., 2008.

i. All patients in Bi-level Positive Airway Pressure mode (BiPAP);
ii. The ABGs were taken between 30 and 60 minutes before ventilator settings were adjusted;
iii. The ABGs were taken between 30 and 180 minutes after ventilator settings were adjusted;
iv. The changes in mean blood pressure (BP) between ventilator adjustments should be within $\pm$15% of the original BP, and,
v. The ratio of the spontaneous breathing rate to the total breathing rate between ventilator adjustments should be less than 15%.

Twenty-nine (29) data sets obtained from 21 patients, were used to validate SOPAVent. The patients consisted of 7 females and 14 males with a mean age of 58 $\pm$ 13 years, a mean height of 170 $\pm$ 9.18 cm and a mean weight of 70.4 $\pm$ 16

kg. Table 4.5 shows the summary for all patients used in this study. Figure 4.12 show the distribution of 29 data sets used in the SOPAVent model validation.

Table 4.5. Summary of patients for SOPAVent validation.

Age	Height (cm)	Weight (kg)	Gender	
			Male	Female
58±13	170±9.18	70.4±16	14	7

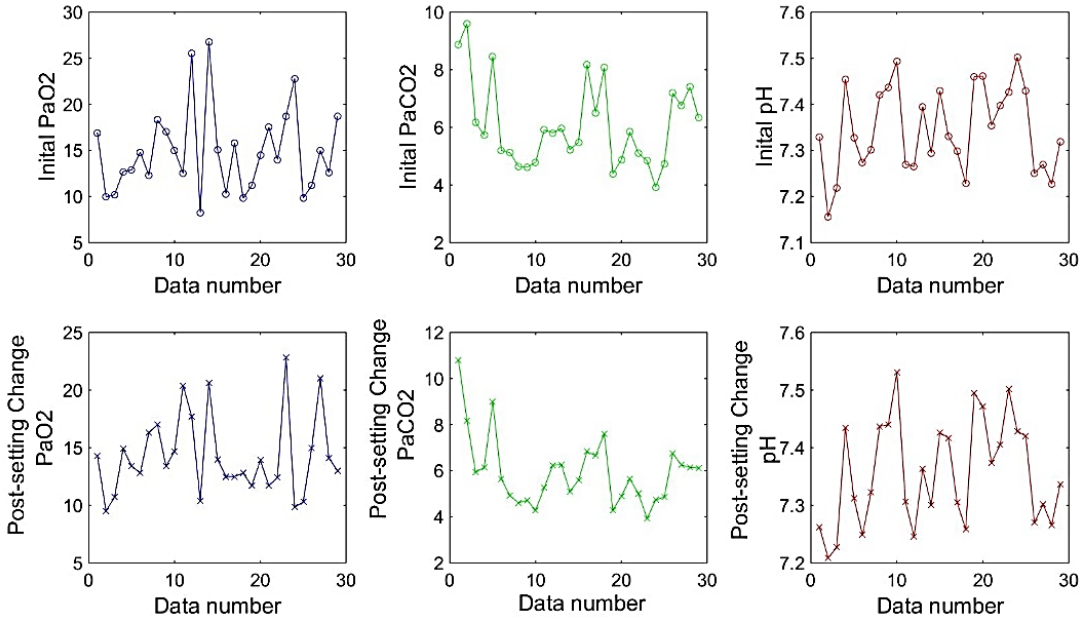

Figure 4.12. SOPAVent validation data. Top: Initial ABG (PaO_2, $PaCO_2$ and pH). Bottom: ABG after ventilator settings change (PaO_2, $PaCO_2$ and pH)

4.4.2 SOPAVent Validation Results

In perspective, the results of the SOPAVent predictions will be compared for the Kd and the VCO_2 models which were designed using the Interval Type-2 Fuzzy Logic System (IT2FLS), the Fuzzy C-Means Clustering (FCM), and the Adaptive Neural-fuzzy Inference System (ANFIS). As the prediction of PaO_2 is dependent on shunt, and there is no physical measurement of shunt to validate the model with, the SOPAVent model with the shunt which was designed using IT2FLS (manual and nPSO tuned) was first compared with the shunt model which was derived using the secant tuning method as described in Wang *et al*., 2008.

This exercise is carried out in order to determine the most suitable shunt models to be integrated with the FCM generated Kd and the FCM generated VCO_2 models. From the simulations performed, the best shunt model achieved was the secant tuning method, and this can be seen from the initial PaO_2 predictions in Table 4.6. The IT2FLS shunt was modelled based on the respiratory index (RI) (as describe in Chapter 3), and since only a limited number of samples were available for modelling of shunt from RI, a degradation in accuracy was observed for initial PaO_2 predictions, as shown in Table 4.6. However, it did not significantly affect the prediction accuracy for the initial and the post-settings change of $PaCO_2$, and the initial and the post-settings change of pH. Nonetheless, only the secant tuning model for shunt is considered for all future evaluations of SOPAVent.

For the initial predictions of PaO_2, the SOPAVent model showed similar performances whether the Kd and the VCO_2 models were designed using IT2FLS, FCM, or ANFIS. For these models, the R^2 were equal to 1 and the MSE and MAE were near zero (see Table 4.6). For the post-setting-change predictions of PaO_2, when the shunt was modelled using the secant tuning method, SOPAVent showed similar performances whether the Kd and the VCO_2 models were elicited using IT2FLS, FCM, or ANFIS, with an MSE averaging at 11.65, an MAE averaging at 15.65 and an R^2 averaging at 0.50 (see Table 4.7).

For the initial predictions of $PaCO_2$, all models outperformed the previous SOPAVent model by Wang *et al*., (2010a), where Kd and VCO_2 were elicited via ANFIS. The best prediction was achieved by the combination of the IT2FLS model with 243 rules for the Kd parameter, and the IT2FLS nPSO model for the VCO_2 parameter, where the MSE was 0.39, the MAE was 9.11 and R^2 was 0.91. This was closely followed by the SOPAVent version where both the Kd and the VCO_2 sub-components were elicited via the IT2FLS nPSO model, which generated an MSE of 0.64, an MAE of 9.85 and R^2 of 0.86. For the post-setting-change predictions of $PaCO_2$, the best performing model was the SOPAVent version where the Kd was elicited via the IT2FLS model with 243 rules, and the VCO_2 was modelled using the IT2FLS nPSO model, which produced an MSE of 0.74, an MAE of 10.31 and R^2 of 0.81, which outperformed the previous SOPAVent model where Kd and VCO_2 were modelled using ANFIS. All other combinations of Kd and VCO_2 were either

marginally less performing or were marginally better performing when compared to the SOPAVent version where the Kd and the VCO_2 models were stimulated via ANFIS.

For the initial predictions of pH, all models also outperformed the previous SOPAVent version, with all models producing R^2 above 0.80. The best performing version was the SOPAVent version where the Kd sub-component was modelled using the IT2FLS model with 243 rules, and the VCO_2 sub-component was elicited via the IT2FLS nPSO model, where the MSE was 2.50e-3, the MAE was 0.54 and R^2 was 0.88. This was followed by the SOPAVent version where both Kd and VCO_2 sub-components were modelled using the IT2FLS nPSO model, where the generated MSE was 2.70e-3, the generated MAE was 0.57 and the R^2 was 0.84. For the post-setting-change predictions of pH, all version of the SOPAVent showed an equal or better prediction accuracy, when compared with the previous SOPAVent model where Kd and VCO_2 were designed using ANFIS.

Samples of the prediction plots for the initial ABG predictions and the post-setting change ABG predictions for the SOPAVent model where both the Kd the and the VCO_2 sub-components were elicited via the FCM nPSO model, are shown in Figures 4.13 and 4.14 respectively. Other samples of prediction plots for the SOPAVent model for initial ABG predictions and post-setting change ABG predictions are available in Appendix B2.

Table 4.6. SOPAVent initial ABG prediction results

Sub-component Modelling Approach			Initial PaO2			Initial PaCO2			Initial pH		
Kd	VCO_2	Shunt	MSE	MAE	R^2	MSE	MAE	R^2	MSE	MAE	R^2
ANFIS	ANFIS	Secant Tuning	1.14e-5	$1.68e^{-2}$	1.00	1.30	11.60	0.69	5.60e-3	0.71	0.67
IT2FLS	IT2FLS	IT2FLS	30.79	32.06	0.73	0.84	12.56	0.78	4.78e-3	0.76	0.74
IT2FLS	IT2FLS	IT2FLS (nPSO)	28.38	31.00	0.70	0.85	12.52	0.78	4.75e-3	0.75	0.74
IT2FLS	IT2FLS	Secant Tuning	1.17e-5	1.55e-2	1.00	0.89	11.88	0.76	4.04e-3	0.71	0.76
IT2FLS (nPSO)	IT2FLS (nPSO)	IT2FLS	23.19	30.47	0.82	0.67	10.89	0.82	3.45e-3	0.64	0.81
IT2FLS (nPSO)	IT2FLS (nPSO)	IT2FLS (nPSO)	21.82	30.43	0.80	0.69	11.02	0.82	3. 50e-3	0.65	0.81
IT2FLS (nPSO)	IT2FLS (nPSO)	Secant Tuning	1.92e-5	2.35e-2	1.00	0.64	9.85	0.86	2.70e-3	0.57	0.84
IT2FLS (243 rules)	IT2FLS (nPSO)	Secant Tuning	1.92e-5	2.66e-2	1.00	0.39	9.11	0.91	2.50e-3	0.54	0.88
T1 FCM	T1 FCM	Secant Tuning	1.50e-5	2.24e-2	1.00	0.84	12.47	0.78	4.06e-3	0.74	0.81
T1 FCM (MSE nPSO)	T1 FCM (MSE nPSO)	Secant Tuning	1.27e-5	2.00e-2	1.00	0.85	11.77	0.77	4.00e-3	0.70	0.81
T1 FCM (R^2 nPSO)	T1 FCM (R^2 nPSO)	Secant Tuning	9.90e-6	2.00e-2	1.00	0.78	10.39	0.81	3.18e-3	0.64	0.80

Table 4.7. SOPAVent post-setting change ABG prediction results

Sub-component Modelling Approach			Post-setting change PaO2			Post-setting change $PaCO_2$			Post-setting change pH		
Kd	VCO_2	Shunt	MSE	MAE	R^2	MSE	MAE	R^2	MSE	MAE	R^2
ANFIS	ANFIS	Secant Tuning	11.41	15.07	0.49	0.87	10.68	0.78	4.70e-3	0.69	0.71
IT2FLS	IT2FLS	IT2FLS	33.48	32.86	0.39	0.97	13.21	0.75	5.35e-3	0.83	0.70
IT2FLS	IT2FLS	IT2FLS (nPSO)	31.27	30.68	0.42	0.96	13.22	0.75	5.22e-3	0.83	0.71
IT2FLS	IT2FLS	Secant Tuning	11.61	19.29	0.48	0.97	12.83	0.75	4.41e-3	0.76	0.73
IT2FLS (nPSO)	IT2FLS (nPSO)	IT2FLS	31.19	31.85	0.45	1.23	11.73	0.66	4.48e-3	0.68	0.74
IT2FLS (nPSO)	IT2FLS (nPSO)	IT2FLS (nPSO)	29.74	30.37	0.46	1.22	11.41	0.67	4.40e-3	0.68	0.74
IT2FLS (nPSO)	IT2FLS (nPSO)	Secant Tuning	11.44	15.18	0.50	1.09	10.11	0.74	3.40e-3	0.60	0.78
IT2FLS (243 rules)	IT2FLS (nPSO)	Secant Tuning	13.30	14.94	0.50	0.74	10.31	0.81	3.00e-3	0.59	0.84
T1 FCM	T1 FCM	Secant Tuning	11.17	14.88	0.51	0.97	12.87	0.74	4.41e-3	0.76	0.79
T1 FCM (MSE nPSO)	T1 FCM (MSE nPSO)	Secant Tuning	11.23	14.94	0.51	1.02	12.45	0.73	4.00e-3	0.75	0.78
T1 FCM (R^2 nPSO)	T1 FCM (R^2 nPSO)	Secant Tuning	11.45	15.27	0.49	1.16	11.77	0.71	4.40e-3	0.74	0.72

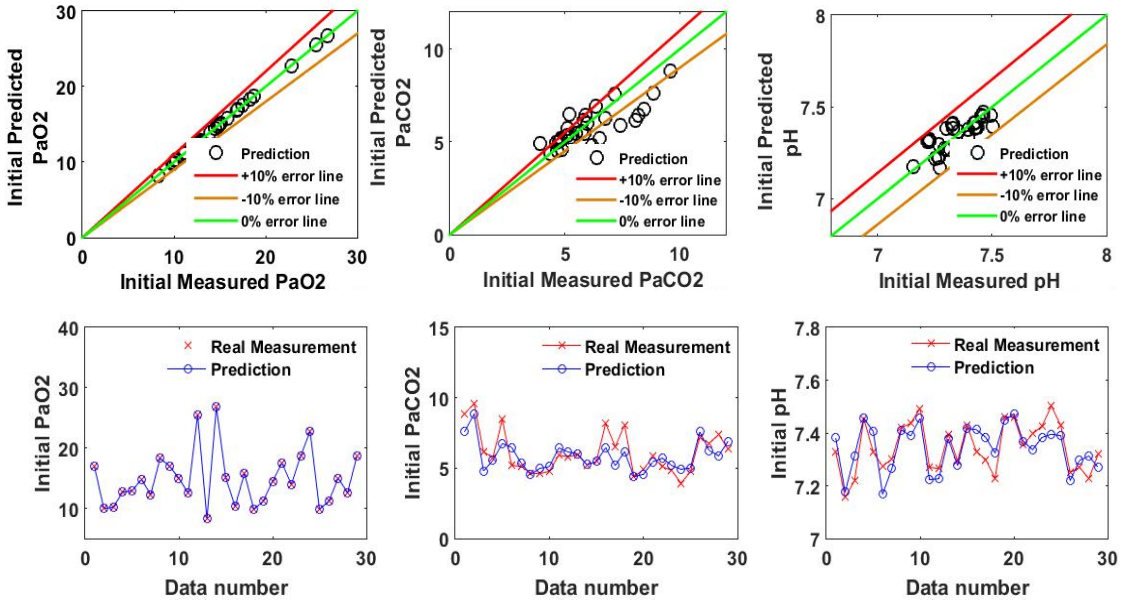

Figure 4.13. SOPAVent initial ABG prediction results for the Kd and the VCO_2 sub-components elicited via the FCM nPSO model

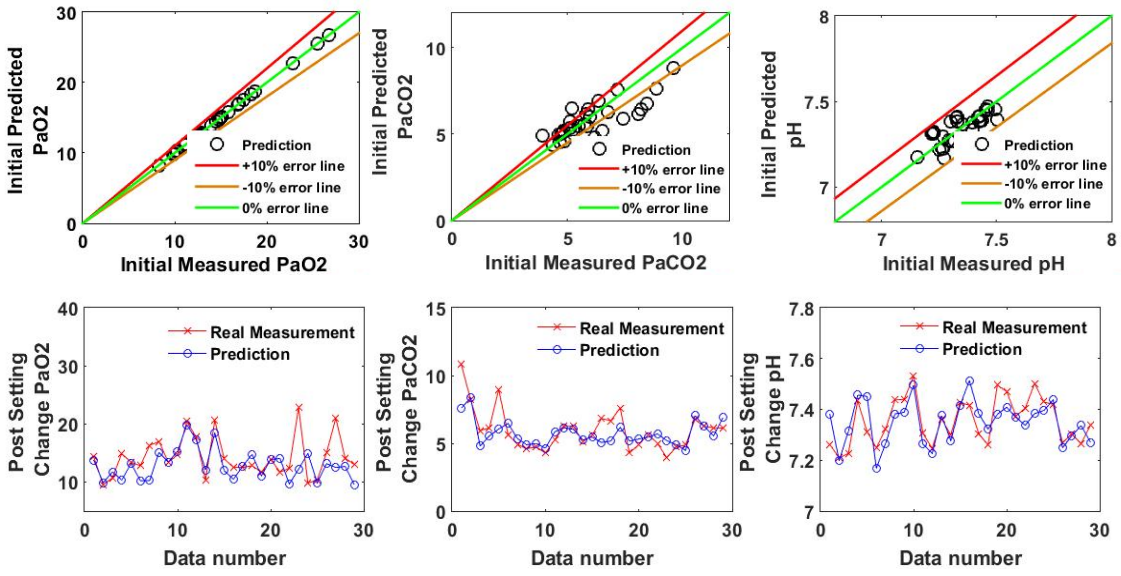

Figure 4.14. SOPAVent post-setting change ABG prediction results for the Kd and the VCO_2 sub-components elicited via the FCM nPSO model.

4.4.3 Analysis of the SOPAVent Model Validation

Four versions of SOPAVent; each using the secant tuning for obtaining shunt, were selected for further analysis. These are: (i) the SOPAVent version where the Kd and the VCO_2 sub-components were elicited via ANFIS, (ii) the SOPAVent

version where the Kd and the VCO_2 sub-components were derived using the IT2FLS nPSO model, (iii) the SOPAVent version where the Kd sub-component was elicited using the IT2FLS model with 243 rules, and the VCO_2 sub-component obtained using the IT2FLS nPSO model, and (iv) the SOPAVent model where the Kd and the VCO_2 sub-components were elicited via the FCM nPSO model with the MSE as the optimization objective. Each model was analysed based on the percentage of error obtained between the predicted ABG parameters and the real ABG parameters. For the PaO_2 and the $PaCO_2$ parameters, the predictions were grouped into one of three categories: (i) less than 10% error, (ii) between 10% to 20% error, and (iii) greater than 20% error. For the pH parameter, the predictions were grouped into one of three categories: (i) less than 2% error, (ii) between 2% to 5% error, and (iii) greater than 5% error. The number of predictions and their percentages for each error category were also recorded.

For the initial PaO_2 predictions, all four models showed a similar performance with all 29 predictions (100%) had errors less than 10%. For post-setting change PaO_2 predictions, the SOPAVent version with the Kd and the VCO_2 sub-components obtained via the FCM nPSO model had the most prediction with errors less than 10% (14 out of 29, or 48.28%). This was followed by the SOPAVent model where the Kd sub-component was derived using the IT2FLS model with 243 rules, and the VCO_2 sub-component was elicited using the IT2FLS nPSO model, where thirteen out of 29 predictions (44.83%) had errors less than 10% (see Table 4.8). For the initial $PaCO_2$ predictions, the SOPAVent version where the Kd sub-component was derived using the IT2FLS model with 243 rules, and the VCO_2 sub-component was elicited via the ITFLS nPSO model had the most prediction with errors less than 10% (19 out of 29, or 65.52%). This was followed by the SOPAVent version where the Kd and the VCO_2 sub-components were simulated using ANFIS. Eighteen out of 29 predictions (62.07%) had errors less than 10%. For the post-setting change predictions of $PaCO_2$, the SOPAVent version where the Kd and the VCO_2 sub-components were elicited via ANFIS had the most prediction with errors less than 10% (18 out of 29, or 62.07%). This was followed by the SOPAVent model where the Kd sub-component was derived using the IT2FLS model with 243 rules, and the VCO_2 sub-component was elicited using the ITFLS nPSO model. Fifteen out of 29 predictions (51.72%) had errors less than 10% (see Table 4.9).

For initial pH predictions, all the SOPAVent version except for when the Kd and the VCO_2 sub-components were simulated using ANFIS, had all predictions (100%) with errors less than 2%. For the SOPAVent model where the Kd and the VCO_2 sub-component were developed using ANFIS, 27 out of 29 predictions (93.10%) had errors less than 2%. This was also observed for the post-setting change predictions of pH, where all SOPAVent versions apart from where the Kd and the VCO_2 sub-components were derived via ANFIS, had all predictions (100%) with errors less than 2% (see Table 4.10).

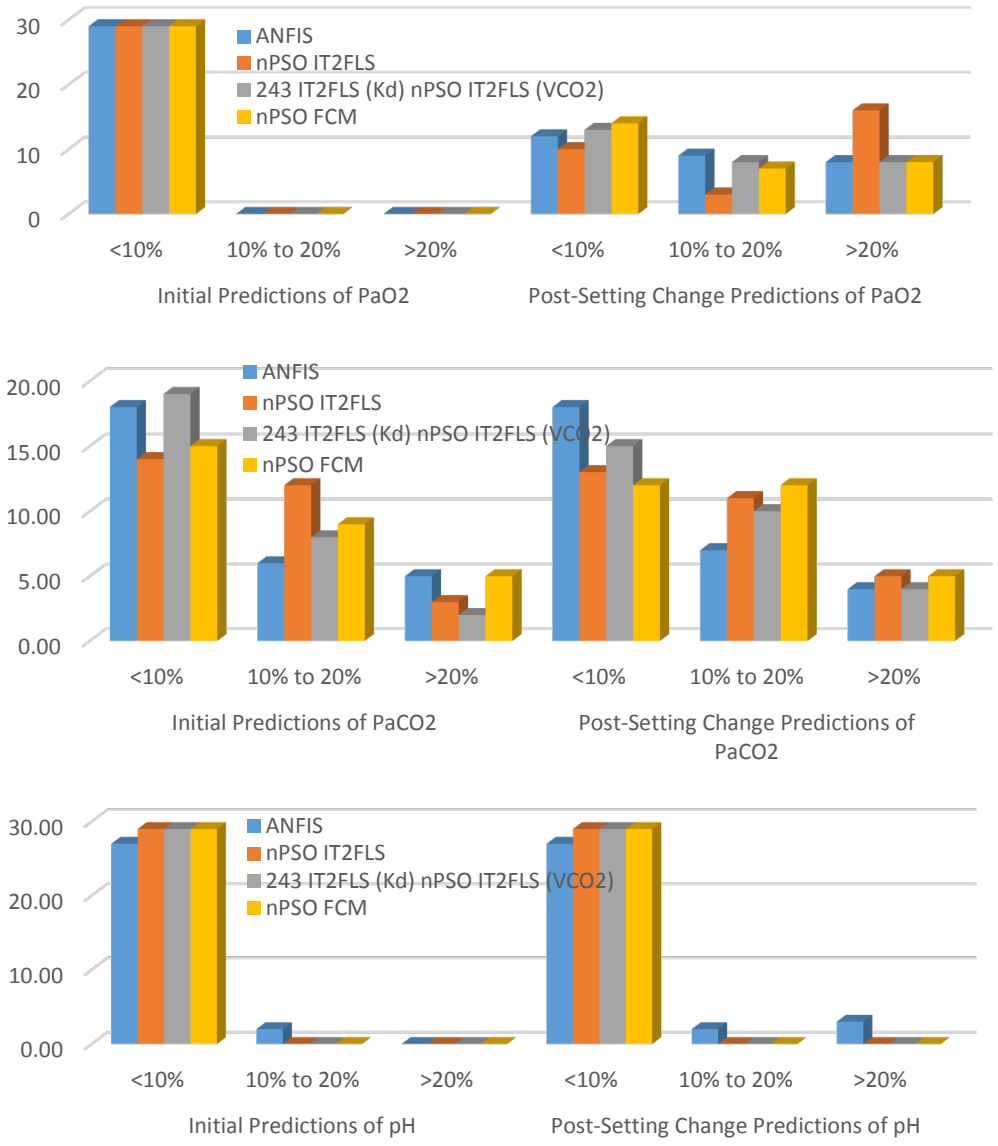

Figure 4.15. Number of errors in SOPAVent's for initial predictions and post-setting change predictions of PaO2 (top), $PaCO_2$ (middle) and pH (bottom).

Table 4.8 SOPAVent ABG prediction errors for PaO_2.

Kd Approach	VCO_2 Approach	Error for initial predictions						Error for post-setting-change predictions					
		< 10%		10% to 20%		> 20%		< 10%		10% to 20%		> 20%	
		Qty	(%)	Qty	(%)	Qty	(%)	Qty	(%)	Qty	(%)	Qty	(%)
ANFIS	ANFIS	29/29	100%	0/29	0%	0/29	0%	12/29	41.38%	9/29	31.03%	8/29	27.59%
nPSO-tuned IT2FLS	nPSO-tuned IT2FLS	29/29	100%	0/29	0%	0/29	0%	10 /29	34.48%	3/29	10.34%	16/29	55.17%
243 rule IT2FLS	nPSO-tuned IT2FLS	29/29	100%	0/29	0%	0/29	0%	13/29	44.83%	8/29	27.59%	8/29	27.59%
nPSO-tuned FCM	nPSO-tuned FCM	29/29	100%	0/29	0%	0/29	0%	14/29	48.28%	7/29	24.14%	8/29	27.57%

Table 4.9 SOPAVent ABG prediction errors for $PaCO_2$.

Kd Approach	VCO_2 Approach	Error for initial predictions						Error for post-setting-change predictions					
		< 10%		10% to 20%		> 20%		< 10%		10% to 20%		> 20%	
		Qty	(%)	Qty	(%)	Qty	(%)	Qty	(%)	Qty	(%)	Qty	(%)
ANFIS	ANFIS	18/29	62.07%	6/29	20.69%	5/29	17.24%	18/29	62.07%	7/29	24.14%	4/29	13.79%
nPSO-tuned IT2FLS	nPSO-tuned IT2FLS	14/29	48.28%	12/29	41.38%	3/29	10.34%	13/29	44.83%	11/29	37.93%	5/29	17.24%
243 rule IT2FLS	nPSO-tuned IT2FLS	19/29	65.52%	8/29	27.59%	2/29	6.90%	15/29	51.72%	10/29	34.48%	4/29	13.79%
nPSO-tuned FCM	nPSO-tuned FCM	15/29	51.72%	9/29	31.03%	5/29	17.24%	12/29	41.38%	12/29	41.38%	5/29	17.24%

Table 4.10 SOPAVent ABG prediction errors for pH.

Kd Approach	VCO_2 Approach	Error for initial predictions						Error for post-setting-change predictions					
		< 2%		2% to 5%		> 5%		< 2%		2% to 5%		> 5%	
		Qty	(%)	Qty	(%)	Qty	(%)	Qty	(%)	Qty	(%)	Qty	(%)
ANFIS	ANFIS	27/29	93.10%	2/29	6.90%	0/29	0%	27/29	93.10%	2/29	6.90%	0/29	0%
nPSO-tuned IT2FLS	nPSO-tuned IT2FLS	29/29	100%	0/29	0%	0/29	0%	29/29	100%	0/29	0%	0/29	0%
243 rule IT2FLS	nPSO-tuned IT2FLS	29/29	100%	0/29	0%	0/29	0%	29/29	100%	0/29	0%	0/29	0%
nPSO-tuned FCM	nPSO-tuned FCM	29/29	100%	0/29	0%	0/29	0%	29/29	100%	0/29	0%	0/29	0%

4.5 Summary

Several Fuzzy C-Means Clustering (FCM) models were developed for the estimation of the relative dead-space (Kd) and the carbon-dioxide production (VCO_2). These models were further optimized using the proposed 'new structure' for Particle Swarm Optimization (nPSO). The FCM models and the models developed using interval type-2 fuzzy logic system (IT2FLS), as presented in Chapter 3, were integrated into the SOPAVent model, which is a non-invasive and automatic blood gas prediction system. The performance of the newly developed models were also compared with the previous models where the Kd and the VCO_2 sub-components were developed using the ANFIS modelling structure.

In order to validate the developed models, real ICU patient data were utilized. Both the IT2FLS and the FCM models led to satisfactory prediction performances with significant improvements in MSE, MAE and R^2 particularly for the prediction of the initial $PaCO_2$, the prediction of the initial pH and the prediction of the post-setting-change pH. Some improvements were also observed for the post-setting-change prediction of $PaCO_2$. These improvements were attributed to the new Kd and VCO_2 sub-models. However, no significant improvements in accuracy were obtained for the post-setting-change prediction of PaO_2. This is due to no new model was proposed for the improvement of cardiac output (CO), which currently is estimated using Body Surface Area (BSA).

The SOPAVent version, where the Kd and the VCO_2 model components were designed using the IT2FLS model outperformed the previous SOPAVent version where the Kd and the VCO_2 sub-components were elicited via ANFIS. The SOPAVent model, where the Kd and the VCO_2 sub-components were elicited using FCM, led to equal performance as compared to the SOPAVent version where the Kd and theVCO_2 model components were elicited via ANFIS. The new IT2FLS models showed better generalization capability as compared to the FCM models, as a result allowing them to be more robust and adaptive to uncertainties and inter/intra ICU patient parameter variability respectively.

Chapter 5

Validation of Blood Gas Models for Patients with Faecal Peritonitis

5.1 Introduction

Faecal Peritonitis (FP) is a common cause for sepsis in patients who are admitted to the intensive care unit (ICU). Peritonitis is identified by the inflammation of the peritoneal cavity, a fluid filled space between two layers of the peritoneum membrane, often caused by an infection on the peritoneal cavity (Tridente *et al.,* 2014). Peritoneum is the membrane that lines both the abdominal wall and the intra-abdominal organs. Figure 5.1 shows the location of the peritoneum membrane and the peritoneal cavity on a cross sectional image of the human abdomen. A secondary peritonitis known as faecal peritonitis, occur when faecal matter spill from the large intestine into the peritoneal cavity, due to weakened bowel wall from ischemia, growth or inflammation (Tridente *et al.,* 2014). FP often results in intensive antibiotic therapy and may involve emergency surgery if it became life-threatening.

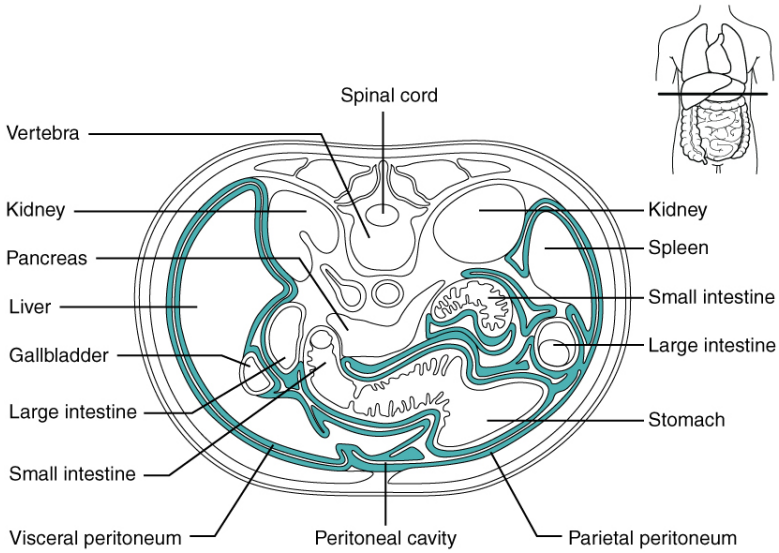

Figure 5.1 Cross section image of the human abdomen (BC Open Textbooks)

5.2 Validation of Relative Dead-Space and Carbon-dioxide Production Models on Faecal Peritonitis Patients

A set of hourly data from 96 patients (51 females and 45 males) diagnosed with FP admitted to the ICU, was obtained from the Anaesthetics Department, at the Sheffield Royal Hallamshire Hospital, UK. The dataset consisted of ventilator settings, ventilator monitoring, blood gas analyses and physiological parameters of patients admitted and discharged between April 2008 and September 2012. Patients were supported by the artificial ventilator in various modes such as bi-level positive airway pressure, (BiPAP), continuous positive airway pressure, (CIPAP), low-flow face mask oxygen (LoFlo), high-flow face mask oxygen (HiFlo), nasal specs, hood CPAP, facial CPAP and non-invasive ventilation (NIV).

BiPAP ventilation provided support for both chronic and acute conditions while CPAP-ASB were used for patients who have gone through the initial acute stage and so were progressing. LoFlo, HiFlo and nasal specs were provided for patients who were able to breathe on their own but required a little more oxygen. Hood CPAP and facial CPAP were also provided for patients who were able to breathe on their own but required some external pressures to expand their airways and lungs. Patient who were on NIV mode were those yet to be intubated for CPAP and so were ventilated through a face mask.

The carbon-dioxide production (VCO_2) models and the relative dead-space (Kd) models discussed in Chapters 3 and 4 were used to validate the new FP patient data. After consulting with the anaesthetic clinician at the Sheffield Royal Hallamshire Hospital, parameters which satisfy the following conditions were selected for validating the VCO_2 and the Kd models.

i. Patients were ventilated under the BiPAP mode;
ii. The total respiration rate (RR) must be equal or higher than set RR;
iii. The end-tidal carbon-dioxide ($EtCO_2$) should be lower than the partial arterial pressure of carbon-dioxide ($PaCO_2$), but no less than **3 kPa** as this would suggest a calibration error;

iv. The tidal volume (VT) should be larger than 300ml as anything lower will affect oxygenation of the blood vessels in the brain;

v. The $EtCO_2$ should be larger than 3.5 kPa;

vi. The carbon-dioxide production (VCO_2) should be larger than 100ml;

vii. The relative dead-space should be larger than 10.

Of the 96 FP patients, 40 patents were ventilated under BiPAP mode. The remaining 56 patients were ventilated in various other modes and thus were not selected for validation. The conditions defined above produced a total of 340 data sets from 21 patients, consisting of 11 males and 10 females. The mean height of the selected FP patients was 168±10.00 cm and the mean weight was 70.22±14.91kg (see Table 5.1). However, there was no information on the age of the patients. Based on the height and weight of the patients it was assumed that the patients were adults. The summary of Kd and VCO_2 data used for validation are shown in Table 5.2 (a) and Table 5.2 (b) respectively.

Table 5.1 Demography of FP patients for VCO_2 and Kd model validation

Number of Patients	Male	Female	Height (cm)	Weight (kg)
21	11	10	168 ± 10.00	70.22 ± 14.91

Table 5.2 (a) Kd validation data for FP patients

Parameter	$PaCO_2$ (kPa)	RR (breath/min)	VT (l)	Pinsp (cmH_2O)	PEEP (cmH_2O)	Kd
Mean	5.85	15.78	0.55	22.28	7.11	28.71
S.D.	1.21	3.08	0.14	5.90	1.96	7.59
Minimum	3.68	8.00	0.31	10.00	5.00	12.00
Maximum	9.73	24.00	1.30	36.00	12.00	50.00

Table 5.2 (b) VCO_2 validation data for FP patients

Parameter	MV (l/min)	VT (l)	$EtCO_2$ (kPa)	VCO_2 (ml/min)
Mean	8.60	0.55	5.00	229.73
S.D.	2.68	0.14	0.97	50.87
Minimum	3.76	0.31	3.50	109.00
Maximum	17.94	1.30	7.70	379.00

Figures 5.2 (a) and 5.2 (b) show the data distribution for Kd in two-dimensional (2D) and three-dimensional (3D) representations respectively. When compared with the retrospective data for Kd used in Chapter 3 (see Table 3.3), the respiration rate (RR) for FP patients has a slightly lower mean and standard deviation (15.78±3.08 compared to 16.96±3.27). The RR also has a lower minimum and maximum value (8 to 24 compared to 12 to 28). The positive end expiratory pressure (PEEP) showed a lower mean and standard deviation value (7.11±1.96 compared to 10.62±3.88). The PEEP for FP data also showed a much lower maximum value (5 to 12 compared to 5 to 20).

The inspiratory pressure (Pinsp) for FP patients, however has a much higher mean and standard deviation value (22.28±5.90 compared to 13.93±3.64). The PEEP of the FP data has a higher minimum and maximum value (10 to 36) when compared to the previous data (6 to 30). The partial arterial pressure of carbon-dioxide ($PaCO_2$), tidal volume (VT) and Kd for both the FP data and previous data showed no significant differences.

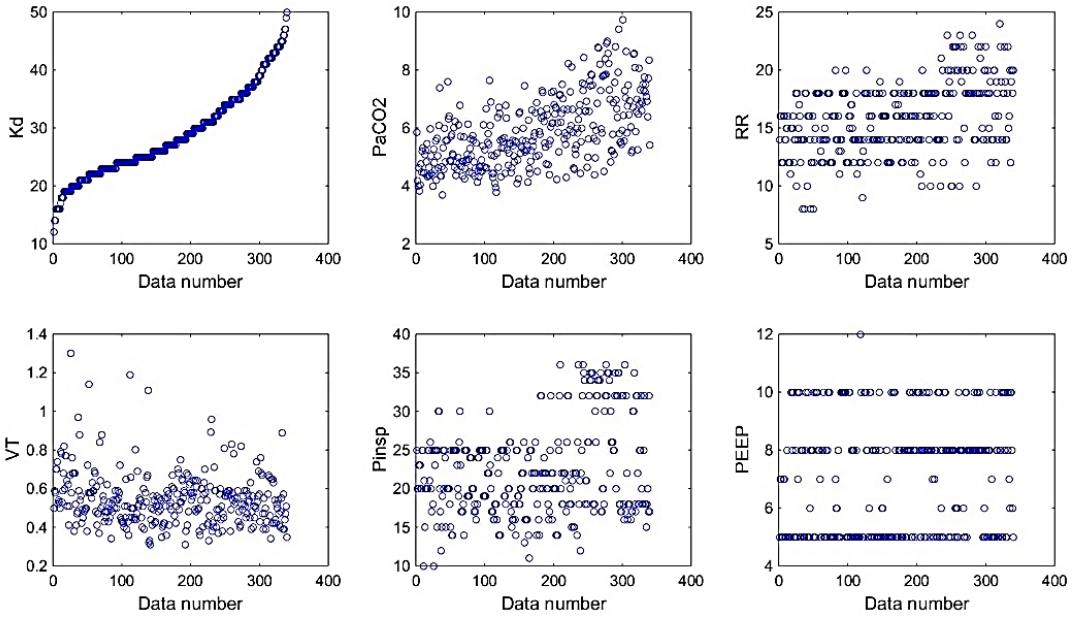

Figure 5.2 (a) Two-dimensional data distribution for the Kd model. Top: increasing Kd, $PaCO_2$ and RR. Bottom: VT, Pinsp and PEEP

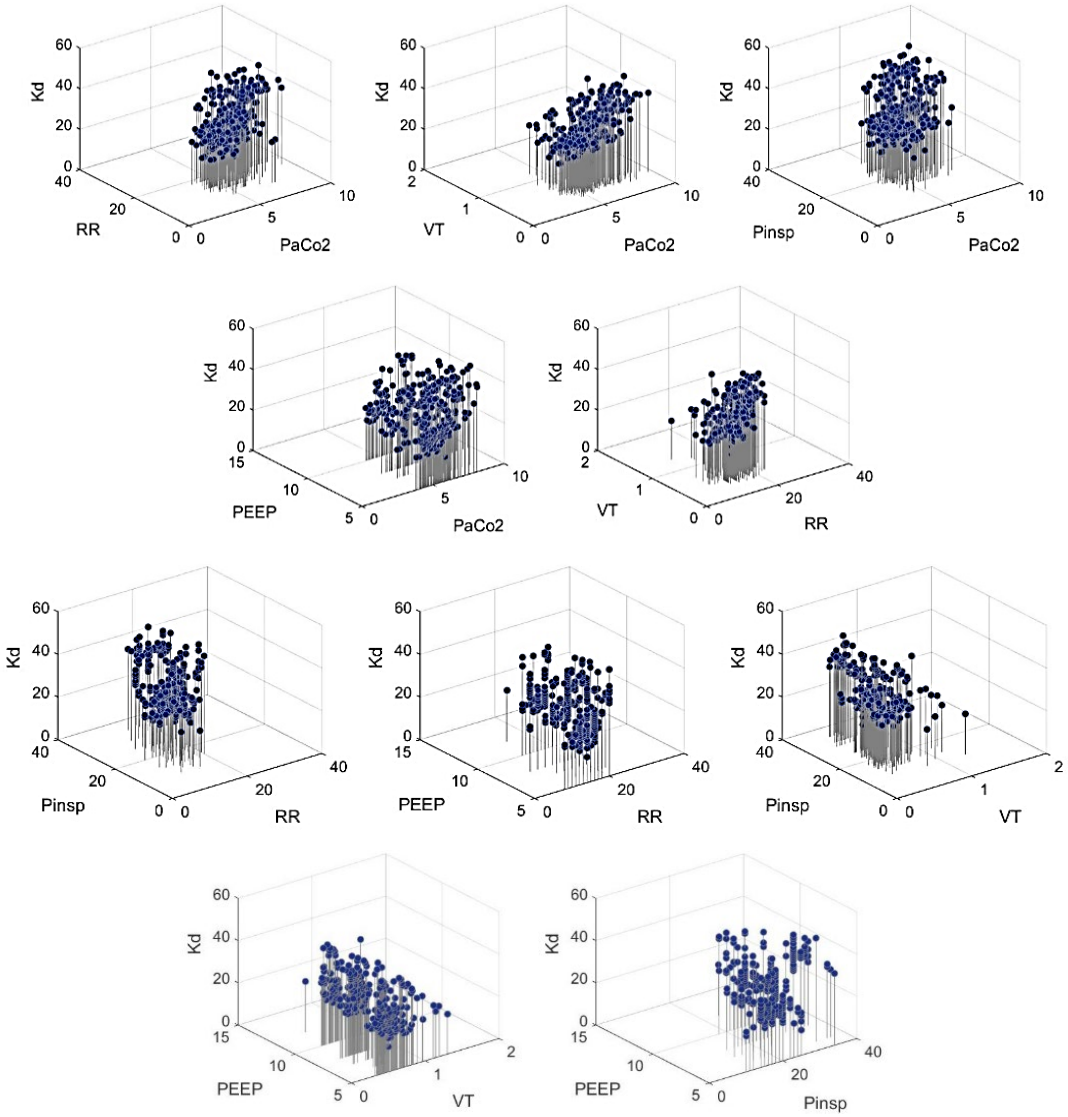

Figure 5.2 (b) Three-dimensional data distribution for the Kd model

Figures 5.3 (a) and 5.3 (b) shows the data distribution for VCO_2 validation in 2D and 3D representations. When the new FP data for VCO_2 was compared to the previous data in Chapter 3 (see Table 3.9), the minute volume (MV) has a slightly higher mean and standard deviation (8.6$\pm$2.68 compared to 7.89$\pm$1.79). The MV for FP data also has a slightly lower minimum value, but a slightly larger maximum value (3.76 to 17.94 compared to 4.09 to 15.55). The VT for FP data has an almost equal mean value, but a larger standard deviation compared to the old data (0.55$\pm$0.14 compared to 0.54$\pm$0.09). VT also a larger maximum value (0.31 to 1.30) when compared to the old data (0.29 to 0.90). The end-tidal CO_2 ($EtCO_2$) of the FP data showed no significant differences when compared to the previous data.

The VCO_2 of the FP data showed a larger mean value of 229.73±50.87 compared to 217327±56.77. However, the new FP data has a lower minimum and maximum values of 109 to 379 as compared to 144 to 405.9 in the old data. These variations in data characteristics for both Kd and VCO_2 are expected to produce less accurate predictions especially in data dependant models such as ANFIS and FCM.

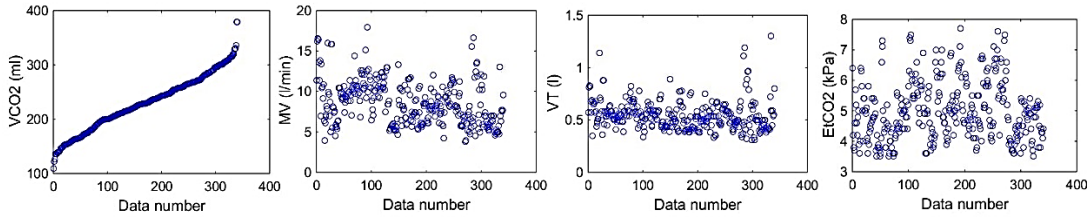

Figure 5.3 (a) Two-dimensional data distribution for the VCO_2 model (increasing VCO_2, MV, VT and $EtCO_2$)

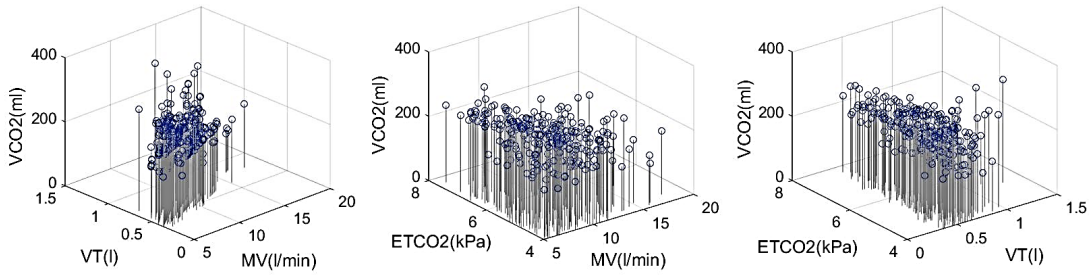

Figure 5.3 (b) Three-dimensional data distribution for the VCO_2 model.

5.2.1 Relative Dead-space and Carbon-dioxide Production Models Validation Results for Faecal Peritonitis Patients

The models used to validate the Kd and the VCO_2 parameters for the FP patients are the ANFIS model proposed by Wang *et al*. (2010a), the interval type-2 (IT2FLS) models and the fuzzy c-means (FCM) models described in Chapters 3 and 4. The validation results for both the Kd and the VCO_2 parameters are shown in Table 5.3. For the Kd predictions, all models did not produce satisfactory results. The highest prediction accuracy with a mean squared error (MSE) of 44.93 and a correlation coefficient (R^2) of 0.54, and it was attributed to the interval IT2FLS (243) model. The same model produced an MSE of 21.76 and R^2 of 0.74 when applied to the previous data. All the other models produced an MSE of more than 50.00 and R^2 less than 0.35. This outcome is possibly due to FP patients having significantly larger Pinsp values

and much lower PEEP values when compared to the previous data, resulting the output, Kd to be cut-off at around 35.

For the VCO_2 prediction, the IT2FLS (nPSO) model produced the highest accuracy with an MSE of 1563 and R^2 of 0.75. However, this was also considerably less accurate when compared with the previous data set using the same model, which produced an MSE of 476.47 and R^2 of 0.92. All other models for FP patients apart from the ANFIS model showed similar performance with R^2 ranging from 0.71 to 0.73. The plot for predicted Kd versus real Kd is shown in Figure 5.4, while the plot for predicted VCO_2 versus real VCO_2 is shown in Figure 5.5.

Table 5.3 Validation results for Kd and VCO_2 models

Model	Kd				VCO_2			
	MSE	MAE	SD	R^2	MSE	MAE	SD	R^2
ANFIS	58.96	20.29	7.51	0.29	2683.58	16.30	51.47	0.65
IT2FLS (manual)	54.58	22.82	7.31	0.32	1781.83	14.91	42.18	0.73
IT2FLS (nPSO)	59.68	22.99	7.73	0.30	1563.01	13.68	39.52	0.75
IT2FLS 243	44.93	19.64	6.67	0.54	NA	NA	NA	NA
FCM	54.58	22.82	7.31	0.32	1832.99	13.96	42.26	0.72
FCM (nPSO MSE)	66.00	19.04	7.36	0.30	1851.53	13.90	42.45	0.72
FCM (nPSO R^2)	67.62	18.94	7.25	0.34	2383.88	15.72	47.99	0.71

NA: not available

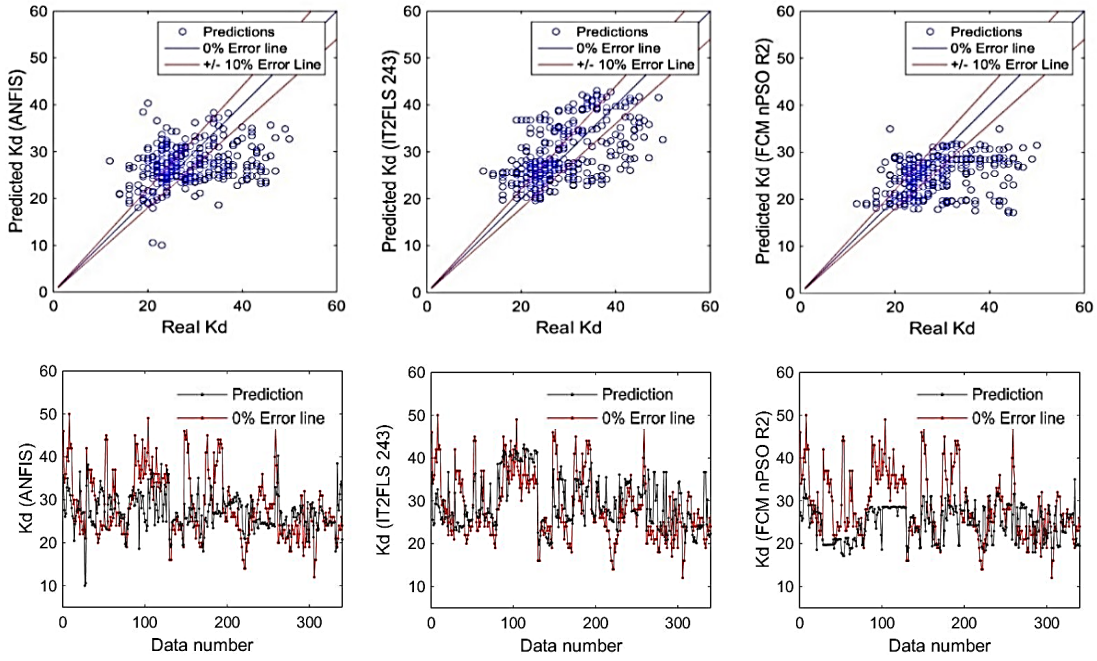

Figure 5.4 Kd prediction results for ANFIS, IT2FLS (243) and FCM (R^2) models. Top: Predicted Kd vs real Kd. Botton: predicted Kd and target Kd

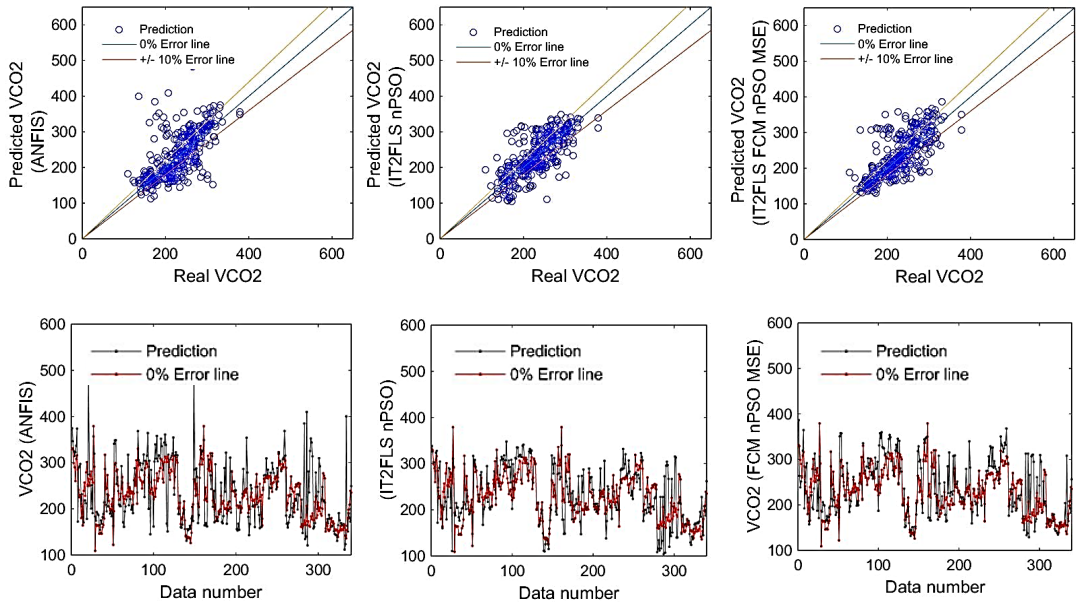

Figure 5.5 VCO_2 prediction results for ANFIS, IT2FLS (243) and FCM (R^2) models. Top: Predicted VCO_2 vs real VCO_2. Bottom: predicted VCO_2 and target VCO_2

5.3 Validation of the SOPAVent Models on Faecal Peritonitis Patients

As previously defined in Chapter 4, the arterial blood gases (ABG) which were selected for SOPAVent validation were taken between 30 and 60 minutes before ventilator setting changes were made, and between 30 and 180 minutes after ventilator setting changes were made. However, for this set of FP data, parameters were only recorded on an hourly basis instead of minute by minute intervals such as the previous data set used in Chapter 4. Due to the nature of this new FP data, there was no way to determine the exact time when each change in ventilator setting was made. Hence, it was decided that two ABGs which were separated between 60 minutes and 240 minutes should be selected for SOPAVent validation. If there were noticeable differences in any one of the ventilator setting parameters at the start of the hour, it should happen at least 30 minutes after the first ABG, and at least 30 minutes prior the second ABG. If there was more than one change for a specific ventilator setting during the ABG intervals, the total sum of change will be considered. Figure 5.6 shows the ABG selection criteria for the new FP data.

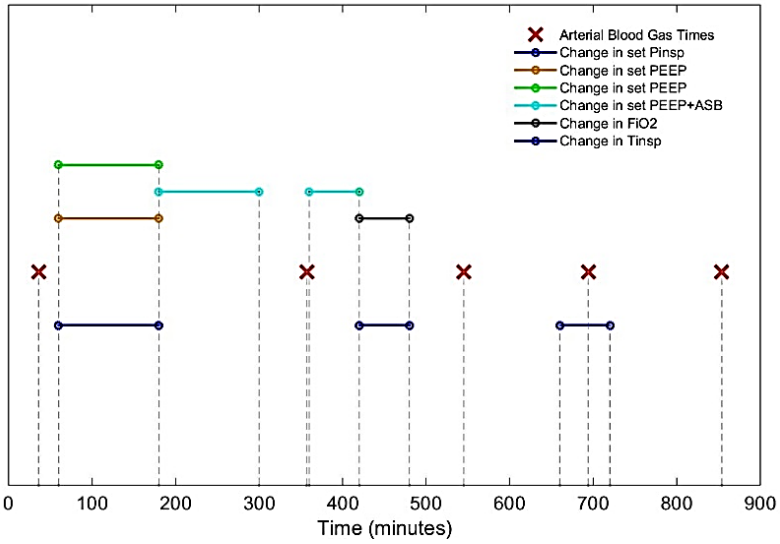

Figure 5.6 ABG Selection

A total of 28 datasets from 11 patients (7 males and 4 females) were obtained for the SOPAVent blood gas models validation. The patients have a mean height of 168 $\pm$ 10.00cm and a mean weight of 72.27$\pm$18.07 kg (see Table 5.4). The summary of ABG validation data of FP patients for initial PaO_2, initial $PaCO_2$, initial pH, post-setting change PaO_2, post setting change $PaCO_2$ and post setting change pH is shown in Table 5.5. The summary of other input parameters used in the SOPAVent model is available in Appendix C1. The frailty index of each patient was also provided in the data set. One patient was noted as mildly frail, two patients were noted as vulnerable, two patients were noted as well, and one patient was noted as very fit. Five more patients had no records of their frailty index (see Table 5.6).

Table 5.4 Demography of FP patients for SOPAVent validation

Number of Patients	Male	Female	Height (cm)	Weight (Kg)
11	7	4	168 $\pm$ 10.00	72.27 $\pm$ 18.07

Table 5.5 Summary of validation ABG for FP patients

ABG Parameter	Initial				Post-setting change			
	Mean	S.D.	Minimum	Maximum	Mean	S.D	Minimum	Maximum
PaO_2	15.62	4.06	9.01	26.10	14.68	3.56	9.53	24.80
$PaCO_2$	5.92	1.21	3.79	8.07	5.83	1.09	4.08	8.21
pH	7.34	0.09	7.17	7.50	7.35	0.08	7.20	7.49

Table 5.6 Frailty index of FP patients for SOPAVent validation

Patient ID	Height	Weight	Gender	Frailty Index
1	1.81	80	Male	Unrecorded
2	1.74	67	Male	Unrecorded
3	1.63	72	Female	Unrecorded
4	1.63	55	Female	Unrecorded
5	1.68	120	Male	Mildly frail
6	1.83	83	Male	Well
7	1.65	55	Male	Unrecorded
8	1.84	90	Male	Vulnerable
9	1.51	67.5	Female	Vulnerable
10	1.69	63.5	Male	Very fit
11	1.57	50	Female	Well

5.3.1 SOPAVent Blood Gas Model Validation Results

The FP patients' record for ventilator settings, ventilator monitoring, previous blood gas analyses and physiological information were used to generate predictions of arterial blood gas (ABG), non-invasively using the SOPAVent model. The Kd and VCO_2 subcomponents were predicted using the models described in Chapters 3 and 4, with their results shown in section 5.2.1 (Table 5.3). The shunt subcomponent was predicted using the secant tuning method described in a previous work by Wang *et al.,* (2010a). Tables 5.7 and 5.8 show the prediction results of initial ABG and post-setting change ABG respectively.

For the initial prediction of PaO_2, all models showed a similar performance with a correlation coefficients (R^2) equal to 1.00. This was also consistent with the previous patient data PaO_2 prediction described in Chapter 4. For the initial prediction of $PaCO_2$ the combination of interval type-2 fuzzy logic system (IT2FLS 243) and IT2FLS (nPSO) resulted in the highest accuracy with R^2 of 0.83 (see Figure 5.7). The type-1 fuzzy c-means clustering (FCM nPSO) based models for Kd and VCO_2 provided satisfactory performances with R^2 of 0.72. The IT2FLS (manual), IT2FLS (nPSO) and the type-1 FCM also provided similar performances with R^2 equal to 0.67, although less accurate when compared to the previously mentioned models. The least accurate model was the ANFIS combination, with R^2 equal to 0.60. In several models, the predictions which were outside of the confidence band were concentrated on the lower side of the -10% error line.

For the initial prediction of pH, all models showed good performances with R^2 for all models exceeding 0.80. Most of the predictions were within the $\pm$1% confidence band, although slightly more concentrated on the upper side of the 0% error line. The best performing models were the IT2FLS (243) and IT2FLS (nPSO) combination, with R^2 equal to 0.92 (see Figure 5.7), and the type-1 FCM (nPSO) for both Kd and VCO_2 subcomponents, with R^2 equal to 0.93. The IT2FLS (nPSO) combination and type-1 FCM combination, both produced R^2 of 0.87, while the IT2FLS (manual) combination, produced an R^2 of 0.83. The ANFIS combination produced an R^2 of 0.84. The initial prediction of pH showed better accuracy for FP patients when compared to the previous patient data. The plots for initial PaO2, $PaCO_2$ and pH predictions for other SOPAVent models are available in Appendix C2.

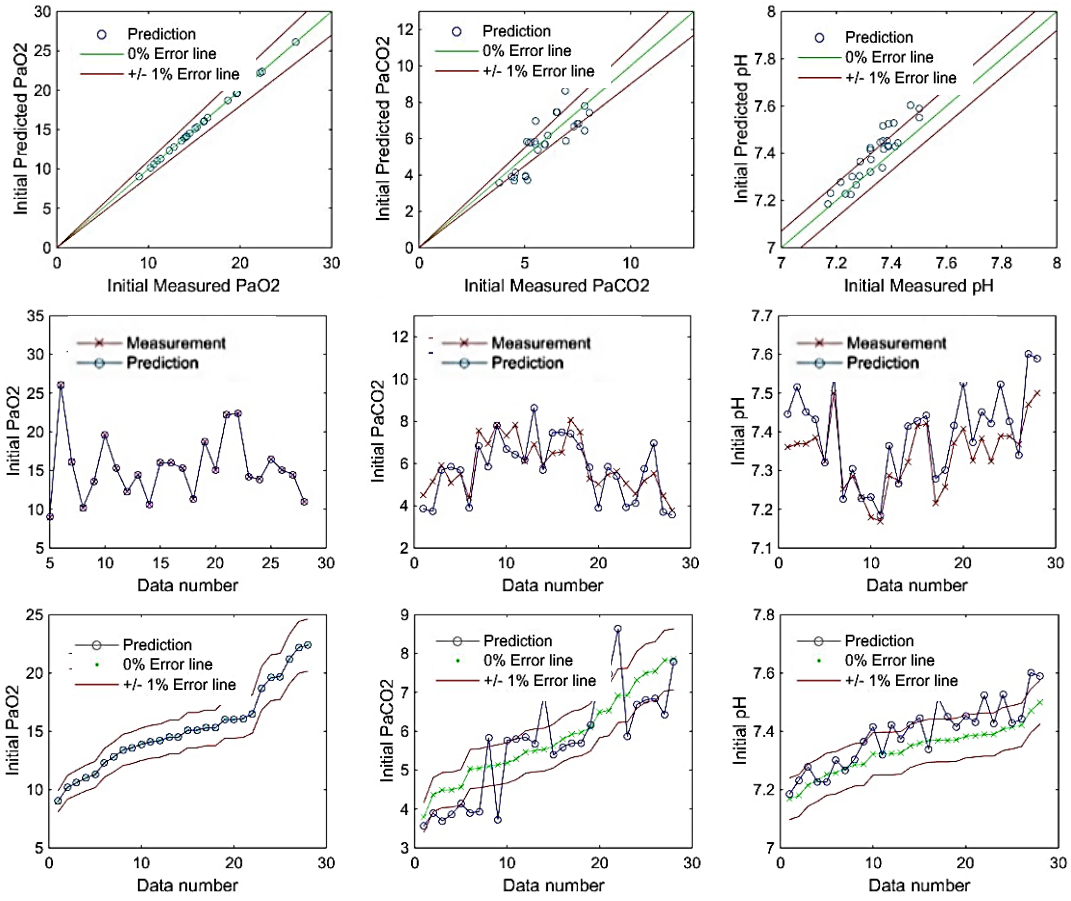

Figure 5.7 Initial ABG prediction for Kd (IT2FLS 243) and VCO_2 (IT2FLS nPSO)

For the post-setting change prediction of PaO_2, all models showed similar performance with R^2 of 0.54 to 0.55. This result is marginally better than the validation results of the previous patient data. However, for post-setting change $PaCO_2$

prediction, most of the models for FP patient produced a lower prediction accuracy compared to the previous patient data. The highest accuracy was produced by the combination of IT2FLS (243) model for the Kd subcomponent, and the IT2FLS (nPSO) model for the VCO_2 subcomponent, with R^2 equal to 0.65 (see Figure 5.8). The Kd subcomponent model was not able to predict Kd values with high accuracy due to deviation in data attributes of the FP patients when compared to the previous dataset.

The performance of the post-setting change prediction of pH was consistent between the new FP data and the old patient data. The highest accuracy was produced by the IT2FLS (243) and IT2FLS (nPSO) model combination, with R^2 equal to 0.82 (see Figure 5.8). All other models also produced R^2 higher than 0.70, with most of the predictions within the $\pm$1% confidence band. The plot for post-setting change prediction PaO_2, post-setting change prediction of $PaCO_2$ and post-setting change prediction of pH for other SOPAVent models are available in Appendix C3.

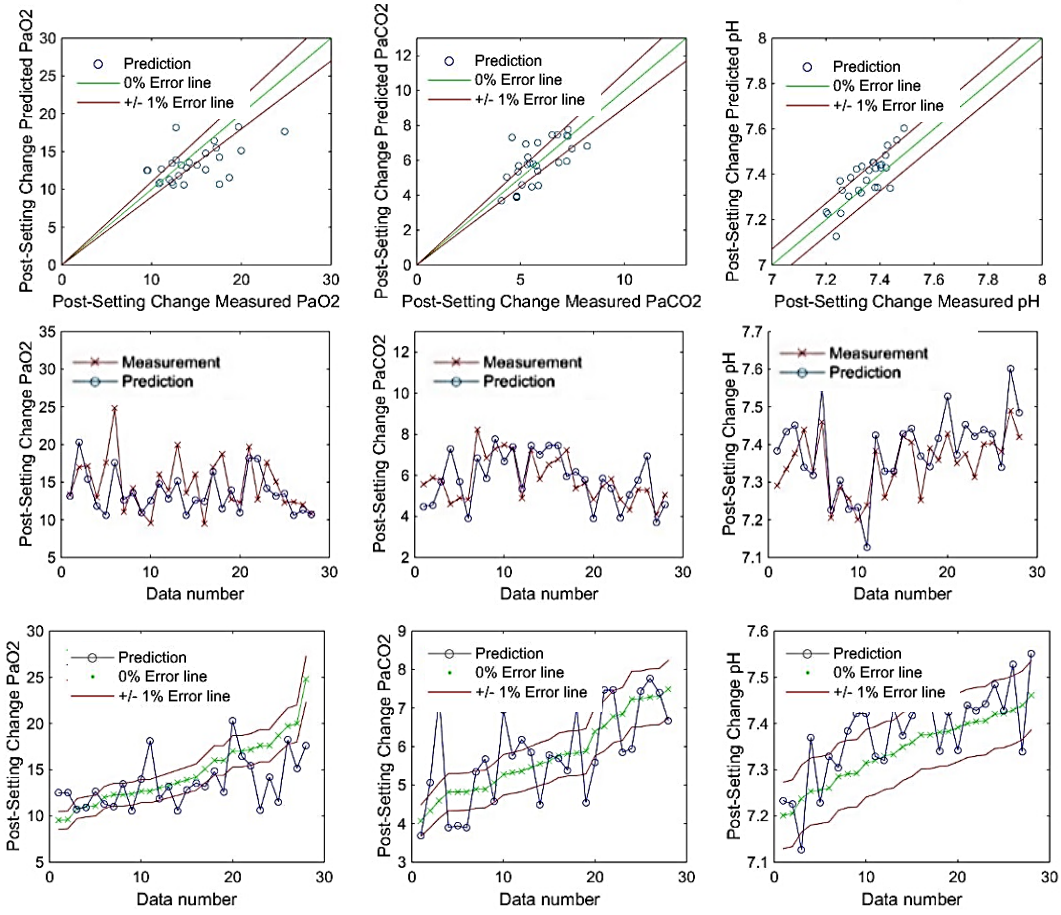

Figure 5.8 Post setting-change ABG prediction for Kd (IT2FLS 243) and VCO_2 (IT2FLS nPSO)

Table 5.7 SOPAVent results for initial ABG predictions for FP patients

Sub-component Modelling Approach		Initial PaO2				Initial $PaCO_2$				Initial pH			
Kd	VCO_2	MSE	MAE	SD	R^2	MSE	MAE	SD	R^2	MSE	MAE	SD	R^2
ANFIS	ANFIS	$2.02e^{-05}$	$2.57e^{-02}$	$4.48e^{-03}$	1.00	1.15	12.71	1.02	0.60	$7.17e^{-02}$	1.06	$5.58e^{-02}$	0.84
IT2FLS	IT2FLS	$1.13e^{-05}$	0.0165	$3.31e^{-03}$	1.00	1.26	15.94	1.11	0.67	$7.93\ e^{-03}$	0.96	$6.48e^{-02}$	0.83
IT2FLS (nPSO)	IT2FLS (nPSO)	$7.13e^{-06}$	$13.27e^{-02}$	$2.72e^{-03}$	1.00	1.15	15.02	1.05	0.67	$6.45\ e^{-03}$	0.93	$5.33e^{-03}$	0.87
IT2FLS (243 rules)	IT2FLS (nPSO)	$1.25e^{-05}$	$1.65e^{-02}$	$3.57e^{-03}$	1.00	0.69	12.07	0.83	0.82	$5.15e^{-03}$	0.80	$4.82e^{-02}$	0.92
T1 FCM	T1 FCM	$1.51e^{-05}$	$1.90e^{-02}$	$3.96e^{-03}$	1.00	0.99	13.04	0.98	0.67	$5.28e^{-03}$	0.88	$4.81e^{-02}$	0.87
T1 FCM (MSE nPSO)	T1 FCM (MSE nPSO)	1.55	$2.04e^{-02}$	$3.89e^{-03}$	1.00	0.95	11.36	0.84	0.72	$6.46e^{-03}$	1.04	$3.22e^{-02}$	0.93
T1 FCM (R^2 nPSO)	T1 FCM (R^2 nPSO)	$1.52e^{-05}$	$2.01e^{-02}$	$3.84e^{-03}$	1.00	0.97	11.56	0.85	0.72	$6.62e^{-03}$	1.05	$3.21e^{-02}$	0.93

Table 5.8 7 SOPAVent results for s post-setting change ABG predictions for FP patient

Sub-component Modelling Approach		Post-setting change PaO2				Post-setting change $PaCO_2$				Post-setting change pH			
Kd	VCO_2	MSE	MAE	SD	R^2	MSE	MAE	SD	R^2	MSE	MAE	SD	R^2
ANFIS	ANFIS	10.4	16.05	3.07	0.54	1.42	15.78	1.2	R^2	$7.01e^{-03}$	1.02	$7.67e^{-02}$	0.71
IT2FLS	IT2FLS	10.25	15.85	3.06	0.55	1.33	16.76	1.17	0.33	$6.47e^{-03}$	0.89	$6.91e^{-02}$	0.74
IT2FLS (nPSO)	IT2FLS (nPSO)	10.29	15.84	3.07	0.54	1.20	15.81	1.11	0.50	$5.05e^{-03}$	0.85	$5.84e^{-02}$	0.78
IT2FLS (243 rules)	IT2FLS (nPSO)	10.34	15.96	3.07	0.54	0.95	14.56	0.99	0.51	$4.76e^{-03}$	0.8	$6.06e^{-02}$	0.82
T1 FCM	T1 FCM	10.23	15.81	3.06	0.55	1.22	15.22	1.13	0.65	$4.34e^{-03}$	0.76	$5.61e^{-02}$	0.77
T1 FCM (MSE nPSO)	T1 FCM (MSE nPSO)	10.27	15.92	3.05	0.55	1.32	14.74	1.13	0.43	$6.37e^{-03}$	0.93	$5.91e^{-02}$	0.75
T1 FCM (R^2 nPSO)	T1 FCM (R^2 nPSO)	10.24	15.9	3.05	0.55	1.32	14.74	1.13	0.40	$6.40e^{-03}$	0.94	$5.82\ e^{-02}$	0.76

5.4 Modelling of Arterial Blood Gases using Ventilator Settings for Faecal Peritonitis Patients

Predicting the arterial blood gases (ABG) using the SOPAVent model is non-invasive and automatic, however, it entails that all parameters associated with SOPAVent to be readily available, optimally with the data recorded on a minute-to-minute basis. The parameters associated to SOPAVent included the initial blood gas analysis results, ventilator monitoring, ventilator settings and various other physiological information that may or may not be integrated in a universal data management system. The unavailability of one or more components can affect the prediction accuracy of the model. This was shown in the previous section; when data was only available on an hourly basis, there was a lack of information on when the actual ventilator settings-change happened, or, if there were more than one change happening within the same one-hour period. This resulted in the decline of prediction accuracy for some of the ABG parameters.

It is understood that ventilator settings were changed by clinicians following the results obtained from ABG analyses, interpretations of ventilator monitoring sensors and the patient's overall condition. A new approach for predicting ABG for FP patients is proposed by using the available hourly ventilator settings data, and the ABG data during blood sampling times, which are recorded every two to four hours. The ventilator settings used for modelling the ABG were the inspiratory pressure (Pinsp), the positive end expiratory pressure (PEEP), assisted spontaneous breathing (ASB) plus PEEP, the fraction of inspired oxygen (FiO_2), the respiration rate (RR), and the inspiration time (Tin). The ABG parameters used were the PaO_2, $PaCO_2$ and pH at blood gas times. The same data selection criteria for FP patients defined in section 5.2 were used together with the following criteria to obtain the ventilator settings and ABG data for the new models:

i. ABG sampling times should be after ventilator settings record time;

ii. The difference between ventilator settings record time and ABG sampling time should not be less than 30 minutes but not larger than 180 minutes.

A total of 286 data from 24 patients were obtained with the data summarized in Table 5.9. The distribution of data is shown in Figure 5.9. An adaptive neural-fuzzy inference system (ANFIS) model, and a fuzzy c-means clustering (FCM) model with the 'new structure' particle swarm optimization (nPSO) were used to generate the predictions of the ABG (PaO_2, $PaCO_2$ and pH), from parameters of ventilator settings data. The ANFIS model used grid partitioning with three membership functions (MFs) for each input, and optimized using the hybrid algorithm available in Matlab's neuro-fuzzy designer toolbox. The FCM nPSO model was previously described in Chapter 4.

Table 5.9 Ventilator settings and ABG data for FP patients

Parameter	Pinsp	PEEP	ASB+PEEP	FIO2	RR	Tin	PaO2	PaO2	pH
Mean	22.04	6.96	21.49	39.97	15.57	1.38	14.85	5.64	7.35
S.D	5.25	2.01	5.01	8.85	2.69	0.23	3.45	1.07	0.08
Minimum	10	5.00	10.00	29.00	10.00	1.00	7.33	3.68	7.15
Maximum	36.00	10.00	32.00	71.00	22.00	1.70	26.70	8.92	7.55

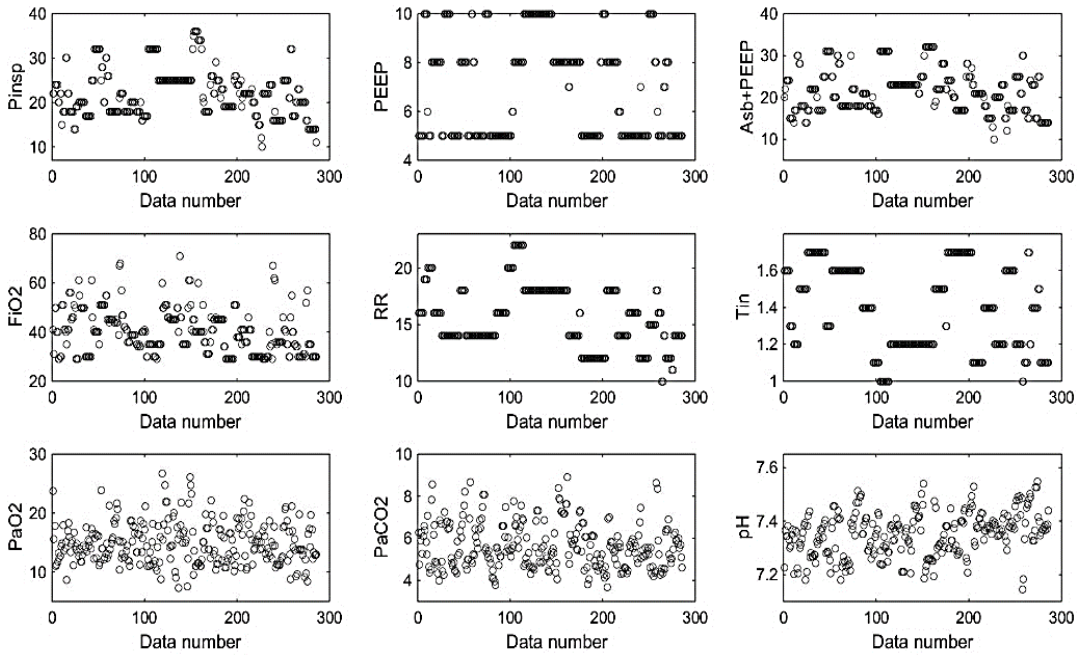

Figure 5.9 Ventilator setting and ABG data distribution

Table 5.10 shows the FCM clustering result for modelling the ABG using ventilator settings for the FP patients. A cluster number of 26 was selected PaO_2, with an MSE of 7.20 and R^2 of 0.63. A cluster number of 30 was selected $PaCO_2$, with an MSE of 0.63 and R^2 of 0.67, while a cluster number of 32 was selected pH, with an MSE $3.86e^{-3}$ and R^2 of 0.63. Figure 5.10 shows the objective functions for selecting the cluster number for each ABG parameter. The FCM models were further optimized using the nPSO algorithm to improve its prediction accuracy.

Table 5.10 Result for FCM clustering of FP patients

ABG Parameter	Cluster number	MSE	MAE	R^2
PaO_2	26	7.20	14.70	0.63
$PaCO_2$	30	0.63	11.40	0.67
pH	32	$3.86e^{-3}$	0.64	0.63

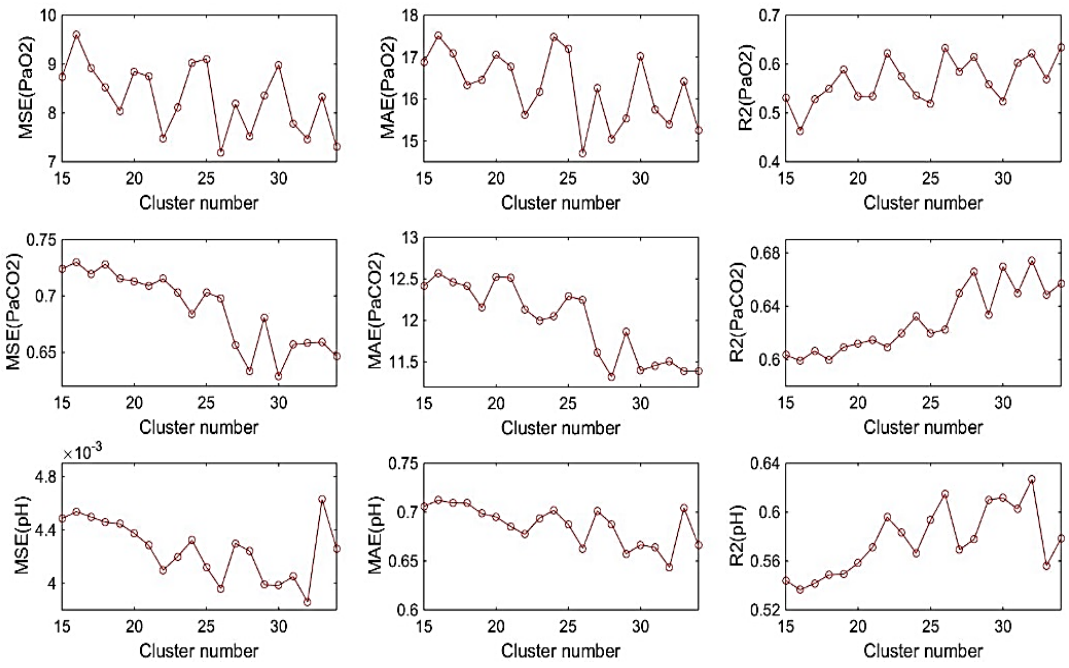

Figure 5.10 Objective function for FCM clustering of FP patients

5.4.1 Results of ABG Predictions using Ventilator Settings for ANFIS and FCM nPSO Based Models

The ventilator settings Pinsp, PEEP, ASB plus PEEP, RR, FiO_2 and T_I were used as input parameters to the ANFIS and FCM nPSO models to predict the arterial blood gases of PaO_2, $PaCO_2$ and pH of FP patients. Table 5.11 shows the result

obtained for both models. For the ANFIS model, the prediction of PaO_2 produced an MSE of 3.76 and R^2 of 0.83, with most of the predictions occurring within the $\pm$10% confidence band. However, a few predictions on the lower-end range produced higher values than the target PaO_2, while a few other predictions on the higher-end range produced predictions which were lower than the target PaO_2. The prediction of $PaCO_2$ produced an MSE of 0.24, with R^2 of 0.89, and with most predictions happening within the $\pm$10% confidence band. A few predictions were lower than the target value, mostly those within the 7 kPa to 9kPa range. For the pH parameter, the ANFIS model produced an MSE of $1.28e^{-3}$ with R^2 of 0.89. The majority of predictions were within the $\pm$1% confidence band, with only several predictions producing pH which were slightly higher than target values of pH between 7.2 and 7.3. The prediction plots for the ANFIS model are shown in Figure 5.11.

The FCM nPSO model PaO_2 predictions produced an MSE of 3.62 and R^2 of 0.84. However, the predictions were slightly less concentrated within the $\pm$10% confidence band when compared to the ANFIS model. The $PaCO_2$ prediction produced an MSE of 0.33 and R^2 of 0.59, with most predictions within the $\pm$10% confidence band. Some predictions of the higher-end range were slightly less than the target values, while some of the predictions of the lower-end range were slightly larger than the target values, although most predictions of both ranges were still within the tolerance band. This can also be seen with pH predictions in Figure 5.12, where some of the higher-end predictions were slightly lower than target values and some of the lower-end predictions were slightly larger than target values. The prediction plots for the FCM nPSO model are shown in Figure 5.12. Overall, the FCM nPSO based model for PaO_2, $PaCO_2$ and pH showed a marginally reduced prediction accuracy when compared to the ANFIS model. However, both models provided satisfactory performance in terms of error and correlation.

Table 5.11. ANFIS and FCM nPSO ABG prediction results for FP patients

ABG Parameter	ANFIS				FCM nPSO			
	MSE	MAE	S.D	R^2	MSE	MAE	S.D	R^2
PaO_2	3.76	8.97	1.94	0.83	3.62	10.14	1.91	0.84
$PaCO_2$	0.24	5.18	0.49	0.89	0.33	8.46	0.57	0.89
pH	$1.28e^{-3}$	0.29	$3.58e^{-2}$	0.89	2.06e-3	0.45	4.55e-2	0.85

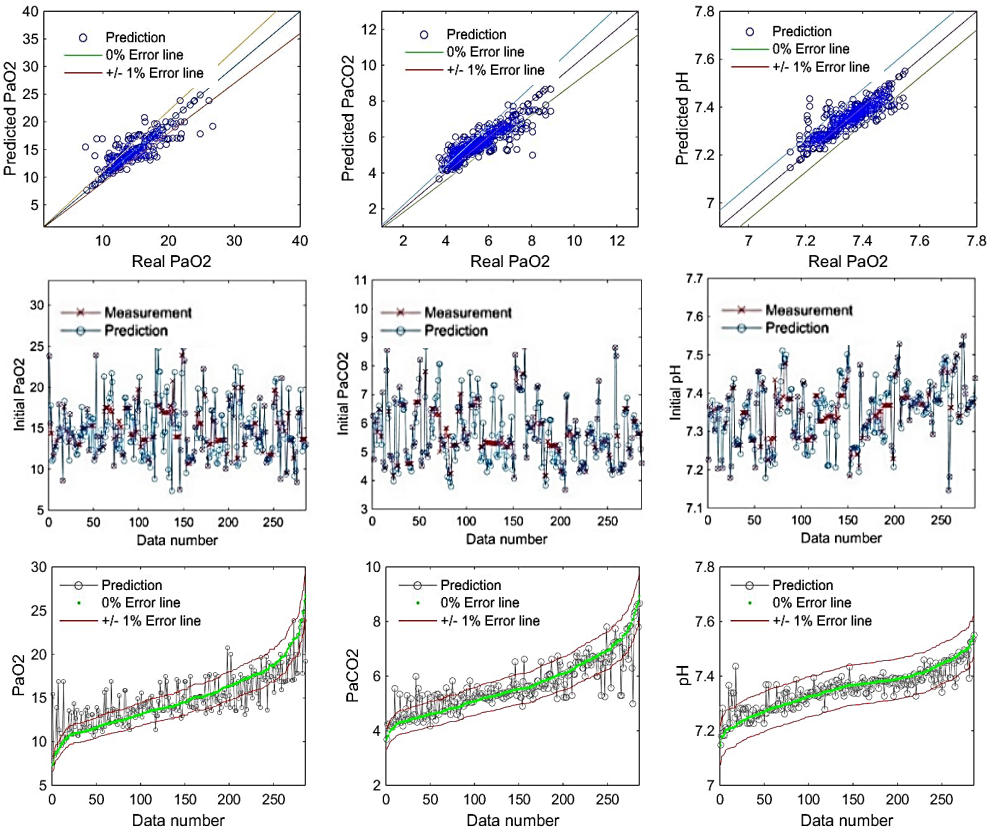

Figure 5.11 ANFIS prediction plots for FP data.

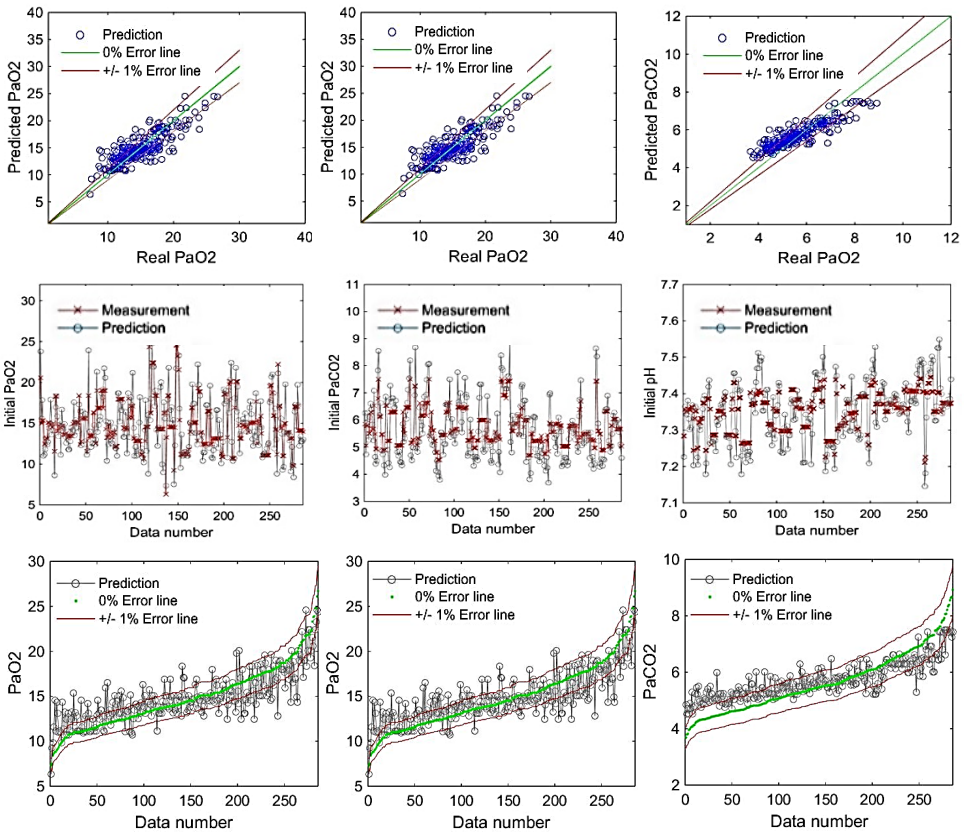

Figure 5.12 FCM nPSO prediction plots for FP data

5.5 Summary

The approaches detailed in Chapters 3 and 4 for modelling the relative dead-space (Kd) and carbon-dioxide production (VCO_2), were used on newly obtained data for patients with faecal peritonitis (FP). The new FP data however, were only available on an hourly basis instead of minute-by-minute basis such in the previous dataset used in Chapters 3 and 4. The new FP patients also led to variations in data characteristics which caused the prediction of Kd to be less accurate when compared to the previous dataset.

The Kd and VCO_2 models were then integrated into the SOPAVent blood gas model to predict blood gas parameters PaO_2, $PaCO_2$ and pH for FP patients. The prediction results of the initial $PaCO_2$, initial pH and post-setting change pH were satisfactory; either performing equal to the previous dataset or with improvements noted in accuracy and error. However, the post-setting change prediction of PaO_2, and the post-setting change prediction of $PaCO_2$ did not show improvements accuracies due to the Kd model not being able to provide satisfactory outcomes. SOPAVent provided the best performance when Kd was modelled IT2FLS (243) and VCO_2 was modelled using IT2FLS (nPSO), which agrees with the findings obtained in Chapter 4.

An innovative approach for prediction of ABG using ventilator setting parameters was also proposed to model the arterial blood gases. It has the advantage of significantly reducing the number of parameters required for modelling the blood gases and provide increased simplicity when compared to the SOPAVent model. The models developed using this approach were ANFIS and the FCM nPSO model. Both models produced satisfactory predictions with good correlation and minimal error. However, the models were not validated by any additional data set, thus its performance was not verified on other patient groups.

Chapter 6

Electrical Impedance Tomography for Monitoring of the Lungs

6.1 The Sheffield MK3.5 Electrical Impedance Tomography System

The Sheffield MK3.5 Electrical Impedance Tomography (EIT) is an 8-electrode, 2D, EIT modular system, which is the final development of the Sheffield MK EIT series (see Table 6.1), first developed by Brown and Seagar (1987). The Sheffield MK3.5 EIT consists of a power supply module, a data acquisition module, and a computer set (see Figure 6.1). The user interface for the Sheffield MK3.5 EIT is shown in Figure 6.2. The data acquisition module consists of a central processor (motherboard) unit, 8 data acquisition (DAQ) cards, 8 drive-measure electrodes and 1 ground electrode. Each DAQ consists of a digital signal processing (DSP) chip, a 12-bit analogue to digital converter (ADC), a 12-bit digital to analogue converter (DAC) and signal conditioning circuitry (see Figure 6.3). The data acquisition software was developed in the C++ environment, while the data processing and the image reconstruction software were developed in Matlab (Wilson *et. al,* 2001). The MK3. EIT uses the four-electrode adjacent drive-and-measure configuration, which drives a 282 μA peak-to-peak current, at 30 selectable frequencies ranging from 2 kHz to 1.6 MHz. Since each DAQ card is a stand-alone unit, the system measures the voltage from five adjacent electrode pairs simultaneously. Eight successive current drives are required to complete one frame, producing 40 independent measurements. The system operates at a rate of 25 frames per second.

Table 6.1 The Sheffield MK EIT systems

Model	Number of electrodes	Drive frequencies	Year
MK1	16	50 kHz	1987
MK2	16	20 kHz	1990
MK3	16	9.6 kHz to 1.2 MHz	1993
MK3.5	8	2 kHz to 1.6 MHz	2000

Figure 6.1. The Sheffield MK3.5 EIT system (Mohamad-Samuri *et.al*, 2011)

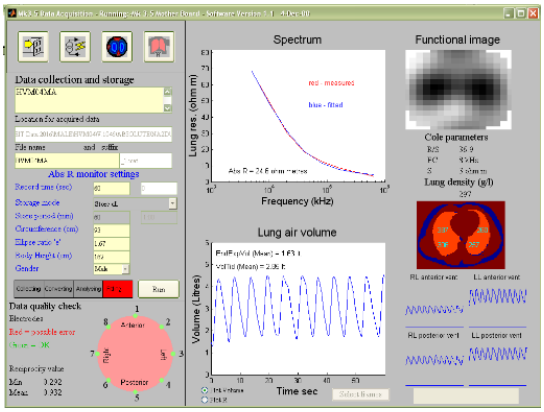

Figure 6.2. User interface for the MK3.5 EIT system applied on a healthy volunteer.

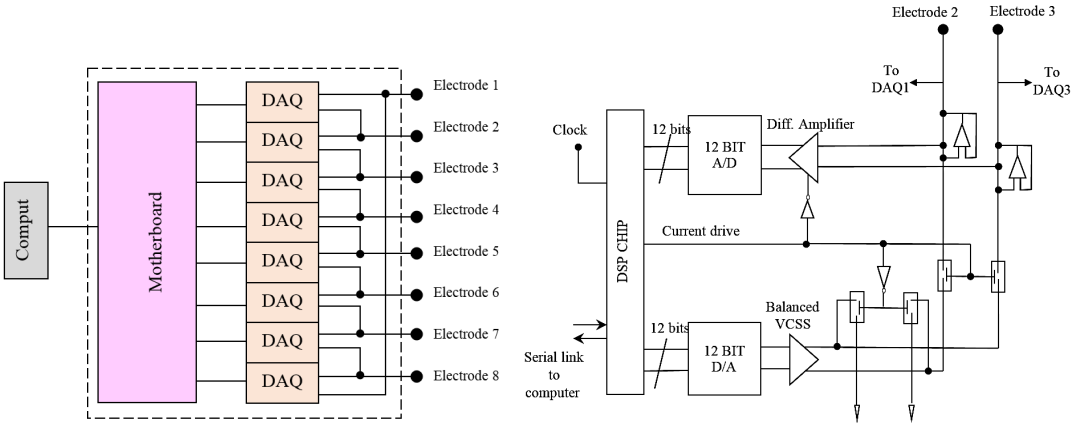

Figure 6.3. DAQ block diagram and schematics (Adapted from Wilson *et. al*, 2001)

6.2 Solving the Forward and Inverse Problems

To find the conductivity distribution of a conducive object, the forward and inverse problem of EIT must be solved. The forward problem calculates the surface potential of the electrode (V), as a function of the drive current (I), and the conductivity distribution (σ). An elliptical partial differential equation (PDE) defines the mesh using Ohm's law. The boundary dataset (I, V) determines the Neuman and Dirichlet boundary conditions (γ), creating a non-linear equation (Cheney *et. al,* 1999):

$$V = \gamma F(\sigma) I \tag{6.1}$$

With γ as the complex admittivity,

The change in conductivity, $x = \sigma_2 - \sigma_1$, is the difference in conductivity distribution, between two data frames at two different time, t_1 and $t2$. The change in conductivity, x corresponds to the change in surface potential, $z = v_2 - v_1$, between two intervals, t_1 and t_2. The Jacobian sensitivity matrix, H, linearizes the equation for minor changes in background conductivity, σ_0. The element of H, H_{ij} correlates a small change in the i^{th} surface potential to a small change in the conductivity of the j^{th} element (Graham and Adler, 2007).

$$z = Hx + n \text{ , with } n \text{ as the measurement system noise} \tag{6.2}$$

$$H_{ij} = \left.\frac{\delta z_i}{\delta x_j}\right|_{\sigma_0} \tag{6.3}$$

The inverse problem leads to the change of conductivity, x from the real difference of measurements between data frames. Several solutions exist for solving the inverse problem, such as the back-projection method, the Landweber iteration, the linear Tikhonov regularized Gauss-Newton algorithm, the non-linear Tikhonov regularized Gauss-Newton algorithm, the linear conjugate gradient algorithm, the preconditioned conjugate gradient (PCG) solver, the gradient projection for sparse reconstruction (GPSR) solver and Barzilai–Borwein GPSR. Online applications for

generating the finite element mesh and solving the inverse problem are also available in the EIDORS and NETGEN platforms (Jahaverian *et al.*, 2016).

6.2.1 Absolute Resistivity of the Lungs using Electrical Impedance Tomography

The absolute EIT represents the lung impedance as the absolute resistivity instead of the difference in resistivity at two separate times. Absolute EIT is achieved by comparing the measured EIT data to a set of computed data. The set of computed data can be generated using a 3D finite element analysis from Computed Tomography (CT) scans or Magnetic Resonance Imaging (MRI) scans of the thorax, where each type of tissue is assigned a specific resistivity value ranging from 1Ωm to 80Ωm. The model is scaled to include the eccentricity value, '*e*', which is the ratio of the measurements of the circumference of the chest to the measurement of the depth of the chest of subjects (Brown *et. al*, 2007). The density of the lung (ρ_{lung}) is defined as follows:

$$\rho_{lung} = \frac{W_{lung}}{V_{air} + V_{tissue}} \tag{6.4}$$

With W_{lung} as the lung weight, V_{air} is the volume of air, and V_{tissue} is the volume of lung tissue. By substituting $\frac{V_{air}}{V_{tissue}}$ with filling factor (FF), and substituting $\frac{W_{lung}}{V_{tissue}}$ with the density of lung tissue (ρ_{tissue}), equation 6.4 becomes:

$$\rho_{lung} = \frac{\rho_{tissue}}{FF+1} \text{, and} \tag{6.5}$$

$$\rho_{lung} = \frac{\rho_{tissue}}{\left(\frac{V_{air}}{W_{lung}}\right)\rho_{tissue} + 1} \tag{6.6}$$

The lung weight, W_{lung} can be calculated using the subject's height as follows (Samuri *et. al*, 2011):

$$\text{Male lung weight} = 800 + \frac{bodyheight^3}{15000} \tag{6.7}$$

$$\text{Female lung weight} = 850 + \frac{bodyheight^3}{20000} \tag{6.8}$$

A model of the human lungs to calculate the absolute lung resistivity (AbR) was developed by Nopp *et al.*, (1997).

$$\rho_{lung} = 3.12 - (3.24)[\ln(AbR)]^{0.3} + (0.81)[\ln(AbR)]^{0.6} \tag{6.9}$$

$$AbR = 1.74 + (194.3)e^{-24.69\rho_{lung}} + 40.04 \tag{6.10}$$

$$\sigma_L = AbR^{-1}W_{lung} \tag{6.11}$$

With σ_L being the lung conductivity.

6.3 Development of an Electrical Impedance Tomography Systems Hardware

This section of the chapter will focus on the design and development of a compact EIT measurement system. The EIT system comes with an array of 16 electrodes to be used either as an 8-electrode 2D EIT system or a two-layer 3D EIT system, where each layer consists of 8 electrodes, based on the system developed by Khaligi *et al.,* (2014). The system drives the electrical current and measures the surface potentials using a combination of analogue and digital circuitry. The current drive circuitry comprises of a voltage-controlled oscillator (VCO), filters, and a voltage to current converter (VCC). The voltage measurement circuitry consists of a pulse generator, a voltage demodulator and an analogue to digital converter (ADC). The switching mechanism for the drive-and-measure operation is done via a microcontroller and a multiplexing circuitry. A computer is connected to the microcontroller for signalling purpose, handling and processing of measured data (see Figure 6.4). The EIT system should be able to drive a small alternating current with a frequency ranging between anywhere 10k Hz and 50 kHz.

As the EIT system will be used for pulmonary application, the drive-and-measure mechanism must have adequate frame rate to accurately represent the dynamic process of inspiration and expiration. The respiratory rate during normal breathing for a healthy adult can be anywhere from 12 to 18 breaths per minute, while it can be much higher for children (see Table 6.2).

A complete cycle of the EIT data acquisition will represent a single frame. In the single layer, 8-electrode MK3.5 EIT system, 25 frames of data are taken for each second. With 40 data measured in each frame, this produced 25x40 or 1000 measurements for each second. A normal adult with a respiratory rate of 15 breaths per minute, will take 4 seconds to complete each breath. Using the MK3.5 EIT system, this will produce 4x25 or 100 frames per breath. For the new 3D EIT system, a sampling rate of 25 frames per second is proposed to match the specification of the MK3.5 EIT system. The new system will have 16 electrodes (in two 8-electrode layers), thus producing 208 measurements for each frame. For a 25-frames per second measurement, the system should be able to sample 5200 data per second, or 192.31μs per measurement. Times delays and conversion times from analogue and digital devices are accounted for calculating the intervals required for the switching mechanism to ensure the sampling width meets the criteria defined. Table 6.3 shows the amount of data measured for each breath for different respiration rates.

Table 6.2 Normal respiratory rate for healthy individuals. (Fleming *et al*., 2013 and Rodriguez-Molinero *et.al*, 2013)

Age	Breath per minute
Infants	30-60
Toddlers and pre-schoolers	20-40
School age	17-22
Adults	12-18
Elderly	15-25

Table 6.3 Number of data measured for each breath for different respiration rate

Breath per minute	Breath length (s)	Frames per breath	Data per breath
10	6	150	31200
20	3	75	15600
30	2	50	10400
40	1.5	37.5	7800
50	1.2	30	6240
60	1	25	5200

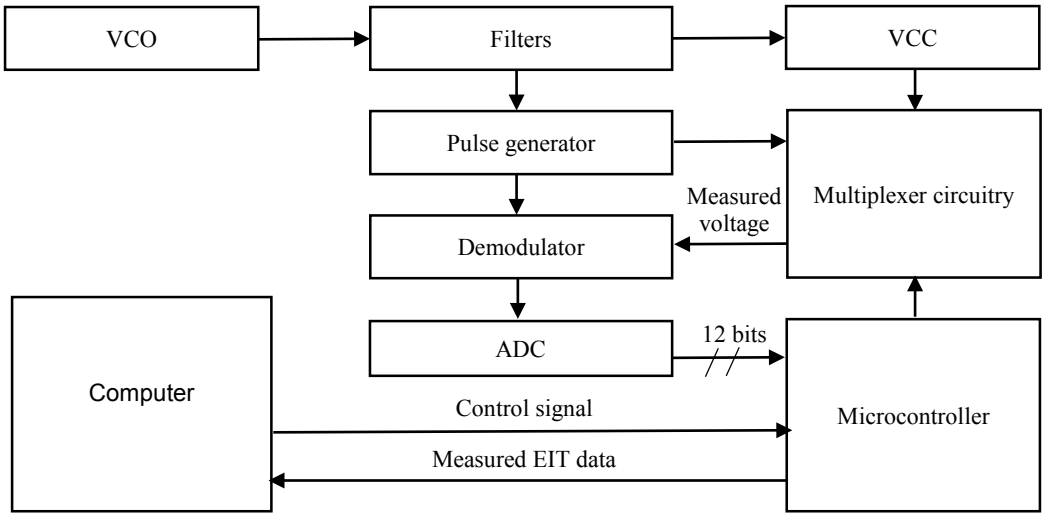

Figure 6.4. Block diagram of the EIT system (adapted from Khaligi *et. al*, 2014)

Figure 6.5 shows the overall schematics of the proposed 3D EIT system. The current source for the EIT is a sinusoidal waveform generated from the voltage-controlled oscillator (VCO), which is then amplified and filtered through a Butterworth band-pass filter. The resulting voltage is converted into current using a voltage to current converter (VCC). The generated alternating current will be used to drive the electrodes pairs, with the drive-and-measure sequencing performed by switching the channels of several multiplexers. The control signals for the switching of multiplexers are sent from the microcontroller. The surface potentials are then measured by the adjacent pairs of electrodes and are converted from analogue to digital values using the analogue to digital converter (ADC). The digitised measurements are then sent to the microcontroller to be transmitted to the computer for processing.

Figure 6.6 shows the VCO with the XR-2206 chip used to generate the waveform which is amplified by the AD844 operational amplifier. The output of the VCO, point *A* on the circuit is connected to the input of the band-pass filter in Figure 6.7. The Butterworth band-pass filter removes noise and limits the frequency of the EIT to between 10 kHz and 250 kHz. A sample output of the band-pass filter is shown in Figure 6.8

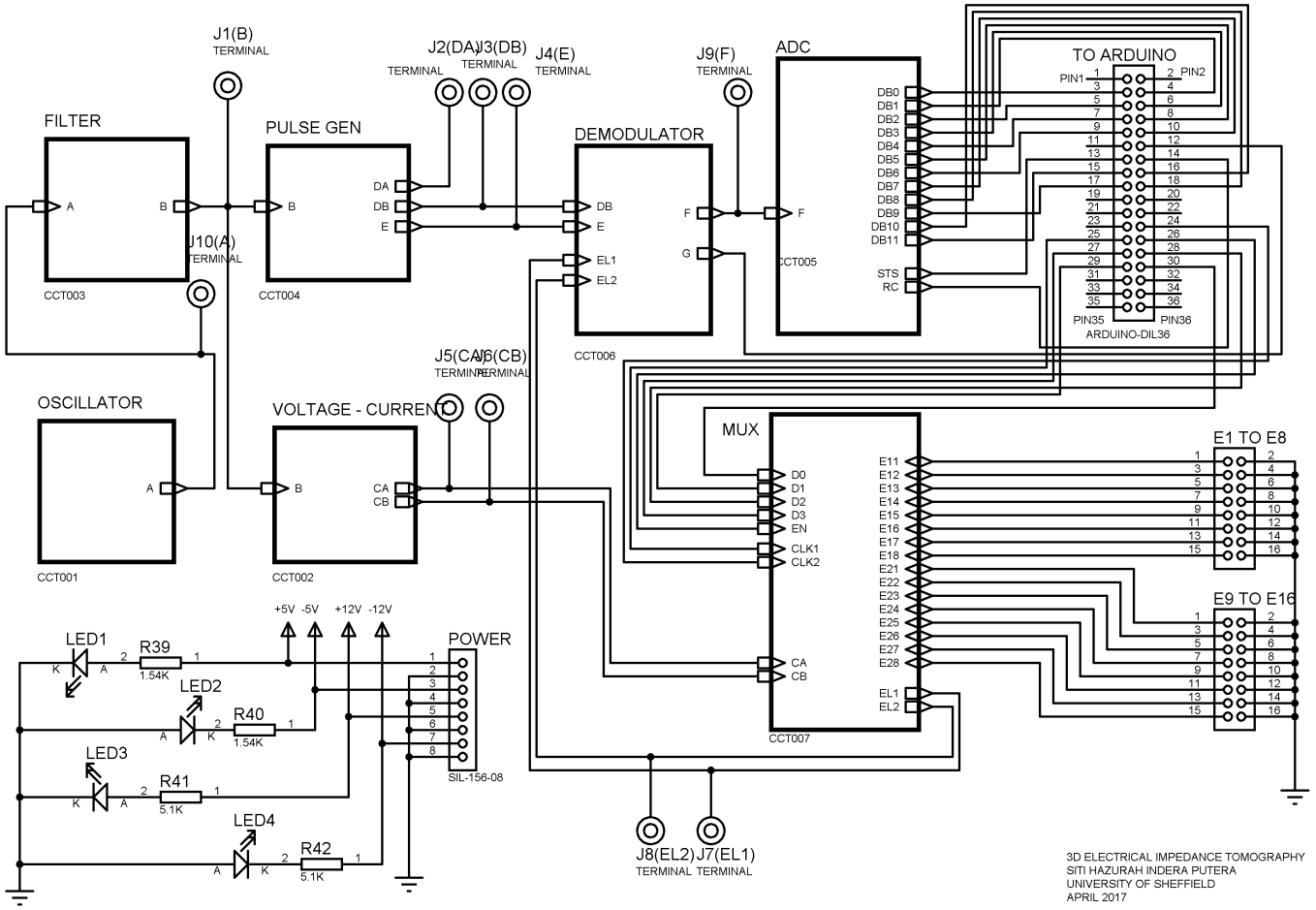

Figure 6.5. The overall schematics for the EIT System

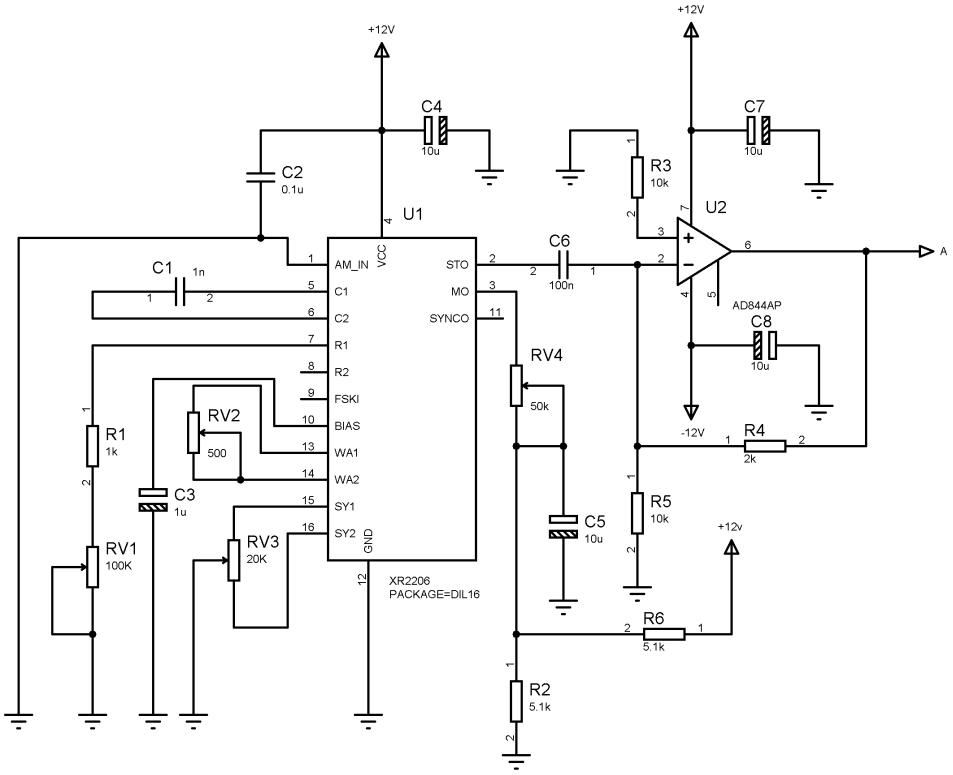

Figure 6.6. Schematic for the voltage controlled oscillator (VCO)

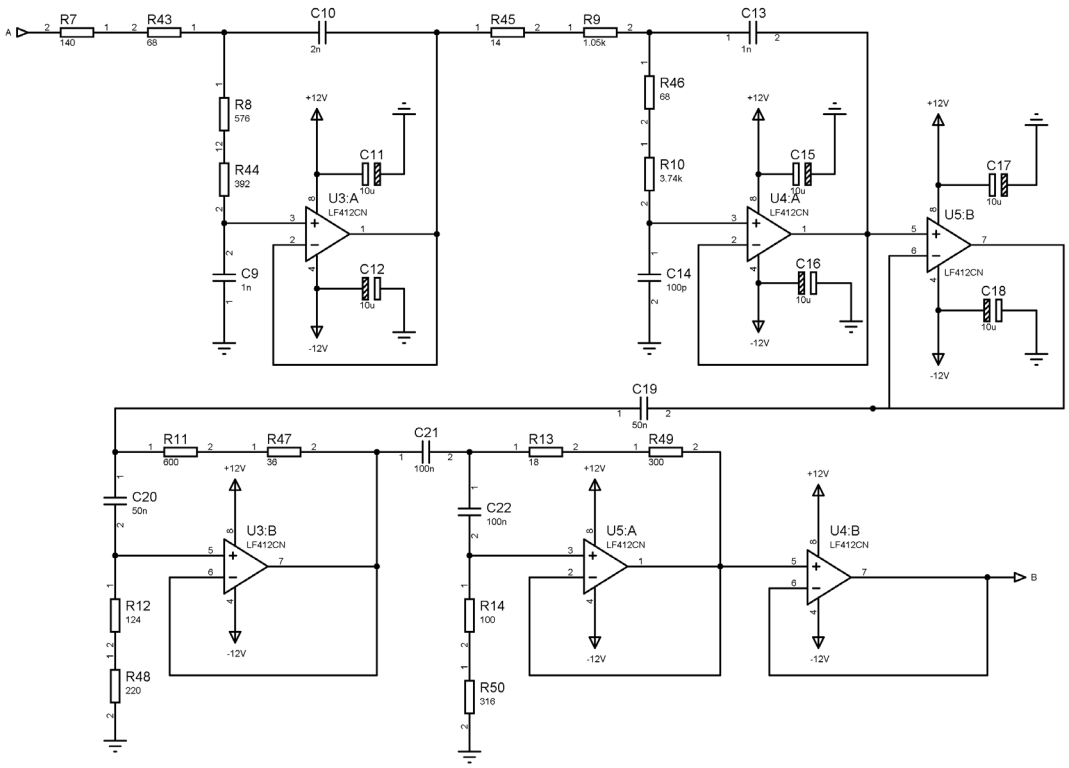

Figure 6.7. Schematic for the Butterworth band-pass filter

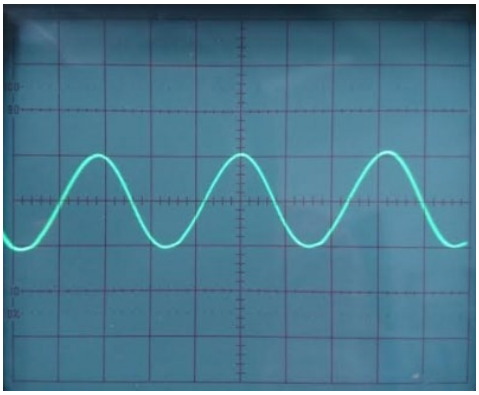

Figure 6.8. Sample output of the band-pass filter

The output of the band-pass filter, point *B,* on the circuit in Figure 6.7 is connected to the input of the voltage to current converter (VCC) (see Figure 6.9). VCC converts the filtered voltage signal to current, using the triple-operational amplifier form. The system has a maximum allowable load of 12 kΩ at 10 kHz and a maximum allowable load of 8 kΩ at 250 Hz (Khaligi *et. al*, 2014). The load current, I_L is used to drive the electrode pairs and are calculated as follows:

$$I_L = \frac{\left(\frac{R_4}{R_3 + R_4}\right) V_i}{\left(\frac{R_1}{R_1 + R_2} - \frac{R_3}{R_3 + R_4}\right) R_L + \frac{R_1 . R_5}{R_1 + R_2}} \tag{6.12}$$

$$if \ \frac{R1_1}{R_1 + R_2} - \frac{R_3}{R_3 + R_4} = 0, \qquad or \ \ R_1 . R_4 = R_2 . R_3 \tag{6.13}$$

$$then \ I_L = \frac{R_4}{R_3 . R_5} . V_i \tag{6.14}$$

The output of the band-pass filter is also connected to the input of a pulse generator (see Figure 6.10), to produce two train pulses. The first train pulse is generated by detecting the positive part of the drive current. The signal can be viewed from point *DB* on the circuit in Figure 6.10. The second train pulse is generated by detecting the zero point of the drive current, and the signal can be observed from point *E* on the circuit. The pulse trains are used to demodulate the surface potentials measured from the electrode pairs. The train pulses are shown in Figure 6.11.

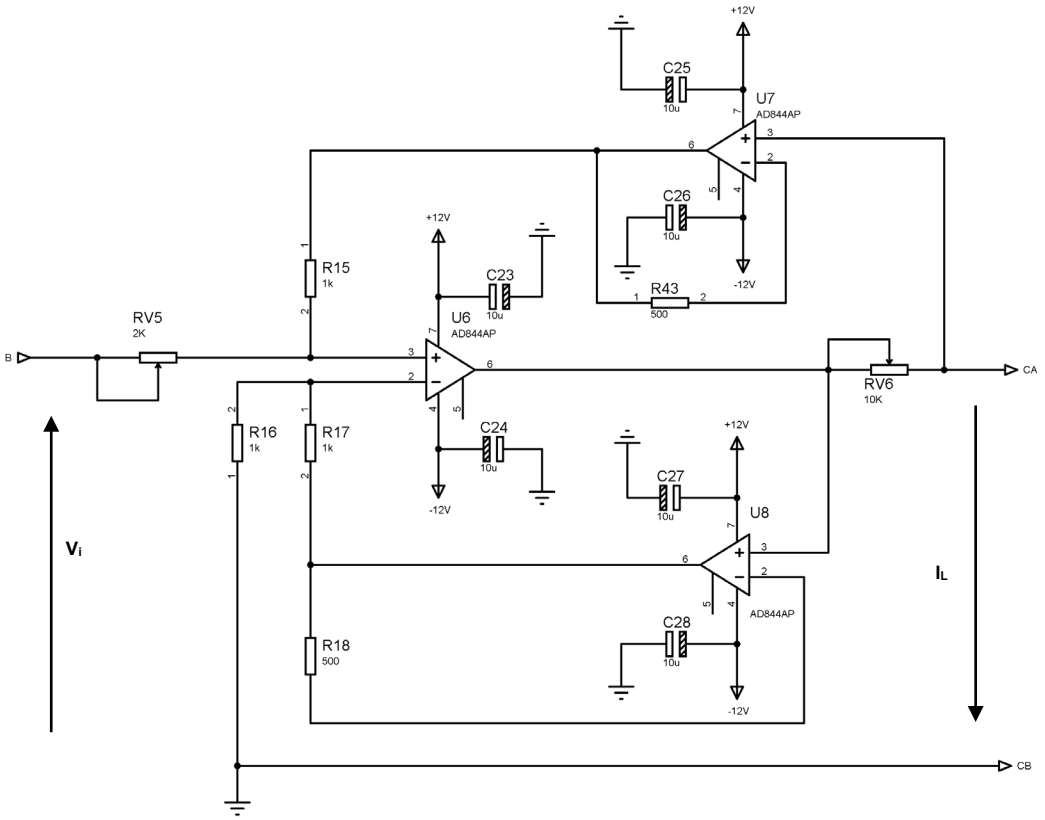

Figure 6.9. Schematic for the voltage to current converter (VCC)

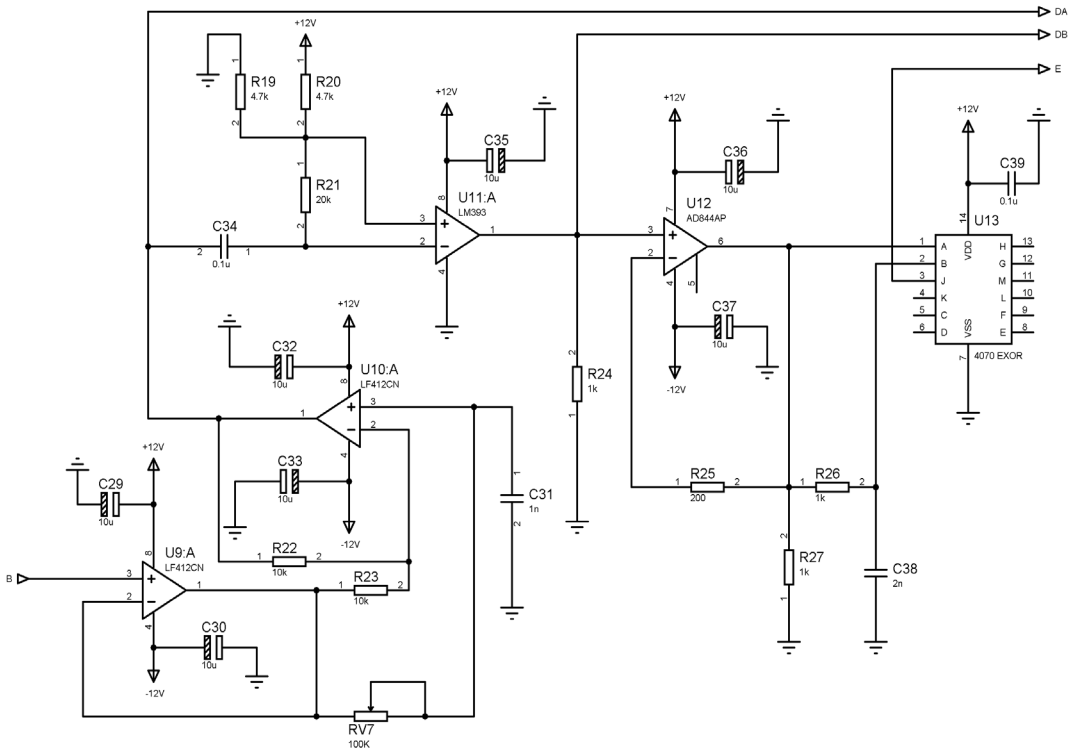

Figure 6.10. Schematic for the pulse generator

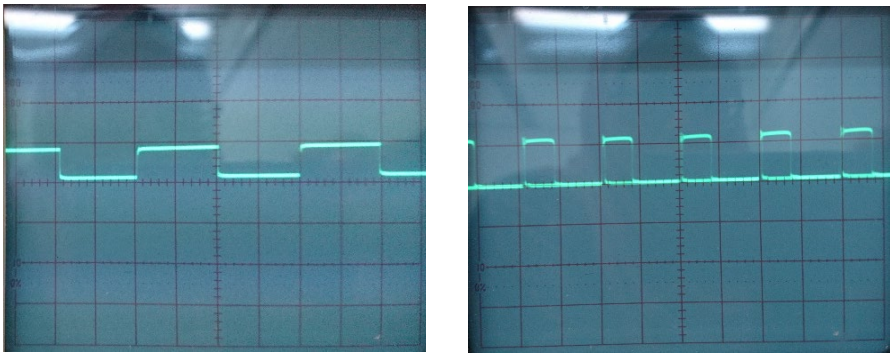

Figure 6.11. Positive peak detection and zero detection train pulses at 50 Hz

The pulse trains from the pulse generator circuit are connected to the inputs of the demodulator circuit (see Figure 6.12). The positive-detector pulse train, point *DB*, is connected to the input of the first opto-coupler, *U21.* The zero-detector pulse train, point *E,* is connected to the input of the second opto-coupler, *U22.* The transistor in the opto-coupler acts as a switch that turns on whenever a pulse is present. The output of the opto-couplers is inverted and connected to an AND gate, *U15* and the signal is sent to the microcontroller. The demodulator circuit also receives signals from the electrode pairs at points *EL1* and *EL2* on the circuit. The inputs to the instrumentation amplifier AD625, *U14*, are the demodulated electrode voltages, and the output of *U14* represents the difference of those potentials.

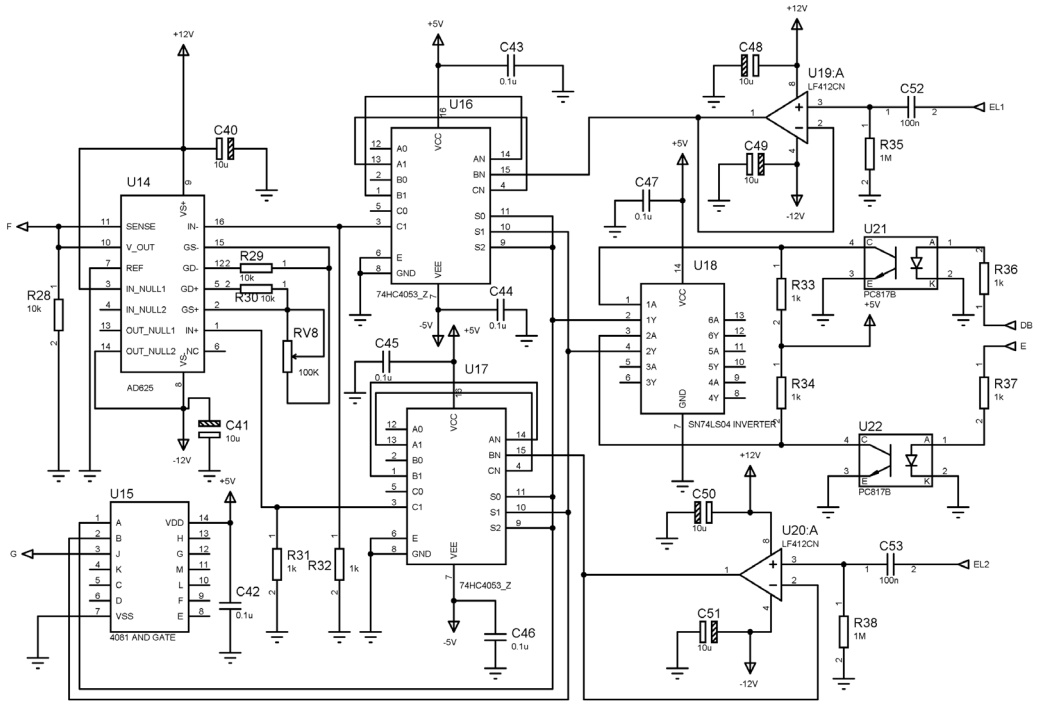

Figure 6.12 Schematic for the demodulator

The demodulated voltages are then converted from analogue values to digital values using the analogue to digital converter (ADC) chip, which generates 12 bits of digital signal (*DB0* to *DB11*) (see Figure 6.13). The resulting digital voltages are the EIT measurements and these measurements are sent to the microcontroller for processing. The ADC has a conversion time of 10µs (100k samples per second). One bit is used for the sign, and the remaining 11 bits of the ADC can detect a change of 2.44mV for a ±5V reference voltage or a 4.88mV for a ±10V reference voltage.

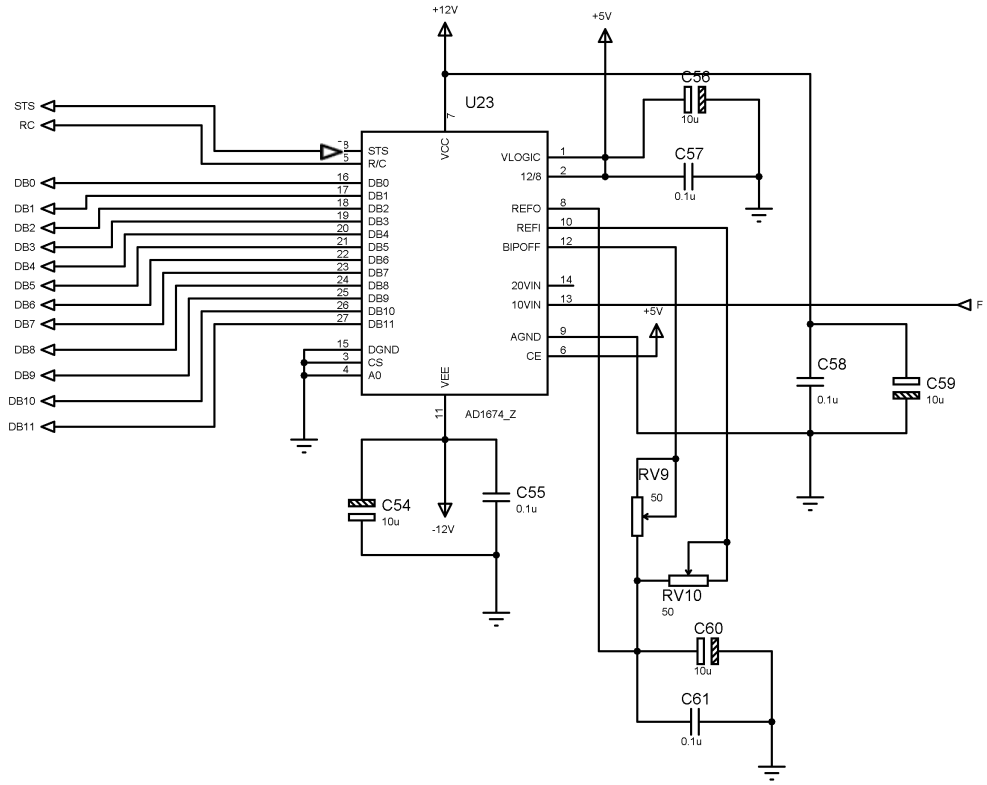

Figure 6.13 Schematic of the analogue to digital converter (ADC)

The switching of electrode pairs for both drive current and voltage measurements are performed by a multiplexing circuit shown in Figure 6.14. The control signals for the switching process are sent from the microcontroller. Four units of 16-channels analogue multiplexers are used, with two of the multiplexers used for selecting the electrodes for drive current and sink (*U24* and *U25*), and two multiplexers used for selecting the measurement electrodes (*U26* and U2*7)*. Channels 1 to 8 on the multiplexers *U24* and *U26* are connected to the electrodes 1 to 8 (*E11* to *E18*) on the first plane of two planes, and channels 9 to 16 on the multiplexers are connected to electrodes 9 to 16 (*E21* to *E28*) on the second plane. The connection of electrodes to

the multiplexer *U25* and multiplexer *U27* are shifted by 1 bit, i.e. the first electrode is connected to the 2nd channel on the multiplexers. For a 16-electrode system, 4 address lines are needed to select the channels on the multiplexers.

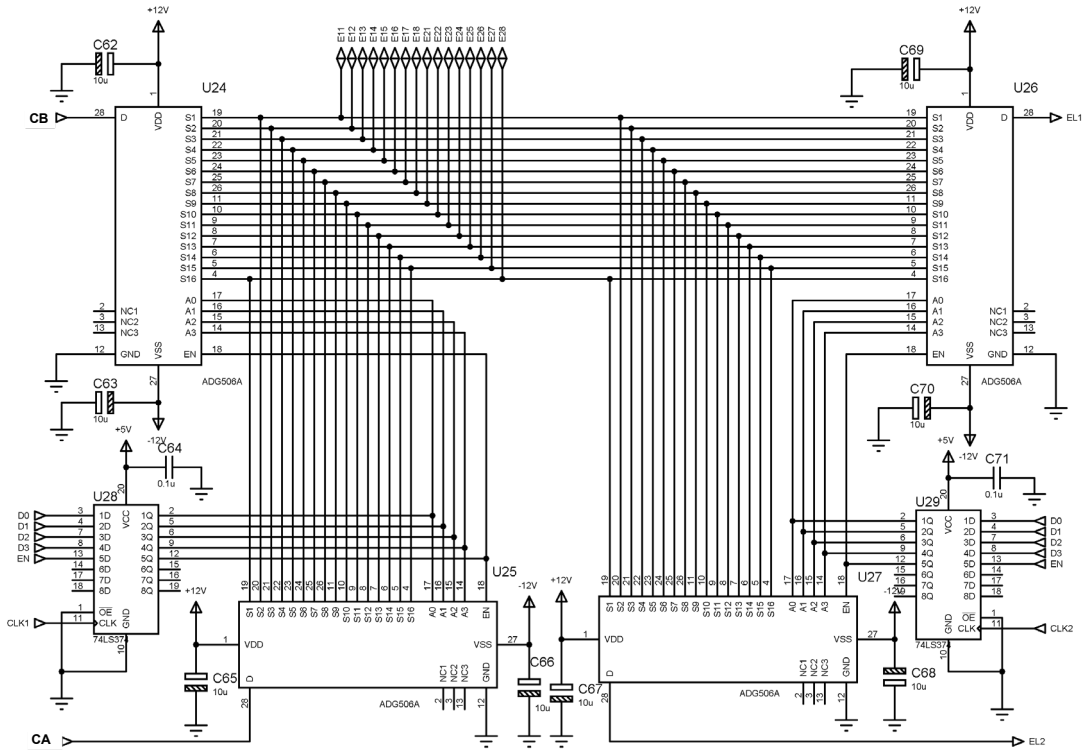

Figure 6.14 Schematic for the multiplexing circuit

The address lines, *D0* to *D3,* are connected from the microcontroller to the inputs of the edge-triggered flip flops (*U28* and *U29* in Figure 6.14). On the positive transition of the clock signal, the outputs of the edge-triggered flip flops are set to the logic states of the inputs of the flip flops. When the clock signal, *CLK1* is '*low',* the outputs of the flip flops are latched to the previous logic state. So, while the flip flop that is used for the drive current, U28, is latched at logic 0001, current will be injected through electrode 1 and electrode 2 will act ask sink. The clock signal on U28 remains '*low'*, while the clock signal on U29, *CLK2* switches between '*high'* and '*low'* until all voltage measurements from adjacent electrode pairs are completed. Next, the clock signal for *CLK1* is latched to the next logic state, and the process is repeated until all the drive electrodes pairs have been utilised.

Figure 6.15 shows the switching sequence of the current drive electrode pairs and voltage measurement electrode pairs. The switching function on the multiplexer circuit is controlled by an Arduino Mega 2560 microcontroller. The microcontroller also receives signals from the demodulator circuit and the 12-bit digital output voltages from the analogue to digital converter. Table 6.4 shows the pins assignment of the microcontroller.

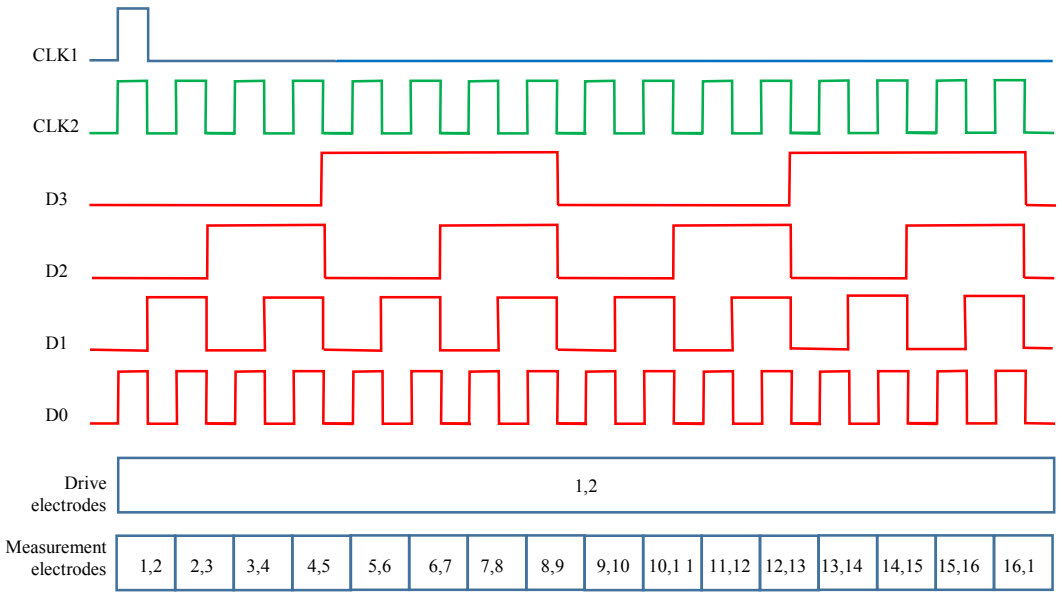

Figure 6.15. Switching of the current drive electrode pairs and the voltage measurement electrode pairs

The printed circuit board (PCB) of the 3D EIT system was designed using the Proteus Design Suite. Figure 6.16 shows the bottom copper and top silk for the PCB, and Figure 6.17 shows the completed PCB. Most of the integrated circuits and analogue/digital devices were available in the library of Proteus. However, some devices which were not available were manually created. The following design rules were applied to the PCB:

- Decoupling capacitors were included for all analogue and digital ICs.
- The trace for 5V power supply should be at least 0.02” or 0.51mm wide, and trace for 12V power supply should be at least 0.04” or 1.27mm wide.
- Sharp angles for traces were avoided wherever possible.
- Ensure that all junctions have no more than 3 nodes.

Table 6.4. Pin assignment for the Arduino microcontroller

Circuit	Assigned function	Pin on PCB board connecter	Microcontroller pin assignment		
			Port name	Digital I/O	Pin number
ADC	DB0	3	PA0	22	78
	DB1	4	PA1	23	77
	DB2	5	PA2	24	76
	DB3	6	PA3	25	75
	DB4	7	PA4	26	74
	DB5	8	PA5	27	73
	DB6	9	PA6	28	72
	DB7	10	PA7	29	71
	DB8	18	PC0	37	53
	DB9	17	PC1	36	54
	DB10	16	PC2	35	55
	DB11	15	PC3	34	56
	R/C	14	PC4	33	57
	STS	13	PC5	32	58
Demodulator	AND gate	12	PC6	31	59
Multiplexer	D0	30	PL0	49	35
	D1	29	PL1	48	36
	D2	28	PL2	47	37
	D3	27	PL3	46	38
	EN	26	PL4	45	39
	CLK1	25	PL5	44	40
	CLK2	24	PL6	43	41

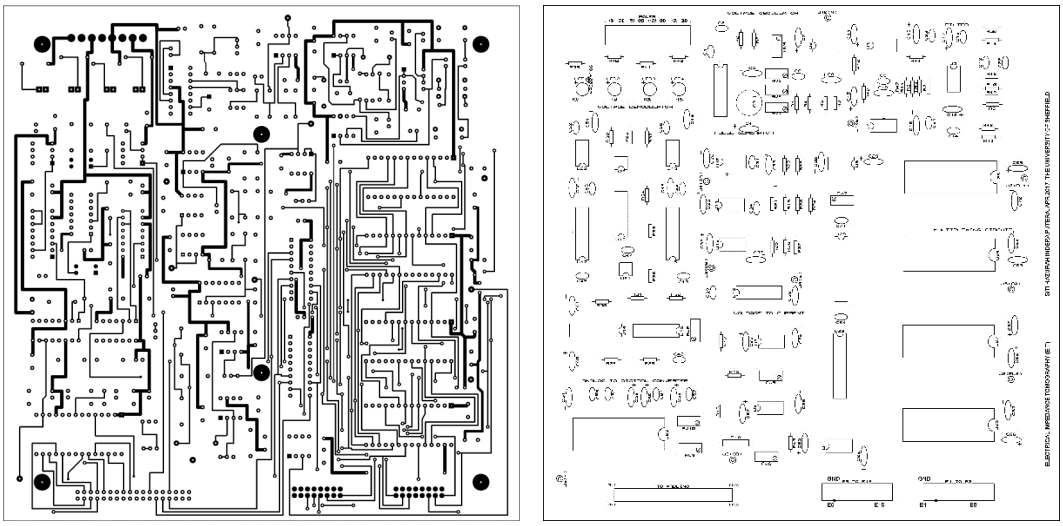

Figure 6.16. Bottom copper of printed circuit board and top silk for printed circuit board

‘The author would like to acknowledge Mr Paul Eastwood for his help in developing the EIT system hardware’

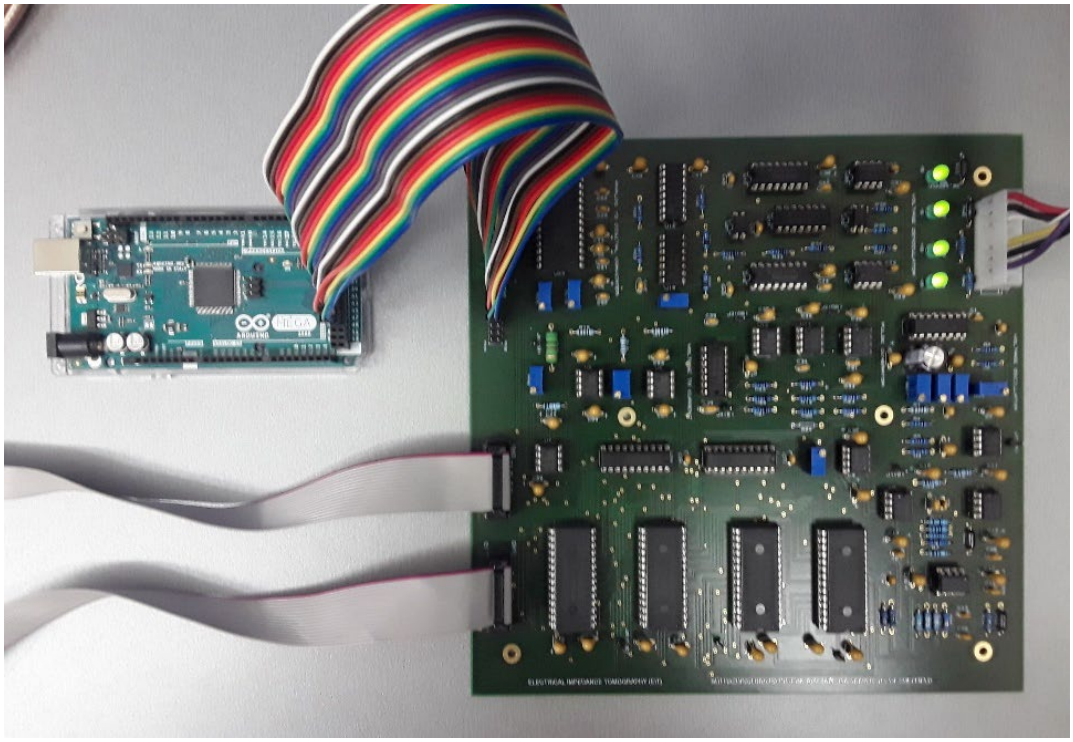

Figure 6.17. Printed circuit board of the 3D EIT system

6.4 Simulation of Three-dimensional Images of the Lungs from Magnetic Resonance and Computed Tomography Images

Magnetic Resonance Imaging (MRI) and Computed Tomography (CT) are medical imaging technique commonly used in hospitals to view tissues in a two-dimensional (2D), cross sectional plane. Digital Imaging and Communications in Medicine (DICOM) is the standardized protocol for handling medical images such MRI and CT. This Section will discuss an approach to generate 3D images of the lung from 2D DICOM images of the thorax using Matlab®. A set of 15 MRI slices of the human thorax is shown in Figure 6.19. This set of images is in DICOM format with a 256x256 pixel resolution. Other resolutions are also available, depending on specifications of the MRI equipment.

Due to the porosity of the lung, the tissues of the lung are lower in density compared to the bones, muscles or skin. This difference in density causes the image of the lung to have a distinctive contrast from surrounding tissues in the MRI or CT

image. To generate a 3D representation of the lung, firstly the lung tissues are isolated from other tissues by selecting an appropriate threshold range in the greyscale images. Once a threshold range is selected, the greyscale images are converted into a binary image to create a pure 'black and white' image. Noise is filtered by selecting only the largest areas in the image and omitting the rest. Finally, 3D rendering is performed by stacking the DICOM slices using Matlab® iso-surface function.

The flow of the 3D rendering process is shown in Figure 6.18. Two sets of DICOM images are examined. The first set of DICOM images consist of 15 MRI slices of 256x256 pixel images (Figure 6.19.). The second set of DICOM images consist of 26 CT slices of 512x512 pixel images (see Figure 6.20.). The DICOM images are retrospective from the Sheffield Royal Hallamshire Hospital and were taken from healthy volunteers.

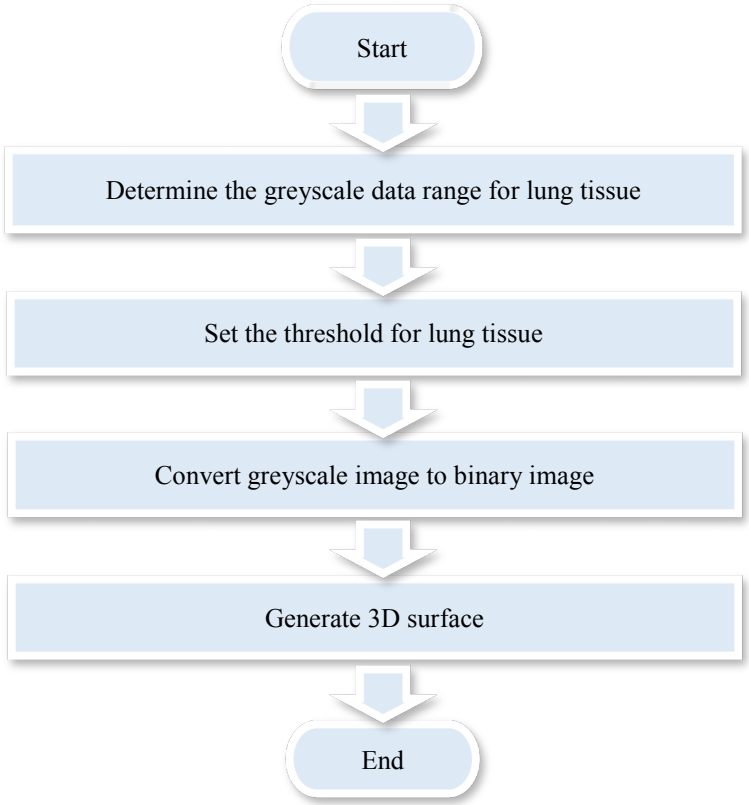

Figure 6.18. Simulation of 3D pulmonary image from MRI slices

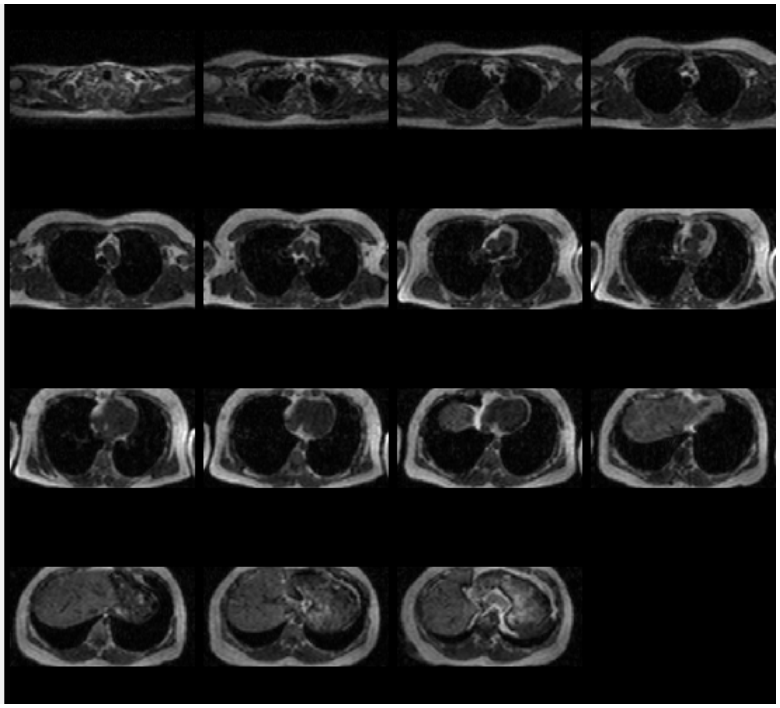

Figure 6.19 15 MRI slices of the thorax

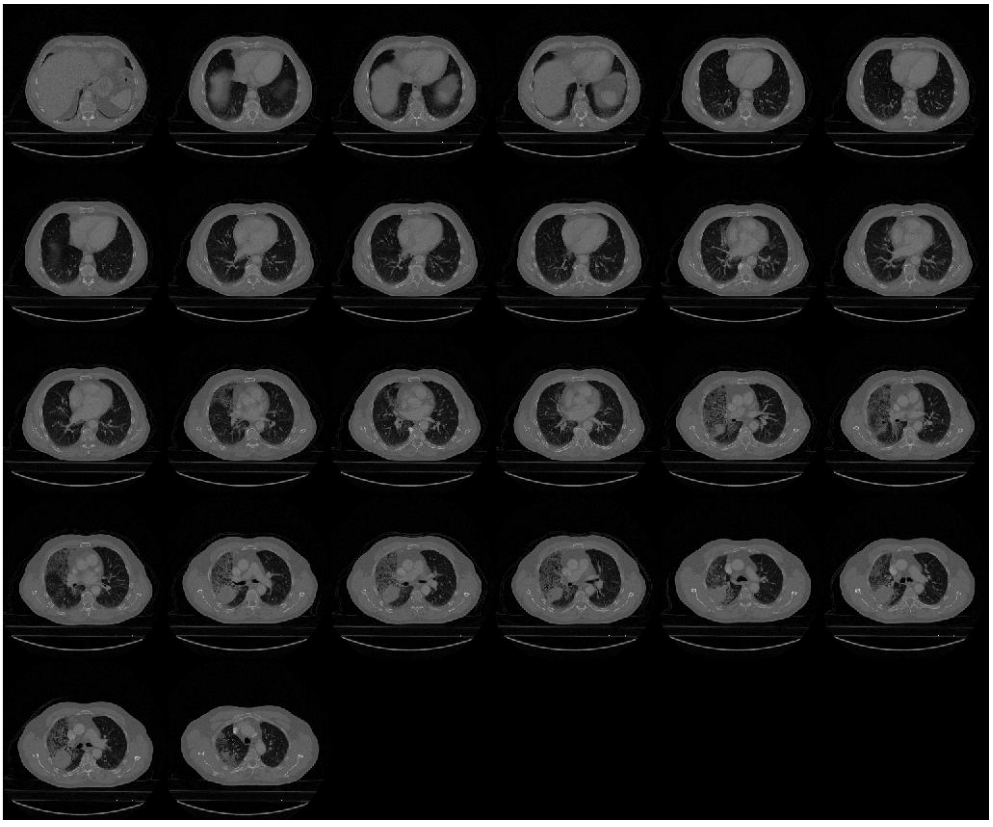

Figure 6.20. 26 CT slices of the thorax

The threshold range for lung tissue is then determined by selecting the minimum and maximum values from the greyscale images which represents lung tissues. Table 6.5 shows the data range in greyscale, the minimum and the maximum values used to identify lung tissues. Images with updated threshold values are then converted into binary images. Pixel areas of the images which are contained within the greyscale threshold range are converted to '1' (white), while pixel areas which were outside of the threshold range are converted to '0' (black). The largest areas are selected to remove unrelated tissues and the final images are converted back to greyscale to retain original features of the images (see Figures 6.21 and 6.22). Connecting points on 2D slices are then merged to create a 3D surface image as seen in Figures 6.23 and 6.24.

Table 6.5. Lung tissue threshold ranges

DICOM type	Number of images	Image resolution	Greyscale range	Lung tissue	
				Minimum	Maximum
MRI	15	256x256	0-4575	25	630
CT	26	512x512	0-2895	13	959

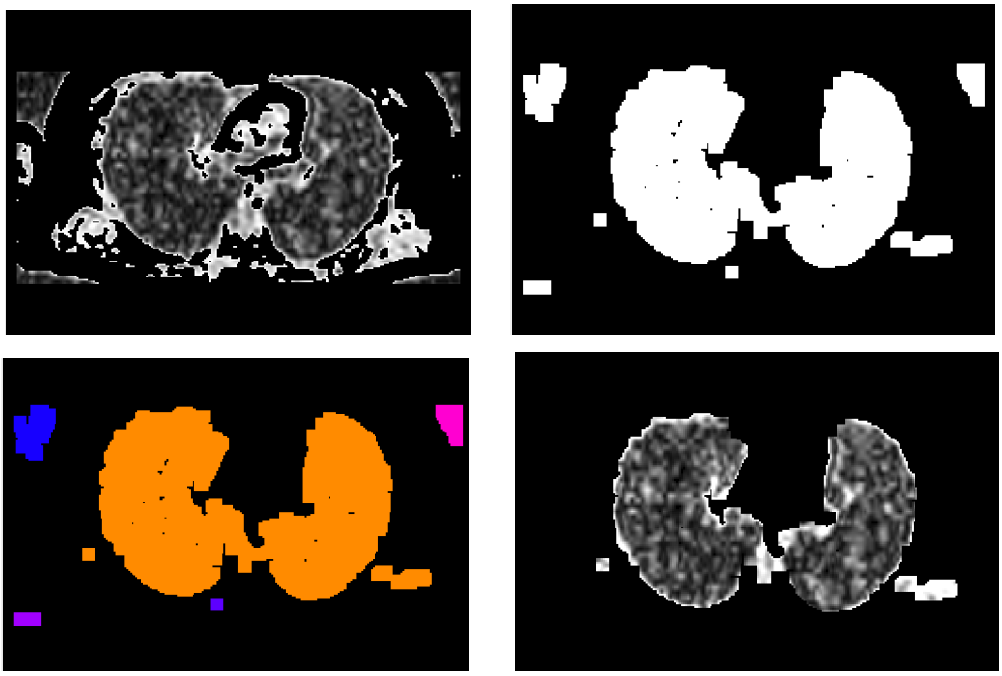

Figure 6.21 MRI sample image. (With applied threshold (top left), image after binary conversion (top right), binary image for selection of largest area (bottom left) and filtered image in greyscale (bottom right))

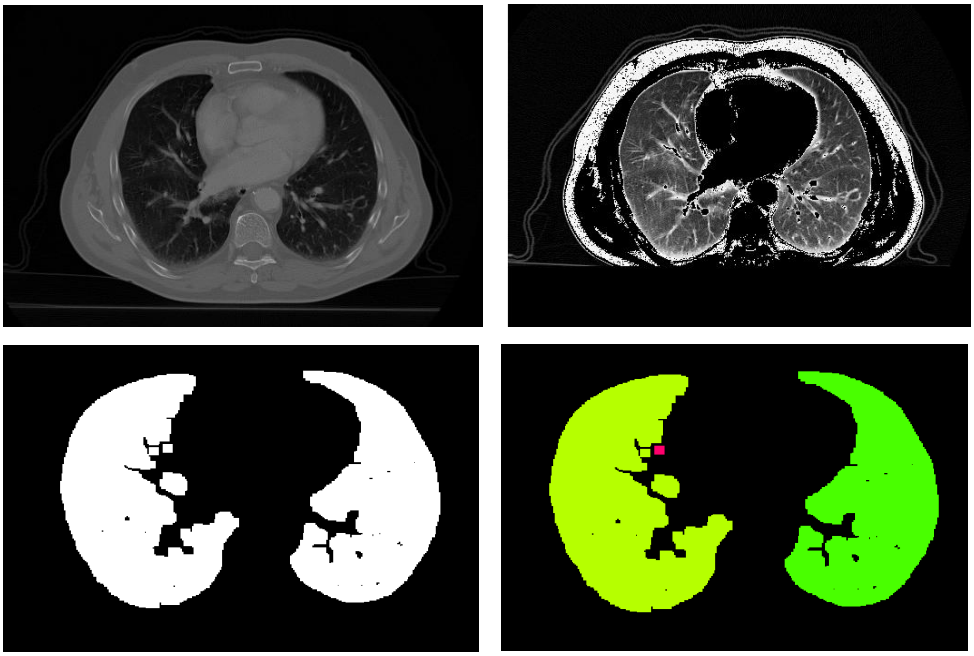

Figure 6.22 CT sample image. (CT original image (top left), with applied threshold (top right), image after binary conversion, (bottom left), and binary image for selection of largest area (bottom right)).

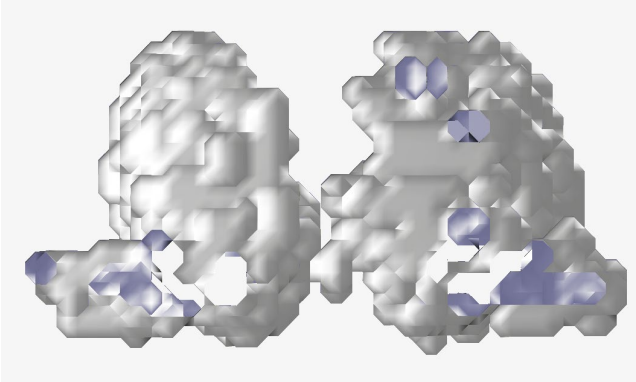

Figure 6.23. Generated 3D lung image from MRI slices

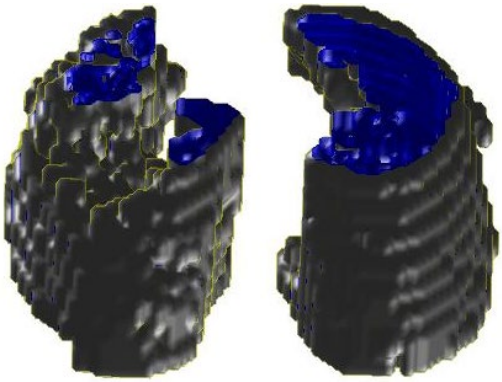

Figure 6.24. Generated 3D lung image from CT slices

As seen from Figures 6.23 and 6.24, the integrity of 3D images is dependent on the resolution of the original DICOM slices and the number of slices available. The set of 15 images with a resolution of 256x256 produced a less precise 3D representation of the lungs when compared to the set of 26 images with a resolution of 512x512. The lower pixel quantity also produced larger artefacts as the greyscale data of lungs were undistinguishable from some surrounding tissues since the pixels values for lungs and some surrounding tissues had similar greyscale values.

6.4.1 Lung Volume Estimation from Magnetic Resonance and Computed Tomography Images

From the DICOM metadata file, useful information was extracted to estimate the lung volume. Both sets of MRI and CT images were used to estimate the total lung volume. Table 6.6 shows the information obtained from the metadata for set 1 (15 MRI slices) and set 2 (26 CT slices). Lung volume was estimated based on the area of lungs obtained from the binary images, denoted as the region of interest (ROI), multiplied by the number of slices and slice thickness. Figure 6.25 shows the flowchart for the lung volume estimation. It is also worth noting that the respiration phase (inspiration or expiration), the volume at the end of inspiration (maximum inspiration or tidal breathing), or if the volunteers were holding their breath when these images were taken were unknown, and the resulting volume can only be verified with a volume measuring instrument such as a spirometer (Mohamad-Samuri *et al*., 2011). An estimation of the area of ROI in the binary image of the i^{th} MRI or CT slice, Y_i, can be determined by its pixel equivalent area X_i, multiplied by the calibration factor, Q, which is the ratio of reconstruction area (mm^2) to reconstruction area in pixels. The estimated i^{th} slice volume, V_i is determined by the area of slice, Y_i multiplied by the slice thickness, W. The estimated total volume, V_T is the sum of all slice volumes, n

$$Yn = X*Q, \tag{6.15}$$

$$Q = \text{reconstruction area in } mm^2/\text{reconstruction area in pixel}, \tag{6.16}$$

$$V_i = Y_i * W \tag{6.17}$$

$$V_T = \sum_{i=1}^{n} V_i \tag{6.18}$$

Table 6.6. Information on image metadata

Information	Set 1 (MRI Images)	Set 2 (CT Images)
Slice thickness, H	6mm	6mm
Reconstructed image diameter	465mm	465mm
Reconstruction area in mm^2	169,822.7mm^2	169,822.7mm^2
Reconstruction in pixel	256x256 = 65536	512x512 = 262,144
Calibration factor, Q	2.591	0.6478
Length of thorax on MRI	6mm x 15 slices = 90mm	6mm x 26 slices = 156mm

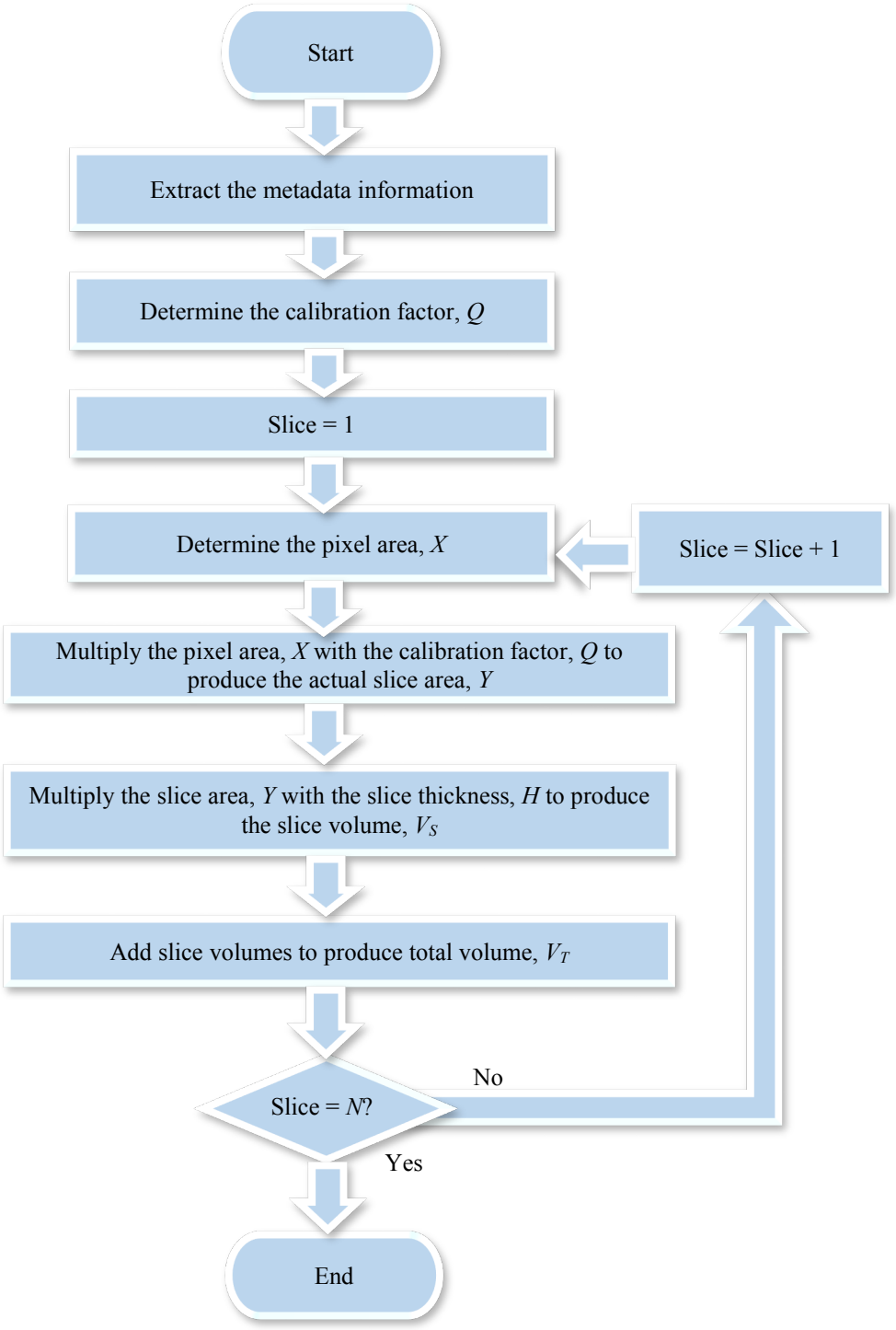

Figure 6.25. Flowchart for lung volume estimation from metadata information

The ROI in pixel area, X was determined by finding the amount of 'on' pixels in a binary image. The binary image shown in Figure 6.21, is the 7th slice taken from the MRI set, and has a total of 13907 'on' pixels representing the lung tissue, seen as white portions in the image. The estimated area, Y is determined by multiplying X with the calibration factor, Q = 2.591. This calibration factor will vary depending on the resolution of the image and the actual reconstruction diameter of the MRI machine. By multiplying the pixel area with the calibration factor, this image has an estimated area, Y of 36033mm^2. The estimated slice volume is Y multiplied by the slice thickness, H = 6mm, therefore producing the slice volume, V_S equivalent to 216198mm^3. By finding the sum of all slice volumes, an estimate of the total lung volume, V_T was made. The estimated total lung volume, V_T for the images contained in the MRI set was therefore 2579880mm^3 or 2579.88ml. The total estimated lung length shown in the MRI was 90mm. Figure 6.26 shows the relationship between the estimated lung area in mm^2 and slice number. The lung area appears to increase with the number of slices and shows a reduction in the estimated area between the 7th and 10th slice.

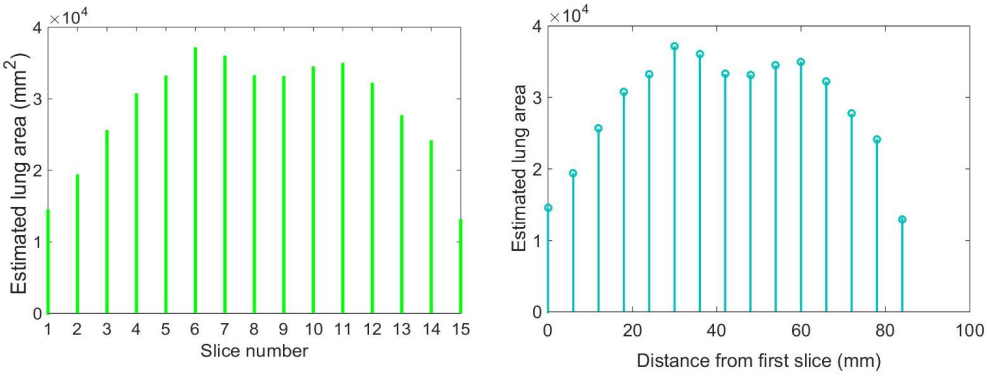

Figure 6.26 Estimated lung area and MRI slice number

It is worth noting that the estimated total volume is dependent on whether the MRI imaging captured the entire region of the thorax. If this is not the case, an extrapolation of the estimated lung was made to ensure all areas of the lung were accounted for. Linear regression was performed (see Figure 6.27) to determine the relationship between the lung area of each slice and the distance of each slice from the first MRI slice. The first equation included all areas up to the largest lung area, i.e. positive slope (slices 1 to 6), and the second equation included the areas starting from the largest lung area to the last slice, i.e. negative slope (slices 6 to 15).

$$A = 761.2x + 15381, (R^2 = 0.98) \quad (6.19)$$

$$A = -334.7x + 39674, (R^2 = 0.69) \quad (6.20)$$

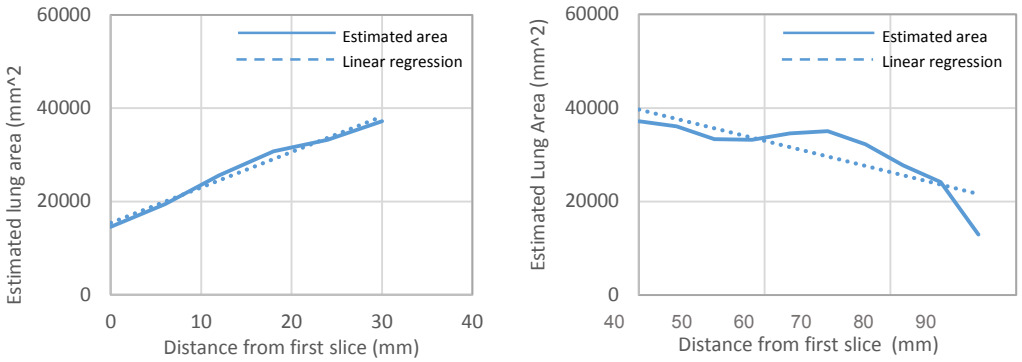

Figure 6.27. Linear Regression. (Slice 1 to 6 (left), and slice 6 to 15 (right)).

Equations 6.19 and 6.20 were used to extrapolate the lung area outside the MRI region until the area produced approaches zero or starts to become a negative value. The total lung volume can now be determined by adding the lung volume from 15 MRI slices and the extrapolated lung volume, which equals 3,273.43ml. This approach produced a total lung length of 168mm. A 2nd order polynomial regression analysis was also done resulting in the following equation (refer Figure 6.28):

$$A = -12.10x^2 + 1034x, (R^2 = 0.93) \quad (6.21)$$

Equation 6.21 was used to extrapolate the lung area outside the 15 MRI slice with an estimated total lung volume of 3,150.18ml and a lung length of 132mm. Table 6.7 shows the comparison of lung volumes for 15 MRI slices from metadata information, linear regression and 2nd order regression.

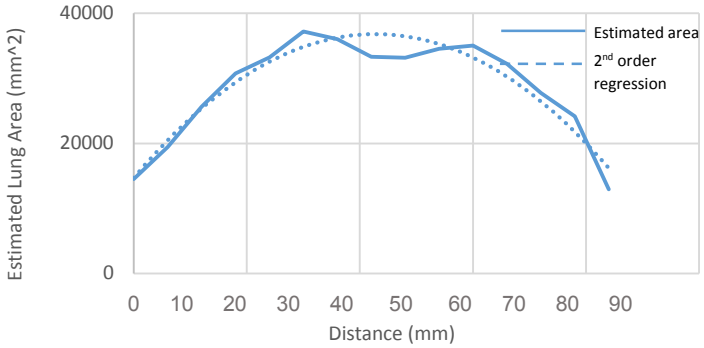

Figure 6.28. 2nd order polynomial regression for set of MRI images

Table 6.7 Comparison of lung volume estimation for MRI set images

Lung volume estimation method	Lung length (mm)	Lung volume (ml)
15 MRI slices only	90	2588
15 MRI slices + linear regression	168	3273.43
15 MRI slices + 2nd order regression	132	3150.18

The estimated total lung volume from 26 CT slices was 2220.97ml and the estimated lung length is 156mm. Figure 6.29 shows the relationship between the slice area in mm^2 and the slice number. The lung area increased from the first slice until the 7th slice before dipping slowly until the last slice. Linear regression analyses were carried out for the positive and for the negative slopes (see Figure 6.30) producing the following equations:

$$A = 451.2x + 1404.2, \ (R^2=0.78) \quad (6.22)$$

$$A = -88.93x + 15899, \ (R^2 = 0.97) \quad (6.23)$$

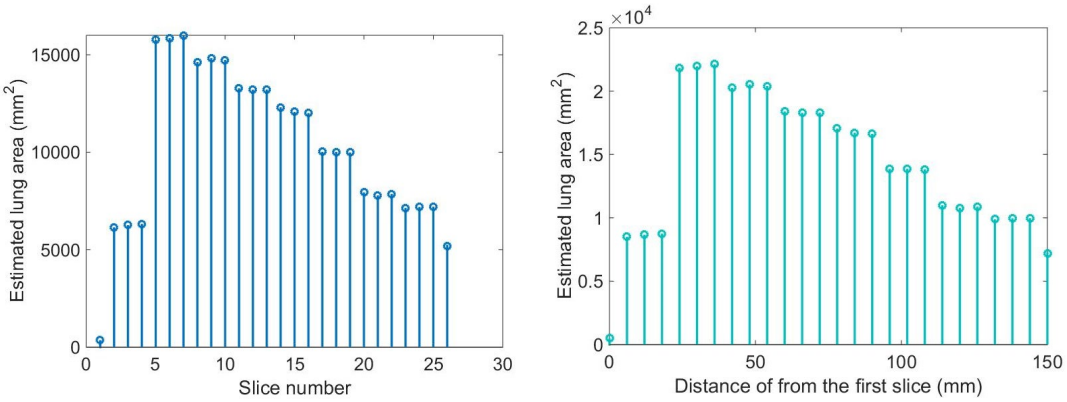

Figure 6.29 Estimated lung area of CT image. (Slice number (left) and distance (right))

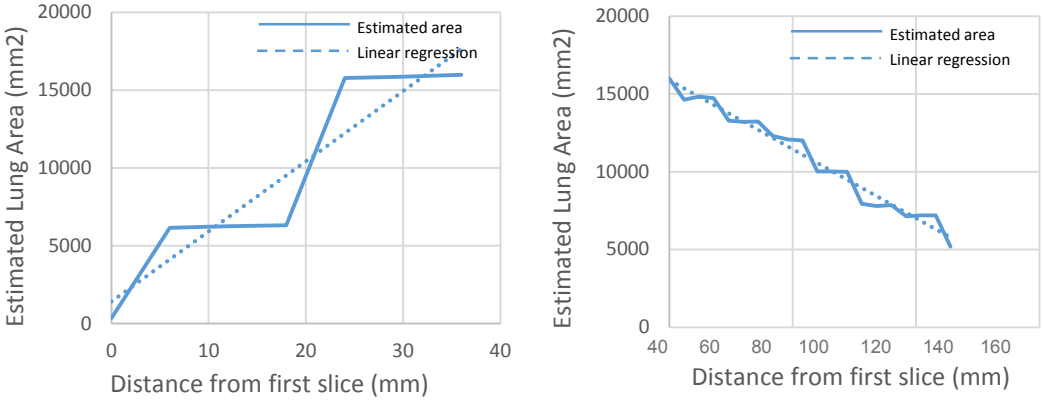

Figure 6.30. Linear regression of CT images. (Positive slope (left), negative slope (right))

Extrapolation of equation 6.23 produced a value that is less than zero (negative value), and thus was not accounted for. The extrapolated lung volume was added to the estimated lung volume from the CT images. This produced a total lung volume of 2223.84ml and total lung length of 180mm. A second order polynomial regression analysis was also done to estimate the total lung volume (see Figure 6.31).

$$A = -1.65x^2 + 229.04x + 5707.4, \ (R^2 = 0.60) \tag{6.24}$$

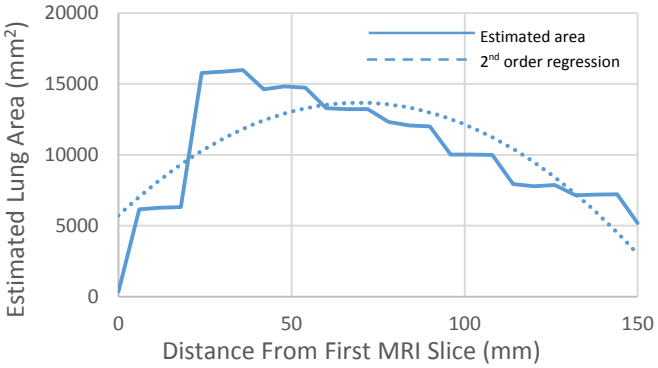

Figure 6.31. 2nd order polynomial regression analysis for set of CT images

By adding the extrapolated lung volumes from equation (6.24) to the lung volume calculated using CT slices only, the total lung volume was estimated at 1891.55ml and the total lung length of 216mm. Table 6.8 shows the comparison for the estimation of the total lung volume for the 26 CT slices from the metadata information, the linear regression equation and the 2nd order regression equation.

Table 6.8 Comparison of lung volume estimation for CT set images

Lung Volume Estimation	Lung Length (mm)	Lung volume (ml)
26 MRI Slices Only	156	2220.97
26 MRI slices & linear regression	216	2223.84
26 MRI slices & 2nd order regression	216	1891.55

6.5 Summary

The hardware for a 16-electrode Electrical Impedance Tomography (EIT) system was proposed in this chapter. The system was able to generate a small oscillating signal with a frequency range between 10 kHz and 250 kHz which will be sufficient for EIT measurement of the lungs. Once measurements on the human subject are completed, the resulting measured voltages and resistivity can then be compared to the MK3.5 EIT system for validation. A suitable image reconstruction algorithm must also be decided to represent the EIT data into 2D and 3D images of the lungs during the respiration process. Also presented in this chapter is a simple 3D imaging of the lungs using image processing from MRI and CT images of the thorax. An approach to calculate the lung volume from the MRI and CT images was also proposed. The images used were retrospective and should in future be validated with actual volume measurements.

Chapter 7

Conclusions and Recommendations for Future Work

A new SOPAVent blood gas model was proposed in the previous chapters through the modelling of Kd and VCO_2 and shunt sub-components. A simplified blood gas prediction system was also proposed to model PaO_2, $PaCO_2$ and pH using ventilator settings as system inputs. An EIT measurement system was developed for monitoring of pulmonary functions. Finally, 3D images of the lungs were produced from 2D MRI and CT medical images, and an estimation of lung volume was also made from 2D MRI and CT images. In this chapter, the summary of achievements of this project will be presented first, followed by recommendations for future work to be potentially undertaken.

7.1 Summary And Achievements

7.1.1 Improvements of the SOPAVent Model and Validation with Real Patient Data

The SOPAVent is a mathematical approach towards modelling of ventilated patients, which was developed by the Sheffield Biomedical Research Group. However, certain sub-components of SOPAVent are not available through routine ICU measurements. These sub-components were either estimated or modelled using data driven approach. In this thesis, the models for relative dead-space (Kd), carbon-dioxide production (VCO_2) and shunt were improved to increase the prediction accuracy of SOPAVent.

The Interval Type-2 Fuzzy Logic System (IT2FLS) was used to design the Kd, VCO_2 and shunt model of artificially ventilated patients in the ICU. The type-1 Fuzzy C-means (FCM) clustering algorithm was also used to design the Kd model and the VCO_2 model. The IT2FLS and type-1 FCM models were optimized using the 'new structure' particle swarm optimization (nPSO) to improve prediction accuracy. The Kd, VCO_2 and shunt models were then validated using real minute-by-minute ICU data. Prediction results show significant improvements in accuracy for the Kd and the VCO_2 sub-components when compared to previously develop models.

The Kd, VCO_2 and shunt models were integrated into the SOPAVent blood gas model for predicting the arterial blood gases (ABG), using real minute-by-minute ICU patient data for validation. Validated results show significant improvements in accuracy for the initial prediction of $PaCO_2$, the initial prediction of pH and the post-setting-change prediction of pH. The SOPAVent model with the Kd and the VCO_2 sub-components designed using IT2FLS showed better generalization property and robustness when compared to the previous model, while the SOPAVent model with the Kd and the VCO_2 sub-components design using type-1 FCM showed equal performances when compared to the previous model.

The SOPAVent model was applied to newly obtained ICU patient data, where patients were diagnosed with Faecal Peritonitis (FP), and data was available on an hourly basis. The initial prediction of PaO_2, the post-setting change prediction of PaO_2, the initial prediction of pH and the post-setting-change predication of pH produced some improvements in accuracy and reduced error when compared to the previously developed model.

7.1.2 Blood Gas Modelling using Ventilator Settings

The ICU data for patients with Faecal Peritonitis (FP) were also used to model the ABG parameters of PaO_2, $PaCO_2$ and pH using the relationship of ventilator settings to blood gas sampling results. The type-1 fuzzy FCM nPSO-optimised model and the adaptive neuro-fuzzy inference system (ANFIS) were proposed to model the ABG from ventilator settings. These two models were successful in reducing the

number of variables needed to model the blood gases when compared to the original SOPAVent model. Both models produced good predictions with minimal errors.

7.1.3 Hardware Development for Electrical Impedance Tomography Measurement System

An integrated and compact 16-electrode EIT measurement system was developed with the aim of measuring the electrical surface potentials of the thorax during respiration process. The proposed EIT system was able to produce a small alternating current with a frequency range suitable for pulmonary applications. The EIT system comprises of a voltage controlled oscillator (VCO) to generate the initial alternating voltage signal, a band-pass filter to remove noise, a voltage to current converter (VCC) to convert the filtered voltage into current, a multiplexing circuit to drive current and to measure the surface voltages, a demodulator and an analogue to digital converter (ADC) to convert the analogue voltages into digital values. The EIT system is integrated with a microcontroller which performs the signalling functions for the multiplexing circuitry and also performs transmission of the EIT data to a computer for further processing. The EIT system is smaller in size and lighter compared to existing modular EIT systems, thus it has the potential to be a portable, non-invasive bedside monitoring tool for ICU patients.

7.1.4 Three-dimensional Images of the Lungs and Lung Volume Estimation From Two-dimensional Medical Images

A simple rendering method for producing three dimensional (3D) lung images from retrospective two-dimensional (2D) MRI and CT medical images of the human thorax was proposed. The tissues representing the lungs were identified by selecting a suitable greyscale range from the MRI and CT images. Simulation results show that the quality and the integrity of the 3D images produced were dependent on the resolution and the number of slices of the original 2D MRI and CT images. An approach to calculating the lung volume from the MRI and the CT images was also

discussed. Simulations performed showed that the lung volumes generated by medical images were similar to the lung volumes generated by the combination of medical images and regressions lines when the number of medical images were higher. However, the images were retrospective and were not validated with standard lung volume measurements techniques.

7.2 Recommendation for Future Work

The cardiac output (CO) in the SOPAVent model was estimated using the Body Surface Area (BSA), which was derived from the patient's height and weight. This approach provided a more patient-specific estimation of CO when compared to using the population mean CO. However, it is highly possible that patients with similar BSA will produce contrasting CO values due to factors such as age, existing physical conditions and the severity of illnesses. In future, a data-driven model can also be elicited for CO estimations. By improving the CO sub-component, the prediction accuracy for SOPAVent can further be enhanced.

The newly obtained ICU data for FP patients were recorded on an hourly basis instead of minute-by-minute basis such as in the previous ICU patient data. This data was slightly problematic as there was no way to determine when the exact change in ventilator setting was made, and if more than a single change was made during the one hour period for a particular ventilator setting. Currently, efforts are being undertaken by the consultants at the Sheffield Royal Hallamshire Hospital to extract the minute-by-minute data from the same group of patients, which can later be used to validate the SOPAVent model.

The EIT system should first be tested on phantom experiments and later measurements from human subjects should be completed. The resulting voltages can then be compared to existing EIT systems such as the MK3.5 EIT system for validation. The estimation of lung impedance, the lung volume and the lung density can then be derived from the EIT measurements. A suitable image reconstruction approach should also be proposed to display the EIT measurements into 2D and 3D images of the lungs.

References

Adler A, Arnold JH, Bayford R, Borsic A, Brown B, Dixon P, Faes TJC, Frerichs I, Gagnon H, Gärber Y, Grychtol B, Hahn G, Lionheart WRB, Malik A, Patterson RP, Stocks J, Tizzard A, Weiler N and Wolf GK, (2009). GREIT: a unified approach to 2D linear EIT reconstruction of lung images. Physiol Meas. Vol. 30(6):35–55

Allerød C, Rees SE, Rasmussena BS, Karbing DS, Kjærgaard S, Thorgaard P and Andreassen SA, (2008). Decision support system for suggesting ventilator settings: Retrospective evaluation in cardiac surgery patients ventilated in the ICU. Computer Methods and Programs in Biomedicine. Vol. 92: 205-212

Al-Otaibi HM and Hardman JG, (2011), Prediction of arterial oxygen partial pressure after changes in FIO2: validation and clinical application of a novel formula. British Journal of Anaesthesia. Vol. 107(5):806–12

Annual quality report 2013/14 for adult, general (ICU, ICU/HDU) critical care, https://onlinereports.icnarc.org/Home, last accessed 2017/11/17

Brown BH, (2003), Electrical impedance tomography (EIT): a review, J. Med. Eng. Technol. Vol. 27(3):97-108

Brown BH and Seagar AD, (1987), The Sheffield data collection system, Clin. Phys. Physiol. Meas. Suppl. A:91-7

Brown BH, Barber DC and Seagar AD, (1985), Applied potential tomography: possible clinical applications. Clin. Phys. Physiol. Meas. Vol. 6(2):109-121

Brown BH, Milnes P, and Mills GH, (2007), Indirect measurement of lung density and air volume from Electrical Impedance Tomography (EIT) data. World Congress on Medical Physics and Biomedical Engineering IFMBE Proceedings. Vol. 14

Brown BH, Primhak RA, Smallwood RH, Milnes P, Narracott AJ and Jackson MJ, (2002), Neonatal lungs – can absolute lung resistivity be determined non-invasively? Medical and Biological Engineering & Computation. Vol. 40:338-394

Brown BH, Wilson AJ, and Bertemes-Filho P, (2000), Bipolar and tetropolar transfer impedance measurements from volume conductor. Electronics Letter. Vol. 36(25):2060-2062

Brown B.H., 2003, Electrical impedance tomography (EIT): a review, J Med. Eng. Technol., vol.27, no.3, pp.97-108, 2003.

Cheney M, Isaacson D and Newell JC, (1999), Electrical impedance tomography. SIAM Rev 41:85–101

Chiu, SL (1994), Fuzzy Model Identification Based on Cluster Information. Journal of Intelligent and Fuzzy Systems. Vol. 2:267-278.

Denaï M, Mahfouf M and Mills GH, (2008), Modelling and simulation of electrical impedance tomography (EIT) on ventilated patients with ARDS lungs. Proceeding for the 8th IEEE International Conference on Bioinformatics and Bioengineering.

Denaï M, Mahfouf M, Mohamad-Samuri S, Panoutsos G, Brown BH, and Mills GH, (2010), Absolute electrical impedance tomography (aEIT) guided ventilation therapy in critical care patients: Simulations and future trends. IEEE Transactions on Information Technology in Biomedicine. Vol. 14(3): 641-649

Fan W, Wang H, Chen X and, Lv Z, (2009), Three dimensional EIT models for human lung reconstruction based on Schur CG algorithm. Proceedings for the International Conference on Complex Medical Engineering (ICME)

Fleming S, Thompson M, Stevens R, Heneghan C, Pluddemann A, Maconochie I, Tarassenko L and Mant D, (2013), Normal ranges of heart rate and respiratory rate in children from birth to 18 years, a systematic review of observational studies. The Lancet. Vol. 337(9970):1011-1018

Goode KM (2000), Model based development of a fuzzy logic advisor for artificially ventilated patients, PhD thesis, the University of Sheffield

Gore JC (2003), Principles and practice of functional MRI of the human brain, The Journal of Clinical Investigation, the American Society for Clinical Investigation. 112(1): 4-9

Graham BM and Adler A (2007), Electrode placement configurations for 3D EIT, Physiological Measurement. Vol. 28:29–44

Holder DS, (2004), Electrical impedance tomography: Methods, history and applications. Institute of Physics Publishing. ISBN: 0750309520

hopentextbc.ca/anatomyandphysiology/chapter/23-1-overview-of-the-digestive-system/ (accessed at 1600hrs on 03/03/2018)

Hospital adult critical care activity 2015-2016. (NHS Website address: https://digital.nhs.uk/catalogue/PUB23426), last accessed 2017/11/17.

Hwang C, and Hung-Hoon F (2007), Uncertain fuzzy clustering: interval type-2 fuzzy approach to C-means. IEEE Transaction on Fuzzy Systems. Vol. 15(1):107-120.

Indera-Putera SH and Mahfouf M, (2017), Evolutionary type-2 fuzzy blood gas models for artificially ventilated patients in ICU. 14th International Conference on Informatic in Control, Automation and Robotics

Indera-Putera SH, Mahfouf M, and Mills GH (2016), Blood-gas modelling for artificially ventilated patients using interval type-2 fuzzy logic system, XIV Mediterranean Conference on Medical and Biological Engineering and Computing

Javaherian A, Soleimani M and Moeller K, (2016), A fast time-difference inverse solver for 3D EIT with application to lung imaging. Med. Biol. Eng. Comput. Vol. 54:1243–1255

Khalighi M, Vosoughi Vahdat B, Mortazavi M And Mikaeili M, (2014), Design and implementation of precise hardware for electrical impedance tomography (EIT). IJST Transactions of Electrical Engineering. Vol. 38(E1):1-20

Kretschmer J, Riedlinger A, Schranz C and Möller K (2014), Medical decision support in mechanical ventilation employing combined model information of gas exchange and respiratory mechanics. 19th World Congress, the International Federation of Automatic Control (IFAC)

Kwok HF, Linkens DA, Mahfouf M and Mills GH (2004a), SIVA: A hybrid knowledge-and-model-based advisory system for intensive care ventilators. IEEE Transactions on Information Technology in Biomedicine. Vol. 8(2): 161-172.

Kwok HF, Linkens DA, Mahfouf M, and Mills GH (2004b), Adaptive ventilator FiO2 advisor: use of non-invasive estimations of shunt. Artificial Intelligence in Medicine. Vol. 32: 157-169.

Kwok HF, Mills GH, Mahfouf M, and Linkens DA (2001), Model-based neuro-fuzzy control of FiO_2 for intensive care mechanical ventilation. Critical Care. Vol. 5(supp1):P002-S1.

Mendel JM (2001), Uncertain Rule-Based Fuzzy Logic Systems: Introduction and New Directions, Prentice-Hall.

Mendel JM, Hagras H, Tan W, Melek WW and Ying H (2014), Introduction to fuzzy type-2. IEEE Press Series on Computational Intelligence.

Mohammad-Samuri S, Mahfouf M, Denaï M, Ross JJ and Mills GH (2011), Absolute EIT coupled to a blood gas physiological model for the assessment of lung ventilation in critical care patients, Journal of Clinical Monitoring and Computing. Vol. 25(1):27-28.

Nopp P, Harris ND, Zhao TX, Brown BH, (1997), Model for the dielectric properties of human lung tissue against frequency and air content. Med. Biol. Eng. Comput. Vol. 35(6):695-702

Pulletz S, Matthias K, Elke G, Schadler D, Vogt B, Weiler N, and Frerichs I, (2012), Dynamics of regional lung aeration determined by electrical impedance tomography in patients with acute respiratory distress syndrome. Multidisciplinary Respiratory Medicine 7:44

Rees SE, Allerød C, Murley D, Zhao Y, Smith BW, Kjærgaard S, Thorgaard P, and Andreassen S, (2006), Using physiological models and decision theory for selecting appropriate ventilator settings. Journal of Clinical Monitoring and Computing. Vol. 20:421–429

Riedel T, Richards T and Schibler A, (2005), The value of electrical impedance tomography in assessing the effect of body position and positive airway pressure on regional lung ventilation in spontaneously breathing subjects. Intensive Care Med. Vol. 31: 522-1528.

Rodriguez-Molinero A, Narvaiza L, Ruiz J and Galvez-Barron C, (2013), Normal respiratory rate and peripheral blood oxygen saturation in the elderly population. Journal of the American Geriatric Society. Vol. 61(12):2238-40

Sim I, Gorman P, Greenes RA, Haynes RB, Kaplan B, Lehmann H and Tang PC, (2001), Clinical decision support systems for the practice of evidence-based medicine. Journal of the American Medical Informatics Association. Vol. 8(6):527-534.

Stephenson DR, Davidson JL, Lionheart WRB, Grieve BD and York TA, (2005), Comparison of 3D image reconstruction techniques using real electrical impedance measurement data. 4th World Congress on Industrial Process Tomography

Tehrani FT and Roum JH (2208), Intelligent decision support systems for mechanical ventilation. Artificial Intelligence in Medicine. Vol. 44:171—182

Tridente A, Clarke GM, Walden A, McKenchnie S, Hutton P, Mills GH, Gordon AC, Holloway PA, Chiche JD, Bion J, Stuber F, Garrad C and Hinds CJ, (2014), Patients with faecal peritonitis admitted to European intensive care units: an epidemiological survey on the GenOSept cohort. Intensive Care Med. Vol. 40(20):201-10

Wang A, Panoutsos G, Mahfouf M and Mills GH, (2008), Goal-directed therapy for general ICU patients using aggregated multi-objective optimization. 17th World Congress, The International Federation of Automatic Control

Wang A, Mahfouf M, Mills GH, Panoutsos G, Linkens DA, Goode K, Kwok HF, and Denaï M, (2010a), Intelligent model-based advisory system for the management of ventilated intensive care patients: Part I: Hybrid blood gas patient model. Computer Methods and Program in Engineering. Vol. 99(2): 195-207.

Wang A, Mahfouf M, Mills GH, Panoutsos G, Linkens DA, Goode K, Kwok HF, and Denaï M, (2010b), Intelligent model-based advisory system for the management of ventilated intensive care patients: Part II: Advisory system design and evaluation. Computer Methods and Program in Engineering (2010). Vol. 99(2): 208-217.

Wilson AJ, Milnes P, Waterworth AR, Smallwood RH, and Brown BH, (2001), Mk3.5: a modular, multi frequency successor to the Mk3a EIS/EIT system, Physiological Measurement, Institute of Physics Publishing. Vol. 22(2001):49-54

Wu D, (2012), On the fundamental differences between interval type-2 and type-1 fuzzy logic controllers. IEEE Transaction on Fuzzy Systems. Vol. 20(5): 832-848.

Wu D, (2017) "A brief tutorial on interval type- 2 fuzzy sets and systems." https://sites.google.com/site/drwu09/publications/completepubs, accessed on 2017/12/04

Wu D and Mendel JM, (2009), Enhanced Karnik-Mendel algorithms. IEEE Transaction on Fuzzy Systems. Vol. 17(4):923-934.

Wu D and Mendel JM, (2014), Designing practical interval type-2 fuzzy logic system made simple, IEEE World Congress on Computational Intelligence, Beijing, China.

Wu D and Nie M, (2011), Comparison practical implementation of type-reduction algorithms for type-2 fuzzy sets and systems. IEEE International Conference on Fuzzy Systems

Yang F, Zhang J and Patterson R, (2013), Development of an anatomically realistic forward solver for thoracic electrical impedance tomography. Journal of Medical Engineering. Vol. 2013 article ID: 983938

Zhang Q and Mahfouf M, (2006), A new structure for particle swarm optimization (nPSO) applicable to single objective and multi-objective problems. 3rd International IEEE Conference Intelligent Systems

Appendix A

Fuzzy Rules for the IT2FLS Kd Model with 243 Rules

Y	UMF	LMF	Y	UMF	LMF	Y	UMF	LMF	Y	UMF	LMF
Y1	0	25	Y41	10.72	35.61	Y81	8	41	Y121	22.11	42.20
Y2	0.1	25.2	Y42	4.1	33.2	Y82	18.34	54.16	Y122	3.70	44.68
Y3	0.2	25.4	Y43	4.2	33.4	Y83	8.2	41.4	Y123	15.33	41.18
Y4	0.3	25.6	Y44	4.3	33.6	Y84	8.3	41.6	Y124	12.3	49.6
Y5	0.4	25.8	Y45	4.4	33.8	Y85	8.25	41.41	Y125	12.4	49.8
Y6	0.5	26	Y46	4.5	34	Y86	17.69	53.48	Y126	12.5	50
Y7	0.6	26.2	Y47	4.6	34.2	Y87	8.6	42.2	Y127	10.43	51.14
Y8	0.7	26.4	Y48	4.7	34.4	Y88	8.7	42.4	Y128	12.7	50.4
Y9	11.95	26.76	Y49	3.76	39.68	Y89	8.8	42.6	Y129	12.8	50.6
Y10	1.94	56.02	Y50	7.69	38.45	Y90	8.9	42.8	Y130	12.9	50.8
Y11	1	56	Y51	5	35	Y91	2.78	27.29	Y131	33.12	28.20
Y12	1.1	27.2	Y52	5.1	35.2	Y92	12.17	36.73	Y132	13.1	51.2
Y13	6.30	31.59	Y53	5.2	35.4	Y93	2.29	23.13	Y133	13.2	51.4
Y14	5.42	30.37	Y54	5.3	35.6	Y94	16.54	34.90	Y134	13.3	51.6
Y15	1.4	27.8	Y55	5.4	35.8	Y95	9.4	43.8	Y135	13.4	51.8
Y16	1.5	28	Y56	5.5	36	Y96	9.5	44	Y136	13.5	52
Y17	1.6	28.2	Y57	5.6	36.2	Y97	9.6	44.2	Y137	13.6	52.2
Y18	1.7	28.4	Y58	5.7	36.4	Y98	9.7	44.4	Y138	13.7	52.4
Y19	1.8	28.6	Y59	5.8	36.6	Y99	9.8	44.6	Y139	13.8	52.6
Y20	10.69	41.88	Y60	5.9	36.8	Y100	9.9	44.8	Y140	9.10	48.95
Y21	2	29	Y61	6	37	Y101	10	45	Y141	14	53
Y22	2.1	29.2	Y62	6.1	37.2	Y102	10.1	45.2	Y142	14.1	53.2
Y23	1.21	20.79	Y63	6.2	37.4	Y103	10.2	45.4	Y143	14.2	53.4
Y24	4.49	34.15	Y64	6.3	37.6	Y104	10.3	45.6	Y144	14.3	53.6
Y25	2.4	29.8	Y65	32.82	62.29	Y105	10.4	45.8	Y145	14.4	53.8
Y26	2.5	30	Y66	6.5	38	Y106	10.5	46	Y146	14.5	54
Y27	2.6	30.2	Y67	6.6	38.2	Y107	10.6	46.2	Y147	14.6	54.2
Y28	2.7	30.4	Y68	20.45	57.78	Y108	10.7	46.4	Y148	14.7	54.4
Y29	2.8	30.6	Y69	6.8	38.6	Y109	31.71	36.85	Y149	14.28	62.15
Y30	2.9	30.8	Y70	6.9	38.8	Y110	10.9	46.8	Y150	14.9	54.8
Y31	27.24	47.87	Y71	7	39	Y111	11	47	Y151	15	55
Y32	3.1	31.2	Y72	7.1	39.2	Y112	5.27	60.15	Y152	15.1	55.2
Y33	3.2	31.4	Y73	7.2	39.4	Y113	7.55	43.93	Y153	15.2	55.4
Y34	3.3	31.6	Y74	7.3	39.6	Y114	11.3	47.6	Y154	15.3	55.6
Y35	3.4	31.8	Y75	7.4	39.8	Y115	11.4	47.8	Y155	15.4	55.8
Y36	3.5	32	Y76	7.5	40	Y116	11.5	48	Y156	15.5	56
Y37	8.39	34.18	Y77	7.6	40.2	Y117	11.6	48.2	Y157	15.6	56.2
Y38	6.76	41.18	Y78	7.7	40.4	Y118	18.45	21.67	Y158	15.7	56.4
Y39	3.8	32.6	Y79	7.8	40.6	Y119	22.83	52.56	Y159	15.8	56.6
Y40	25	36.49	Y80	7.9	40.8	Y120	14.50	56.95	Y160	15.9	56.8

Y	UMF	LMF	Y	UMF	LMF	Y	UMF	LMF
Y161	16	57	Y201	20	65	Y241	24	73
Y162	16.1	57.2	Y202	20.1	65.2	Y242	24.1	73.2
Y163	20.07	24.57	Y203	27.91	47.64	Y243	24.2	73.4
Y164	16.3	57.6	Y204	23.86	49.22			
Y165	16.4	57.8	Y205	20.4	65.8			
Y166	16.5	58	Y206	20.5	66			
Y167	16.6	58.2	Y207	20.6	66.2			
Y168	16.7	58.4	Y208	20.7	66.4			
Y169	16.8	58.6	Y209	20.8	66.6			
Y170	16.9	58.8	Y210	20.9	66.8			
Y171	17	59	Y211	21	67			
Y172	17.1	59.2	Y212	21.1	67.2			
Y173	17.2	59.4	Y213	21.2	67.4			
Y174	14.96	40.86	Y214	21.3	67.6			
Y175	17.4	59.8	Y215	21.4	67.8			
Y176	17.5	60	Y216	21.5	68			
Y177	17.6	60.2	Y217	21.6	68.2			
Y178	17.7	60.4	Y218	21.7	68.4			
Y179	17.8	60.6	Y219	21.8	68.6			
Y180	17.9	60.8	Y220	21.9	68.8			
Y181	18	61	Y221	22	69			
Y182	18.1	61.2	Y222	22.1	69.2			
Y183	18.2	61.4	Y223	22.2	69.4			
Y184	18.3	61.6	Y224	22.3	69.6			
Y185	18.4	61.8	Y225	22.4	69.8			
Y186	18.5	62	Y226	22.5	70			
Y187	18.6	62.2	Y227	28.57	62.56			
Y188	18.7	62.4	Y228	22.7	70.4			
Y189	18.8	62.6	Y229	22.8	70.6			
Y190	18.9	62.8	Y230	22.9	70.8			
Y191	36.52	58.41	Y231	23	71			
Y192	19.1	63.2	Y232	23.1	71.2			
Y193	19.2	63.4	Y233	23.2	71.4			
Y194	19.3	63.6	Y234	23.3	71.6			
Y195	19.4	63.8	Y235	23.4	71.8			
Y196	19.5	64	Y236	23.5	72			
Y197	19.6	64.2	Y237	23.6	72.2			
Y198	19.7	64.4	Y238	23.7	72.4			
Y199	4.99	41.85	Y239	23.8	72.6			
Y200	34.64	47.68	Y240	23.9	72.8			

Appendix B1

FCM Generated Fuzzy Sets and Surface Plots for the Kd and the VCO_2 Sub-components

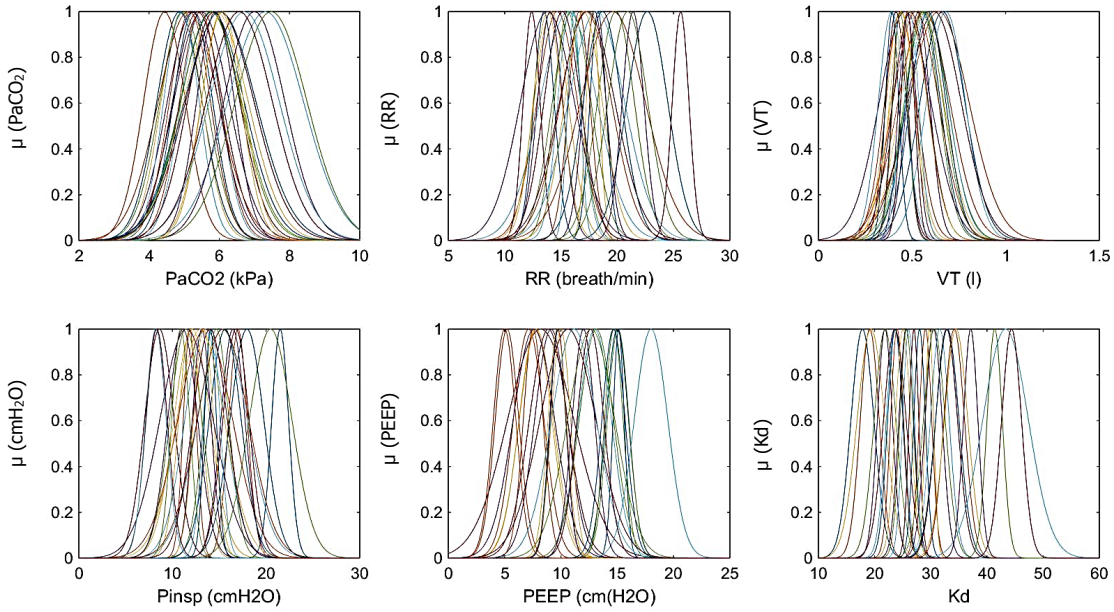

FCM generated fuzzy sets for the Kd model. Top: input parameters $PaCO_2$ and RR and VT. Bottom: input parameters Pinsp, PEEP and output parameter Kd.

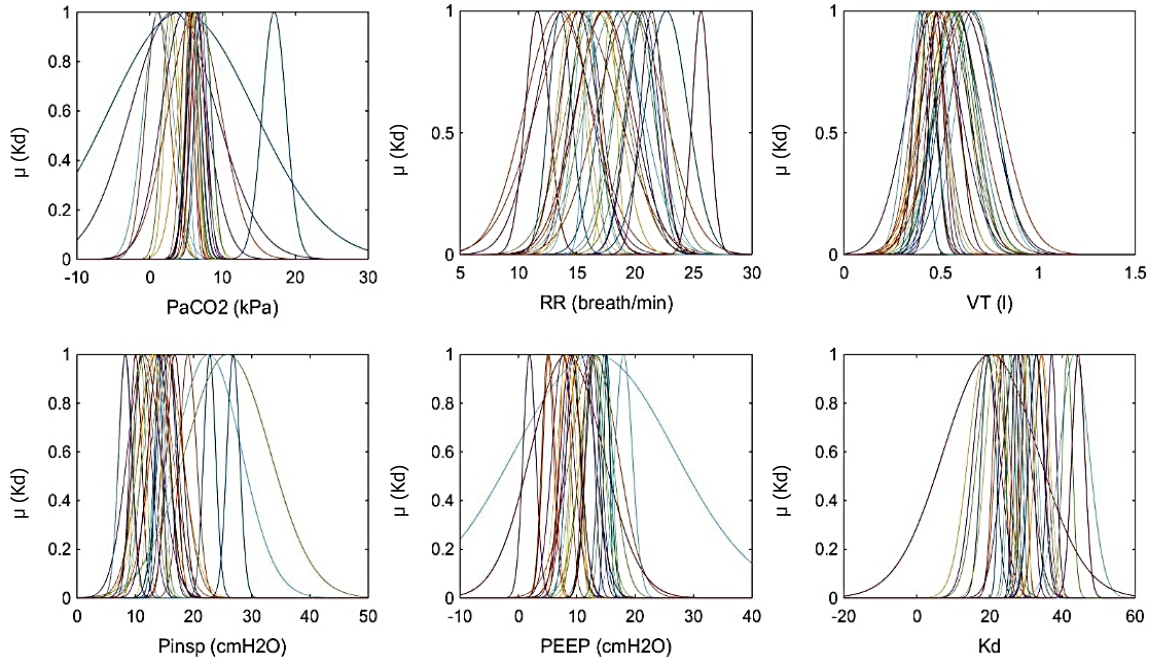

nPSO FCM generated fuzzy sets for the Kd model, based on least MSE. Top: input parameters $PaCO_2$, RR and VT. Bottom: input parameters Pinsp, PEEP and output parameter Kd.

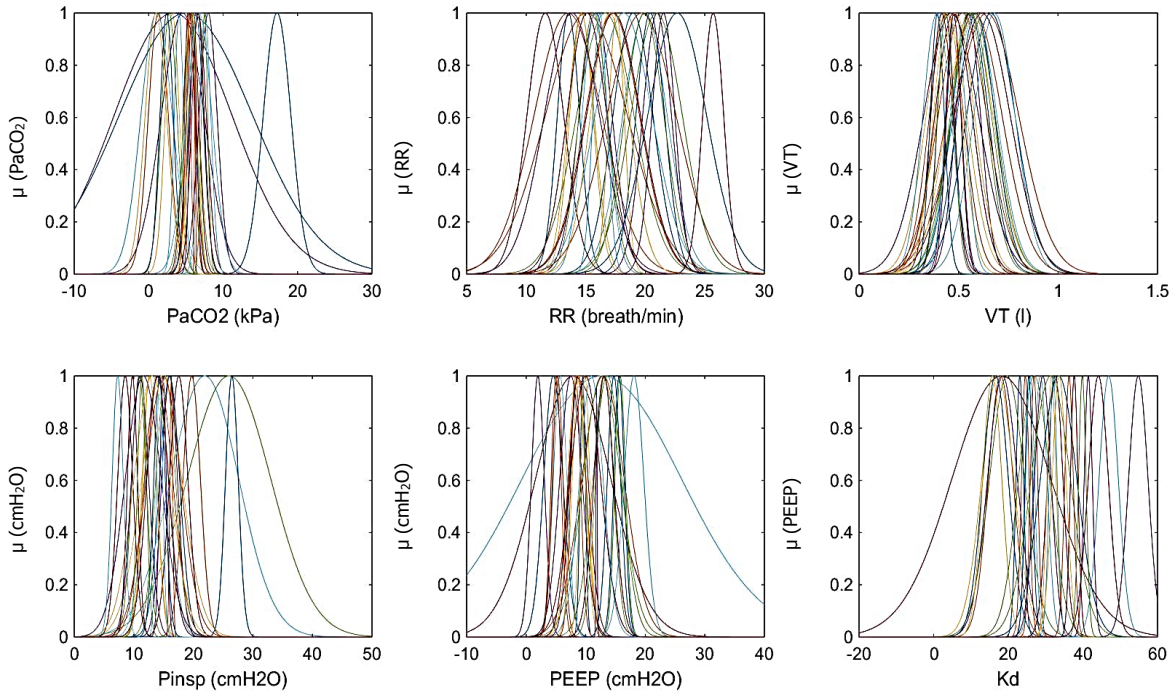

nPSO FCM generated fuzzy sets for the Kd model, based on largest R^2. Top: input parameters $PaCO_2$, RR and VT. Bottom: input parameters Pinsp, PEEP and output parameter Kd.

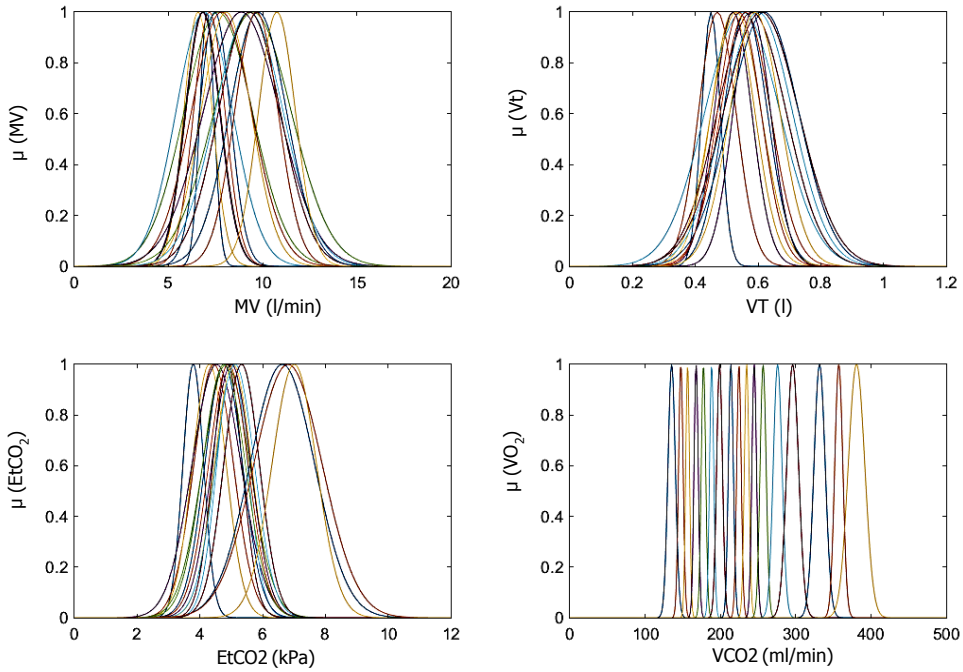

FCM generated fuzzy sets for the VCO_2 model. Top: input parameters MV and Vt. Bottom: input parameter $EtCO_2$ and output parameter VCO_2.

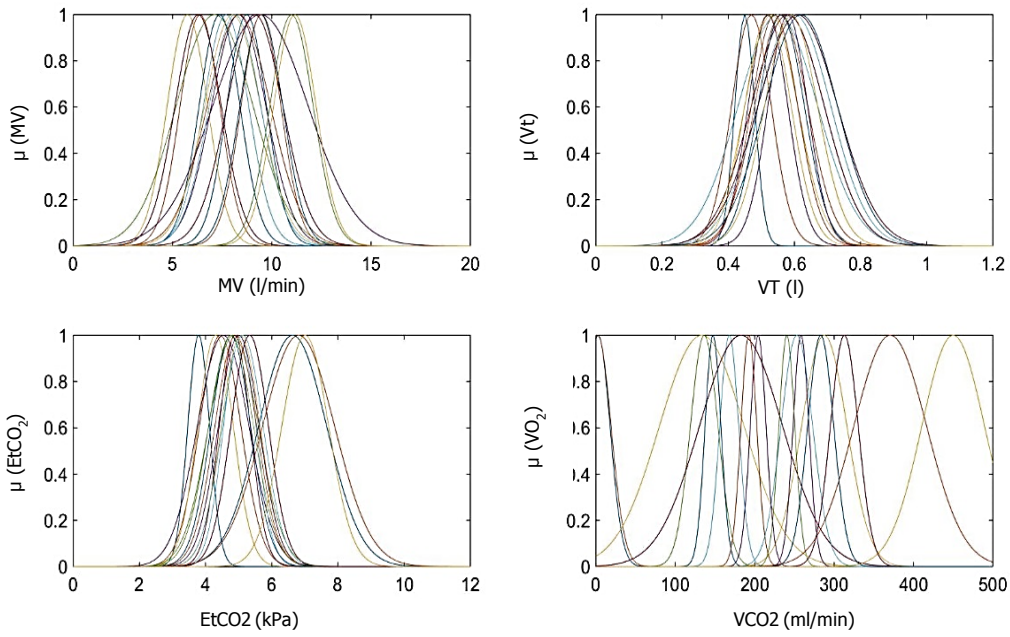

nPSO FCM generated fuzzy sets for the VCO_2 model based on least MSE. Top: input parameters MV and Vt. Bottom: input parameter $EtCO_2$ and output parameter VCO_2.

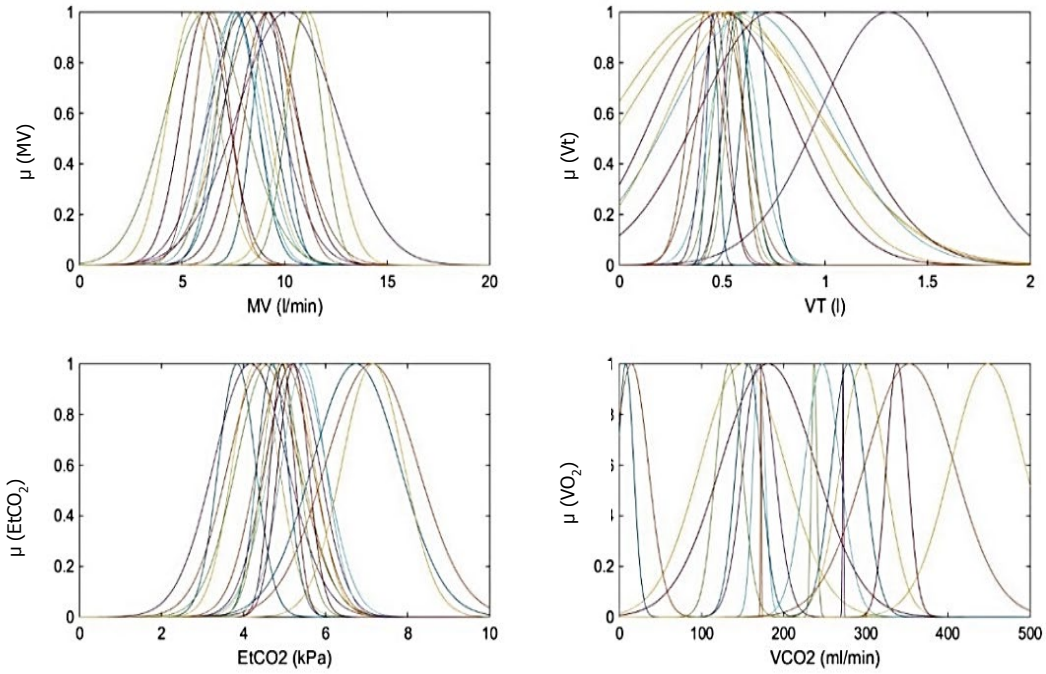

nPSO FCM generated fuzzy sets for the VCO_2 model, based on largest R^2. Top: input parameters MV and Vt. Bottom: input parameter $EtCO_2$ and output parameter VCO_2.

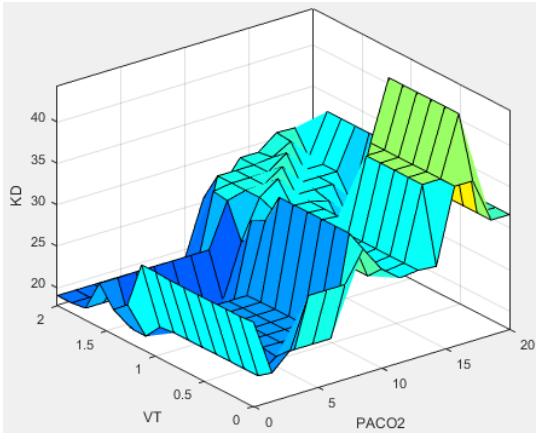

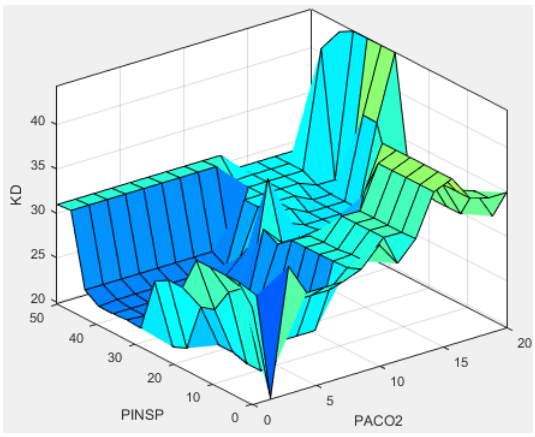

FCM generated fuzzy surface plot for the Kd model. Left: $PaCO_2$ and Vt against Kd. Right: $PaCO_2$ and Pinsp against Kd

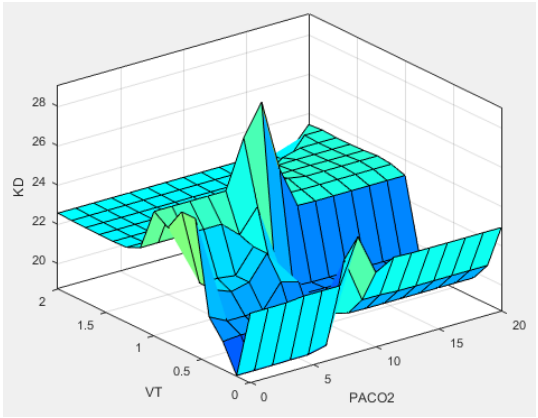

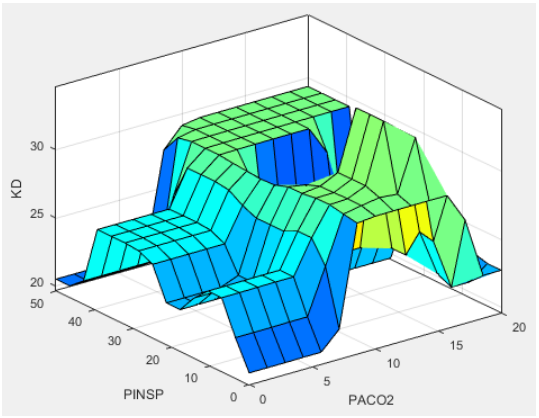

nPSO FCM generated fuzzy surface plot for the Kd model, based on least MSE. Left: $PaCO_2$ and Vt against Kd. Right: $PaCO_2$ and Pinsp against Kd.

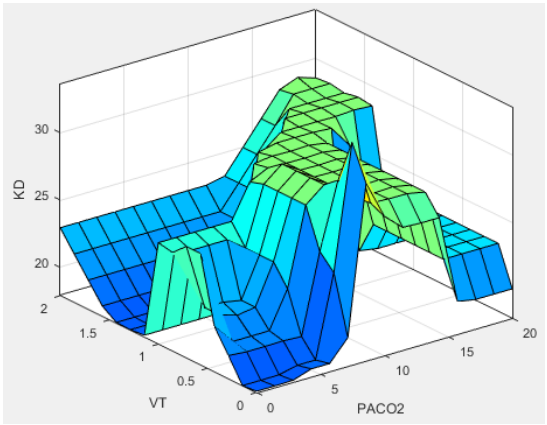

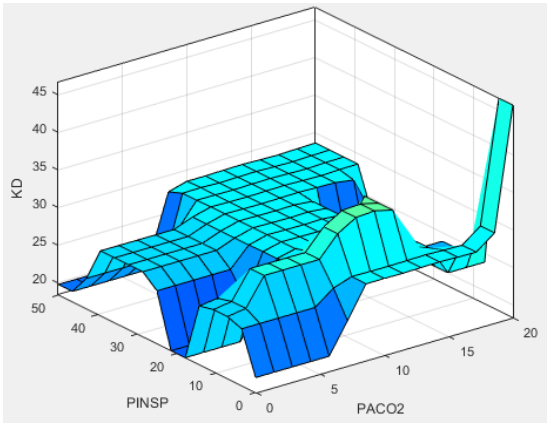

nPSO FCM generated fuzzy surface plot for the Kd, model based on largest R^2. Left: $PaCO_2$ and Vt against Kd. Right: $PaCO_2$ and Pinsp against Kd

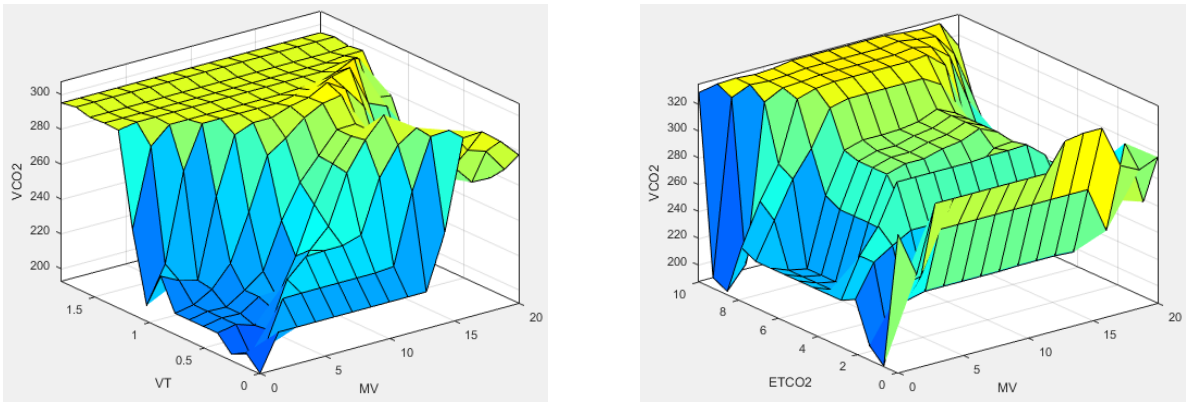

FCM generated fuzzy surface plot for the VCO_2 model. Left: MV and Vt against VCO_2. Right: MV and $EtCO_2$ against VCO_2.

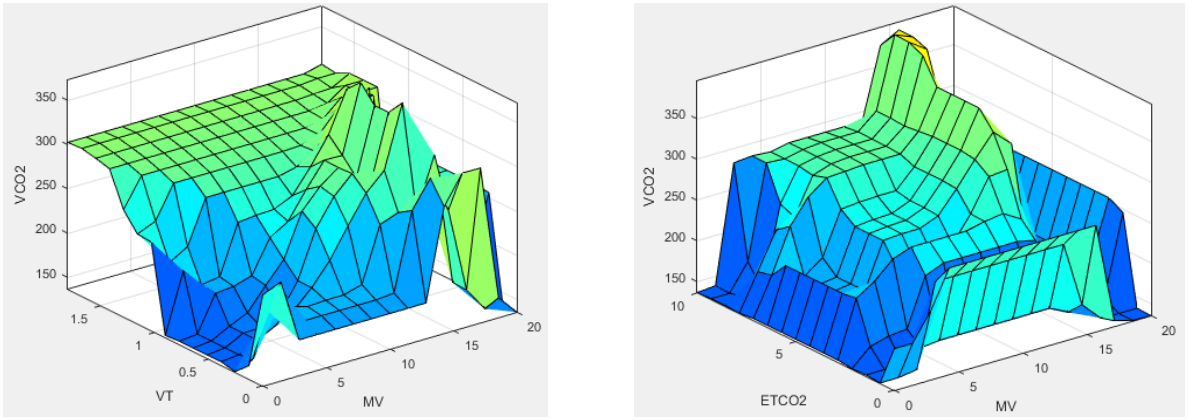

nPSO FCM generated fuzzy surface plot for the VCO_2 model based on least MSE. Left: MV and VT against VCO_2. Right: MV and $EtCO_2$ against VCO_2.

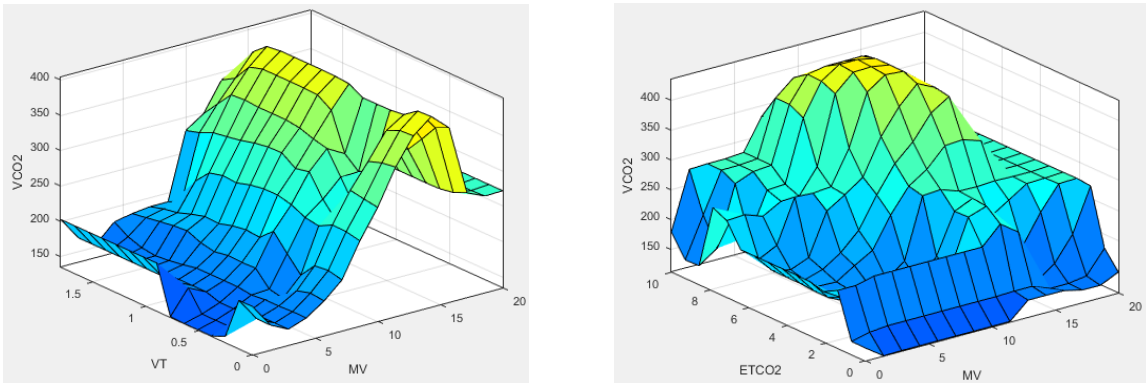

nPSO FCM generated fuzzy surface plot for the VCO_2 model, based on the largest R^2. Left: MV and VT against VCO_2. Right: MV and $EtCO_2$ against VCO_2.

Appendix B2

Prediction Results for Initial and Post-Setting Change Predictions of PaO_2, $PaCO_2$ and pH for SOPAVent Models

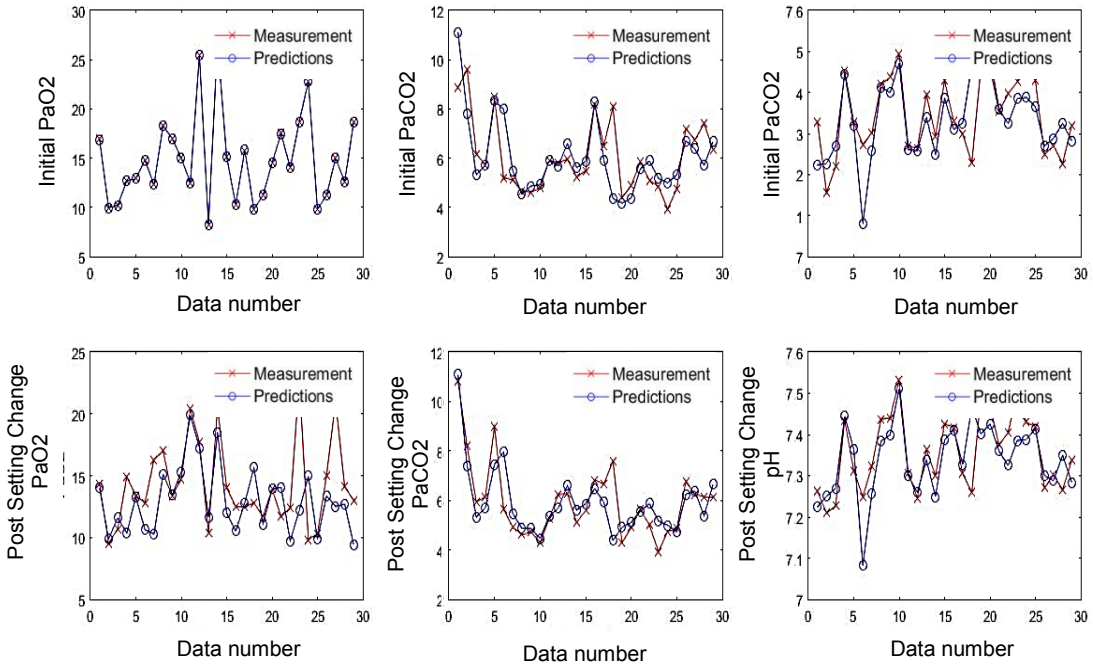

SOPAVent validation result: Kd (ANFIS), VCO2 (ANFIS), shunt (secant tuning)

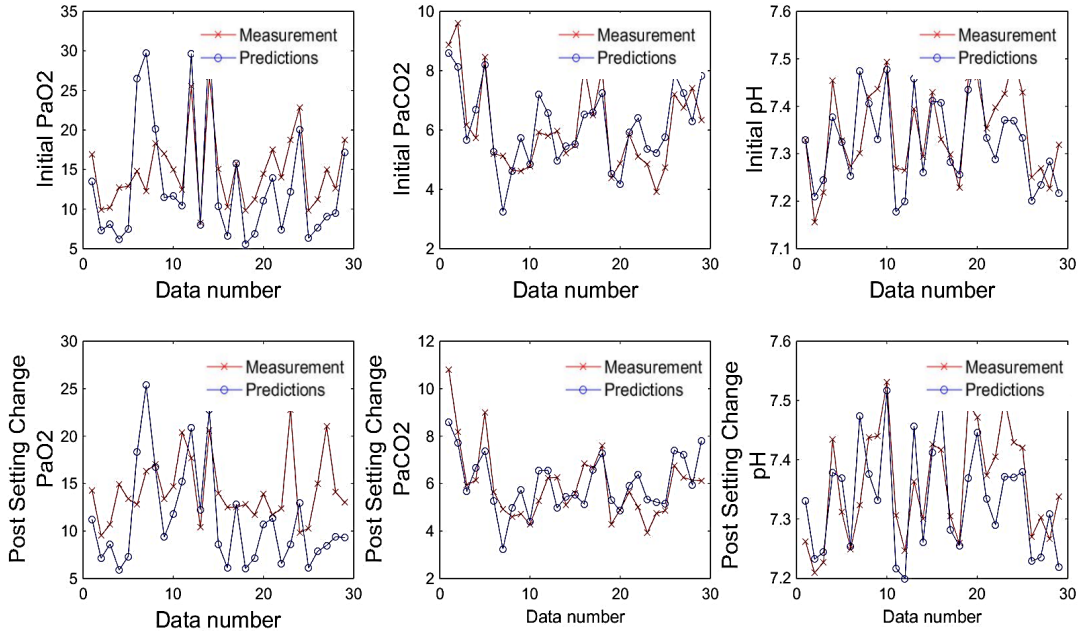

SOPAVent validation result: Kd (manually-tuned IT2FLS), VCO2 (manually-tuned IT2FLS), shunt (manually-tuned IT2FLS)

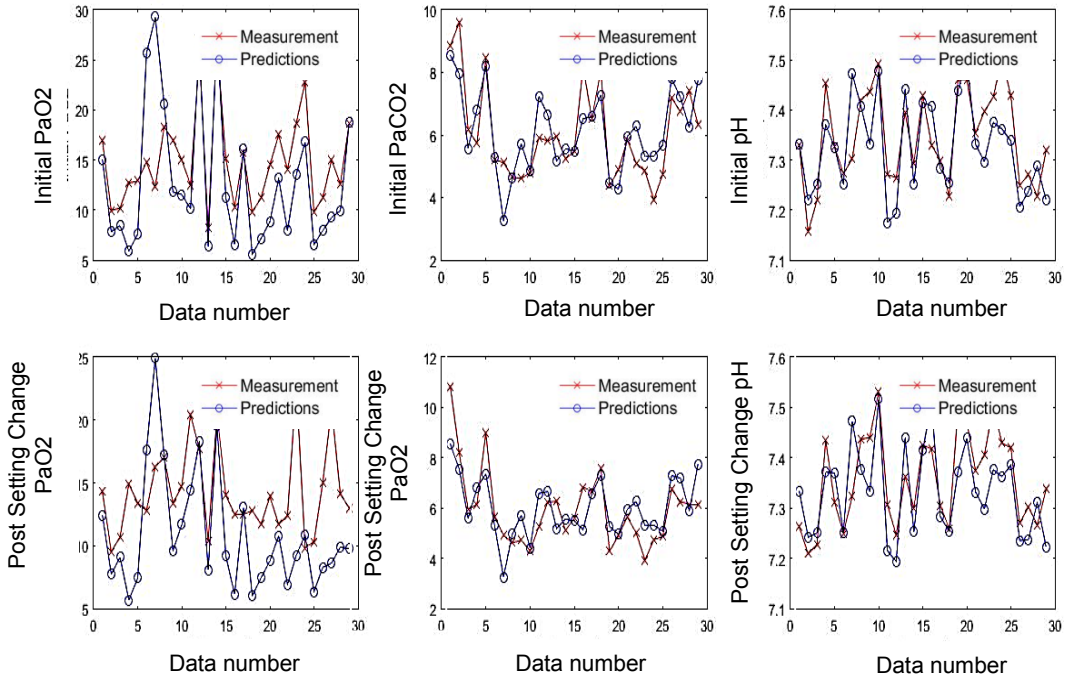

SOPAVent validation result: Kd (manually-tuned IT2FLS), VCO2 (manually-tuned IT2FLS), shunt (nPSO-tuned IT2FLS)

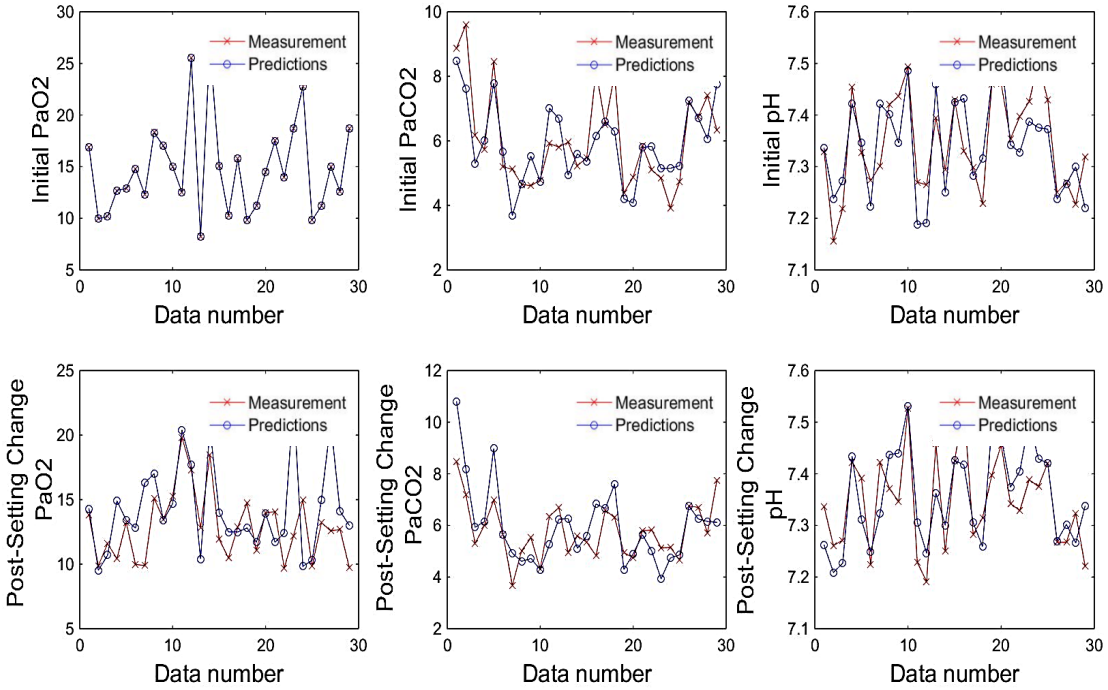

SOPAVent validation result: Kd (manually-tuned IT2FLS), VCO2 (manually-tuned IT2FLS), shunt (secant tuning)

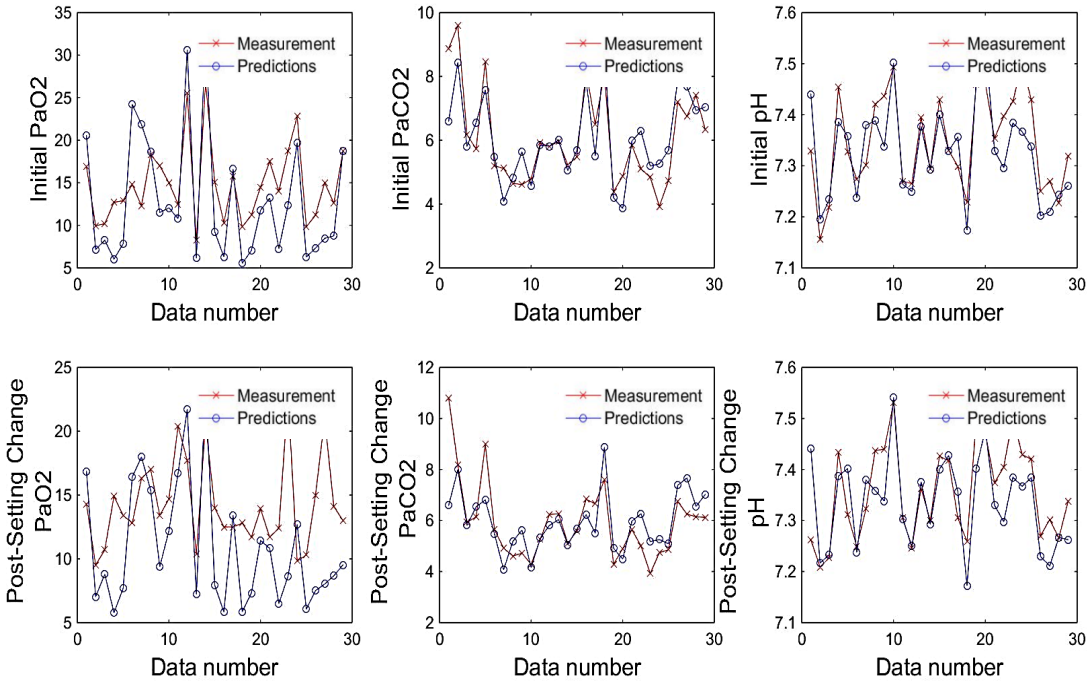

SOPAVent validation result: Kd (nPSO-tuned IT2FLS), VCO2 (nPSO-tuned IT2FLS), shunt (manually-tuned IT2FLS)

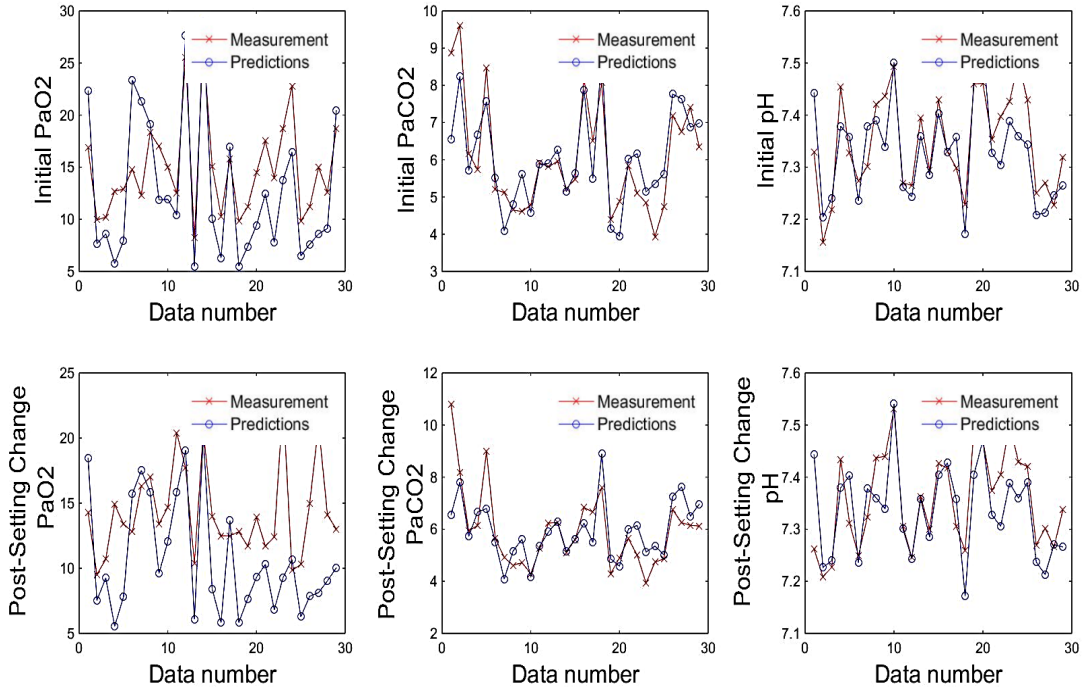

SOPAVent validation result: Kd (nPSO-tuned IT2FLS), VCO2 (nPSO-tuned IT2FLS), shunt (nPSO-tuned IT2FLS)

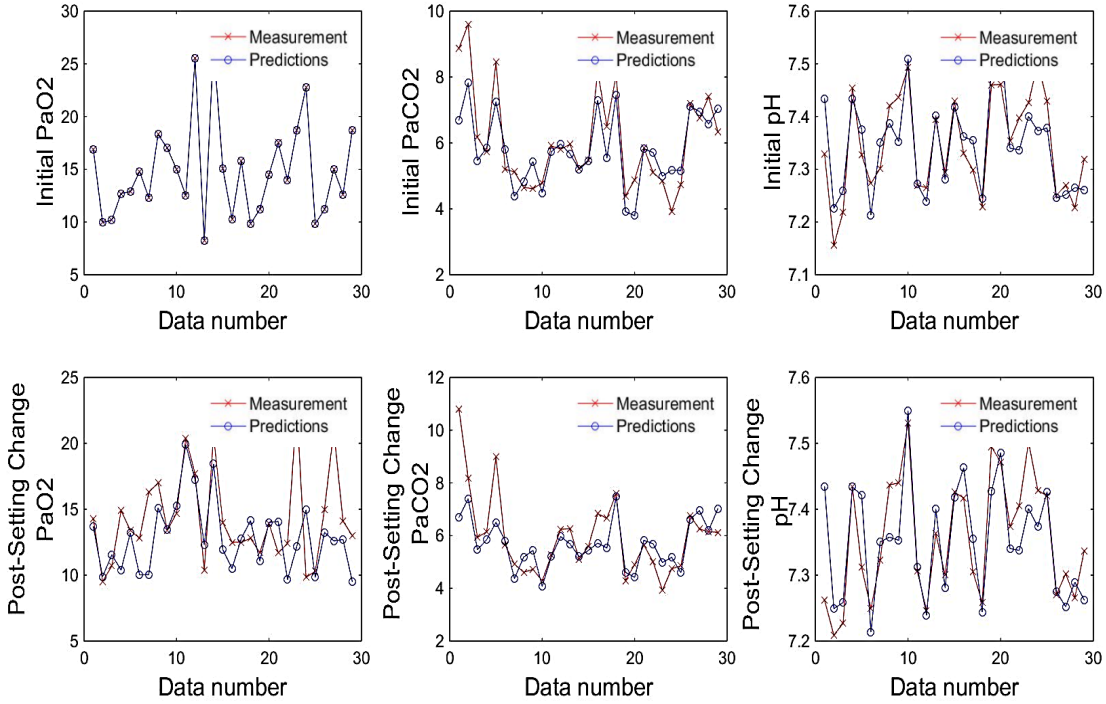

SOPAVent validation result: Kd (nPSO-tuned IT2FLS), VCO2 (nPSO-tuned IT2FLS), shunt (secant tuning)

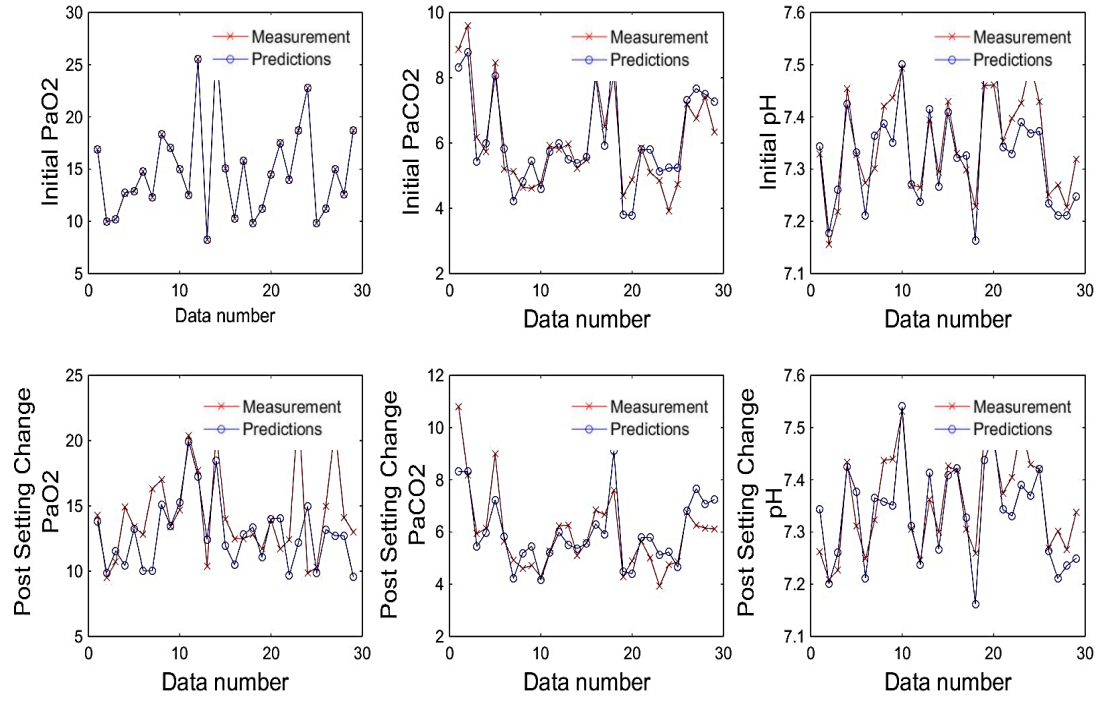

SOPAVent validation result: Kd (manually-tuned IT2FLS 243 rules), VCO2 (nPSO-tuned IT2FLS), shunt (secant tuning)

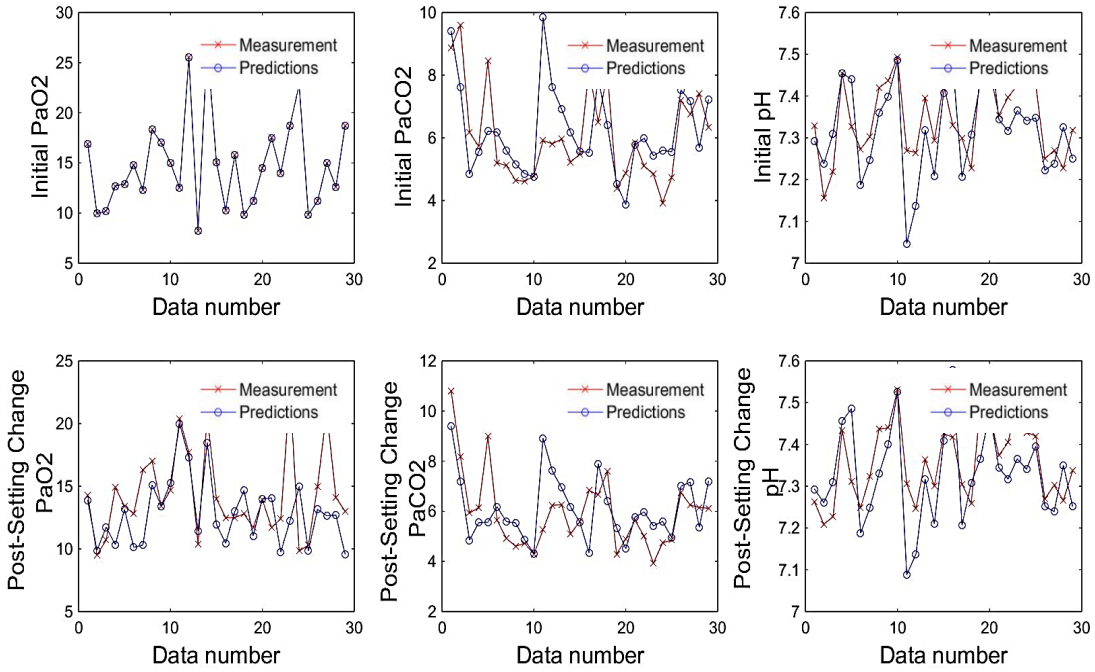

SOPAVent validation result: Kd (FCM), VCO2 (FCM), shunt (secant tuning)

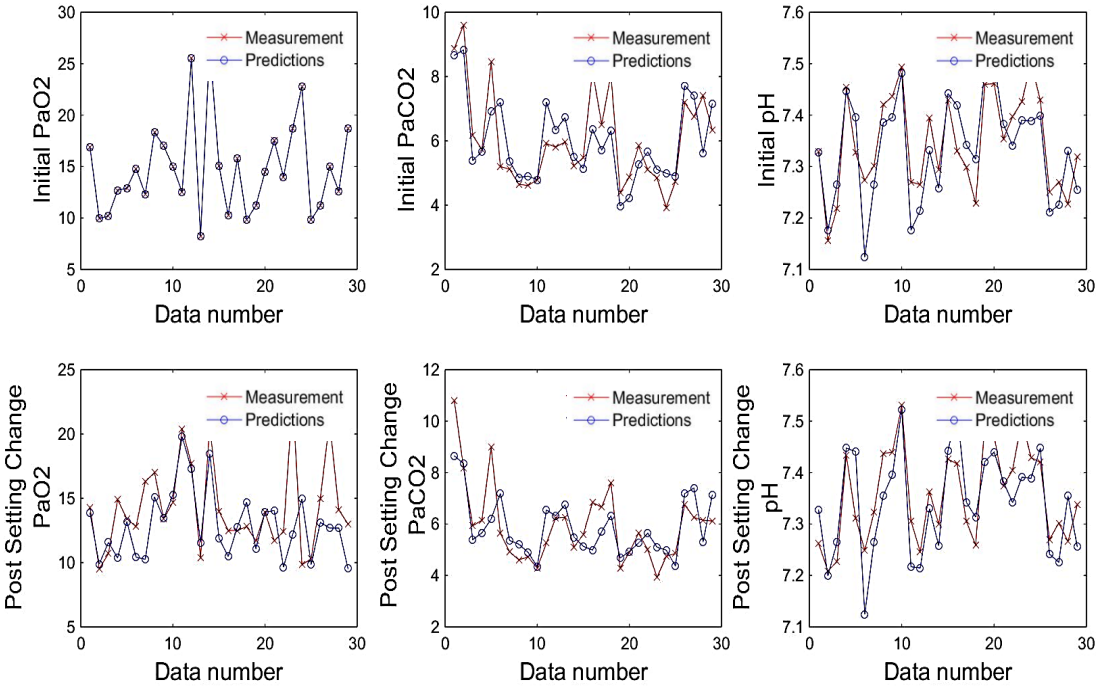

SOPAVent validation result: Kd (nPSo-MSE-tuned FCM), VCO2 (nPSO-MSE-tuned FCM), shunt (secant tuning)

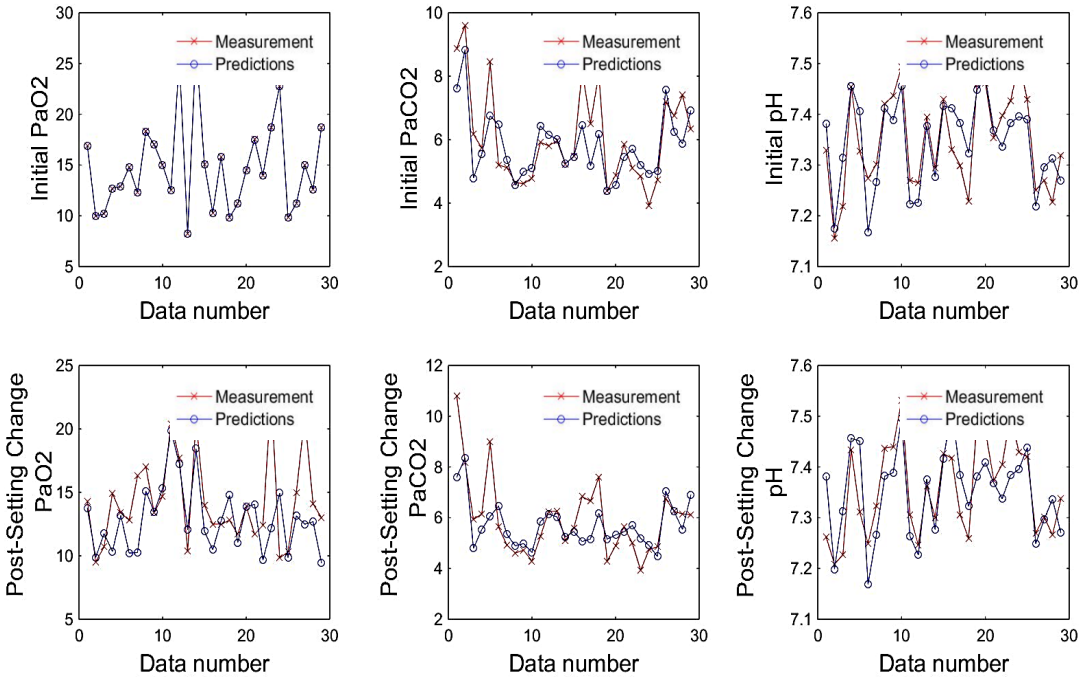

SOPAVent validation result: Kd (nPSo-R^2-tuned FCM), VCO2 (nPSO- R^2-tuned FCM), shunt (secant tuning)

Appendix C1

Summary of SOPAVent of other Input Parameters for FP Patients

SOPAVent Input Parameter	Mean	S.D.	Minimum	Maximum
BPd (mmHg)	57.03	9.09	37.5	73.5
BPm	76.04	12.12	50	98
BPs	114.05	18.18	75	147
IE exp	1.81	0.39	1.2	2.9
IE inp	1	0	1	1
Res	47.7	23.71	18.29	128.21
Tot RR	16.29	2.8	12	22
MV	8.96	2.96	4.68	16.4
VT	0.54	0.13	0.36	0.96
$EtCO_2$	5.03	0.9	3.5	6.6
PEEP	6.39	1.79	5	10
RR	16.18	2.8	12	22
FIO_2	40.89	9.46	29	68
PIP	28.5	7.56	19	44
SpO_2	97.19	4.5	77	100
Tinsp	1.37	0.24	1	1.7
Hba	87.36	13.02	66	123
HCO_3	2.63	0.48	1.79	3.9
SaO_2	98.24	1.42	93.5	99.8
new PEEP	6.39	1.79	5	10
new RR	16.07	2.69	12	22
new FIO_2	38.14	7.34	29	57
new PIP	28.29	7.9	16	44
new Tinsp	1.36	0.25	1	1.7
post VT	0.57	0.18	0.34	1.14
post Res	45.19	17.56	18.8	112.78
post $EtCO_2$	4.9	0.84	3.6	7
post MV	9.23	3.02	4.76	15.96
BodyTemp	36.53	1.04	34.6	38.8

(BPd: diastolic blood pressure, BPm: mean blood pressure, BPs: systolic blood pressure, IE exp: expiration IE ratio, IE insp: inspiration IE ratio, Res: airway resistance, Tot RR: total respiration rate, MV: minute volume, VT: tidal volume, $EtCO_2$: end-tidal carbon-dioxide, PEEP: positive end expiratory pressure, RR: respiration rate, FiO_2: fraction of inspired oxygen, PIP: peak inspiratory pressure, SpO_2: oxygen saturation (indirect measurement), Tinsp: inspiration time, Hba: haemoglobin, HCO_3: bicarb, SaO_2: oxygen saturation (blood gas), new/post: values after settings change, BodyTemp: body temperature.)

Appendix C2

Prediction Results for Initial Predictions of PaO_2, $PaCO_2$ and pH for SOPAVent Models for Patients with Faecal Peritonitis

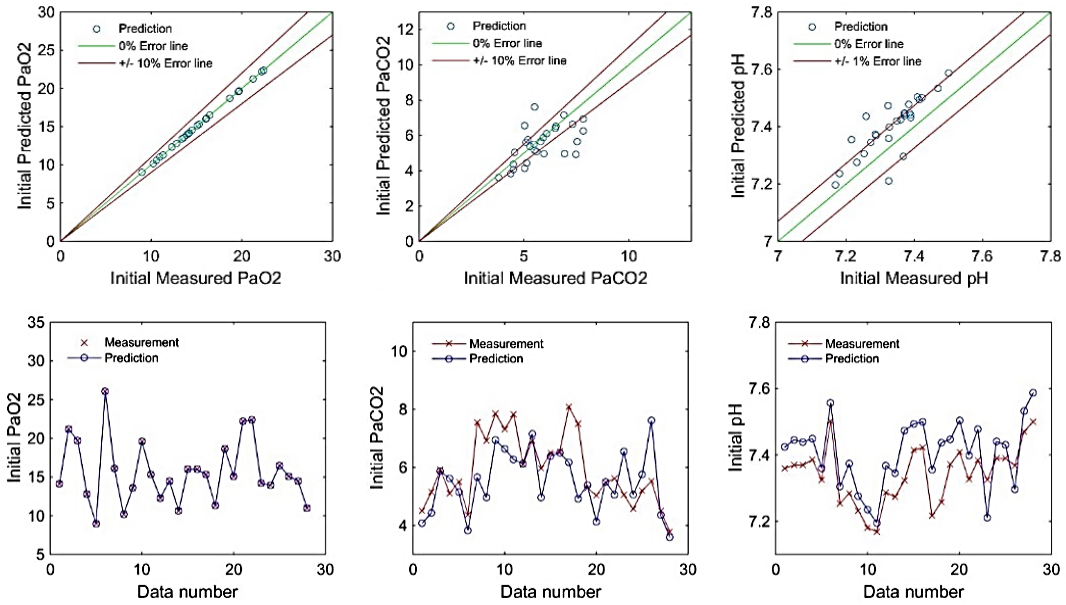

SOPAVent initial ABG prediction for Kd (ANFIS) and VCO_2 (ANFIS)

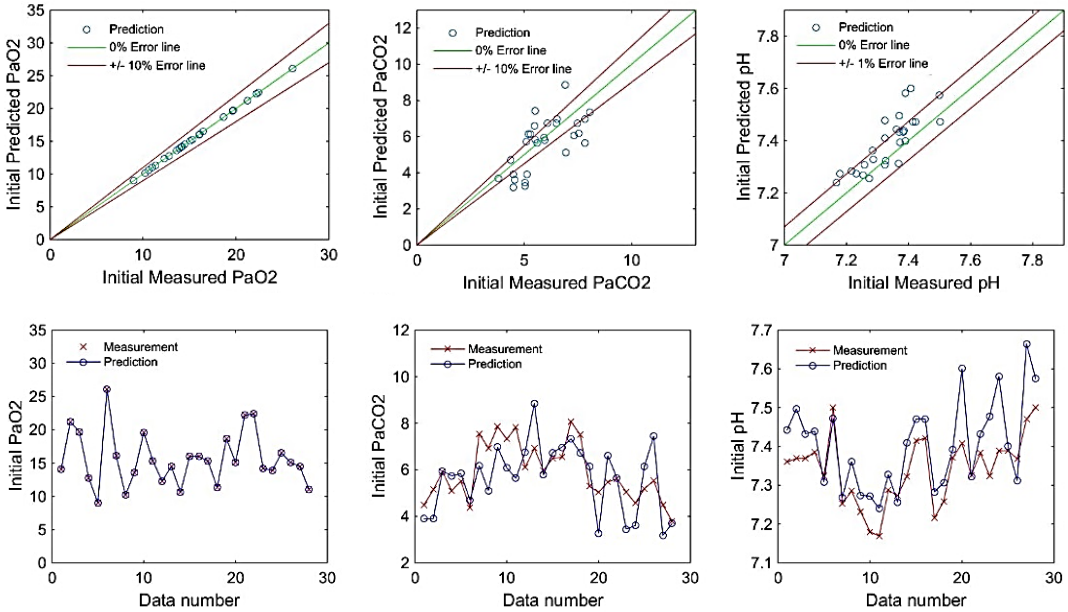

SOPAVent initial ABG prediction for Kd (IT2FLS) and VCO_2 (IT2FLS)

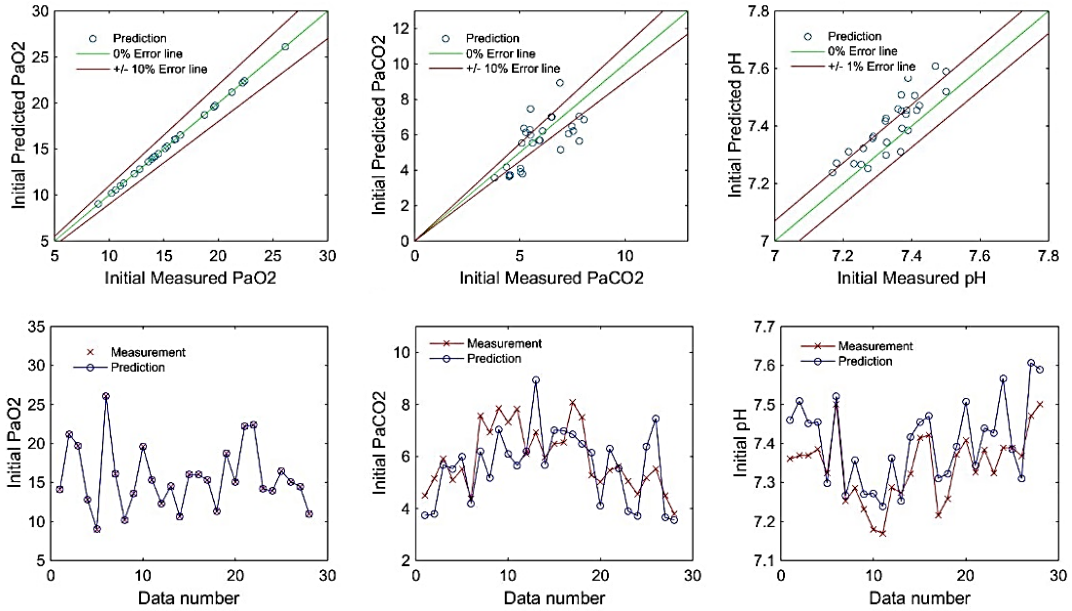

SOPAVent initial ABG prediction for Kd (IT2FLS nPSO) and VCO_2 (IT2FLS nPSO)

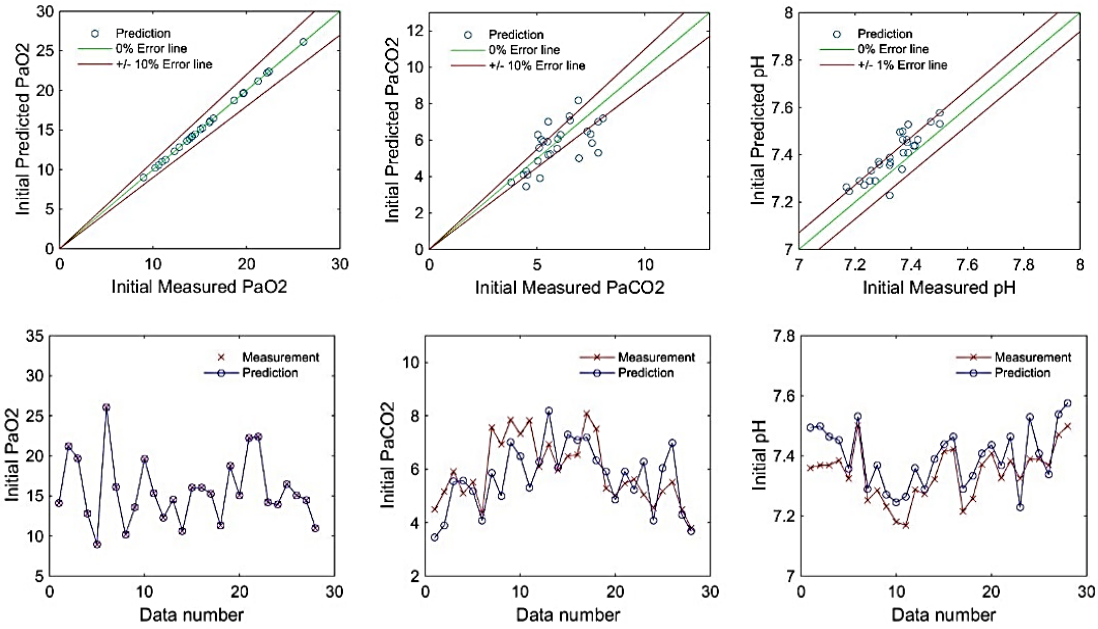

SOPAVent initial ABG prediction for Kd (FCM) and VCO_2 (FCM)

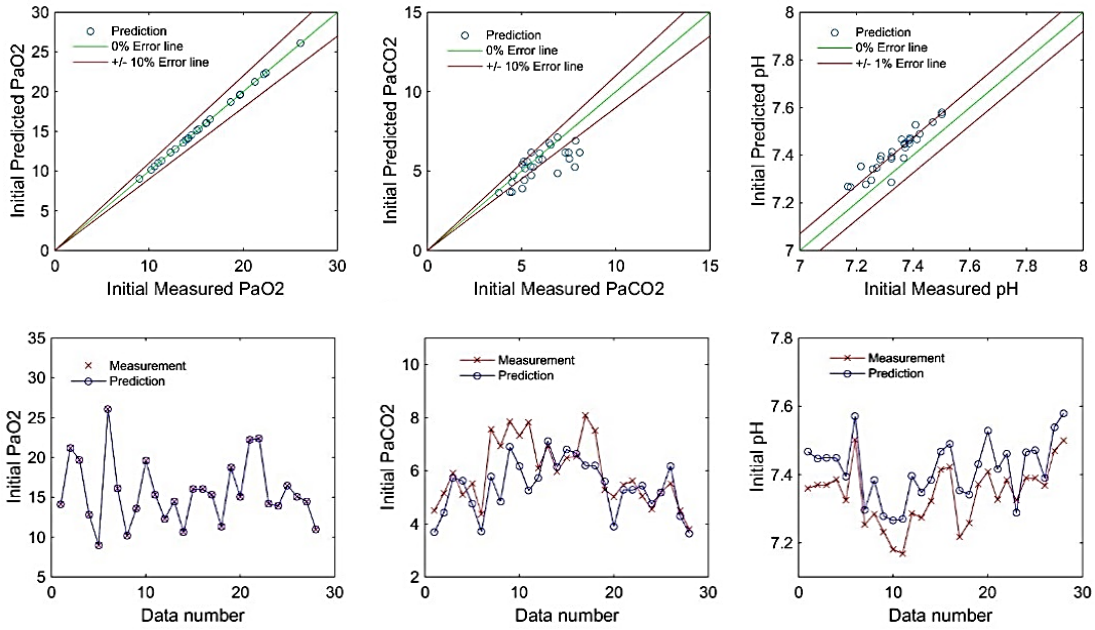

SOPAVent initial ABG prediction for Kd (FCM nPSO MSE) and VCO_2 (FCM nPSO MSE)

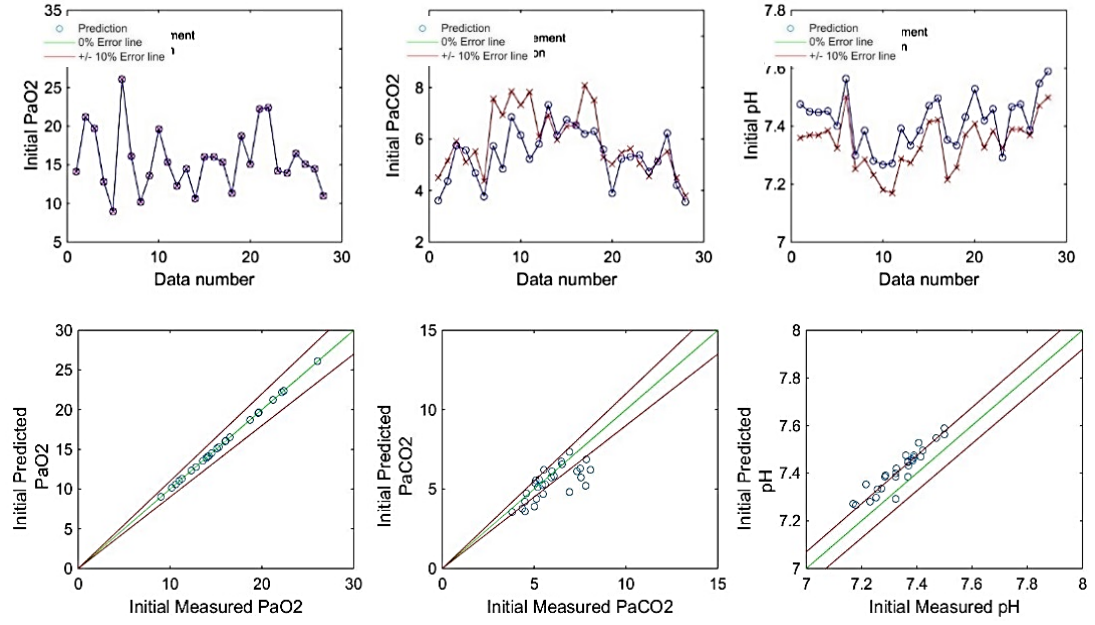

SOPAVent initial ABG prediction for Kd (FCM nPSO R^2) and VCO_2 (FCM nPSO R^2)

Appendix C3

Prediction Results for Post-Setting Change Predictions of PaO_2, $PaCO_2$ and of pH for SOPAVent Models for Patients with Faecal Peritonitis

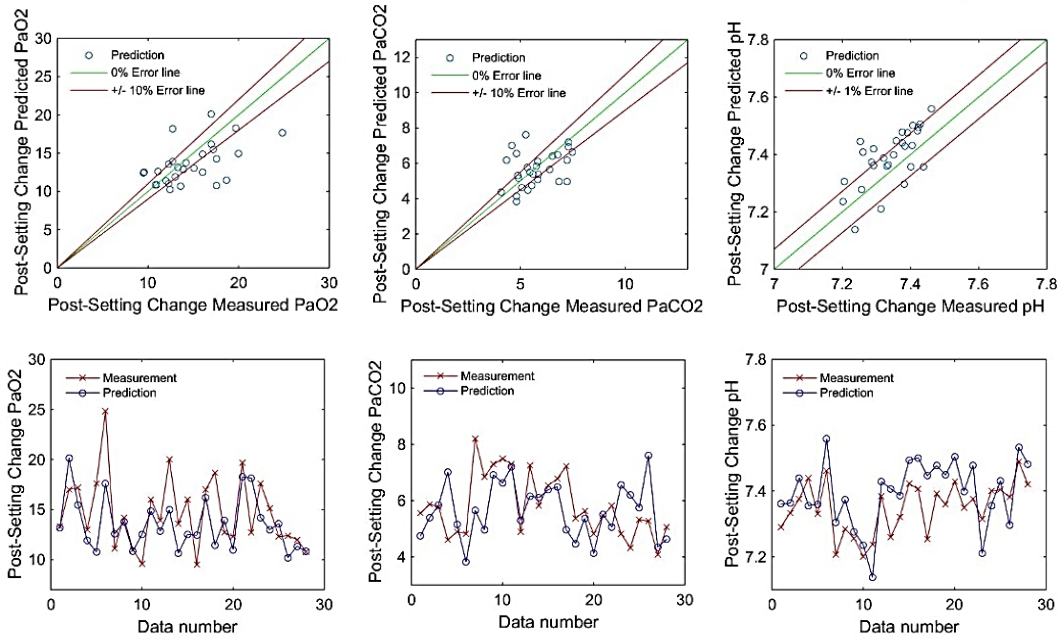

SOPAVent post setting-change ABG prediction for Kd (ANFIS) and VCO2 (ANFIS)

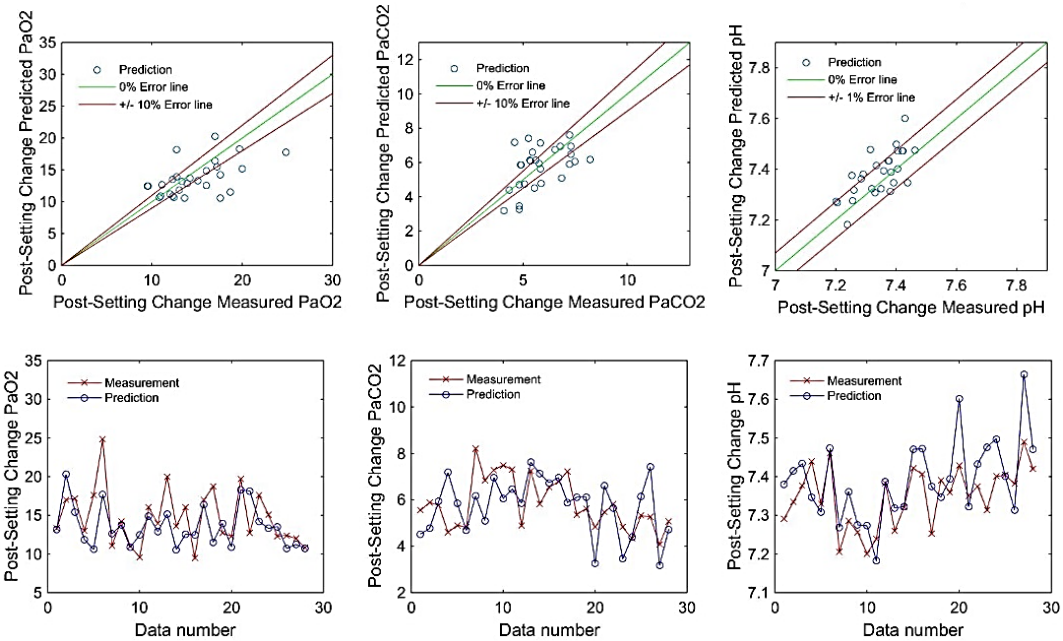

SOPAVent post setting-change ABG prediction for Kd (IT2FLS) and VCO_2 (IT2FLS)

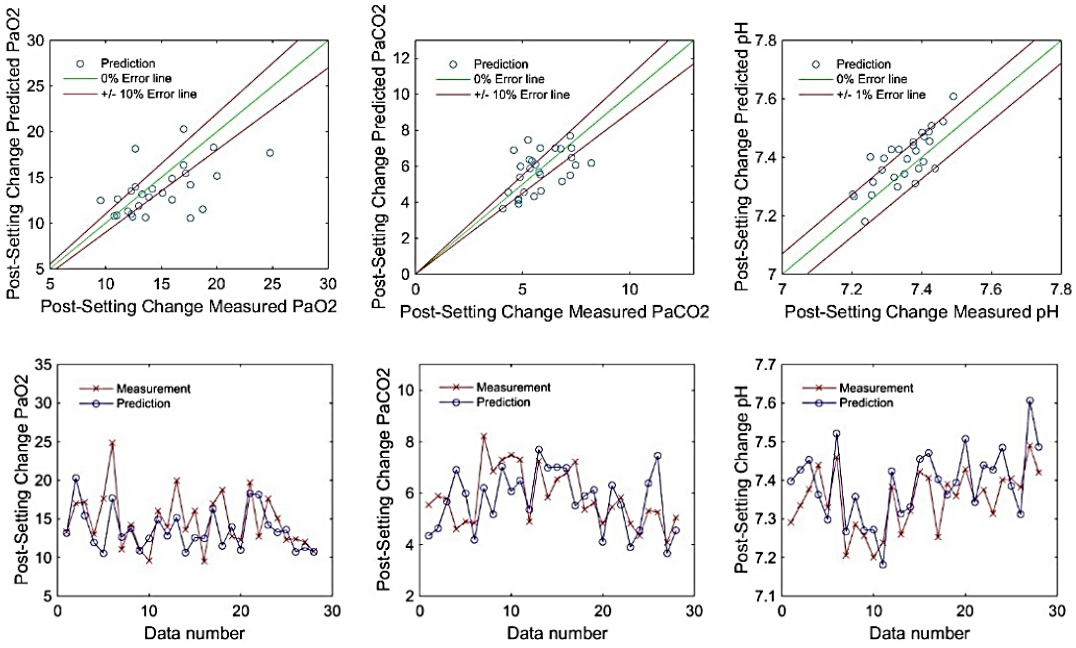

SOPAVent post setting-change ABG prediction for Kd (IT2FLS nPSO) and VCO_2 (IT2FLS nPSO)

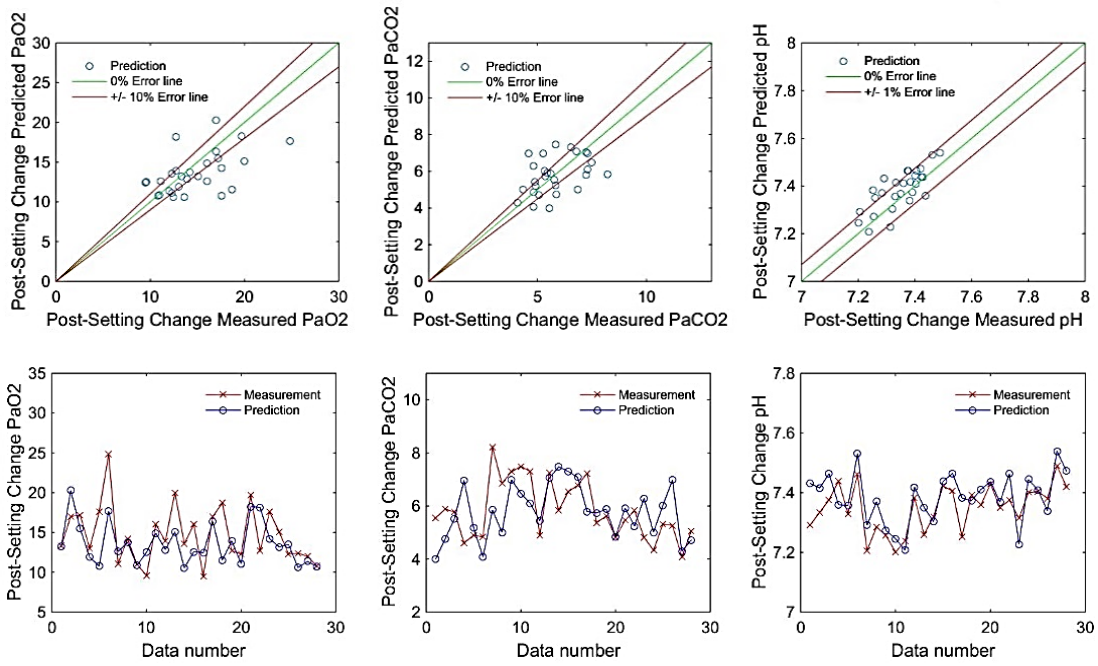

SOPAVent post setting-change ABG prediction for Kd (FCM) and VCO_2 (FCM)

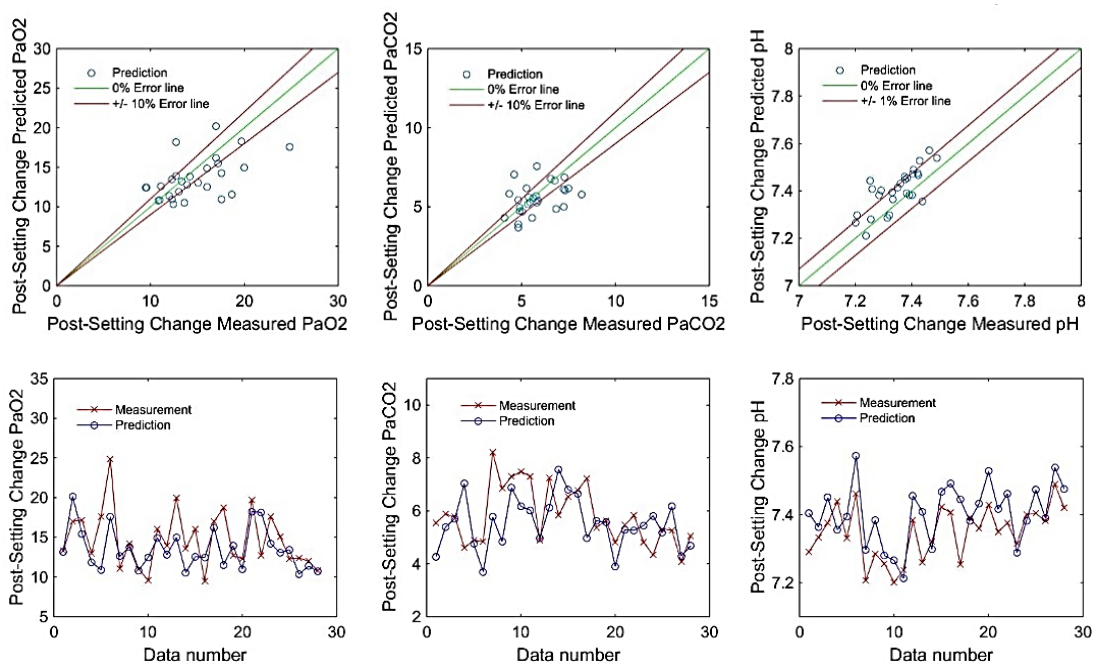

SOPAVent post setting-change ABG prediction for Kd (FCM nPSO MSE) and VCO_2 (FCM nPSO MSE)

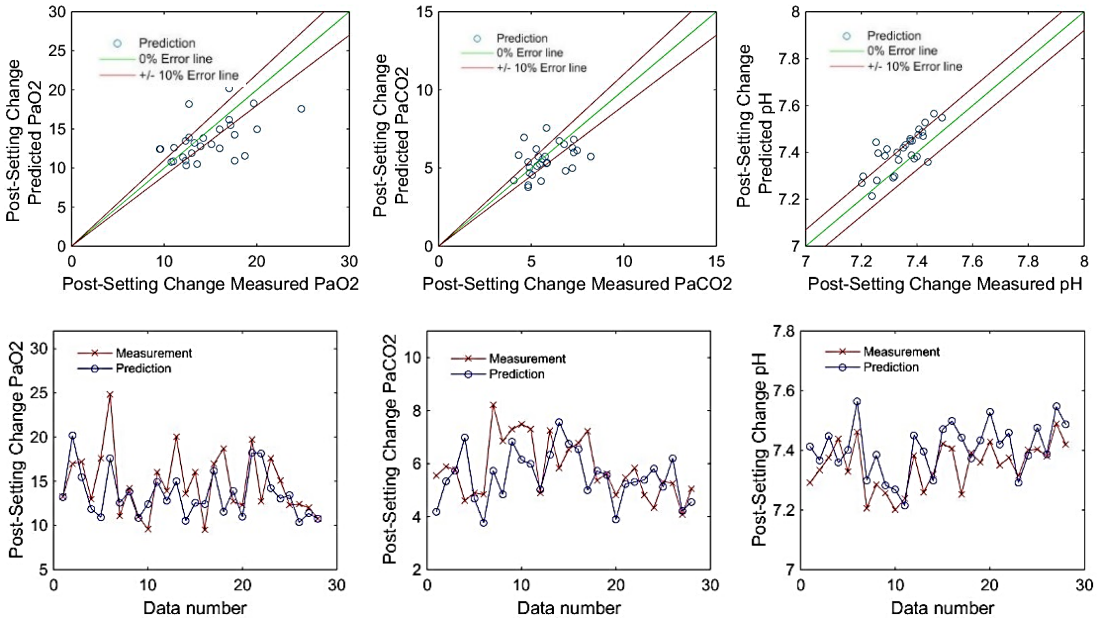

SOPAVent post setting-change ABG prediction for Kd (FCM nPSO R^2) and VCO_2 (FCM nPSO R^2)